FOSSIL ENERGY

DOE/BC/15101-2
(OSTI ID: 797644)

DISCRETE FEATURE APPROACH FOR HETEROGENEOUS RESERVOIR PRODUCTION ENHANCEMENT

Final Report
October 1, 1998-September 30, 2001

By:
William S. Dershowitz
Brendan Curran
Herbert Einstein
Paul LaPointe
Dawn Shuttle
Kate Klise

Date Published: July 2002

Work Performed Under Contract No. DE-AC26-98BC15101

Golder Associates Inc.
Redmond, Washington

National Energy Technology Laboratory
National Petroleum Technology Office
U.S. DEPARTMENT OF ENERGY
Tulsa, Oklahoma

DISCLAIMER

This report was prepared as an account of work sponsored by an agency of the United States Government. Neither the United States Government nor any agency thereof, nor any of their employees, makes any warranty, expressed or implied, or assumes any legal liability or responsibility for the accuracy, completeness, or usefulness of any information, apparatus, product, or process disclosed, or represents that its use would not infringe privately owned rights. Reference herein to any specific commercial product, process, or service by trade name, trademark, manufacturer, or otherwise does not necessarily constitute or imply its endorsement, recommendation, or favoring by the United States Government or any agency thereof. The views and opinions of authors expressed herein do not necessarily state or reflect those of the United States Government.

This report has been reproduced directly from the best available copy.

DOE/BC/15101-2
Distribution Category UC-122

Discrete Feature Approach for Heterogeneous Reservoir Production Enhancement

By
William S. Dershowitz
Brendan Curran
Herbert Einstein
Paul LaPointe
Dawn Shuttle
Kate Klise

July 2002

Work Performed Under DE-AC26-98BC15101

Prepared for
U.S. Department of Energy
Assistant Secretary for Fossil Energy

Purna Halder, Project Manager
U.S. Department of Energy
National Energy Technology Laboratory
National Petroleum Technology Office
One West Third Street, Suite 1400
Tulsa, OK 74103

Prepared by
Golder Associates Inc.
4104 148th Avenue, NE
Redmond, WA 98052

TABLE OF CONTENTS Page No.

1. EXECUTIVE SUMMARY 1

2. INTRODUCTION 3

2.1 Technology Development and Demonstration 3
2.2 Project Deliverables 7

3. RESULTS AND DISCUSSION 9

3.1 Research Summary 9
3.2 Task 1: Heterogeneous Reservoir Data Integration 9
3.2.1 Task 1.1.1 Fracture Size Analysis 9
3.2.1.1 Task 1.1.1 Fracture Size Analysis 10
3.2.1.2 Seismic Wave Methods 14
3.2.1.3 Ground Penetrating Radar (GPR) Methods 19
3.2.1.4 Hydraulic Interference Approaches 21
3.2.1.5 Analytical Development 25
3.2.1.6 Estimation of True Trace Length Distribution $f(l)$ 40
3.2.1.7 Effect of Sampling Plane Orientation on Trace Lengths 43
3.2.1.8 Verification by Numerical Simulation 45
3.2.1.9 Approach Implementation 51
3.2.1.10 Summary 67
3.2.2 Task 1.1.2 Fracture Shape Analysis 68
3.2.2.1 Literature Review 69
3.2.2.2 Analysis of Existing Information on Discontinuity Shape 74
3.2.2.3 Summary and Conclusions 77
3.2.3 Task 1.1.3 Application of Neural Nets to the Identification of Fracture Sets 77
3.2.3.1 Background 77
3.2.3.2 Kohonen Neural Network Algorithm 79
3.2.3.3 Implementation for Heterogeneous Reservoir Data 80
3.2.3.4 Algorithm Demonstration, Yates Field Tract 17 83
3.2.3.5 Applications for Heterogeneous Reservoir Data 87
3.2.4 Task 1.1.4 Fractal Methods for Derivation of Fracture Statistics 89
3.2.4.1 Fractal Fracture Size Distributions 89
3.2.4.2 Trace Length Statistics 93
3.2.4.3 Derivation of Size Distribution from Trace Data 93
3.2.4.4 Verification of Fractal Algorithm for Fracture Size 98
3.2.4.5 Fractal Fracture Size Distribution from Non-planar Surfaces 104
3.2.5 Task 1.1.5 Transmissivity/Connectivity Analysis 106
3.2.6 Task 1.1.6 Fracture Correlations 109
3.2.7 Task 1.2 Data Scaling Procedures 111

3.2.7.1 Multiscale Modeling 126
3.2.7.2 Data Scaling for Equivalent Continuum Modeling 127
3.2.7.3 Data Scaling for Discrete Feature Network Modeling. 127
3.2.8 Task 1.3.0 Heterogeneous Reservoir Interdisciplinary Database 129
3.3 Task 2: DFN Model Development 133
3.3.1 Task 2.1 DFN Model Approaches 133
3.3.1.1 Statistical Models 133
3.3.1.2 Geocellular Models 136
3.3.1.3 Geomechanical Models 140
3.3.2 Tasks 2.2, 2.3, and 2.4 Site DFN Model Development, Implementation, and Validation 145
3.4 Task 3: Reservoir Improvement Strategy 145
3.4.1 Task 3.1. Strategic Plan: Yates Field Reservoir Improvement 150
3.4.1.1 Surfactant Flood DFN Analysis 150
3.4.1.2 Strategic Completion DFN Analysis 163
3.4.2 Task 3.2 Strategic Plan, Stoney Point Reservoir Improvement 178
3.4.2.1 Strategic Placement and Water Control 178
3.4.2.2 DFN Analysis for IOR Strategic Plan 179
3.4.3 Task 3.3 Strategic Plan: South Oregon Basin Reservoir Improvement 188
3.4.3.1 DFN Strategy for IOR 188
3.4.3.2 DFN Analysis for Strategic Plan 188
3.4.4 Task 3.4 Strategic Plan : North Oregon Basin Reservoir Improvement 197
3.4.4.1 Gel Treatment DFN Analysis 197
3.5 Task 4: Application Tasks 205
3.5.1 Task 4.1 Reservoir IOR Demonstration, Yates Field 205
3.5.1.1 Introduction to Strategic Completion Analysis 205
3.5.1.2 Strategic Completion Modeling 206
3.5.1.3 Well Productivity Correlation 207
3.5.1.4 Strategic Completion Recommendations 214
3.5.1.5 Evaluation 223
3.5.2 Task 4.2 Reservoir IOR Demonstration, Stoney Point 226
3.5.2.1 Discrete Fracture Network Model 226
3.5.2.2 Evaluation 234
3.5.3 Task 4.3 Reservoir IOR Demonstration, South Oregon Basin 234
3.5.3.1 South Oregon Basin DFN Model 234
3.5.3.2 South Oregon Basin Gel Simulations 261
3.5.3.3 Evaluation 261
3.5.4 Task 4.4 Reservoir IOR Demonstration, North Oregon Basin 266
3.5.4.1 Evaluation – North Oregon Basin 267
3.6 Task 5: Technology Transfer 272
3.6.1 Task 5.1. Project Web Site 272
3.6.2 Task 5.2.1 Reports 272
3.6.3 Task 5.2.3 Presentations and Publications 272
4. CONCLUSIONS 273

5. REFERENCES 275

LIST OF FIGURES

Figure 2-1: DFN Approach for Reservoir Characterization and Engineering 4
Figure 2-2: DFN Approaches for IOR 5
Figure 3-1 Fracture Interpolation 10
Figure 3-2 Forward Modeling Approach (after Dershowitz, 1992) 13
Figure 3-3 VSP Identification for Fracture Size 14
Figure 3-4 VSP Tomography 15
Figure 3-5 VSP Approaches (a) Offset and (b) Walkway 16
Figure 3-6 Seismic Wave Reflection by Features of Multiple Scales 17
Figure 3-7 Loss of Seismic Signals Due to Karsts and Inclusions 18
Figure 3-8 Wellbore Seismics 18
Figure 3-9 Wellbore Seismic Surveys 19
Figure 3-10 Radar Tomography 21
Figure 3-11 Hydraulic Interference Testing 22
Figure 3-12 Fracture Network Effects 23
Figure 3-13 Packer Testing 23
Figure 3-14 Tracer Testing at URL (Novakowski et al., 1985) 24
Figure 3-15 Parameters used in the definitions of discontinuity 28
Figure 3-16 Construction used in deviation of relationship between discontinuity size distribution and trace length distribution 29
Figure 3-17 Relationship between *h, l,* and *a* 33
Figure 3-18 Discontinuities intersect a circular sampling window in three ways 41
Figure 3-19 Variation of mean trace length with β 45
Figure 3-20 Variation of standard deviation of trace length with β 46
Figure 3-21 (a) Simulation volume is a box, i.e., the elliptical discontinuities are generated inside the box; (b) Sampling window at x = 0 m 47
Figure 3-22 Comparison of theoretical mean trace lengths with predicted mean trace lengths from simulations 50
Figure 3-23 Comparison of the theoretical standard deviation of trace lengths with predicted standard deviation of trace lengths from simulations 53
Figure 3-24 Variation of μ_a and σ_aw ith aspect ratio *k* for assumed major axis orientation 1 (0°/0°): assuming a lognormal distribution form of *g(a)* 55
Figure 3-25 Variation of μ_a with aspect ratio *k* for assumed major axis orientation 1 (0°/0°): assuming a negative exponential distribution form of *g(a)* 56
Figure 3-26 Variation of μ_a and σ_a with aspect ration *k* for assumed major axis orientation 1 (0°/0°): assuming a Gamma distribution form of *g(a)* 57
Figure 3-27 Variation of μ_a and σ_a with aspect ration *k* for assumed major axis orientation 2 (30°/0°): assuming a lognormal distribution form of *a* 58
Figure 3-28 Variation of μ_a with aspect ration *k* for assumed major axis orientation 2 (30°/0°): assuming a negative exponential distribution form of *a* 59
Figure 3-29 Variation of μ_a and σ_a with aspect ration *k* for assumed major axis orientation 2 (30°/0°): assuming a Gamma distribution form of *a* 60
Figure 3-30 Variation of μ_a and σ_a with aspect ration *k* for assumed major axis orientation 3 (60°/0°): assuming a lognormal distribution form of *a* 61

Figure 3-31 Variation of μ_a with aspect ration k for assumed major axis orientation 3 (60°/0°): assuming a negative exponential distribution form of a 62
Figure 3-32 Variation of μ_a and σ_a with aspect ration k for assumed major axis orientation 3 (60°/0°): assuming a Gamma distribution form of a 63
Figure 3-33 (a) An unrestricted discontinuity; and (b) A restricted discontinuity 70
Figure 3-34 (a) Strike and dip of a discontinuity; and (b) Strike and dip traces 71
Figure 3-35 Dip dimension vs. strike dimension for nominally unrestricted faults from four regions (see Table 3-15) (from Nicol et al. 1996) 73
Figure 3-36 A polygon is used to represent an elliptical discontinuity (fracture) (from Dershowitz et al. 1993) 75
Figure 3-37 Three possible cases at which the average strike length is about equal to the average dip length: (a) Discontinuities are equidimensional (circular); (b) discontinuities are non-equidimensional (elliptical) with long axes in a single orientation. The discontinuities are oriented so that the average strike length is about equal the average dip length; and (c) Discontinuities are non-equidimensional with long axes such randomly oriented that the average strike length is about equal to the average dip length. 76
Figure 3-38 Self-Organizing (Kohonen) Network Model 80
Figure 3-39 Contour Plot of Test Data with Three Fracture Sets 82
Figure 3-40 Neural Net Performance Results for 3 Set Test Case 84
Figure 3-41 Contour Plot of Joint Orientations in Three Yates Wells 85
Figure 3-42 Contour Plot of Sets Identified by Structural Geologist 86
Figure 3-43 Contour Plots of Sets Identified by Neural Network 88
Figure 3-44 Fracture Intersection with Trace Plane 97
Figure 3-45 Example DFN Model for Size Analysis 99
Figure 3-46 Complementary Cumulative Density Functions (CCDF) for Fracture Radius 102
Figure 3-47 Fitted Trace Length Distributions 103
Figure 3-48 Flow Dimension 112
Figure 3-49 Channels in Fracture Plane 113
Figure 3-50 Channels in Faults and Fractures 114
Figure 3-51 Background Fracture Porosity and Connectivity 115
Figure 3-52 Productivity Test with Single Channel, Well on Channel 116
Figure 3-53 Production Test with Single Channel, Well on Fault 116
Figure 3-54 Production Test with Single Channel, Well in Background Fractures 117
Figure 3-55 Size Transmissitivity Relationship at Äspö Sweden 117
Figure 3-56 Data Scaling for Continuum Approaches 118
Figure 3-57 Multiscale Modeling with Discrete Fracture Networks 119
Figure 3-58 Fractal Dimension Calculation 120
Figure 3-59 Example Strata model Data from South Oregon Basin 121
Figure 3-60 Example Tracer Breakthrough Curves from North Oregon Basin 122
Figure 3-61 Cone Photos from Orchard 14, North Oregon Basin 123
Figure 3-62 Yates Tops Cross Section 124
Figure 3-63 South Oregon Basin Seismic Lineaments 124
Figure 3-64 South Basin Geocellular ModelExample 125
Figure 3-65: Stoney Point, Trenton Structure 130
Figure 3-66: Stoney Point, Geophysical Cross Sections 131
Figure 3-67: Stoney Point, Lost Circulation 132
Figure 3-68 Fracture Growth Model (after Swaby and Rawnsly, 1996) 144
Figure 3-69 3Dmove Palinspastic Reconstruction (Midland Valley, 2001) 144
Figure 3-70 Goesec2D Palinspasic Reconstruction 145

Figure 3-71 Strain Fields for Fracture Generation 146
Figure 3-72 Geomechanical Modeling of 3D Fracture Populations 146
Figure 3-73 Preliminary Yates DFN Model 147
Figure 3-74 Preliminary Stoney Point DFN Model 148
Figure 3-75 Preliminary North Oregon Basin DFN Model 149
Figure 3-76 Preliminary South Oregon Basin DFN Model 149
Figure 3-77 DFN Model Illustrating Surfactant Imbibition 151
Figure 3-78 Surfactant Injection Strategies 153
Figure 3-79 Well 2913 was treated with surfactant late in 1997 and responded with stimulated liquid productivity and reduced water-oil ratio (WOR) after recovery of treatment fluid. The stimulated fluid productivity has been maintained while the WOR has resumed an upward trend. 154
Figure 3-80 Response to injection over one mile away is observed almost immediately at a well which is producing at an elevation over 100 feet above the fracture flow feature taking the surfactant in the injection well 155
Figure 3-81 Conceptual Fracture Model 156
Figure 3-82 Surfactant Concentration Profile in Fracture 160
Figure 3-83 Schematic View of Reservoir Model 161
Figure 3-84 Comparison of Results from Simulation and Analytical Model 162
Figure 3-85 Effects of Convection Rate on Fracture Area Treated 162
Figure 3-86 Effects of Molecular Diffusion on Fracture Area Treated 163
Figure 3-87 Intersection Statistics for Deepening Candidate Wells 164
Figure 3-88 Compartment Volume Distribution, W1304 167
Figure 3-89 Compartment Projected Area Distribution, W1304 167
Figure 3-90 Compartment Volume, Yates Deepening Candidates 169
Figure 3-91 Compartment Projected Area Distribution, Yates Deepening Candidates 169
Figure 3-92 Block Volume Statistics 172
Figure 3-93: Block Volume Distribution 173
Figure 3-94 Block Sigma Factor Statistics 174
Figure 3-95 Block Sigma Factor Distributions 175
Figure 3-96 Median Block Aspect Ratio 176
Figure 3-97 Distribution of Block Aspect Ratio 177
Figure 3-98 Median Ratio of Height to Horizontal Area 177
Figure 3-99 Mean Ratio of Height to Horizontal Area 178
Figure 3-100 Tributary Drainage Volume Algorithms 180
Figure 3-101 Compartments in Stoney Point DFN 182
Figure 3-102 Projected Areas of Compartments 183
Figure 3-103 Volumes of Compartments in Stoney Point Model 184
Figure 3-104 Well Configuration for Tributary Volume Analysis of Stoney Point Model 185
Figure 3-105 Tributary Volumes of Stoney Point Model 186
Figure 3-106 Well Pattern and Tributary Volumes Intersected in Stoney Point Model 187
Figure 3-107 South Oregon Basin Gel Treatment Analysis Region 189
Figure 3-108 Network Analysis for Gel Treatment Design 190
Figure 3-109 Gel Injection into Fracture Network 190
Figure 3-110 South Oregon Basin Compartmentalization Analysis 193
Figure 3-111 Tributary Volumes in South Oregon Basin Model for P_{32} = 0.2 Model 194
Figure 3-112 Tributary Volumes in South Oregon Basin Model for P_{32} = 0.3 Model 195
Figure 3-113 South Oregon Basin Tributary Volume Analysis 196
Figure 3-114 Tensleep Formation Water Injection DFN Study. 197
Figure 3-115 Compartments in North Oregon Basin Model with P_{32}=0.2 200
Figure 3-116 North Oregon Basin Compartmentalization Analysis 201

Figure 3-117 North Oregon Basin Model with $P_{32} = 0.2$ 202
Figure 3-118 Side View of Tributary Volumes of Vertical and Horizontal Wells in North Oregon Basin Model with $P_{32} = 0.2$ 203
Figure 3-119 North Oregon Basin Tributary Volume Analysis 204
Figure 3-120: Mean East/West Fracture Spacing 215
Figure 3-121: Mean North-South Fracture Spacing 216
Figure 3-122: Mean Vertical Fracture Spacing 217
Figure 3-123: Mean Vertical to East/West Fracture Spacing 218
Figure 3-124: Mean Vertical to North/South Fracture Spacing 219
Figure 3-125: Mean East/West Spacing to North/South Fracture Spacing 220
Figure 3-126: Mean Vertical Block Height to Cross-Sectional Area 221
Figure 3-127: Mean Vertical to Averaged Horizontal Fracture Spacing 222
Figure 3-128: Median Sigma Factor 223
Figure 3-129 Efficacy of Surfactant Treatment on YU 1106 225
Figure 3-130 Efficacy of Surfactant Treatment on Project Study Site Yates (Tract 29) 226
Figure 3-131: Stoney Point DFN Model, 2000 meter Extent, Fractures Only 228
Figure 3-132: Simulation Volume (800x400x189m) Stoney Point DFN Model (Fractures and Matrix Features) 229
Figure 3-133: Full Fracture Set for Stoney Point, Fractures, and Matrix 229
Figure 3-134: Flow solution after 0.1 hours, pre-gel treatment. Note pressure has connected directly from injector to producer 231
Figure 3-135: Stoney Point Flow Solution Pre-Gel treatment: Close up showing pressure bypassing matrix through fractures 232
Figure 3-136 Stoney Point: Pressure after 0.1 with gel treatment reducing the fracture permeability by a factor of 10. 233
Figure 3-137 Stoney Point Pressure field at 0.1 hours after gel-treatment reduces permeability by a factor of 100 234
Figure 3-138: Fracture Set Orientations for South Oregon Basin 237
Figure 3-139: All Seismic Lineaments for South Oregon Basin 237
Figure 3-140 EW Seismic Lineament Set 238
Figure 3-141: NS Lineament Set 239
Figure 3-142: NE Lineament Set 240
Figure 3-143 ESE Seismic Lineament Set 241
Figure 3-144: Trace Length Distribution, All Lineaments 242
Figure 3-145: Trace Length Distribution, EW Lineaments 243
Figure 3-146: Trace Length Distribution, ESE Lineament 244
Figure 3-147: Trace Length Distribution, NE Lineaments 245
Figure 3-148 Trace Length Distribution, NS Lineaments 246
Figure 3-149: Simulation of ESE Lineaments 10 ft. Scale 248
Figure 3-150: Simulation of ESE Lineaments, 100 ft. scale 249
Figure 3-151: Simulation of ESE Lineament, 500 ft. Scale 250
Figure 3-152 Simulation of ESE Lineaments, 1300 ft. Scale 251
Figure 3-153: Simulation of ESE Lineaments, 2000 Ft. Scale 252
Figure 3-154 Simulation of ESE Lineaments, Exponent 1.5 253
Figure 3-155 Simulation of ESE Lineaments, Exponent 2.5 254
Figure 3-156: Simulation of ESE Lineaments, Exponent 3 255
Figure 3-157: Simulation of ESE Lineaments, Exponent 3.5 256
Figure 3-158: Simulation of ESE Lineaments, Intensity $P_{32} = 0.001\ m^2/m^3$ 257
Figure 3-159: Simulation of ESE Lineaments, Intensity $P_{32} = 0.01\ m^2/m^3$ 258
Figure 3-160: Simulation of ESE Lineaments, Intensity $P_{32} = 0.01\ m^2/m^3$ 259
Figure 3-161: Fractures for South Oregon Basin Simulation 259

Figure 3-162: Matrix Discrete Features for South Oregon Basin Simulation 260
Figure 3-163: Fractures and Matrix Close up for South Oregon Basin Simulation 260
Figure 3-164 South Oregon Basin simulation pre gel. Time = 0.001 Hours 262
Figure 3-165: South Oregon Basin simulation pre gel. Time = 0.01 Hours 262
Figure 3-166: South Oregon Basin simulation pre gel. Time = 1 Hour 263
Figure 3-167: South Oregon Basin simulation after gel treatment reduces fracture permeability 1 order of magnitude 263
Figure 3-168: South Oregon Basin simulation after gel treatment reduces fracture permeability 2 orders of magnitude 264
Figure 3-169: South Oregon Basin simulation after gel treatment reduces fracture permeability 3 orders of magnitude 265
Figure 3-170: North Oregon Basin Structure and Well Control 267
Figure 3-171: North Oregon Basin DFN model 269
Figure 3-172: North Oregon Basin DFN model before gel treatment 270
Figure 3-173: North Oregon Basin DFN model after gel treatment 271

LIST OF TABLES

Table 1-1: Major Accomplishments of DOE/FETC Project "Discrete Feature Approach for Heterogeneous Reservoir Production Enhancement" 2
Table 2-1: Project Deliverables and Milestones 7
Table 3-1 Expression for determining μ_a and σ_a from μ_l and σ_l 39
Table 3-2 Expression for determining μ_l and σ_l from μ_a and σ_a 39
Table 3-3 Common Distribution Forms of Trace Lengths 43
Table 3-4 Parameters for simulation 1 using FracMan (see also Figure 3-21) 48
Table 3-5 Theoretical values of Trace Length Mean and Standard Deviation 49
Table 3-6. Comparison of theoretical (or true) and predicted mean trace lengths 49
Table 3-7 Comparison of theoretical (or true) and predicted standard deviation of trace lengths 52
Table 3-8 Derived true trace length distributions 54
Table 3-9 Assumed major axis orientations and their corresponding β values 64
Table 3-10 Predicted values of k, μ_a and σ_a at major axis orientation (30°/0°) 64
Table 3-11 Checking the distribution of $g(a)$ for sampling window 1 (β = 63.4°) 65
Table 3-12 Checking the distribution of $g(a)$ for sampling window 2 (β = 33.7°) 66
Table 3-13 Checking the distribution of $g(a)$ for sampling window 3 (β = 0°) 67
Table 3-14 Mean of strike trace lengths and mean of dip trace lengths of two discontinuity sets (from Einstein et al. 1979) 72
Table 3-15 Details of the four data sets plotted in Figure 3-35 (from Nicol et al. 1996) 73
Table 3-16 Example Dataset for Kohonen Network Demonstration 81
Table 3-17 Kohonen Network for Example Data Set 82
Table 3-18 Kohonen Network for Yates Tract 17 Data Set 83
Table 3-19 Parameters used in simulations 100
Table 3-20 List of file names for verification tests. 100
Table 3-21 Verification of Fractal Fracture Size Algorithm 101
Table 3-22 Parameter values estimated for the observed trace lengths. 103
Table 3-23 Parameters for the radius distribution of fractures intersecting the trace plane. 103
Table 3-24: Correlation of Fracture Geometrical Hydraulic Properties 110
Table 3-25 Heterogeneous Reservoir Interdisciplinary Database 130
Table 3-26 POC Dimensions 136
Table 3-27 Summary of Intersection Simulations, Yates Deepening Candidates 165

Table 3-28 Compartment Projected Area Statistics, Well W1304 166
Table 3-29 Compartment Projected Area Statistics, Well W1304 166
Table 3-30 Compartment Volume Statistics, Yates Deepening Candidate Wells 168
Table 3-31 Compartment Projected Area Statistics, Yates Deepening Candidate Wells 168
Table 3-32 Matrix Block Volume Statistics 170
Table 3-33 Matrix Block Sigma Factor Statistics 170
Table 3-34 Matrix Block Z/X Ratio Statistics 171
Table 3-35 Matrix Block Aspect Ratio Z/Y Statistics 171
Table 3-36 Matrix Block Aspect Ratio X/Y Statistics 171
Table 3-37 Ratio of Block Height to Horizontal Area 172
Table 3-38 Compartment Area and Volume Analysis, Stoney Point 181
Table 3-39 Tributary Volume Analysis, Stoney Point 181
Table 3-40 IOR Engineering Issues, South Oregon Basin 188
Table 3-41 Compartment Area and Volume Analysis, South Oregon Basin 191
Table 3-42 Tributary Volume Analysis, South Oregon Basin 192
Table 3-43 Implications of Tributary Volume Analysis, South Oregon Basin 192
Table 3-44 IOR Engineering Issues at North Basin 198
Table 3-45 Compartment Area and Volume Analysis, North Oregon Basin 198
Table 3-46 Tributary Volume Analysis, North Oregon Basin 198
Table 3-47 Implications of Tributary Volume Analysis, North Oregon Basin 205
Table 3-48 Conditioned DFN Model for TAGS Support Simulations (Extended Tract 17 Model) 207
Table 3-49: Variable name acronyms and calculation definitions for matrix block shape factors 207
Table 3-50: Correlation coefficients for the fracture models surrounding the five wells: 1304, 1307,1495, 2513 and 2722 210
Table 3-51: Correlation coefficients for the fracture models surrounding all wells. 211
Table 3-52 Correlation coefficients with barrels of fluid per day for the five wells 1304, 1307,1495, 2513 and 2722 212
Table 3-53: Probability (p-values) for the regression coefficients between independent matrix block shape parameters and BFPD for five wells: 1304, 1307,1495, 2513 and 2722 213
Table 3-54: Stoney Point DFN Model Parameters, Trenton Formation 230
Table 3-55: South Oregon Basin Lineament Analysis 236
Table 3-56: Intensity from Lineament Data 247
Table 3-57: South Oregon Basin DFN Model 248
Table 3-58: North Oregon Basin Bed Thickness 267

1. EXECUTIVE SUMMARY

This report is the final report for the project, "Discrete Feature Approach for Heterogeneous Reservoir Production Enhancement." The report presents summaries of technology development for discrete feature modeling in support of the improved oil recovery (IOR) for heterogeneous reservoirs. In addition, the report describes the demonstration of these technologies at project study sites.

In the discrete feature network (DFN) approach, conductive and flow barrier structures are modeled explicitly, facilitating a more realistic analysis of flow. The DFN approach models these features at all scales simultaneously, from the individual fractures intersecting a well to the major faults which define the reservoir. These discrete features are extrapolated from geological and geophysical measurements using a combination of geological and geostatistical methods.

During this project, Golder Associates' team improved the data analysis and geological modeling capabilities of the DFN approach, and developed practical applications of that approach for IOR in heterogeneous reservoirs.

Major accomplishments of this research project are summarized in Table 1-1. These include development of approaches for gel treatment, strategic completion, and water control in heterogeneous reservoirs. The discrete fracture network technologies developed within this project are directly applicable to a large percentage of the secondary and tertiary oil recovery projects currently underway in the United States, and can be of significant value to the design of future oil recovery projects.

This project achieved significant technological advances in the development of the discrete fracture network modeling approach for heterogeneous oil reservoirs. Advances include:

- the first large scale, fracture network multiphase DFN flow simulations (Oregon Basin)
- direct DFN simulation of gel injection to realistic fracture networks (Oregon Basin, Stoney Point)
- three dimensional, heterogeneous, geo-cellular based DFN modeling for strategic completion (Yates)
- neural network algorithm development for fracture set identification
- fractal, analytical, and numerical solutions for calculation of fracture size distributions from geological and geophysical trace data
- a discrete fracture network approach for conditioning of fractured reservoir connectivity based on tracer tests
- new approaches to evaluating fracture shapes and correlations between fracture properties.

Table 1-1: Major Accomplishments of DOE/FETC Project "Discrete Feature Approach for Heterogeneous Reservoir Production Enhancement"

Production Issue	**Study Site**	**Geology**	**DFN Approach to Support Secondary/Tertiary Recovery**
Declining oil production due to decreases in formation pressures and higher viscosity of remaining OIP	Yates, Texas	Thick, high quality carbonate reservoir with heterogeneous, solution enhanced fracture connectivity	Strategic completions to maximize fracture intersections for steam injections and gravity drainage. Location of strategic completions using a DFN model based on a geological extrapolation of fracture patterns measured in geophysical logs
Higher water cut due to discrete flow in solution enhanced fractures	South Oregon Basin, Wyoming	Permian age carbonate with several scales of fracture overprint	Gel treatment to improve sweep efficiency through the interbedded sandstones, while reducing water cut
Higher water cut during water injections, as fracture networks at interbeds provide direct pathways from water injection wells to production wells	North Oregon Basin, Wyoming	High quality eolian dune sandstones of varying connectivity interbedded with lower permeability dolomites	Gel treatment to improve sweep efficiency through the interbedded sandstones, while reducing water cut
Interwell connectivity of highly oriented fractures along a wrench fault providing imperfect fracture connections throughout a very low quality dolomite matrix	Stoney Point, Michigan	Dolomitized carbonates containing significant large scale karstic porosity and fracture connectivity	Strategic completion placement to improve the probability of fracture connections to supplement flow through the dolomite
Water production due to discrete connections to overlying aquifers	Stoney Point, Michigan	Dolomitized carbonates containing significant large scale karstic porosity and fracture connectivity	DFN gel injection simulations to assess the feasibility of blocking water pathways

2. INTRODUCTION

2.1 Technology Development and Demonstration

Often less than half of the original oil in place (OIP) in reservoirs is recovered. In reservoirs where discontinuous features such as fractures or discontinuous sands play a significant role in reservoir permeability, the ultimate recovery can be less than 10% of the estimated OIP. The remaining oil is either technically or economically unrecoverable. This unrecovered oil represents a significant potential resource for the mature petroleum industry in the United States.

During this project, the Golder Associates team developed and demonstrated the use of discrete feature network (DFN) models as the key tool for integrating geological, geophysical, and engineering data to improve reservoir development and increase oil production efficiency. Discrete feature network approaches have a unique ability to integrate the data used to characterize reservoir heterogeneity from a wide range of scales into a comprehensive model which can be used directly to improve reservoir engineering. This is possible because unlike conventional continuum approaches, the DFN approach is based on parameters directly gained from field measurements (Figure 2-1).

This project developed and demonstrated practical technologies for improvement of production efficiency in heterogeneous reservoirs through integration of diverse data at a range of scales. DFN approaches were used to directly address key issues which control oil production (Figure 2-2):

1. **Strategic Completion Placement**: In heterogeneous depositional systems as well as in fractured reservoirs, the placement of injection and production completions can have a key role in determining production efficiency and ultimate recovery. For example, fracture networks delivering water to the well need to be avoided in production wells, while fractures that are part of extensive fracture networks feeding oil to the well need to be intersected. The key to efficient production thus requires an understanding of the flow architecture in the fracture network at the scale of the well, as well as an understanding of the larger scale networks which feed oil and water toward production wells.
2. **Enhanced Completion Connection:** In reservoirs of highly varying flow capacity there is often a need to improve the connection between the well completion and the discrete reservoir flow network. Marathon Oil has developed advanced techniques for hydraulic fracture stimulation, extreme overbalanced perforation-stimulation, and horizontal well placement. These techniques can be applied most effectively with an understanding of the discrete feature network flow characteristics of the reservoir.

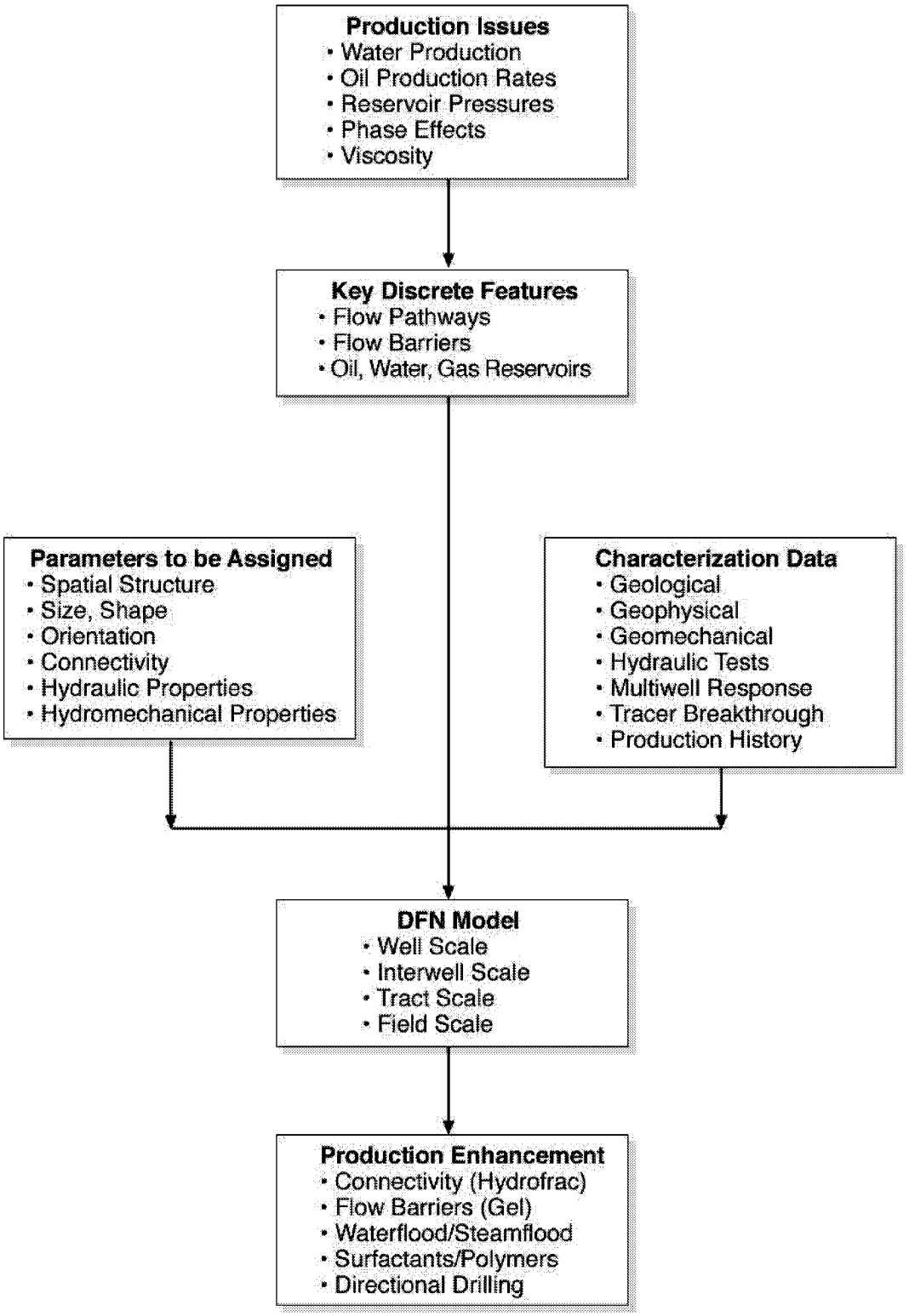

Figure 2-1: DFN Approach for Reservoir Characterization and Engineering

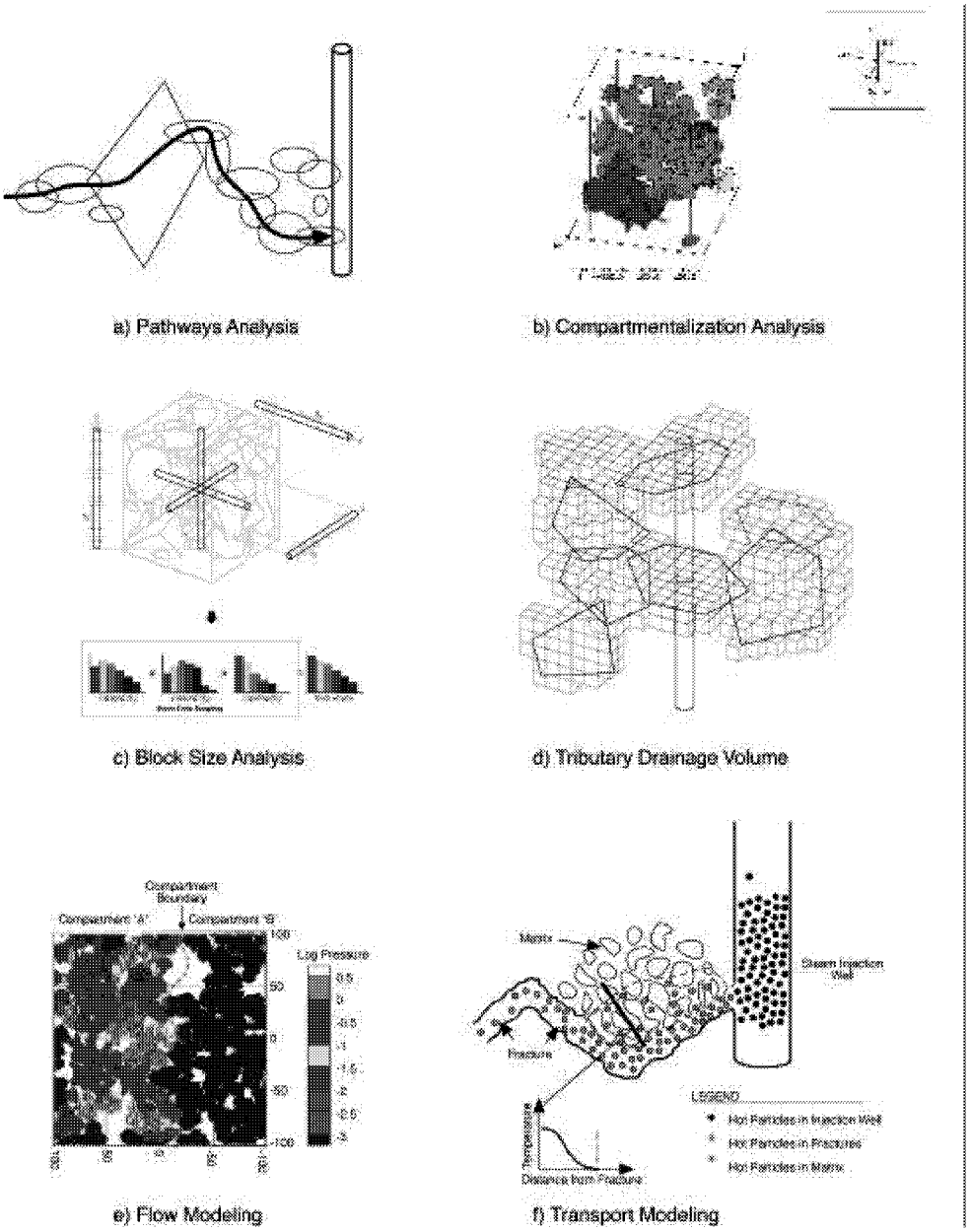

Figure 2-2: DFN Approaches for IOR

3. **Strategic Completion Connection Reduction-Gel Treatment**. Gel treatment provides a method for effectively sealing the fractures and discrete feature networks, forcing injected water to sweep oil from the rock matrix rather than flowing directly to production wells. The key issue for gel treatment is therefore the identification of well intervals that contain the fractures or discrete features which would benefit from gel treatment, and the quantity and type of gel which would most effectively seal the flow. The DFN approach was used to integrate geological, geophysical, and well production data to identify these intervals. The benefit of gel treatment, and the benefit of the DFN approach for data integration and decision support can then be quantified by comparing production before and after gel treatment.

2.2 Project Deliverables

Table 2-1: Project Deliverables and Milestones

	Deliverable	Milestones Included in Report	Scheduled Date	Date Submitted
Deliverables	First Progress Report	M1, M2, M4, M9, M10, M11, M25-M28, M60	Jan 15, 1999	Feb 19, 1999
	Second Progress Report	M3, M9, M10, M12, M13, M29-M32, M61,	July 15, 1999	August 12, 1999
	Third Progress Report	M1, M4, M7, M23, M33-M36, M37-M48, M62, M14, M15	Feb 15, 2000	March 7, 2000
	Fourth Progress Report	M1, M2, M7, M4, M63, M49-M60, M16, M17	July 15, 2000	August 15, 2001
	Fifth Progress Report	M5, M6, M49, M50, M52, M53, M55, M56, M58, M59, M18, M19	Feb 15, 2001	April 18, 2001
	Final Report	All	Sept 30, 2001	Sept 30, 2001
Milestones	M1: Feature Size; M2: Feature Shape;M3: Feature Orientation;M4: Spatial Structure; M5: Hydraulic Properties; M6: Correlations; M7: Data Integration Procedures (Prelim); M8: Data Integration Procedures (Final); M9: Data Available on WWW; M10-M22 Data Updates; M23: Prelim Data Integration Procedure; M24: Data Integration Procedure			
	M25: Yates Field; M26: North Stoney Point ;M27: South Oregon Basin; M28: North Oregon Basin			
	M29: Yates Field; M30: North Stoney Point ; M31: South Oregon Basin; M32: North Oregon Basin			
	M33: Yates Field; M34: North Stoney Point ; M35: South Oregon Basin; M36: North Oregon Basin			
	M37: Prelim. Strategy; M38: DFN Simulations; M39: Strategic Plan; M40: Prelim. Strategy; M41: DFN Simulations; M42: Strategic Plan;			
	M43: Prelim. Strategy; M44: DFN Simulations; M45: Strategic Plan; M46: Prelim. Strategy; M47: DFN Simulations; M48: Strategic Plan			
	M49: Yates Initial Phase; M50: Second Phase; M51: Evaluation Phase			
	M52: Stoney Point Initial Phase; M53: Second Phase; M54: Evaluation Phase			
	M55: South Oregon Basin Initial Phase; M56: Second Phase; M57: Evaluation Phase			
	M58: North Oregon Basin Initial Phase; M59: Second Phase; M60: Evaluation Phase			
	M60-M72: Milestone Reports and Biannual reports available online			

3. RESULTS AND DISCUSSION

3.1 Research Summary

This project was carried out according to a phased approach, in which technologies were applied as they were developed, and project study site applications were successively refined as more information was assembled. In this report, research is organized by technology, and by study site.

3.2 Task 1: Heterogeneous Reservoir Data Integration

This section describes research carried out under Task 1: Heterogeneous Reservoir Data Integration. Golder Associates developed the DFN approach as an integrated structure from site characterization data at multiple scales, through data analysis to an integrated DFN model, and finally to application of the DFN model to reservoir production enhancement.

Field data collection can be a very expensive aspect of reservoir development, and the economic benefit of this data is frequently unclear. Geological, geophysical, and well test results are collected and compiled, but do not always find a useful application in reservoir design and engineering. To some extent, ineffective use of field data is caused by adopting a continuum modeling approach for even the most fractured or heterogeneous reservoirs.

For each of the project study sites, data was assembled and directed from each discipline with the view as to how that data can be used to support an integrated DFN model (see Figure 2-1). In Task 1, we developed the overall methodology and specific technologies to support the DFN approach for integration of heterogeneous reservoir characterization using data from multiple scales.

3.2.1 Task 1.1.1 Fracture Size Analysis

Fracture size is a key parameter for discrete feature network (DFN) modeling for heterogeneous reservoir production enhancement. Fracture size strongly influences fracture connectivity, bother within the fracture network and to injection and production wells. In general, the data available is limited to data available at the wellbore. Thus, the problem becomes one of extrapolation from measurements at wells to describe fracture size within the fracture network (Figure 3-1).

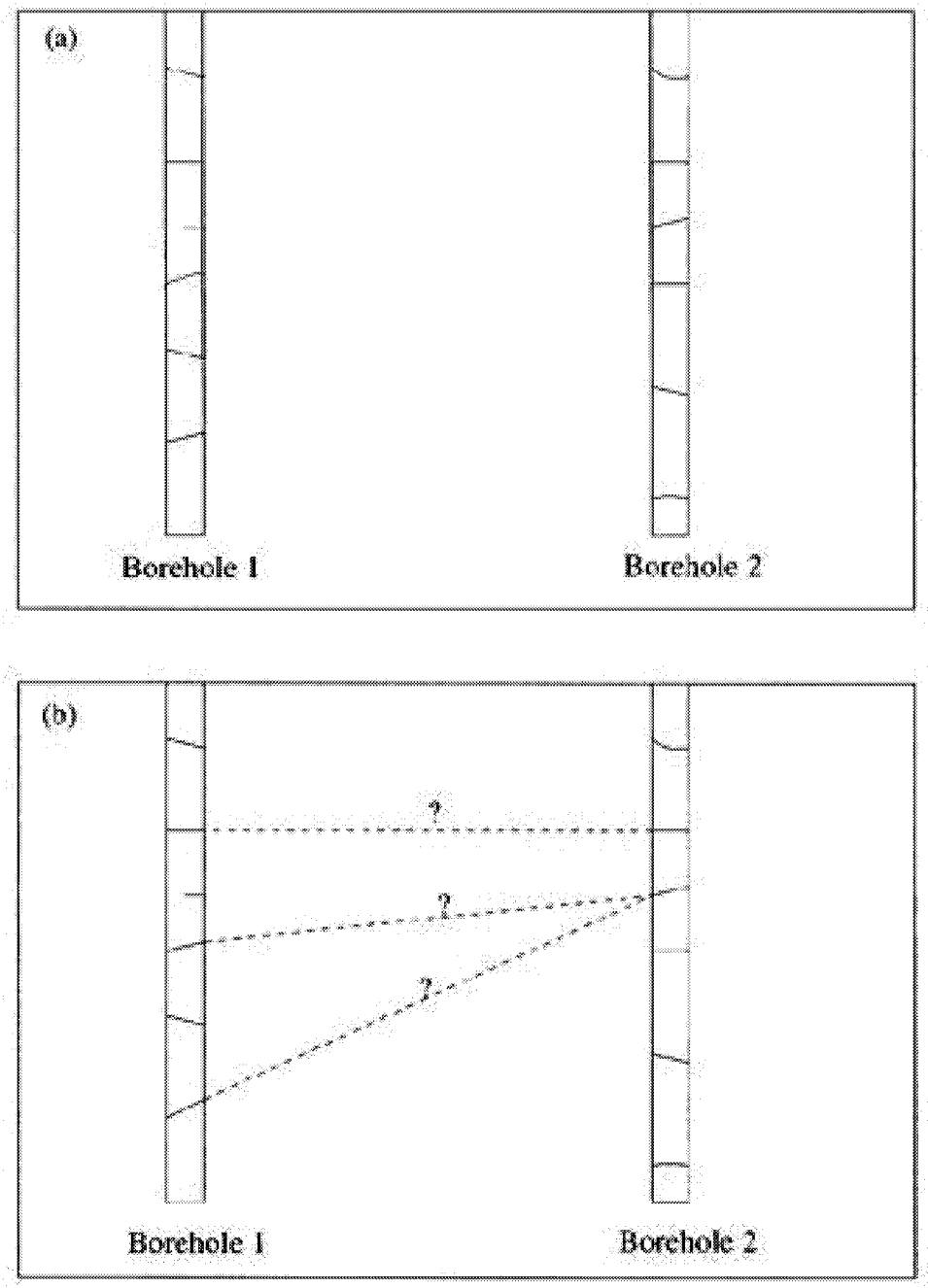

Figure 3-1 Fracture Interpolation

3.2.1.1 Task 1.1.1 Fracture Size Analysis

Discontinuities (or fractures) have a profound effect on the mechanical and hydraulic properties of rock masses. Characterizing discontinuities in the rock mass such as the number of discontinuity sets, and for each discontinuity set, the number, orientation, spacing, location, shape and size of discontinuities is, therefore, very important. Because rock mass properties are three-dimensional (3D) entities, discontinuities must be characterized in 3D space.

As the rock structure cannot be directly examined in three dimensions, discontinuity characteristics must be inferred from data sampled at exposed rock faces (including both natural outcrops and excavations faces) and/or in wells (Priest 1993). Taking measurements on exposed rock faces, either at or below the ground surface, enables one to obtain data on orientation, spacing, trace lengths and number of traces. In most cases, wellbore sampling provides the only viable exploratory tool that directly reveals geologic evidence of subsurface site conditions. In normal-size wellbore sampling various techniques can be used for acquiring the data on orientation and spacing of discontinuities, either from core samples or through inspection of the well walls. From all this one can conclude that information of discontinuity size can be obtained indirectly from trace lengths on exposed rock faces while wellbore sampling usually provides no relevant information.

Hence, characterizing 3D discontinuity size distributions is an important but difficult problem in rock engineering. Currently, there are two groups of methods for estimating the discontinuity size distributions: analytical/numerical methods and the forward modeling method. The analytical/numerical methods use stereological relations between the discontinuity size distribution and the (true) trace length distribution to infer the discontinuity size distribution. The trace length distribution is derived from the measured trace lengths at exposed rock faces by correcting the sampling biases (Baecher and Lanney 1978; Einstein et al 1979; Priest and Hudson 1981; Kulatilake and Wu 1984; Zhang and Einstein 1998). In order to use the stereological relations between the discontinuity size distribution and the (true) trace length distribution to infer the discontinuity size distribution, assumptions need to be made about the discontinuity shape. Due to the mathematical convenience, discontinuities are often assumed to be thin circular discs in 3D space (Baecher et al. 1977; Warburton 1980a; Chan 1986; Kulatilake 1993). However, in many cases, discontinuities may be non-equidimensional (Bridges 1975; Einstein et al. 1979; Warburton 1980b). Therefore, Warburton (1980b) assumed that discontinuities in a set are parallelograms of various sizes. For simplicity, he also assumed that discontinuities in a set are geometrically similar (i.e., the ratio of longer to shorter sides for all parallelograms is a constant). It is noted that the equations for the discontinuity size distribution for the parallelogram assumption are more complex and difficult to solve than those at the circle assumption.

The forward modeling method infers discontinuity parameters by constructing 3D discrete models of discontinuity systems (Figure 3-2) (Dershowitz, 1992). Based on an initial analysis of field data, a statistical description of discontinuity orientation, size, shape and spatial distribution is assumed. The process used to collect the available data is then simulated, including processes of bias, censoring and truncation. This produces a simulated set of field data, which can then be compared to field measurements. Based on this comparison, the assumed statistical description can then be modified. The process is repeated until a statistical description is found to be consistent with field observations. The goodness of fit between measured and simulated measurements can be evaluated visually, by comparison of observed and predicted analytical functions, and by statistical tests such as the χ^2 and Kolmogorov-Simirnov tests.

Uniqueness is a problem for both the analytical/numerical and the forward modeling methods. E.g., for the analytical/numerical methods, it is possible to obtain two different size distributions from the same trace length distribution (Baecher et al. 1977). In the forward modeling method, it is possible to obtain more than one "best" description of the in situ discontinuity system, with each of the obtained descriptions being consistent with field observations.

In this report, a new approach is proposed for estimating the discontinuity size distributions. To be general, discontinuities are assumed to be elliptical in shape. By changing the aspect ratio k (i.e., the ratio of the major to minor axes) of the ellipses, most of the discontinuities in reality can

be reasonably represented. With this assumption, a general stereological relationship between trace length distributions and discontinuity size (expressed by the major axis length a of the ellipse) distributions is derived for area (or window) sampling, following the methodology of Warburton (1980a, b). From this relationship, expressions are derived for calculating the mean (μ_a) and standard deviation (σ_a) of the discontinuity size a, respectively for lognormal, negative exponential and Gamma distributions of discontinuity sizes. To overcome the problem of uniqueness, a relationship between the ratio of the 4th and 1st moments of the discontinuity size distribution and the 3rd moment of the trace length distribution is derived to check the suitability of the assumed discontinuity size distribution form (Section 3.2.1.5).

The trace length distribution in the derived stereological relationship is the true distribution of trace lengths. The true trace length distribution corresponds to trace lengths in a sampling window or surface of infinite size. Since, in practice, sampling windows are of finite size and only the portions of traces within the window can be measured in window sampling, the measured trace lengths are usually biased. Zhang and Einstein (2000a) developed a method for estimating the true trace length distribution by considering the sampling biases for circular window sampling. For convenience, the method is presented in Section 3.2.1.6.

In Section 3.2.1.7, the effect of sampling plane orientation on trace lengths is investigated by using the derived stereological relationship. The results show that the sampling plane orientation has an important effect on both the mean and standard deviation of trace lengths.

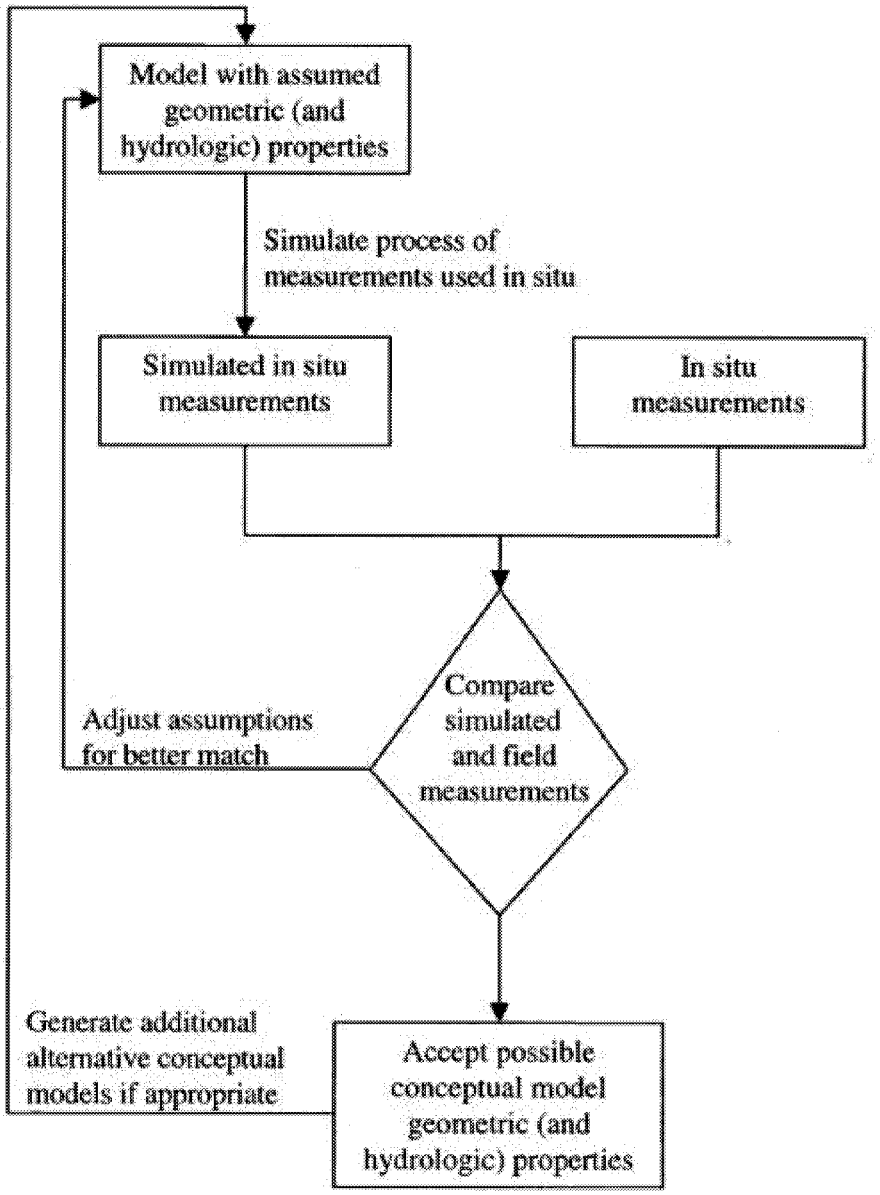

Figure 3-2 Forward Modeling Approach (after Dershowitz, 1992)

Finally, in Section 3.2.1.8, the derived stereological relationship between the trace length distribution and the discontinuity size distribution is used to analyze the trace (length) data simulated using the FracMan discrete fracture code. In the simulation, the size of a discontinuity set is described by a lognormal distribution, following Baecher et al. (1977), Barton (1978) and Warburton (1980a, b). For simplicity, only one discontinuity set with a deterministic orientation is considered. The discontinuities are generated in a 20 m $\times$ 20 m $\times$ 20 m box. Three circular sampling windows in different orientations are used to collect the trace (length) data.

3.2.1.2 Seismic Wave Methods

The seismic wave method has been widely used in petroleum exploration (Selley, 1998). To characterize fractures between wells, the seismic wave method may be used in two ways: (a) measuring the seismic waves reflected from the fracture, and (b) measuring the sound transmitted along the fracture.

The simplest way to detect fractures is to place both the energy source and the receivers at the ground surface (see Figure 3-3). The energy source is used to produce seismic waves and the receivers are used to record the amplitudes and travel times of waves returning to the surface after being reflected from the goal fracture (i.e., the fracture that one wants to characterize). By analyzing the recorded data about the reflected waves, the goal fracture can be detected (characterized). The seismogram obtained [Figure 3-4(b)] can successfully detect the fracture zones [Figure 3-4(a)]. For example, the narrow band of reflections between 15.5 ms and 19.5 ms is related to fracture zone 2.

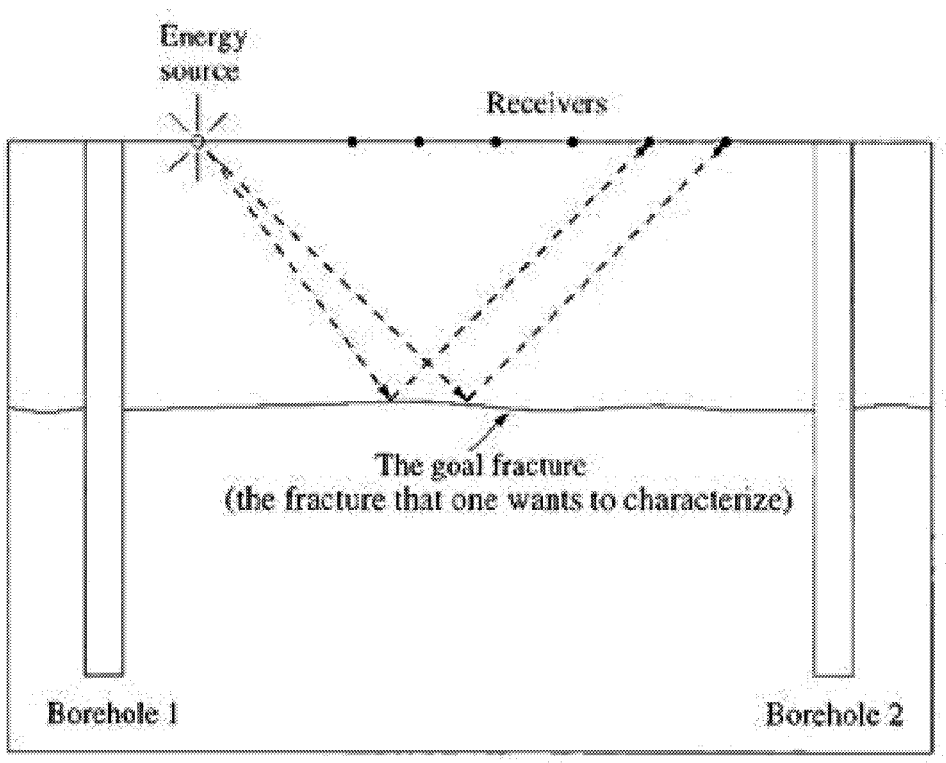

Figure 3-3 VSP Identification for Fracture Size

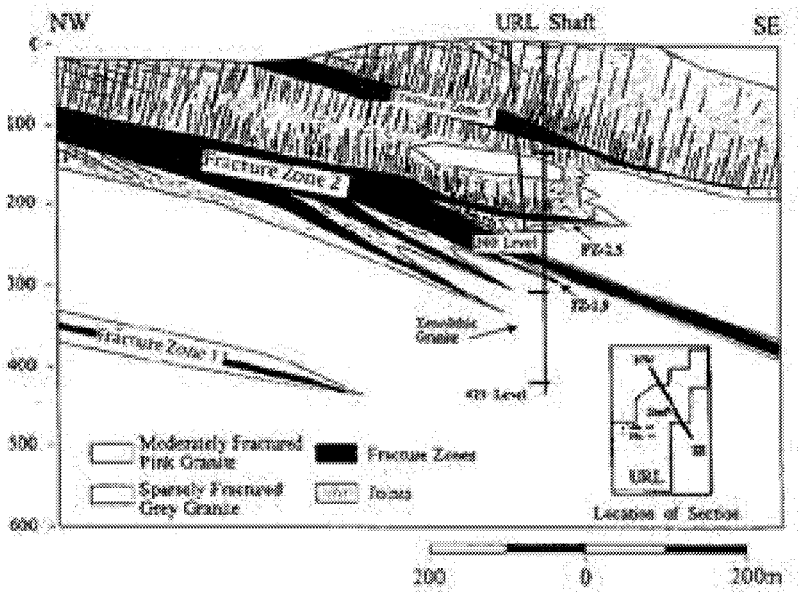

(a)

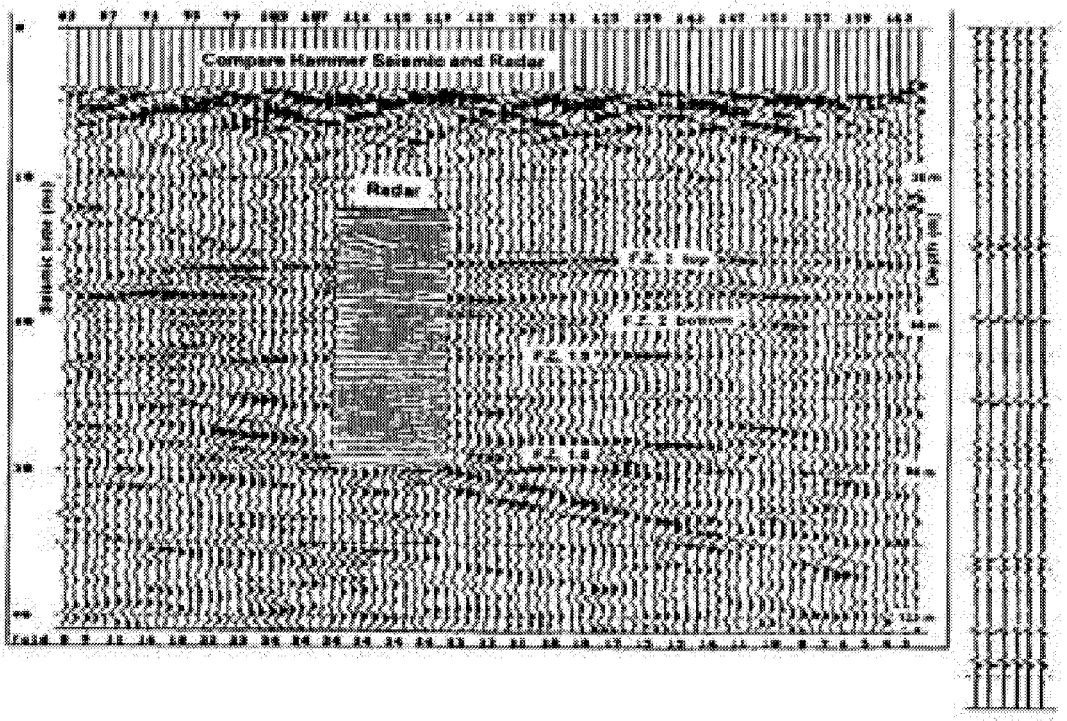

(b)

Figure 3-4 VSP Tomography

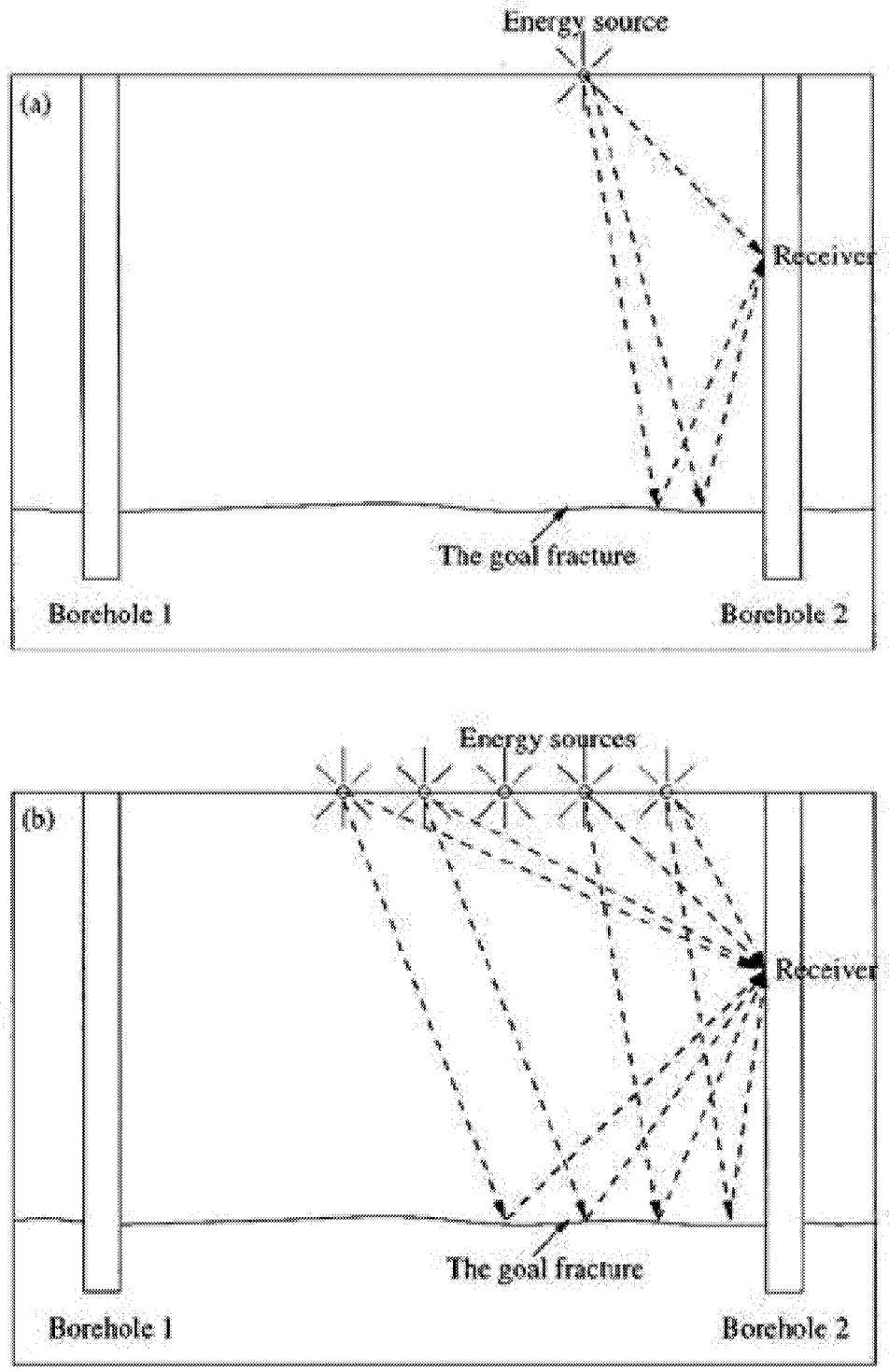

Figure 3-5 VSP Approaches (a) Offset and (b) Walkway

The receivers can also be placed in the wells as shown in Figure 3-5. This is the vertical seismic profiling (VSP) technique. The simplest instance of this technique is the offset VSP in which there is only a single energy source at the surface located immediately adjacent to the well [Figure 3-5(a)]. Using the walkway VSP in which a series of surface energy sources are arranged in a straight line away from the well or even in radial patterns like the spokes of an umbrella [Figure 3-5(b)], a 3D image adjacent to well can be produced and thus the fracture characterized in 3D.

The processing and interpretation of recorded seismic wave data is critically important in detecting (characterizing) fractures in the rock mass. For the details about data processing and interpretation in seismic surveying, one can refer to Selley (1998). It should be noted that the reflected wave method might not be effective in following two cases:

(a) the rock mass contains many other fractures in addition to the goal fracture (see Figure 3-6).

(b) the rock mass is heterogeneous; e.g., there is a cave in the rock mass (see Figure 3-7).

In the above two cases, the goal fracture can be characterized by measuring the sound transmitted along it, as described in Section 3.2.1.2.

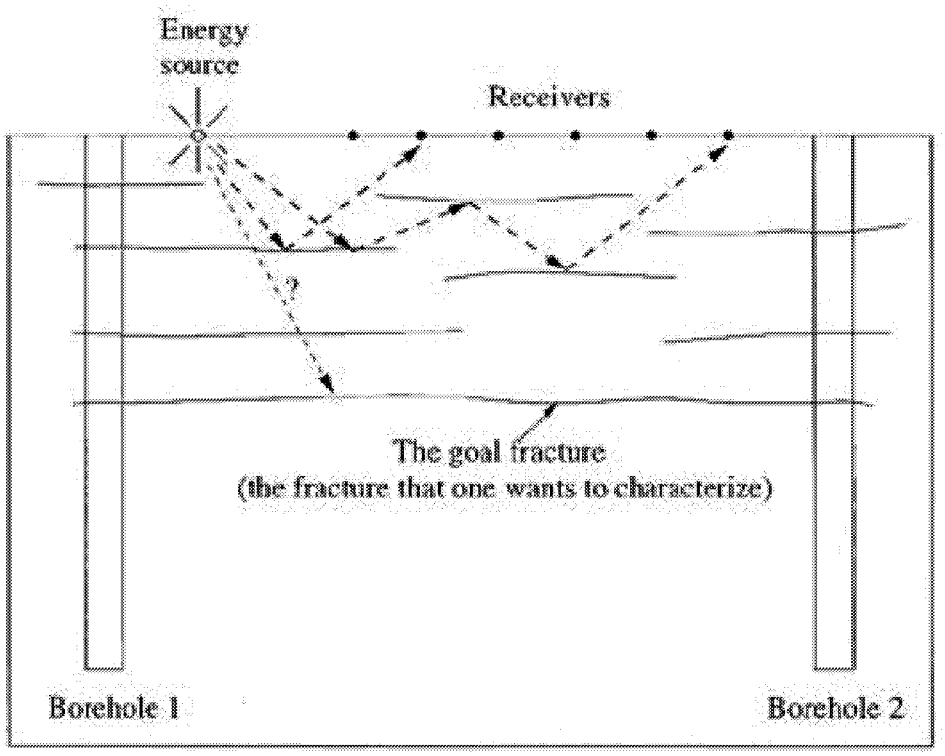

Figure 3-6 Seismic Wave Reflection by Features of Multiple Scales

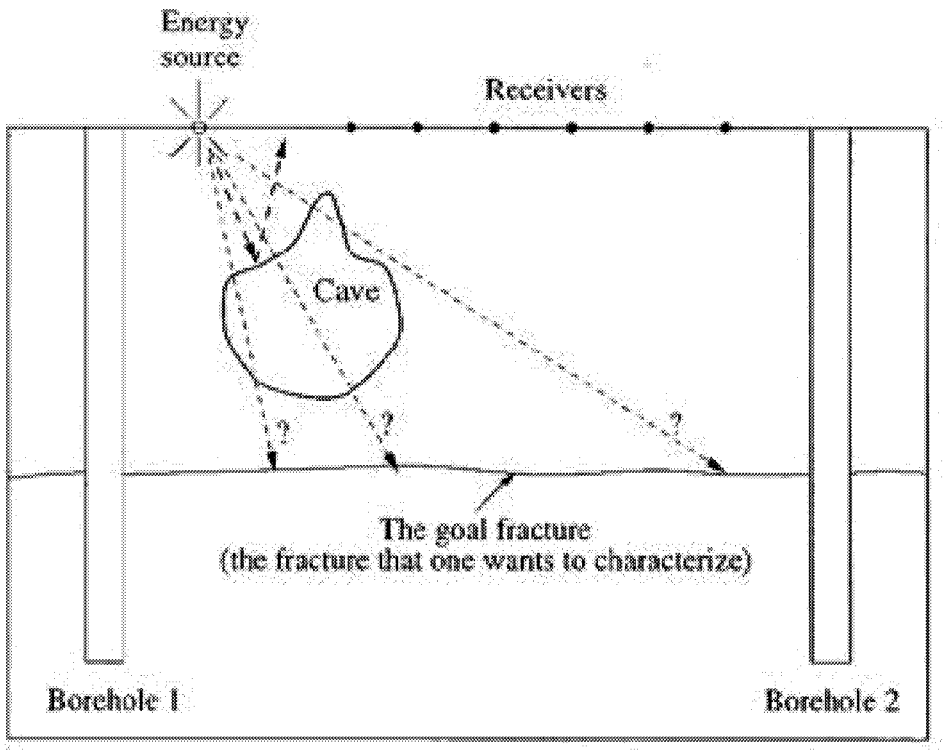

Figure 3-7 Loss of Seismic Signals Due to Karsts and Inclusions

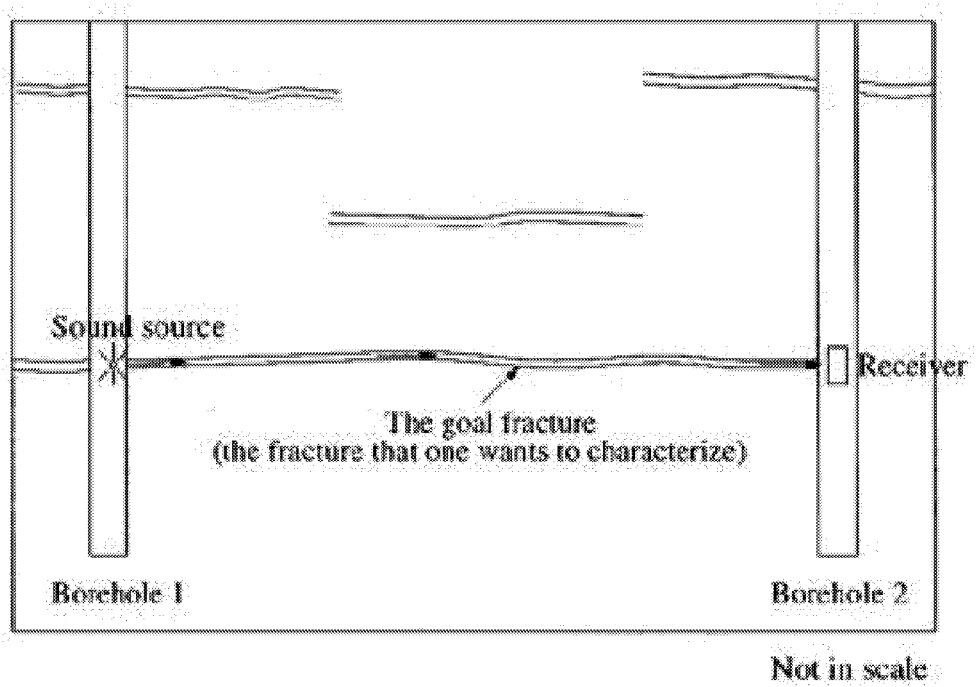

Figure 3-8 Wellbore Seismics

As shown in Figure 3-9, a sound source or a pressure pulse is placed near the goal fracture in a wellbore. If the fracture is connected to other wells, the sound will transmit along the fracture and can be heard (measured) in those wells. It is assumed that gas, water or oil is in the fracture. The principle used here is similar to that for sound transmission along a pipe, although the fracture case is 2D while a pipe case is 1D.

For this method, the following special cases should be considered:

(a) If there is clay filler in the fracture, the sound transmitted through the fracture may not be strong enough to be measured because the clay filler absorbs the sound.

(b) Measuring the sound at different locations in the receiver well can be used to check the intersections of the goal fracture with other fractures, although the intersection locations cannot be determined (see Figure 3-9).

Conventionally, VSP is used to identify specific, major discrete features. The distribution of size can then be derived by extrapolation from the sizes of measured fractures.

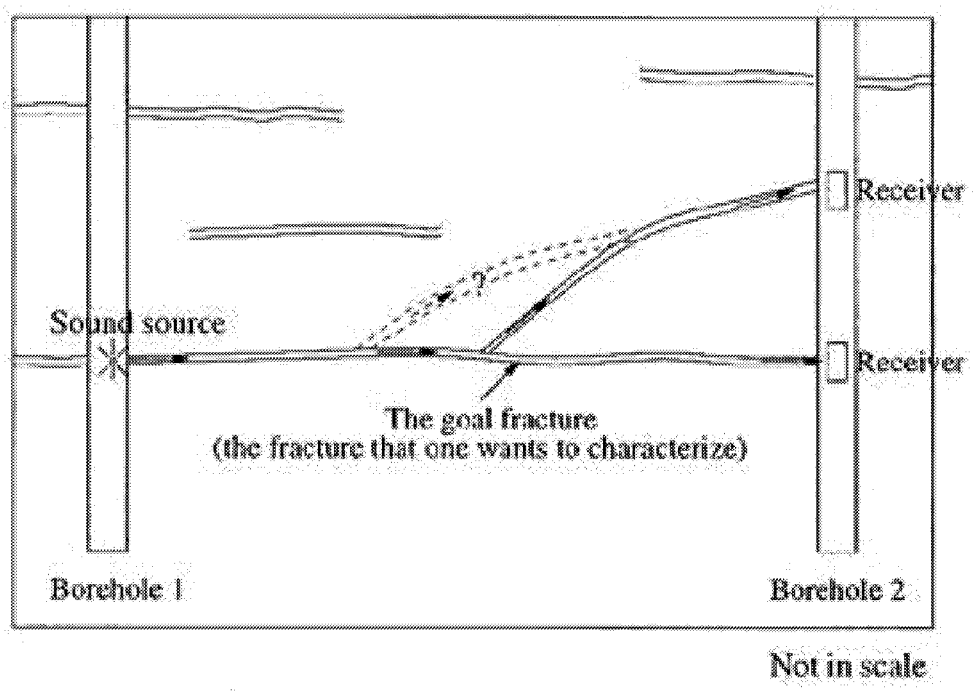

Figure 3-9 Wellbore Seismic Surveys

However, it may also possible to use VSP to obtain a distribution for the sizes of fractures which cannot be positively identified. This might be done by adapting the VSP imaging software to detect lineaments of different sizes, and then using this information to build size distributions.

3.2.1.3 Ground Penetrating Radar (GPR) Methods

Ground Penetrating Radar (GPR), also known as ground probing radar, ground radar or geo-radar, has been widely used in high-resolution mapping of soil and rock stratigraphy (Deng 1996; Sharma 1997). The GPR method uses high-frequency (80 to 1,000 MHz) electromagnetic (EM)

waves transmitted from a radar antenna to probe the earth. The transmitted EM waves are reflected from various interfaces within the ground and are detected by the radar receiver. Reflecting interfaces may be soil horizons, the groundwater surface, soil/rock interfaces, man-made objects, or any other interfaces possessing a contrast in dielectric properties. The GPR method is analogous to seismic reflection except for the energy source (Sharma 1997; ASCE 1998).

Contrasts in dielectric properties across an interface cause EM waves to be reflected. Fracture fillings with dielectric properties differing from their adjacent rock materials can cause radar reflections and thus can be detected.

The GPR method is that the penetration depth of radar is limited (usually less than 20 meters) (Cummings 1990; Kearey and Brooks 1991; Sharma 1997; ASCE 1998). At the Gypsy Outcrop Site in Northeastern Oklahoma, the maximum depth with noticeable radar response is about 10 meters (Deng 1996). Therefore, the GPR method can only be used to detect fractures at shallow depth or a short distance from the well. While this is useless for conventional oil reservoir stratigraphic characterization, it is potentially useful for deriving the size distribution for fractures to be incorporated in DFN models. GRP methods can potentially fill in the portion of the size distribution between the 0.1 to 10 m features seen in wells and the 100 m and larger features seen in VSP and 3D seismics.

Similar to the seismic wave method, the processing and interpretation of recorded GPR data is critically important. Due to the kinematic similarities between radar and seismic wave propagation, seismic processing techniques are widely used to process the GPR data (Deng 1996; Sharma 1997).

GPR was successfully used to detect fracture zone 2 in Figure 3-4(a) (Soonawala et al. 1990; Stevens et al. 1995). As shown in Figure 3-10, there is a large continuous reflection, 40 m deep at the northwest end of the profile and about 50 m deep at the southeast end. This reflection corresponds to the location of fracture zone 2 which is also shown in the fracture log of well M-10 located near the northwest end of the profile. Other examples of GPR applied to fracture detection in hard rocks can be found in Grasmueck (1996) and Grandjean and Gourry (1996).

During 2000, we plan to develop approaches for deriving size distributions for intermediate scale features from GPR data.

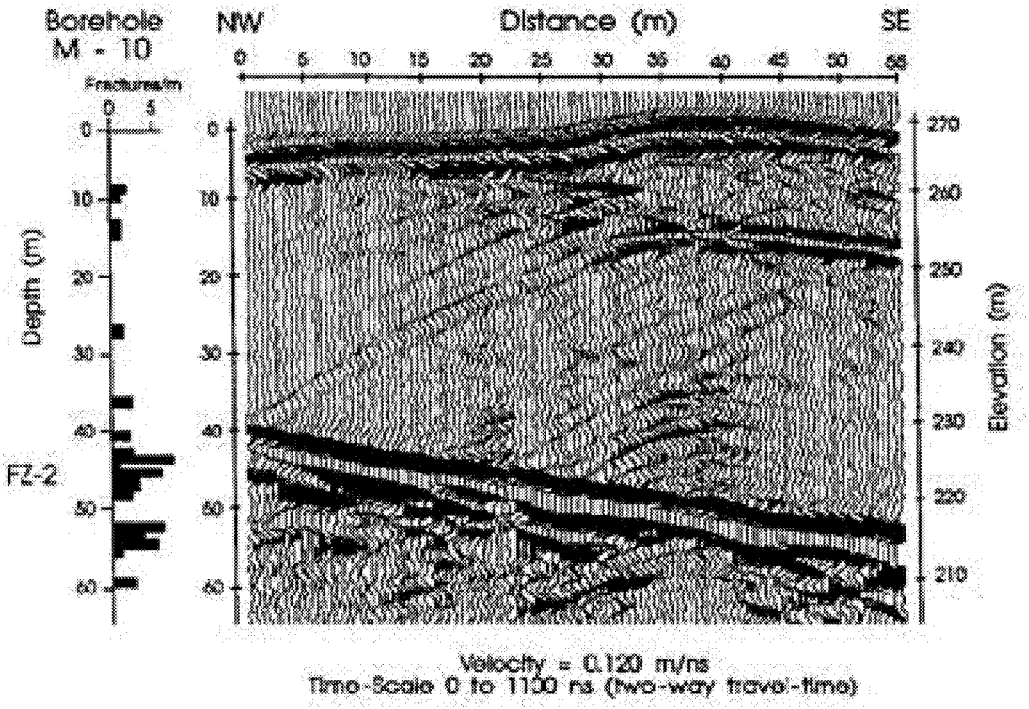

Figure 3-10 Radar Tomography

3.2.1.4 Hydraulic Interference Approaches

Hydraulic interference analysis can be used to identify the hydraulic connections between wells in three ways: (a) pumping and observation, (b) injection and observation, and (c) chemical/radioactive tracers.

Pumping and Observation
Paillet (1993) used the pumping and observation method to identify the hydraulic connections between wells. By measuring the vertical flows in both the pumped and observation wells, the points where water enters and exits the wellbore can be found and then the hydraulic connections between wells can be identified (see Figure 3-11).

If there are multiple water entrance points in the pumped well and multiple water exit points in observation well, it may be difficult to identify how these fractures are interconnected (see Figure 3-12). To address this problem, we suggest the following procedure (see Figure 3-12):

(a) Isolate the entrance points in the pumped wellbore with packers.

(b) Pump water from one interval including only one entrance point.

(c) Find the water exit point(s) in the observation wellbore and identify the hydraulic connections to the fracture in the pumping interval.

(d) For other entrance points in the pumped well, repeat steps (b) and (c).

Obviously, the pumping and observation method can be used only in saturated rock masses with water or oil.

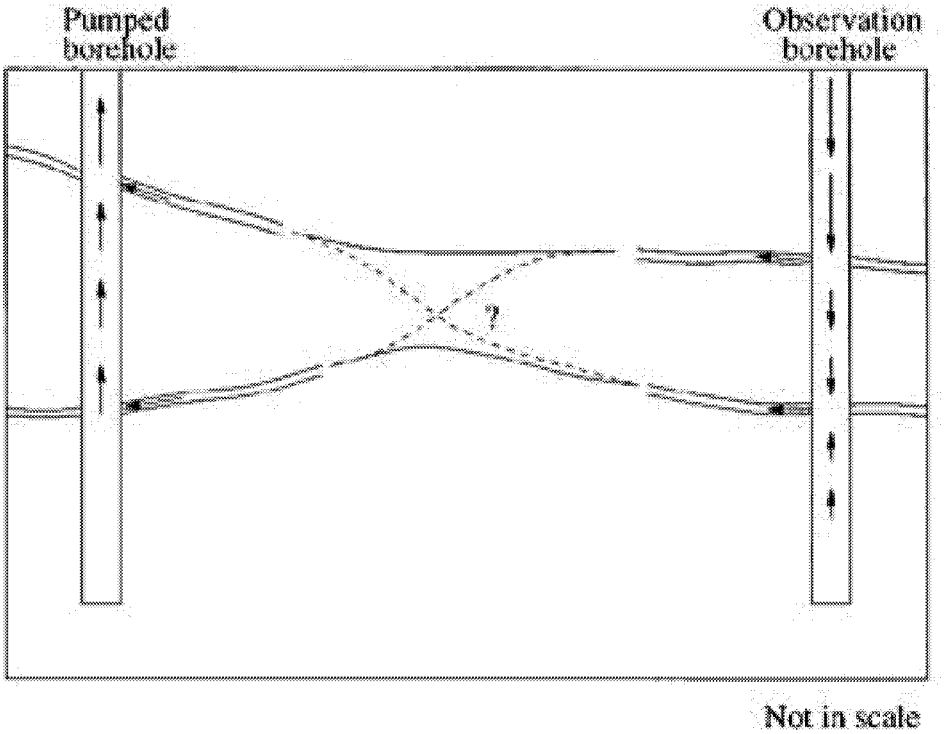

Figure 3-11 Hydraulic Interference Testing

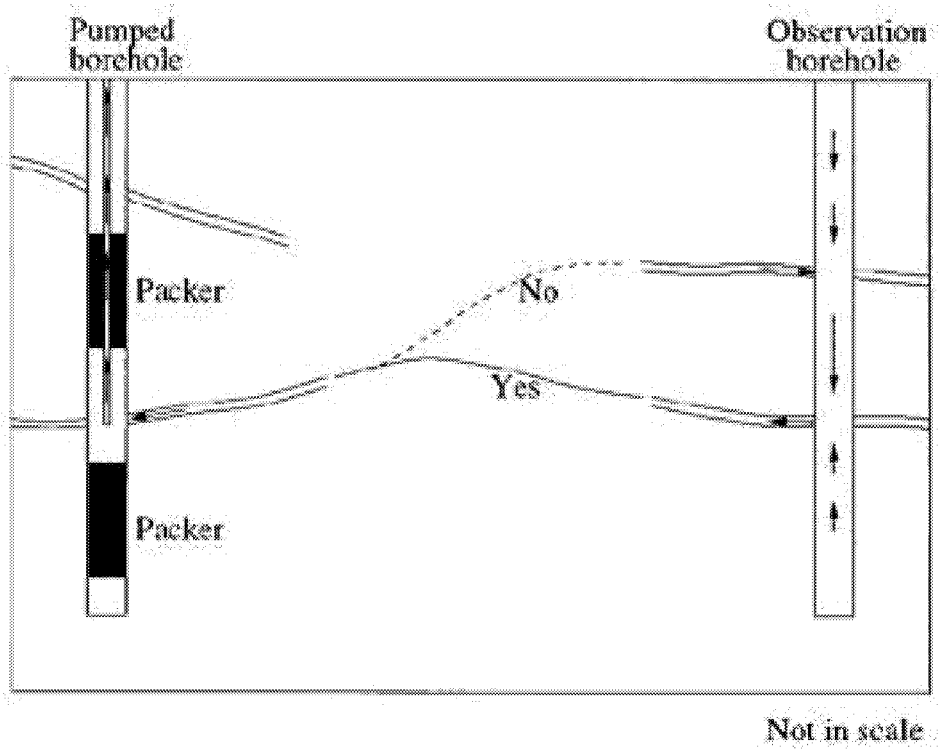

Figure 3-12 Fracture Network Effects

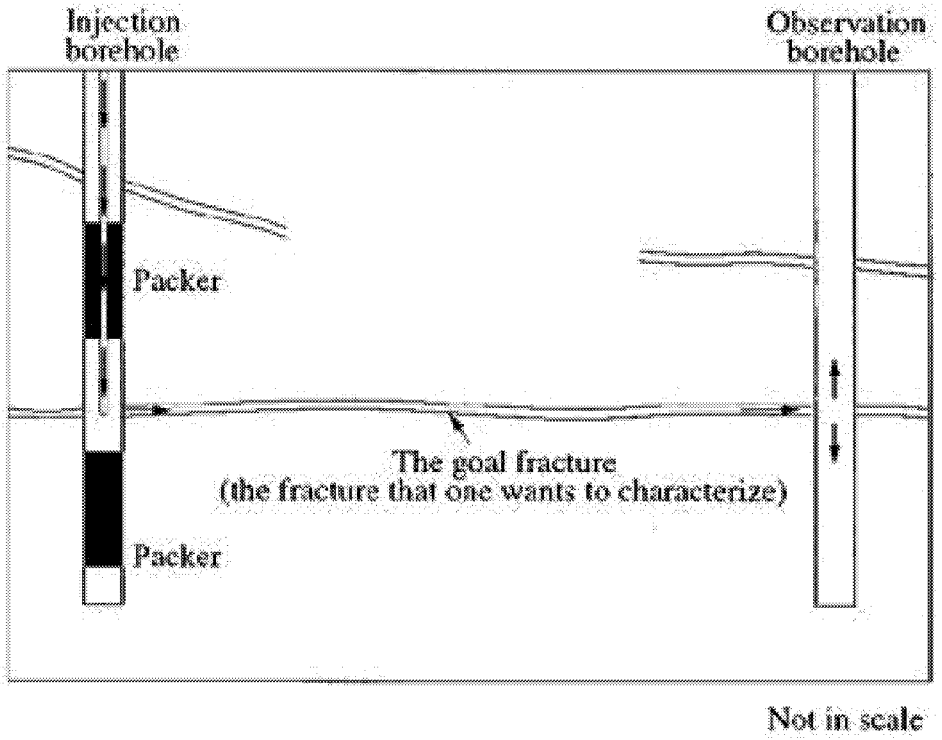

Figure 3-13 Packer Testing

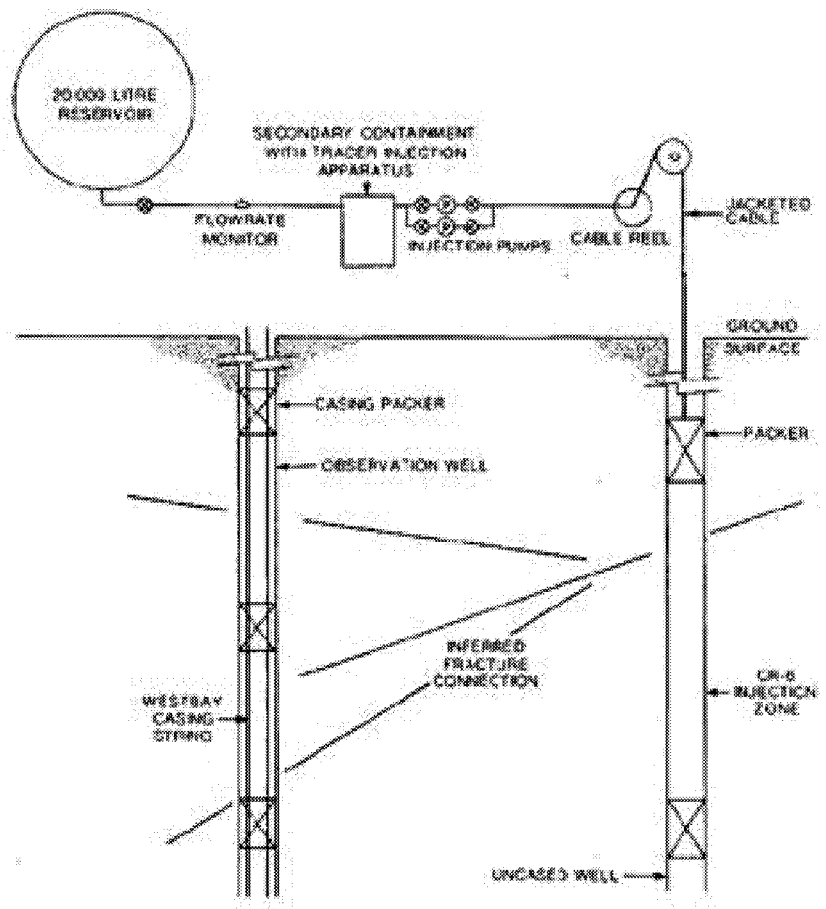

Figure 3-14 Tracer Testing at URL (Novakowski et al., 1985)

Injection and Observation

The injection and observation method can be used to characterize fractures with the following procedure (see Figure 3-13):

(a) Isolate the target fracture from other fractures in the injection well.

(b) Inject a fluid (generally oil or water) to the target fracture.

(c) Find the water entrance point(s) in the observation well and identify the hydraulic connections to the goal fracture.

(d) For other fractures in the injection well, repeat steps (a) to (c).

The injection and observation method can be used in both saturated or unsaturated rock masses. Benito et al. (1999) used the injection and observation method to assess the pneumatic connectivity of unsaturated fractured basalt by injecting air.

Chemical/Radioactive Tracers

The chemical/radioactive tracer method can be considered an extension of the injection and observation method. By injecting a chemical or radioactive tracer (which is usually diluted in water) into a well and monitoring its movement in observation wells surround the injection well, fractures or fracture zones connecting the injection well and the observation wells can be identified.

Novakowski et al. (1985) described an experiment carried out at the Chalk River Nuclear Laboratories, Ontario, Canada, to identify fracture zones using a radioactive tracer (^{131}I). Figure 3-14 shows the instrumentation used for the ^{131}I tracer test. After injecting the ^{131}I tracer (which is diluted with water) into a fractured interval isolated by straddle packers in a central well, the research team monitored its movement in observation wells surrounding the injection well, using a γ-ray logging device.

Hydraulic interference tests are used extensively in heterogeneous oil reservoirs to characterize hydraulic compartments and design infill drilling campaigns. Both thermal (steam) and chemical tracers have been used at the project study site in Yates, Texas to understand hydraulic connectivity. In theory, a series of hydraulic interference tests could be deconvolved fracture size distributions from fracture network responses. This has been attempted as part of the SKB Stripa project in Sweden (Doe and Geirer, 1991) and the SKB Äspö project (Winberg et al., 1999). However, these results have not yet been successful for derivation of fracture size distributions due to the complexity of fracture network behavior, and uncertainties arising from boundary conditions.

3.2.1.5 Analytical Development

3.2.1.5.1 Basic Assumptions

The following are the assumptions that underlie the constructions of the model:

1) All discontinuities are planar.
2) Discontinuities are elliptical in shape. Discontinuities in a set are geometrically similar, i.e., all discontinuities in a set have the same aspect ratio k (i.e., the ratio of major to minor axes of an ellipse).
3) The centers of discontinuities are randomly and independently distributed in space. The volume density of discontinuity centers has a Poisson distribution with mean N_v, i.e., the probability density function of the number of discontinuity centers in a given region denoted by x is $p(N;N_V x)=\frac{e^{-N_V x}(N_V x)^N}{N!}$, $N = 0, 1, 2,$
4) The size distribution of discontinuities is independent of spatial location.

In some cases, the above assumptions may not be valid in describing a given discontinuity network. However, these are postulated here, as they provide an elementary but still not totally unrealistic means of describing discontinuity geometry. Eventually, some of these assumptions can be relaxed. Following is a discussion of the above assumptions.

Planar Discontinuities: The assumption of planar discontinuities is made in order to obtain a simple parametric description of the discontinuity geometry. Although discontinuities can be curved or wavy in some cases, this curvature is often negligible (Warburton 1980a). It is a

common practice in rock engineering to assume that discontinuities to be planar (Priest and Hudson 1976; Baecher et al. 1977; Warburton 1980a, b; Kulatilake 1993).

Elliptical Discontinuities: Zhang and Einstein (2000b) conducted a brief literature review about the shape of (unrestricted) discontinuities, including the reported in situ data and the shapes assumed by different researchers. Analysis of the available information on the shape of discontinuities leads to the following conclusions (Zhang and Einstein 2000b):

1. The conclusion that discontinuities are equidimensional (circular) drawn from the fact that the average strike length of a discontinuity set is approximately equal to its average dip length is questionable. Investigators assume circular discontinuity shape possibly because of mathematical convenience.

2. The possible shape of unrestricted discontinuities is more likely to be elliptical than circular.

3. Elliptical discontinuities can be effectively represented by polygons with a large number of sides. This is one of the reasons why polygons are used to represent discontinuities in discrete fracture codes. Convenience of numerical analysis and the ability to represent irregular discontinuities, such as restricted discontinuities, are another two reasons for using polygons to represent discontinuities in discrete fracture codes.

In this study, discontinuities are assumed to be elliptical in shape so that an analytical relationship between trace length distributions and discontinuity size (expressed by the major axis length a of the ellipse) distributions can be derived. By changing the aspect ratio k (i.e., the ratio of major to minor axes) of the ellipses, most of the discontinuities in reality can be reasonably represented.

Discontinuities Randomly Distributed in Space: The hypothesis that discontinuities are randomly distributed in space is very convenient and is widely adopted by investigators. The assumption leads to an exponential distribution of trace spacings along a sampling line, in agreement with most reported field studies (e.g., Priest and Hudson 1976, Call et al. 1976, Baecher et al. 1977, Einstein et al. 1979). This assumption is convenient, but implies that clustering is not considered.

Discontinuity Sizes Independent of Position: This is again an assumption for the sake of simplicity. Although this assumption is open to debate, it is implicit in most rock mechanics analysis (Baecher et al. 1977). To make this and the former assumptions more acceptable, one can divide the site into regions in which this assumption seems approximately correct (see, e.g., Meyer et al. 1999). Again, this implies that clustering is not considered.

It is noted that the above assumptions are made so that a general stereological relationship between trace length distributions and discontinuity size distributions can be conveniently derived. However, these assumptions, while convenient, are not necessary. For example, the clustering of discontinuities could be considered using the methodology proposed by Dershowitz (1993), Ivanova (1998) and Meyer (1999).

Figure 3-15 shows the parameters used in the definition of discontinuity shape. To simplify the derivation, the parameters are specified with reference to the trace directions that would be produced on a sampling plane. β is the angle between the discontinuity major axis and the trace line (note that β is measured in the discontinuity plane). Obviously, β will change for different sampling planes. For a specific sampling plane, however, there will be only one β value for a

discontinuity set with a deterministic orientation. The parameter a, which is a characteristic dimension (c.d.) defining the discontinuity size, is chosen to be the length of the discontinuity major axis. The length of the discontinuity minor axis is a/k, where k is the aspect ratio of the discontinuity. The probability density (or frequency) function $g(a)$ for the characteristic dimension is independent of spatial location.

Consider a sampling plane located inside the rock mass. Every discontinuity that intersects this plane creates a linear trace, which is in fact a chord of the discontinuity. For simplicity we shall initially consider a typical discontinuity with c.d. a. Let us examine under what conditions the discontinuity produces a trace with midpoint at a given point O in the sampling plane. Obviously one way in which this can occur is if the discontinuity center coincides with the point O, as shown in Figure 3-16(a). Let us draw lines, such as line A, on the discontinuity planes and parallel to the trace line through point O. These lines will intersect the discontinuity producing cords, such as cord A_1A_2 produced by line A. If the discontinuity center is at the midpoint A_0 of cord A_1A_2, the discontinuity will produce a trace with midpoint at point O. Extending this argument, we can find that if the discontinuity center is on a straight line $B_0A_0OC_0D_0$, the discontinuity will produce a trace with midpoint at point O. The angle between the straight line $B_0A_0OC_0D_0$ and the trace line through point O is

$$\beta_0 = \beta + \beta_1 = \beta + \arctan\left(\frac{1}{k^2 \tan\beta}\right) \qquad \text{Equation 1}$$

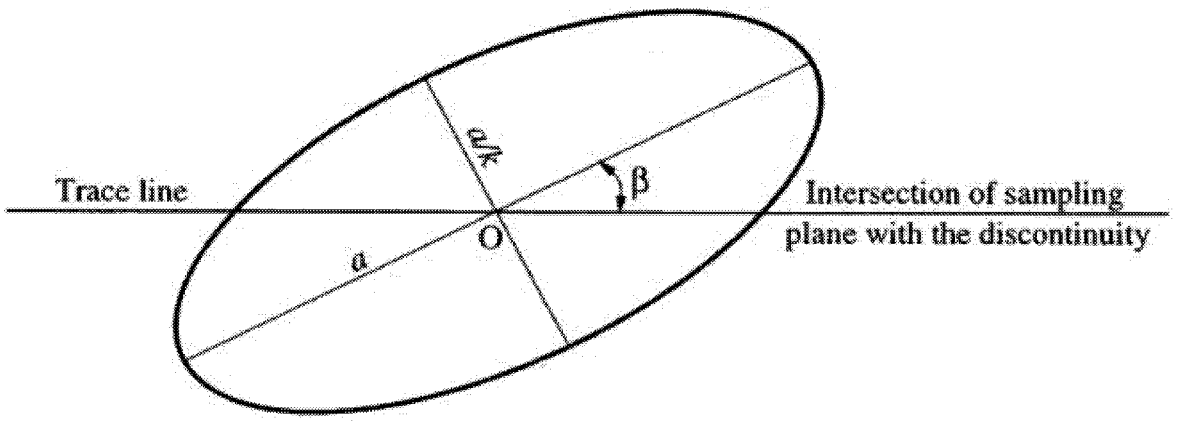

Figure 3-15 Parameters used in the definitions of discontinuity

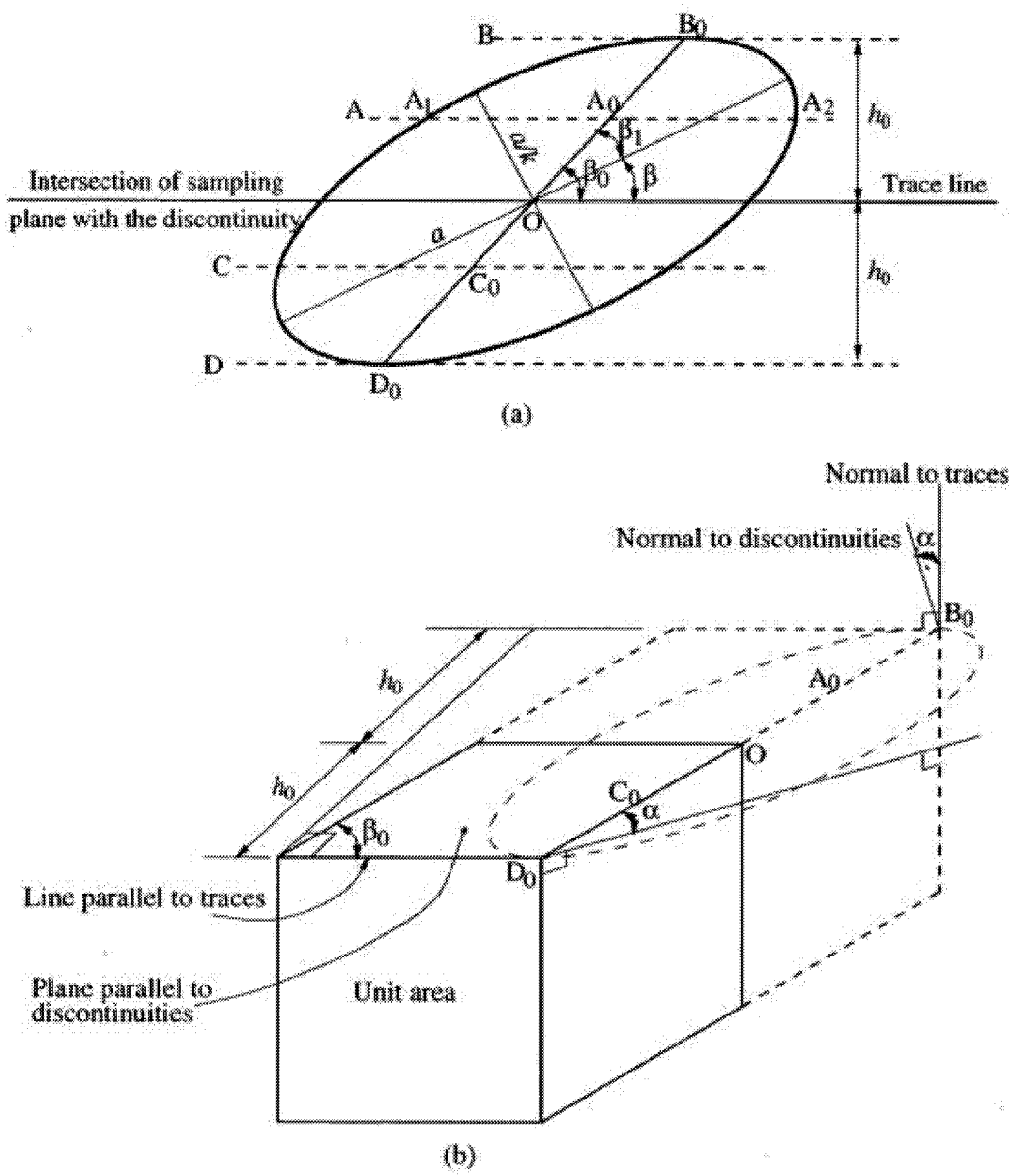

Figure 3-16 Construction used in deviation of relationship between discontinuity size distribution and trace length distribution

Consider the construction of the box in Figure 3-16(b). The page represents the sampling plane, and the discontinuity normal is inclined at an angle α to the plane. Since in the figure this angle is taken to lie in a vertical plane normal to the page, the discontinuity would create a horizontal trace where it intersects the page. The box extends equally on both sides of the page following the contour of line $B_0A_0OC_0D_0$. The distance h_0 of the front or back of the box from the page in the discontinuity plane is

$$h_0 = \frac{a\sqrt{k^2 \tan^2 \beta + 1}}{2k\sqrt{\tan^2 \beta + 1}}$$

Equation 2

where β is the angle between the discontinuity major axis and the trace line [see Figure 3-16(a)]. If the center of our typical discontinuity is at this distance from the page, the discontinuity will touch the page. So if the discontinuity is to intersect the page its center must be somewhere between the front and back of the box. It is also noted that all cross sections of the box parallel to the page have the same unit area. The significance of the box now becomes apparent: each of our typical discontinuities whose center is in the box will produce a trace whose midpoint is in the unit area, and the number of such trace midpoints will be equal to the number of typical discontinuities with centers in the box [see Figure 3-16(b)].

Since the volume of the box is

$$V = \frac{\sqrt{k^2 \tan^2 \beta + 1}}{k\sqrt{\tan^2 \beta + 1}} a \cos \alpha$$

Equation 3

the total number of discontinuity centers in the box, on the average, is

$$N_V \frac{\sqrt{k^2 \tan^2 \beta + 1}}{k\sqrt{\tan^2 \beta + 1}} a \cos \alpha$$

Equation 4

where N_v is the mean volume density of discontinuity centers (see assumption 3 above). A fraction $g(a)da$ of these discontinuities have c.d. between a and $a + da$ and can be considered to be our typical discontinuities, where $g(a)$ is the probability density function of a. Consequently, the average number of trace midpoints per unit area produced by discontinuities with c.d. between a and $a + da$ = the average number of such discontinuities with centers in the marked volume

$$= N_V \frac{\sqrt{k^2 \tan^2 \beta + 1}}{k\sqrt{\tan^2 \beta + 1}} a \cos\alpha g(a) \mathrm{d}a \qquad \text{Equation 5}$$

Integrating (5) over the range of all discontinuity c.d. a and assuming a theoretically infinite upper limit, we find that the average total number of trace midpoints per unit area is given by

$$N_A = N_V \frac{\sqrt{k^2 \tan^2 \beta + 1}}{k\sqrt{\tan^2 \beta + 1}} \cos\alpha \mu_a \qquad \text{Equation 6}$$

where the mean of a is, by definition,

$$\mu_a \equiv \int_0^\infty a g(a) \mathrm{d}a \qquad \text{Equation 7}$$

Dividing (5) by (6), the fraction of total traces produced by discontinuities with c.d. between a and $a + \mathrm{d}a$

$$= \frac{a}{\mu_a} g(a) \mathrm{d}a \qquad \text{Equation 8}$$

Eq. (8) applies over the whole plane section [the "plane section" is parallel to the "unit area" in Figure 3-16(b)]. It is worth noting that Eq. (8) shows that the probability density function of traces produced by discontinuities with c.d. a is given by

$$f(a) = \frac{a}{\mu_a} g(a) \qquad \text{Equation 9}$$

Figure 3-17 illustrates a typical discontinuity of c.d. a. The discontinuity intersects a sampling plane to produce a trace of length l located at a distance h from the discontinuity center in the

discontinuity plane. It is assumed that the discontinuity is located randomly relative to the sampling plane; this means that the distance h will be distributed uniformly in the range 0 to $h_0 = \frac{a\sqrt{k^2 \tan^2 \beta + 1}}{2k\sqrt{\tan^2 \beta + 1}}$ and hence with a constant density of $\frac{2k\sqrt{\tan^2 \beta + 1}}{a\sqrt{k^2 \tan^2 \beta + 1}}$. Of these discontinuities that have c.d. between a and $a + \mathrm{d}a$ and are intersected by the sampling plane there, a fraction $\frac{2k\sqrt{\tan^2 \beta + 1}}{a\sqrt{k^2 \tan^2 \beta + 1}}\mathrm{d}h$ have centers at distances between h and $h + \mathrm{d}h$ from their intersections with the sampling plane. Multiplying this fraction by the probability density given by Eq. (8) gives the fraction of the total number of traces that have parent discontinuity c.d. between a and $a + \mathrm{d}a$ and discontinuity center locations in the range h to $h + \mathrm{d}h$, as follows

$$P_{ah} = \frac{2k\sqrt{\tan^2 \beta + 1}}{\mu_a \sqrt{k^2 \tan^2 \beta + 1}} g(a)\mathrm{d}a\mathrm{d}h \qquad \text{Equation 10}$$

The length l of a trace is related to its distance h from the discontinuity center in the discontinuity plane as follows

$$l = \frac{2\sqrt{\tan^2 \beta + 1}\sqrt{(a/2)^2 (k^2 \tan^2 \beta + 1) - h^2 k^2 (\tan^2 \beta + 1)}}{k^2 \tan^2 \beta + 1} \qquad \text{Equation 11}$$

When $h = 0$, l takes the maximum value

$$l_{\max} = \frac{\sqrt{\tan^2 \beta + 1}}{\sqrt{k^2 \tan^2 \beta + 1}} a = Ma \qquad \text{Equation 12}$$

which is the maximum trace length of a discontinuity with c.d. a. In Eq. (12),

$$M = \frac{\sqrt{\tan^2 \beta + 1}}{\sqrt{k^2 \tan^2 \beta + 1}}$$ Equation 13

By deriving h as a function of l from Eq. (11) and then taking the derivative of h over l, we have

$$\mathrm{d}h = \frac{-(k^2 \tan^2 \beta + 1) l \mathrm{d}l}{2k(\tan^2 \beta + 1)\sqrt{\frac{\tan^2 \beta + 1}{k^2 \tan^2 \beta + 1} a^2 - l^2}}$$ Equation 14

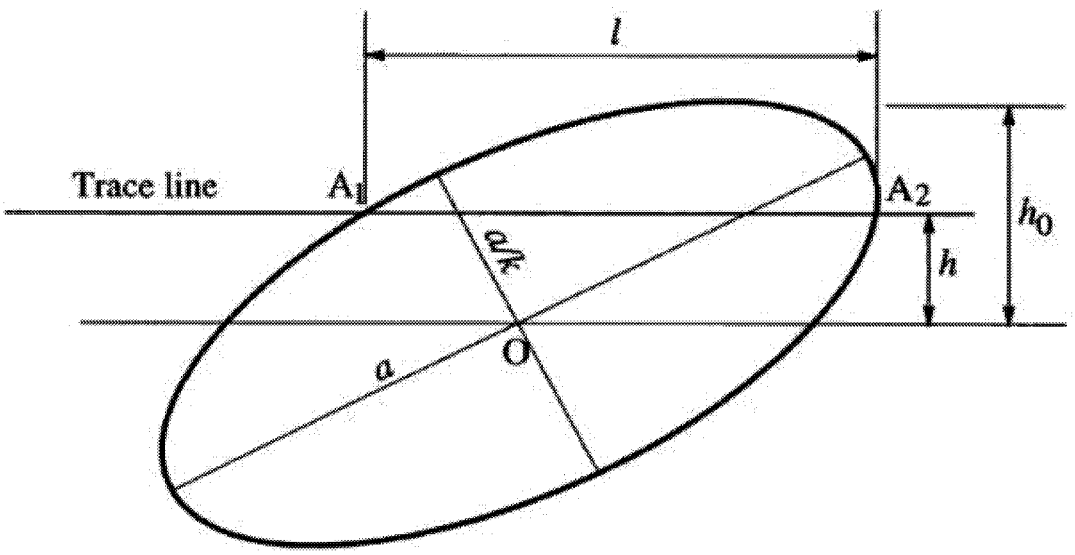

Figure 3-17 Relationship between *h, l,* and *a*

Here the negative sign simply means that l decreases as h increases. Taking the absolute value and substituting for dh in Eq. (10) gives the fraction of total traces that have lengths between l and l + dl and that are produced by discontinuities with c.d. between a and a + da

$$P_{al} = \frac{\sqrt{k^2 \tan^2 \beta + 1}}{\mu_a \sqrt{\tan^2 \beta + 1}} g(a)\mathrm{d}a \frac{l\mathrm{d}l}{\sqrt{\frac{\tan^2 \beta + 1}{k^2 \tan^2 \beta + 1} a^2 - l^2}} \qquad \text{Equation 15}$$

$$= \frac{g(a)\mathrm{d}a}{M\mu_a} \frac{l\mathrm{d}l}{\sqrt{(Ma)^2 - l^2}}$$

A trace length between l and l + dl could be produced by a discontinuity with a c.d. a that is greater than l/M [see Eq. (12)]. Consequently, the proportion, P_l, of the total number of traces that have lengths between l and l + dl is found by integrating Eq. (15) over the range of all possible discontinuity c.d. a between l/M and ∞, as follows

$$P_l = \frac{l\mathrm{d}l}{M\mu_a} \int_{l/M}^{\infty} \frac{g(a)\mathrm{d}a}{\sqrt{(Ma)^2 - l^2}} \qquad \text{Equation 16}$$

This gives the probability density function of trace length l

$$f(l) = \frac{l}{M\mu_a} \int_{l/M}^{\infty} \frac{g(a)\mathrm{d}a}{\sqrt{(Ma)^2 - l^2}} \qquad (l \le aM) \qquad \text{Equation 17}$$

It is noted that when k = 1 (i.e., the discontinuities are circular), M =1 and Eq. (17) reduces to:

$$f(l) = \frac{l}{\mu_a} \int_l^{\infty} \frac{g(a)\mathrm{d}a}{\sqrt{a^2 - l^2}} \qquad \text{Equation 18}$$

This is the result derived by Warburton (1980a) for circular discontinuities.

3.2.1.5.2 Inference of Discontinuity Size Distribution from Trace Length Distribution or Vice Versa

With the probability density function of the trace length, $f(l)$, the mth moment of the trace length, $E(l^m)$, can be obtained by

$$E(l^m) = \int_0^\infty l^m f(l) dl \qquad \text{Equation 19}$$

Substitution of Eq. (17) into Eq. (19) gives

$$E(l^m) = \frac{1}{M\mu_a} \int_0^\infty l^m dl \int_{l/M}^\infty \frac{lg(a)da}{\sqrt{(Ma)^2 - l^2}} \qquad (l \le aM) \qquad \text{Equation 20}$$

Reversing the order of integration in Eq. (20) and performing the resulting integration with respect to l, we obtain

$$E(l^m) = \frac{1}{M\mu_a} \int_0^\infty g(a)da \int_0^{Ma} \frac{l^{m+1} dl}{\sqrt{(Ma)^2 - l^2}}$$

Equation 21

$$= \frac{M^m J_{m+1}}{\mu_a} \int_0^\infty a^{m+1} g(a) da$$

where

$$J_{m+1} = \begin{cases} \dfrac{(1)(3)\cdots(m)}{(2)(4)\cdots(m+1)}\dfrac{\pi}{2} & \text{if } m \text{ is odd} \\ \\ \dfrac{(2)(4)\cdots(m)}{(3)(5)\cdots(m+1)} & \text{if } m \text{ is even} \end{cases}$$ Equation 22

$\int_0^\infty a^{m+1} g(a)da$ is the (m+1)th moment of a, i.e.,

$$E(a^{m+1}) = \int_0^\infty a^{m+1} g(a)da$$ Equation 23

So Eq. (21) can be rewritten as

$$E(l^m) = \frac{E(a^{m+1})}{\mu_a} M^m J_{m+1}$$ Equation 24

For m =1 and m = 2, we have

$$E(l) = \frac{\pi M E(a^2)}{4\mu_a}$$ Equation 25

and

$$E(l^2) = \frac{2M^2 E(a^3)}{3\mu_a}$$ Equation 26

Using $E(l) = \mu_l$, $E(l^2) = [(\mu_l)^2 + (\sigma_l)^2]$, $E(a) = \mu_a$ and $E(a^2) = [(\mu_a)^2 + (\sigma_a)^2]$, Eqs. (25) and (26) can be rewritten as

$$\mu_l = \frac{\pi M[(\mu_a)^2 + (\sigma_a)^2]}{4\mu_a} \qquad \text{Equation 27}$$

and

$$(\mu_l)^2 + (\sigma_l)^2 = \frac{2M^2 E(a^3)}{3\mu_a} \qquad \text{Equation 28}$$

(a) If $g(a)$ is lognormally distributed with mean μ_a and standard deviation σ_a, then

$$E(a^3) = \left[\frac{(\mu_a)^2 + (\sigma_a)^2}{\mu_a}\right]^3 \qquad \text{Equation 29}$$

Substituting Eq. (29) into Eq. (28) and solving Eqs. (27) and (28) for μ_a and σ_a gives

$$\mu_a = \frac{128(\mu_l)^3}{3\pi^3 M^2[(\mu_l)^2 + (\sigma_l)^2]} \qquad \text{Equation 30}$$

and

$$(\sigma_a)^2 = \frac{1536\pi^2[(\mu_l)^2 + (\sigma_l)^2](\mu_l)^4 - 128^2(\mu_l)^6}{9\pi^6 M^2[(\mu_l)^2 + (\sigma_l)^2]^2} \qquad \text{Equation 31}$$

(b) If $g(a)$ has a negative exponential distribution with mean μ_a, then $\sigma_a = \mu_a$ and from Eq. (27) we obtain

$$\mu_a = \frac{2}{\pi M}\mu_l \qquad \text{Equation 32}$$

(c) If $g(a)$ has a Gamma distribution with mean μ_a and standard deviation σ_a, then

$$E(a^3) = \frac{[(\mu_a)^2 + (\sigma_a)^2][(\mu_a)^2 + 2(\sigma_a)^2]}{\mu_a} \qquad \text{Equation 33}$$

Substituting Eq. (33) into Eq. (28) and solving Eqs. (27) and (28) for μ_a and σ_a gives

$$\mu_a = \frac{64(\mu_l)^2 - 3\pi^2[(\mu_l)^2 + (\sigma_l)^2]}{8\pi M \mu_l} \qquad \text{Equation 34}$$

and

$$(\sigma_a)^2 = \frac{\{64(\mu_l)^2 - 3\pi^2[(\mu_l)^2 + (\sigma_l)^2]\}\{3\pi^2[(\mu_l)^2 + (\sigma_l)^2] - 32(\mu_l)^2\}}{64\pi^2 M^2 (\mu_l)^2} \qquad \text{Equation 35}$$

Table 3-1 summarizes the above expressions for determining μ_a and σ_a from μ_l and σ_l, respectively for lognormal, negative exponential and Gamma distribution of discontinuity diameters. Conversely, with known μ_a and σ_a, and the distribution form of $g(a)$, the mean μ_l and standard deviation σ_l of trace lengths can also be obtained. The expressions are summarized in Table 3-2.

It is noted that, with the same μ_l and σ_l, we can have different μ_a and σ_a if the assumed distribution form of $g(a)$ is different. This means that the estimation of discontinuity size distributions from Eq. (17) or (19) may not be robust. To overcome the problem of uniqueness, a relationship between the ratio of the 4th and 1st moments of the discontinuity size distribution and the 3rd moment of the trace length distribution will be used to check the suitability of the assumed discontinuity size distribution form.

Table 3-1 Expression for determining μ_a and σ_a from μ_l and σ_l

Distribution form of $g(a)$	μ_a	$(\sigma_a)^2$
Lognormal	$\dfrac{128(\mu_l)^3}{3\pi^3 M[(\mu_l)^2+(\sigma_l)^2]}$	$\dfrac{1536\pi^2[(\mu_l)^2+(\sigma_l)^2](\mu_l)^4-128^2(\mu_l)^6}{9\pi^6 M^2[(\mu_l)^2+(\sigma_l)^2]^2}$
Negative exponential	$\dfrac{2}{\pi M}\mu_l$	$\left[\dfrac{2}{\pi M}\mu_l\right]^2$
Gamma	$\dfrac{64(\mu_l)^2-3\pi^2[(\mu_l)^2+(\sigma_l)^2]}{8\pi M\mu_l}$	$\dfrac{\{64(\mu_l)^2-3\pi^2[(\mu_l)^2+(\sigma_l)^2]\}\times\{3\pi^2[(\mu_l)^2+(\sigma_l)^2]-32(\mu_l)^2\}}{64\pi^2 M^2(\mu_l)^2}$

Table 3-2 Expression for determining μ_l and σ_l from μ_a and σ_a

Distribution form of $g(a)$	μ_l	$(\sigma_l)^2$
Lognormal	$\dfrac{\pi M[(\mu_a)^2+(\sigma_a)^2]}{4\mu_a}$	$\dfrac{32M^2[(\mu_a)^2+(\sigma_a)^2]^3-3\pi^2M^2(\mu_a)^2[(\mu_a)^2+(\sigma_a)^2]^2}{48(\mu_a)^4}$
Negative exponential	$\dfrac{\pi M}{2}\mu_a$	$\dfrac{(16-\pi^2)M^2}{4}(\mu_a)^2$
Gamma	$\dfrac{\pi M[(\mu_a)^2+(\sigma_a)^2]}{4\mu_a}$	$\dfrac{32M^2[(\mu_a)^2+(\sigma_a)^2][(\mu_a)^2+2(\sigma_a)^2]-3\pi^2M^2[(\mu_a)^2+(\sigma_a)^2]^2}{48(\mu_a)^2}$

For $m = 3$, Eq. (24) becomes

$$\frac{E(a^4)}{E(a)}=\frac{16E(l^3)}{3\pi M^3} \qquad \text{Equation 36}$$

For the three distribution forms of $g(a)$ discussed above, Eq. (36) can be rewritten as:

(a) If $g(a)$ is lognormally distributed with mean μ_a and standard deviation σ_a,

$$\frac{[(\mu_a)^2+(\sigma_a)^2]^6}{(\mu_a)^9}=\frac{16E(l^3)}{3\pi M^3} \qquad \text{Equation 37}$$

(b) If $g(a)$ has a negative exponential distribution with mean μ_a,

$$24(\mu_a)^2=\frac{16E(l^3)}{3\pi M^3} \qquad \text{Equation 38}$$

(c) If $g(a)$ has a Gamma distribution with mean μ_a and standard deviation σ_a,

$$\frac{[(\mu_a)^2+(\sigma_a)^2][(\mu_a)^2+2(\sigma_a)^2][(\mu_a)^2+3(\sigma_a)^2]}{(\mu_a)^3}=\frac{16E(l^3)}{3\pi M^3} \qquad \text{Equation 39}$$

So the following procedure can be used to infer the discontinuity size distribution $g(a)$:

1. Obtain the true trace length distribution of $f(l)$ (see Section 3.2.1.6 for the details) and compute $E(l^3)$.
2. Assume one of the distribution forms for $g(a)$ in Table 3-3and compute μ_a and σ_a using corresponding expressions, e.g., for a lognormal distribution form of $g(a)$, equations (30) and (31) are used.
3. Check the equality of equation (36) corresponding to the assumed distribution form of $g(a)$, e.g., for a lognormal distribution form of $g(a)$, the equality of equation (37) is checked. The assumed distribution form of $g(a)$ corresponding to the case that the left and right sides are the closest to, is the best distribution form of $g(a)$ and thus can be used, together with the corresponding μ_a and σ_a, to represent the discontinuity distribution.

3.2.1.6 Estimation of True Trace Length Distribution $f(l)$

Because the discontinuity size distribution $g(a)$ is related to the true trace length distribution $f(l)$, we need to estimate $f(l)$ from the measured trace (length) data by correcting the sampling biases. Zhang and Einstein (2000a) developed a method for estimating the true trace length distribution

by considering the sampling biases for circular window sampling, which is reproduced in the following.

Measured trace lengths can be obtained from three types of sampling on an exposure (including natural outcrops, rock cuts and tunnel walls): (a) sampling the traces that intersect a line drawn on the exposure, which is known as scanline sampling; (b) sampling the traces that intersect a circle drawn on the exposure, which is known as circle sampling; and (c) sampling the traces within a finite size area (usually rectangular or circular in shape) on the exposure, which is known as area (or window) sampling. It is important to note that in window sampling as it is defined here only the portions of the discontinuity traces within the window are measured, while the portions of traces intersecting such a window but lying outside are not considered. In this study, circular window sampling (see Figure 3-18) is considered. If the outcrop is circular in shape, it can be conveniently used as a sampling window. Circular window sampling has the advantage that no discontinuity orientation data is needed when estimating the true mean trace lengths (Mauldon 1998; Zhang and Einstein 1998).

In sampling for trace lengths, errors can occur due to the following biases (Baecher, Lanney, and Einstein 1978; Einstein et al. 1979; Priest and Hudson 1981; Kulatilake and Wu 1984):

1. Orientation bias: the probability of a joint appearing in an outcrop depends on the relative orientation between the outcrop and the joint (see also Terzaghi 1965);

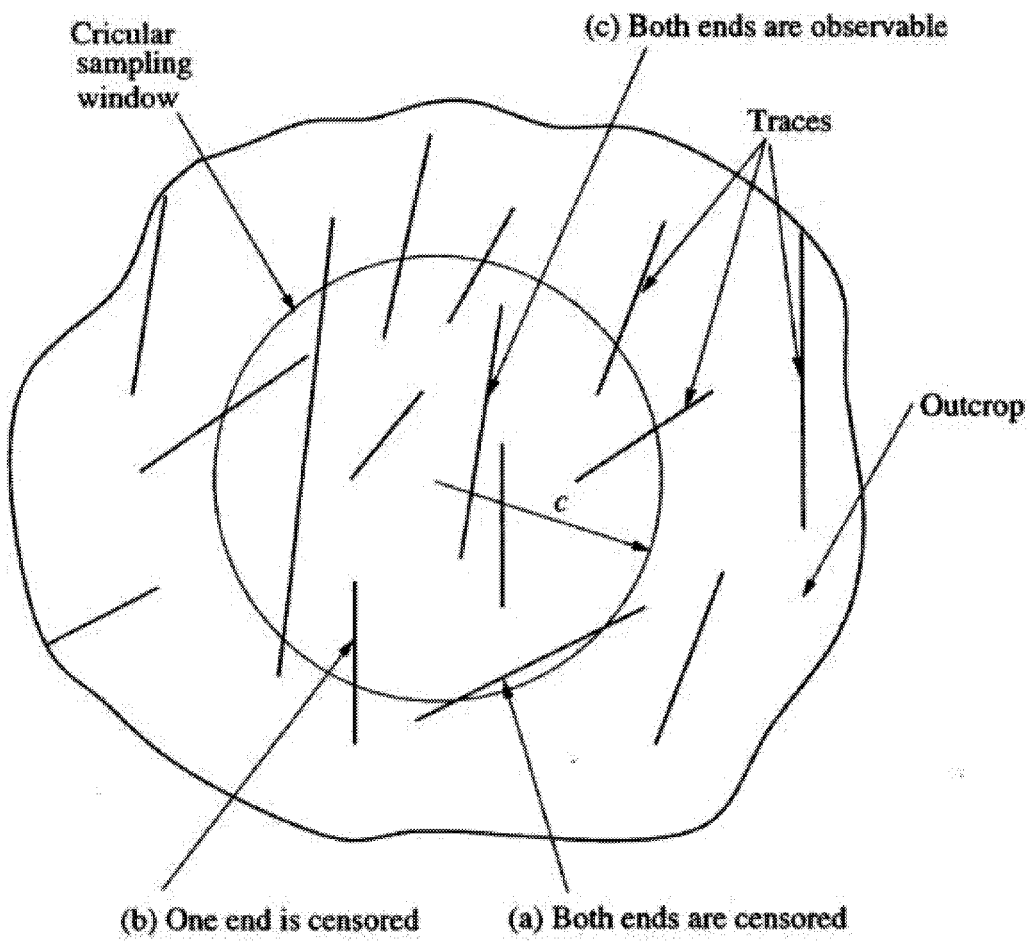

Figure 3-18 Discontinuities intersect a circular sampling window in three ways

2. Size bias: large joints are more likely to be sampled than small joints. This bias affects the results in two ways: (a) a larger joint is more likely to appear in an outcrop than a smaller one; and (b) a longer trace is more likely to appear in a sampling area than a shorter one.
3. Truncation bias: Very small trace lengths are difficult or sometimes impossible to measure. Therefore, trace lengths below some known cutoff length are not recorded.
4. Censoring bias: Long joint traces may extend beyond the visible exposure so that one end or both ends of the joint traces can not be seen.

In inferring the true trace length distribution (i.e., the trace length distribution on an infinite sampling surface) from the measured trace lengths on a finite size area on this surface, biases (2b), (3) and (4) should be considered. Biases (1) and (2a) should be considered when inferring the discontinuity size distribution from the true trace length distribution. Truncation bias (3) can be corrected using the method of Warburton (1980a). Decreasing the truncation-level in discontinuity surveys can reduce effects of truncation bias on trace length estimates. It is practically feasible to observe and measure trace lengths as low as 10 mm both in the filed and from photographs (Priest and Hudson 1981). Truncation at this level will have only a small effect on the data, particularly if the mean trace length in the order of meters (Priest and Hudson 1981; Einstein and Baecher 1983). Therefore, the effect of truncation bias on trace length estimates is usually ignored (Kulatilake et al. 1993; Zhang and Einstein 1998). However, biases (2b) and (4) are important and will be considered.

According to Zhang (1999), the following procedure is proposed for estimating $f(l)$:

(a) Estimate the true mean trace length $\hat{\mu}_l$ by (Zhang and Einstein 1998)

$$\hat{\mu}_l = \frac{\pi(\hat{N} + \hat{N}_0 - \hat{N}_2)}{2(\hat{N} - \hat{N}_0 + \hat{N}_2)} c \qquad \text{Equation 40}$$

where $\hat{N}$, $\hat{N}_o$ and $\hat{N}_2$ are respectively the total number of traces that appear on the window, the number of traces with both ends censored and the number of traces both ends observable; and c is the radius of the sampling window (see Figure 3-18).

(b) Analyze the measured trace lengths to obtain the mean $(\mu_l)_m$, the standard deviation $(\sigma_l)_m$, the coefficient of variation COV_m $[=(\sigma_l)_m/(\mu_l)_m]$ and the suitable distribution form of the measured trace lengths. To find the suitable distribution $h(l)$ of the measured trace lengths of each discontinuity set, the distribution forms in Table 3-3 can be checked by using χ^2 and Kolmogorov-Smirnov goodness-of-fit tests.

(c) Obtain the true trace length distribution $f(l)$ by assuming: (1) $f(l)$ and $g(l)$ have the same distribution form; and (2) the mean and standard deviation of $f(l)$ are respectively $\hat{\mu}_l$ and $\hat{\mu}_l(COV_m)$.

When applying Eq. (40), the following two special cases may occur and should be avoided:

1) If $\hat{N}_o = \hat{N}$, then $\hat{\mu}_l \rightarrow \infty$. In this case, all the discontinuities intersecting the sampling window have both ends censored. This implies that the area of the window used for the discontinuity survey may be too small.

2) If $\hat{N}_2 = \hat{N}$, then $\hat{\mu}_l = 0$. In this case, all the discontinuities intersecting the sampling window have both ends observable. According to Pahl (1981), this results is due to violation of the assumption that the midpoints of traces are uniformly distributed in the two dimensional space.

These two special cases can be addressed by increasing the sampling window size and/or changing the sampling window position (Zhang 1999). Another method to address these two special cases is to use multiple windows of the same size and at different locations (Zhang and Einstein 1998).

Table 3-3 Common Distribution Forms of Trace Lengths

Investigator	Distribution Form
Robertson (1970)	Exponential
McMahon (1974)	Lognormal
Bridges (1975)	Lognormal
Call et al. (1976)	Exponential
Barton (1977)	Lognormal
Cruden (1977)	Exponential
Baecher et al (1977)	Lognormal
Einstein et al. (1979)	Lognormal
Priest and Hudson (1981)	Exponential
Kulatilake (1993)	Exponential and Gamma (Gamma better)
Barton and Hsieh (1989)	Power Law
Barton and Larsen (1985)	Power Law
LaPointe and Hudson (1985)	Power Law

3.2.1.7 Effect of Sampling Plane Orientation on Trace Lengths

In this section, the effect of sampling plane orientation on trace lengths is investigated by using the derived stereological relationship between the trace length distribution and the discontinuity size distribution. For simplicity, only one discontinuity set with a deterministic orientation is considered. The discontinuity size of the set is assumed to be in lognormal distribution with μ_a = 8.0 m and σ_a = 4.0 m.

Figure 3-19 shows the variation of the mean trace length with β. Since β is the angle between the trace line and the discontinuity major axis, it is an indication of the sampling plane orientation relative to the discontinuity. It can be seen from Figure 3-19 that, despite the considerable difference between the maximum and the minimum of mean trace length, there are extensive

ranges of sampling plane orientations reflected by β over which the mean trace lengths show little variation, especially for large *k* values.

Figure 3-20 shows the variation of the standard deviation of trace lengths with β. It can be seen that the standard deviation of trace lengths varies with the sampling plane orientation reflected by β in the same general way as the mean trace length.

The results in Figure 3-19 and Figure 3-20 could well explain why Bridges (1975), Einstein (1979) and McMahon (1982) found different mean trace lengths on differently oriented sampling planes, whereas Robertson (1970) and Barton (1977) observed them to be approximately equal. In each of these reports, the number of differently oriented sampling planes was very limited and, depending on the relative orientations of the sampling planes, the authors could observe either approximately equal mean trace lengths or significantly different mean trace lengths. For example, in Bridges (1975), Einstein (1979) and McMahon (1982), the strike and dip sampling planes might be respectively in the β = 0° – 20° (or 160° – 180°) range and the β = 40° – 140° range, or vice versa. From Figure 3-19, this would result in very different mean trace lengths. On the other hand, in Robertson (1970) and Barton (1977), the strike and dip sampling planes might be both in the β = 40° – 140° range (i.e., in the "flat" trace length part of Figure 3-19) or respectively in some β ranges approximately symmetrical about β = 90°. It should be noted that the above is just an assumption because no information about the β values can be found in the original papers or reports.

The implications of Figure 3-19 and Figure 3-20 about field sampling are as follows:

If different sampling planes are used to collect trace (length) data, the sampling planes should be oriented such that significantly different mean trace lengths can be obtained from different planes. For example, if two sampling planes are used, one should be oriented in the β = 0° – 20° (or 160° – 180°) range and the other in the β = 60° – 120° range.

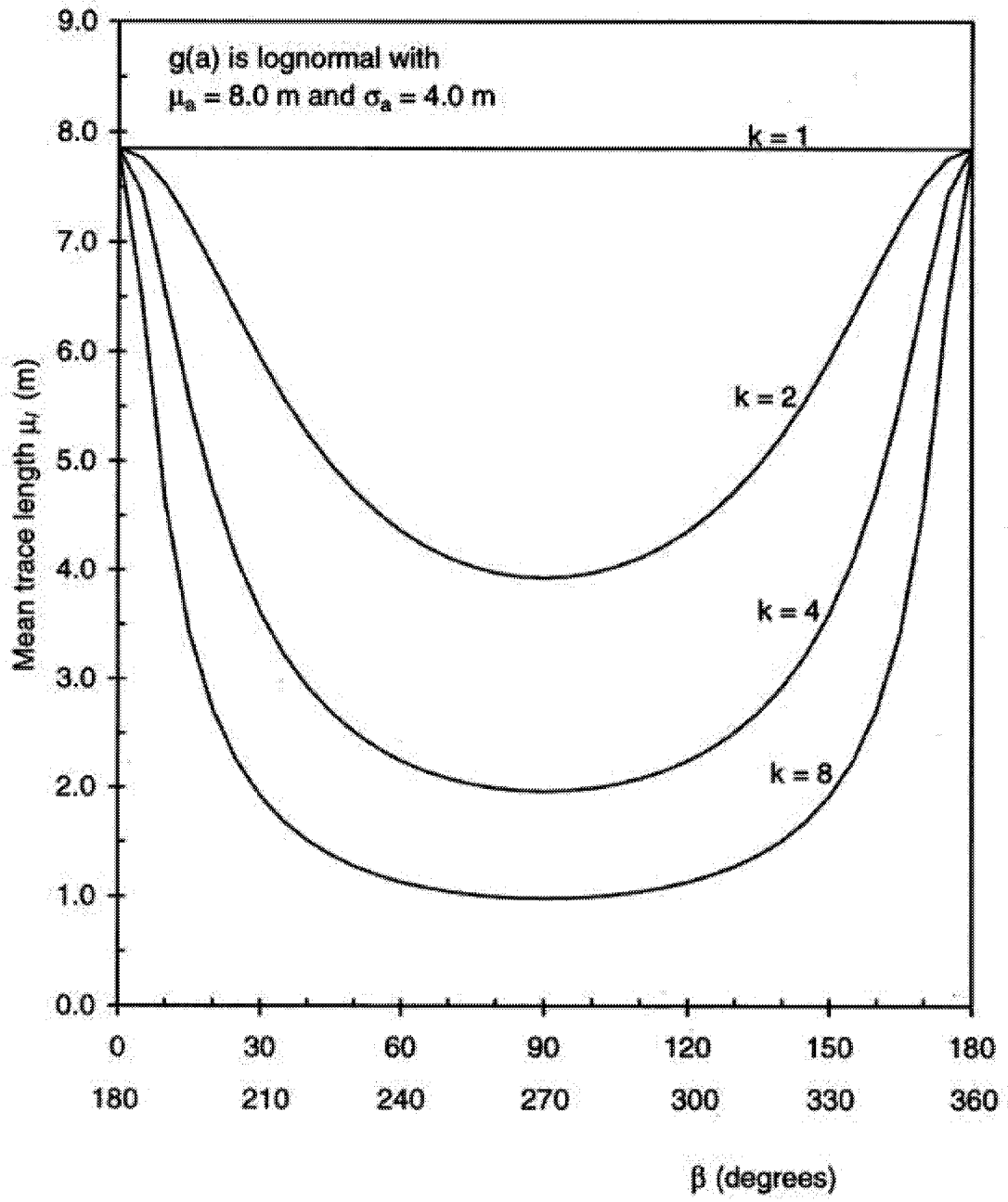

Figure 3-19 Variation of mean trace length with β

3.2.1.8 Verification by Numerical Simulation

To check the derived stereological relationship between trace length distributions and discontinuity size distributions, the trace data simulated using the FracMan discrete fracture code (Dershowitz et al. 1998) are analyzed. It should be noted that the FracMan discrete fracture code is just used to create discontinuity networks with known discontinuity size distribution and intensity, and to simulate the field sampling processes so that the proposed method can be checked. The assumptions used in FracMan do not affect the effectiveness for checking the

proposed method. The parameters for the simulations are shown in Table 3-4. Following Baecher et al. (1977), Barton (1978) and Warburton (1980a, b), the size of a discontinuity set is described by a lognormal distribution. For simplicity, only one discontinuity set with a deterministic orientation is considered. 2000 discontinuities are generated in a 20 m × 20 m × 20 m box [see Figure 3-21(a)]. Three circular sampling windows of radius 8 m respectively in plane $x = 0$ m, $y = 0$ m and $z = 0$ m are used to collect the trace (length) data [see Figure 3-21(b)].

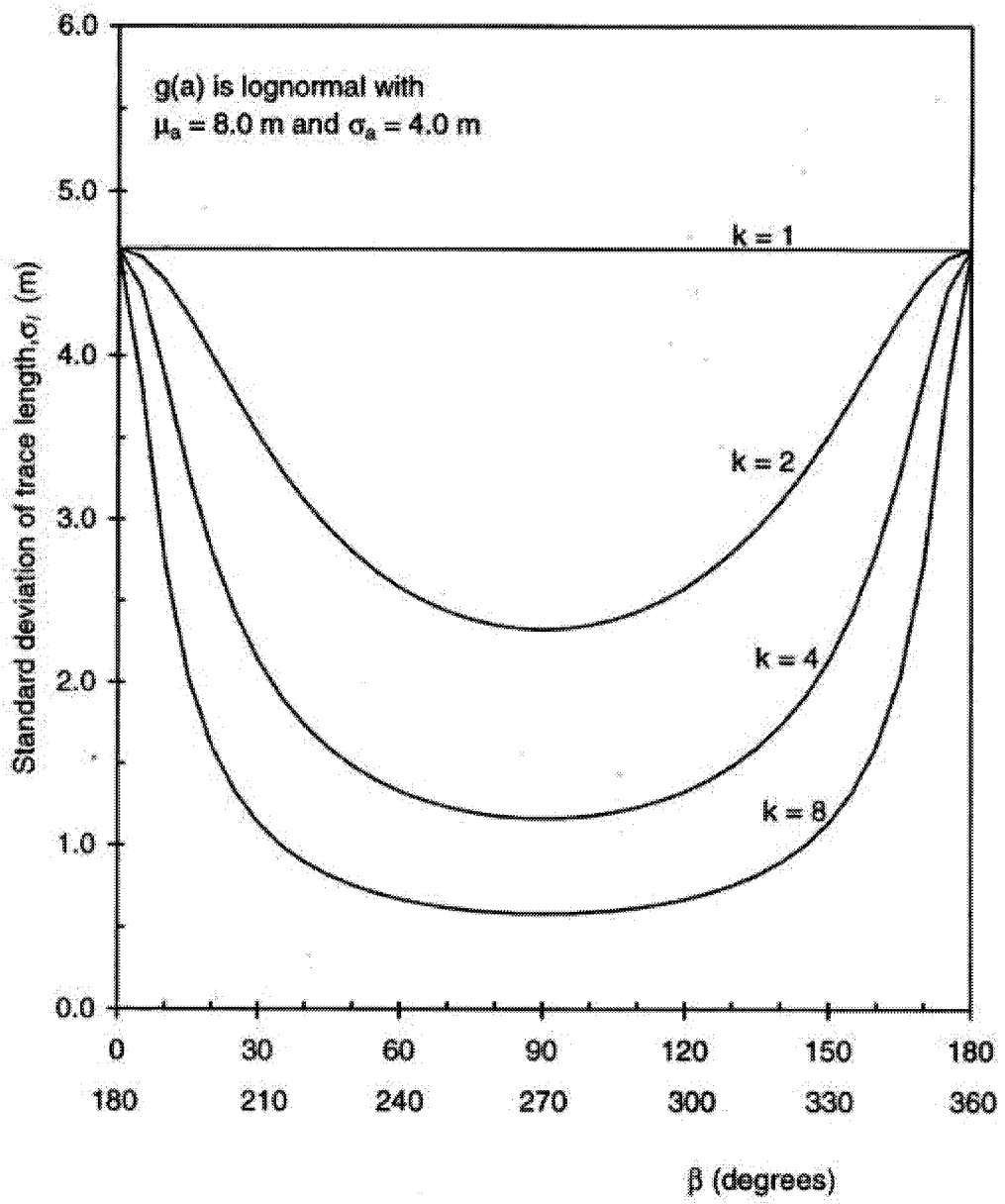

Figure 3-20 Variation of standard deviation of trace length with β

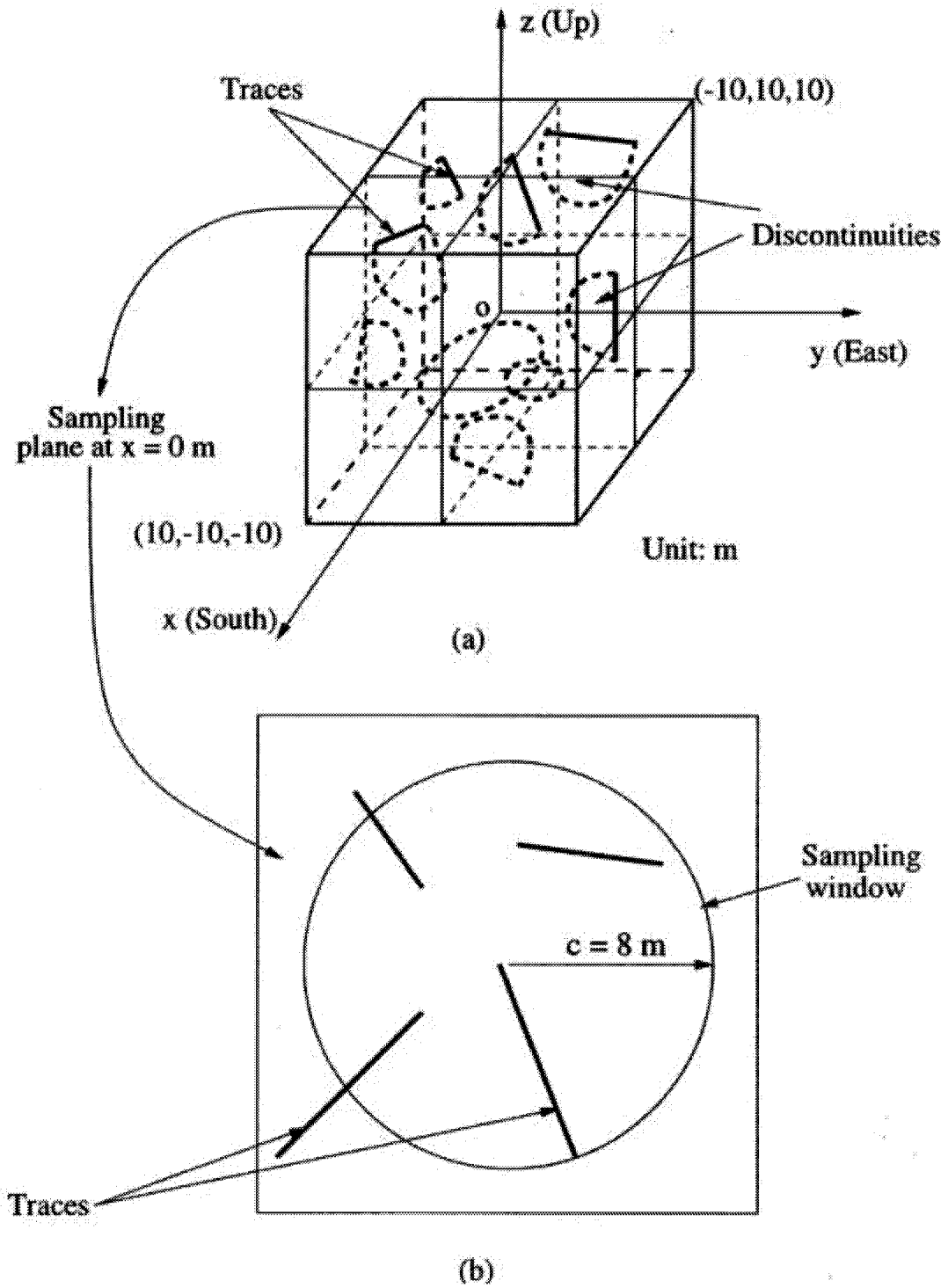

Figure 3-21 (a) Simulation volume is a box, i.e., the elliptical discontinuities are generated inside the box; (b) Sampling window at x = 0 m

Table 3-4 Parameters for simulation 1 using FracMan (see also Figure 3-21)

Discontinuities	
Number	2000
Pole direction (θ/ϕ)	300.0°/60.0°
Shape	Elliptical
Aspect ratio	4.0
Direction of major axis	30.0°/0.0°
Size a (Distribution)	Lognormal
Size a (Mean μ_a)	8.0 m
Size a (Standard deviation σ_a)	4.0 m
Simulation volume	20 m × 20 m × 20 m box
Sampling windows	
Circular window 1	c = 8.0 m; (θ/ϕ)= (0.0°/0.0°); β^* = 63.4°
Circular window 2	c = 8.0 m; (θ/ϕ)= (90.0°/0.0°); β^* = 33.7°
Circular window 3	c = 8.0 m; (θ/ϕ)= (0.0°/90.0°); β^* = 0.0°

*β is the angle between the trace line and the major axis of a discontinuity (see Figure 3-15)

For the three sampling windows shown in Table 3-4 and Figure 3-21, the theoretical (true) mean and standard deviation values of trace lengths can be obtained using the expressions for lognormal $g(a)$ is shown in Table 3-5.

Table 3-5 Theoretical values of Trace Length Mean and Standard Deviation

Sampling Window	M	Trace Length Mean μ_l *(m)*	Trace Length Standard Deviation σ_l *(m)*
1	0.277	2.18	1.29 m
2	0.422	3.31	1.96
3	1.0	7.85	4.65

For each discontinuity network realization, the discontinuity traces in a sampling window can be obtained. With the trace data, the values of $\hat{N}$, $\hat{N}_o$ and $\hat{N}_2$, respectively for each realization and for each sampling window, can be determined and the corresponding mean trace length $\hat{\mu}_l$ can then be predicted using Eq. (40). The predicted mean trace length values are shown in Figure 3-22. The average values of the predicted mean trace lengths of 10 realizations, for each sampling window, are shown in Table 3-5. For comparison, the theoretical mean trace length values obtained above from the expressions in
Table 3-2 are also shown in Figure 3-22 and Table 3-5. It can be seen that the theoretical and the predicted mean trace lengths are in excellent agreement.

Table 3-6. Comparison of theoretical (or true) and predicted mean trace lengths

Sampling Window (1)	μ_l (m) (2)	$\bar{\mu}_l$ (m) (3)	*Error* = $(\bar{\mu}_l - \mu_l)/\mu_l$ (%) (4)
Circular window 1 (β = 63.4°)	2.18	2.16	-0.9
Circular window 2 (β = 33.7°)	3.31	3.36	1.5
Circular window 3 (β = 0.0°)	7.85	7.63	-2.8

Note: $\bar{\mu}_l$ is the average of the predicted mean trace lengths $\hat{\mu}_l$ of 10 realizations; μ_l is the theoretical mean trace length obtained from the expressions in
Table 3-2.

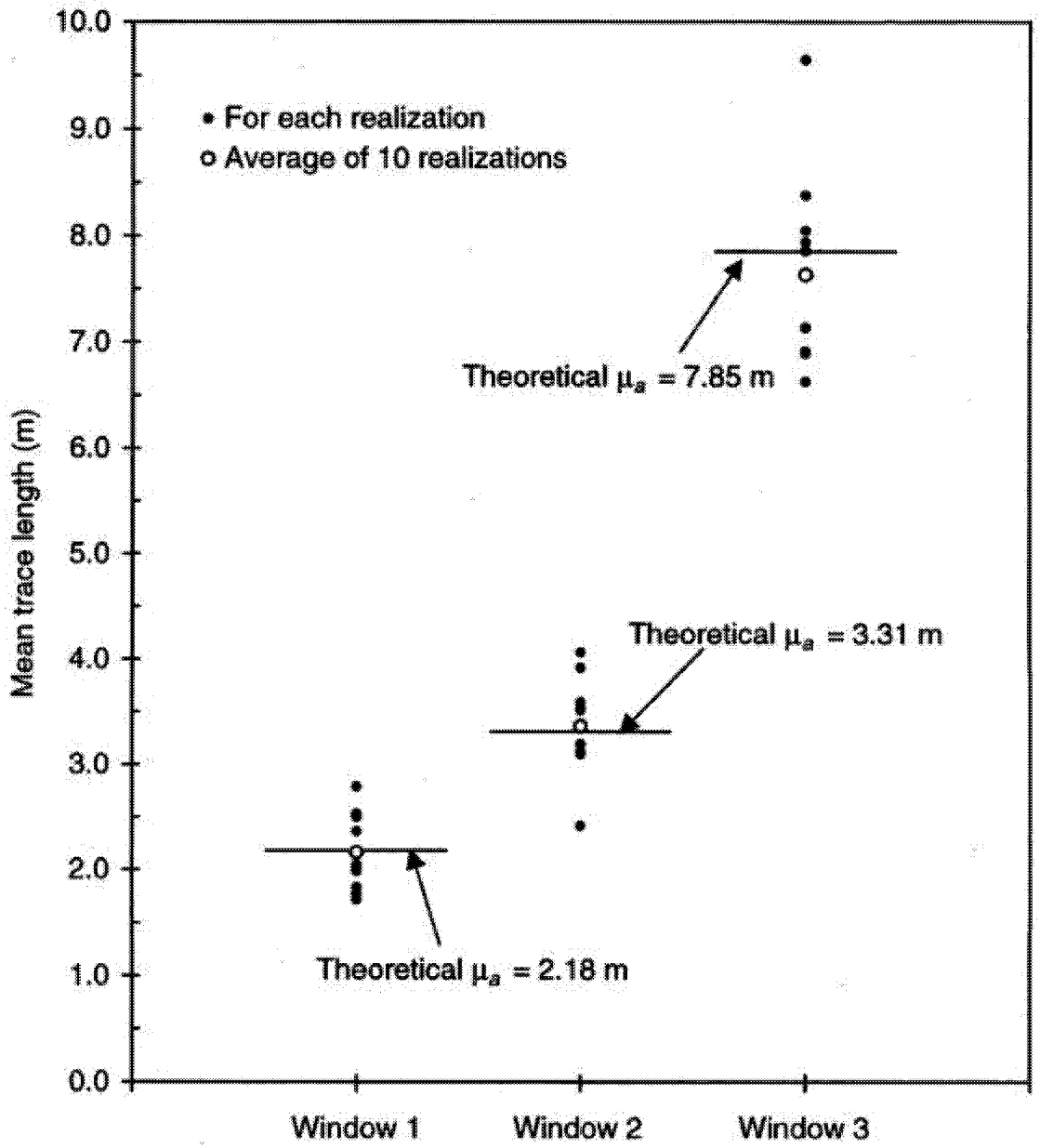

Figure 3-22 Comparison of theoretical mean trace lengths with predicted mean trace lengths from simulations

From the trace length data of each realization, the mean $(\mu_l)_m$, standard deviation $(\sigma_l)_m$ and coefficient of variation COV_m, which is the ratio of the standard deviation and mean, of measured trace lengths in each sampling window can be obtained. The obtained COV_m can then be combined with the corresponding mean trace length $\hat{\mu}_l$ to estimate the standard deviation $\hat{\sigma}_l$ as $\hat{\mu}_l (COV_m)$. The estimated standard deviation values are shown in Figure 3-23. The average values of the estimated standard deviation values of 10 realizations, for each sampling window, are shown in Table 3-7. For comparison, the theoretical standard deviation values obtained from the expressions in
Table 3-2 are also shown in Figure 3-23 and Table 3-7. It can be seen that the theoretical and the estimated standard deviation values are in good agreement.

The good agreement between the theoretical and estimated values is a validation of both the derived expressions in
Table 3-2 and the method presented in Section 3.2.1.6 for predicting the true mean and standard deviation of trace lengths.

The distribution forms of the measured trace lengths of 10 realizations for each sampling window are also investigated. χ^2 and Kolmogorov-Smirnov goodness-of-fit tests are used to check the suitability of lognormal and Gamma distributions (the negative exponential distribution is a special case of the Gamma distribution) in representing the measured trace lengths. The results of both χ^2 and Kolmogorov-Smirnov goodness-of-fit tests show that the lognormal distribution can represent the measured trace length distributions for all sampling windows at the 0.05 significance level. The Gamma distribution, however, can represent the measured trace length distributions in only some of the sampling windows at the 0.05 significance level. Therefore, according to Section 3.2.1.6, the true trace length distribution is assumed to be lognormal.

3.2.1.9 Approach Implementation

In this section, we show how to use the estimated true trace length distributions corresponding to different sampling windows to infer the major axis orientation, aspect ratio and size distribution of discontinuities.

Using the average of 10 realizations for each sampling window, the true trace length distributions can be derived as shown in Table 3-8.

Table 3-7 Comparison of theoretical (or true) and predicted standard deviation of trace lengths

Sampling Window (1)	σ_l (m) (2)	$\overline{\sigma}_l$ (m) (3)	$Error = (\overline{\sigma}_l - \sigma_l)/\sigma_l$ (%) (4)
Circular window 1 ($\beta = 63.4°$)	1.29	1.29	0
Circular window 2 ($\beta = 33.7°$)	1.96	2.07	5.6
Circular window 3 ($\beta = 0.0°$)	4.65	4.19	-9.9

Note: $\overline{\sigma}_l$ is the average of the predicted standard deviations of trace lengths $\hat{\sigma}_l$ of 10 realizations; σ_l is the theoretical standard deviation of trace lengths obtained from the expressions in Table 3-2.

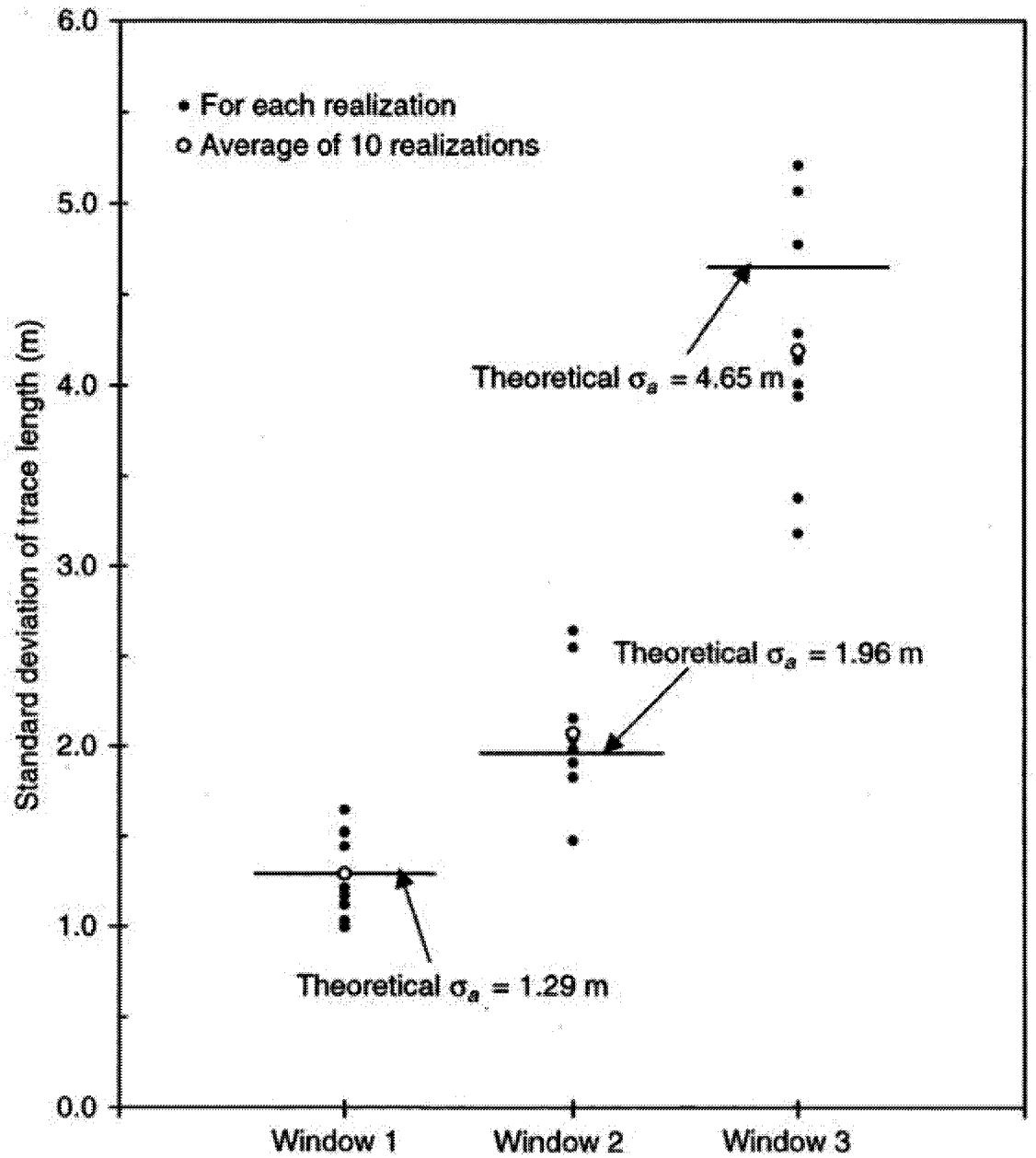

Figure 3-23 Comparison of the theoretical standard deviation of trace lengths with predicted standard deviation of trace lengths from simulations

Table 3-8 Derived true trace length distributions

Sampling Window (1)	μ_l (m) (2)	σ_l (m) (3)	Distribution Form (4)
Circular window 1 ($\beta = 63.4°$)	2.16	1.29	Lognormal
Circular window 2 ($\beta = 33.7°$)	3.36	2.07	Lognormal
Circular window 3 ($\beta = 0.0°$)	7.63	4.19	Lognormal

Note: μ_l is from column 3 of Table 3-5 and σ_l from column 3 of Table 3-6.

To simulate the actual sampling condition, we assume that we know the pole orientation (i.e., 300.0°/60.0°) but not the major axis orientation of discontinuities. This is a reasonable assumption given the fact that discontinuity orientations can be quite reliably observed. Thus the unknowns that we need to infer are:

1. The major axis orientation
2. The aspect ratio k
3. μ_a, σ_a and distribution form of $g(a)$.

Assuming three major axis orientations, the corresponding β values for each sampling window can be obtained (see Table 3-9). For ***each*** assumed major axis orientation and by assuming an aspect ratio k and a distribution form of $g(a)$, μ_a and σ_a can be calculated from μ_l and σ_l obtained for each sampling window. The relations between the calculated values of μ_a and σ_a and aspect ratio k for lognormal, negative exponential and Gamma distribution forms of $g(a)$ are shown in Figure 3-24, Figure 3-26 to Figure 3-29 and Figure 3-30 to Figure 3-32 for the three assumed major axis orientations, respectively. Since the trace length data of the three sampling windows correspond to a ***single*** discontinuity network, the relations between inferred μ_a (and σ_a) and k corresponding to the three sampling windows, i.e., the curves in Figure 3-24 to Figure 3-32, should intersect in one point. This point corresponds to the ***actual*** major axis orientation, which in practice is not known and needs to be inferred. Inspection of Figure 3-24 to Figure 3-32 show that the μ_a (and σ_a) versus k curves intersect only in Figure 3-27 to Figure 3-29 but do so very distinctly. Figure 3-27 to Figure 3-29 are for the major axis orientation of 30°/0°, which is the actual major axis orientation, used in the simulation. The k, μ_a and σ_a values at the intersection points (see Figure 3-27 to Figure 3-29) are the corresponding predicted values. The prediction results for the lognormal, negative exponential and Gamma distribution forms of $g(a)$ are also shown in Table 3-10.

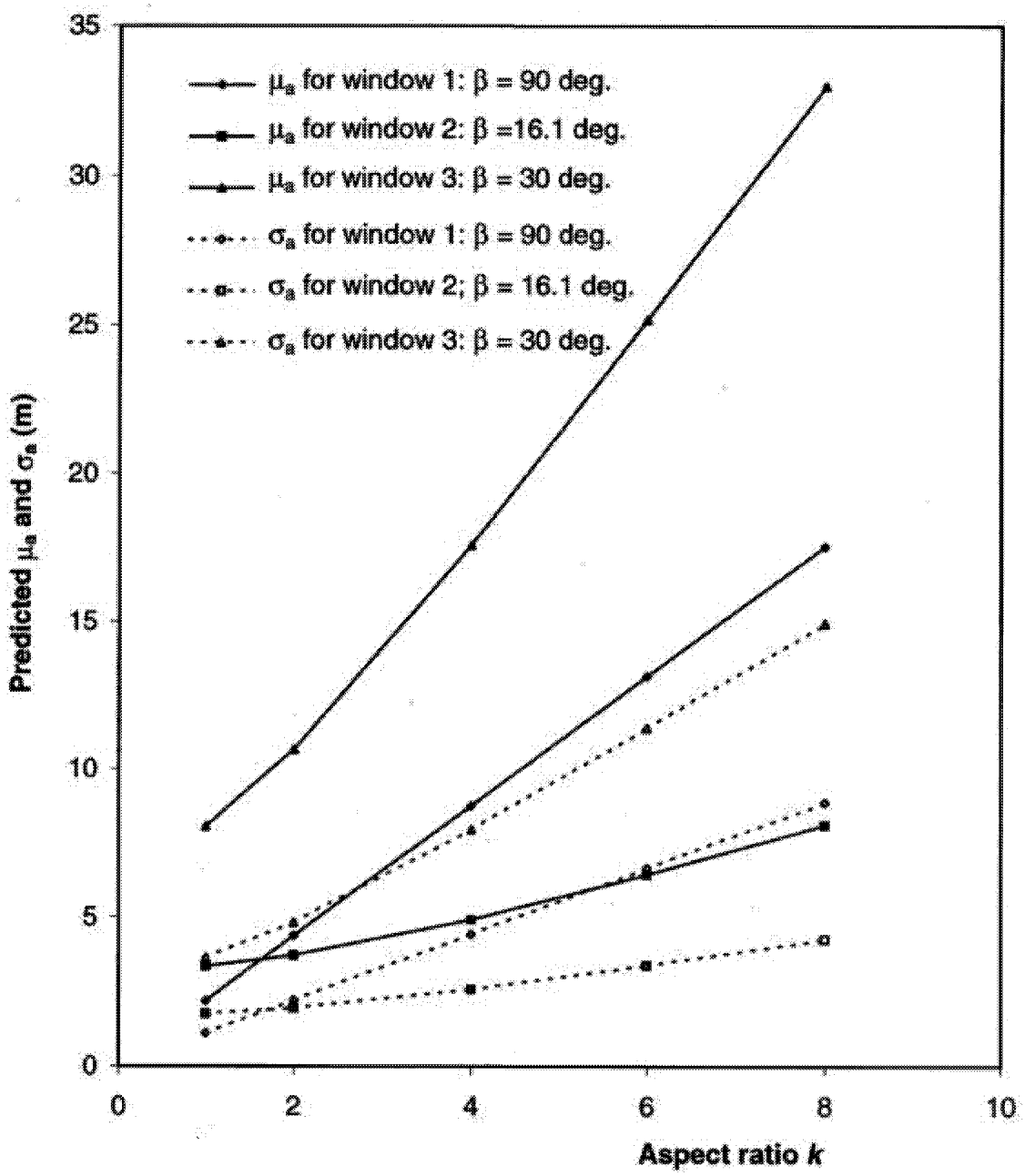

Figure 3-24 Variation of μ_a and σ_a with aspect ratio k for assumed major axis orientation 1 (0°/0°): assuming a lognormal distribution form of *g(a)*

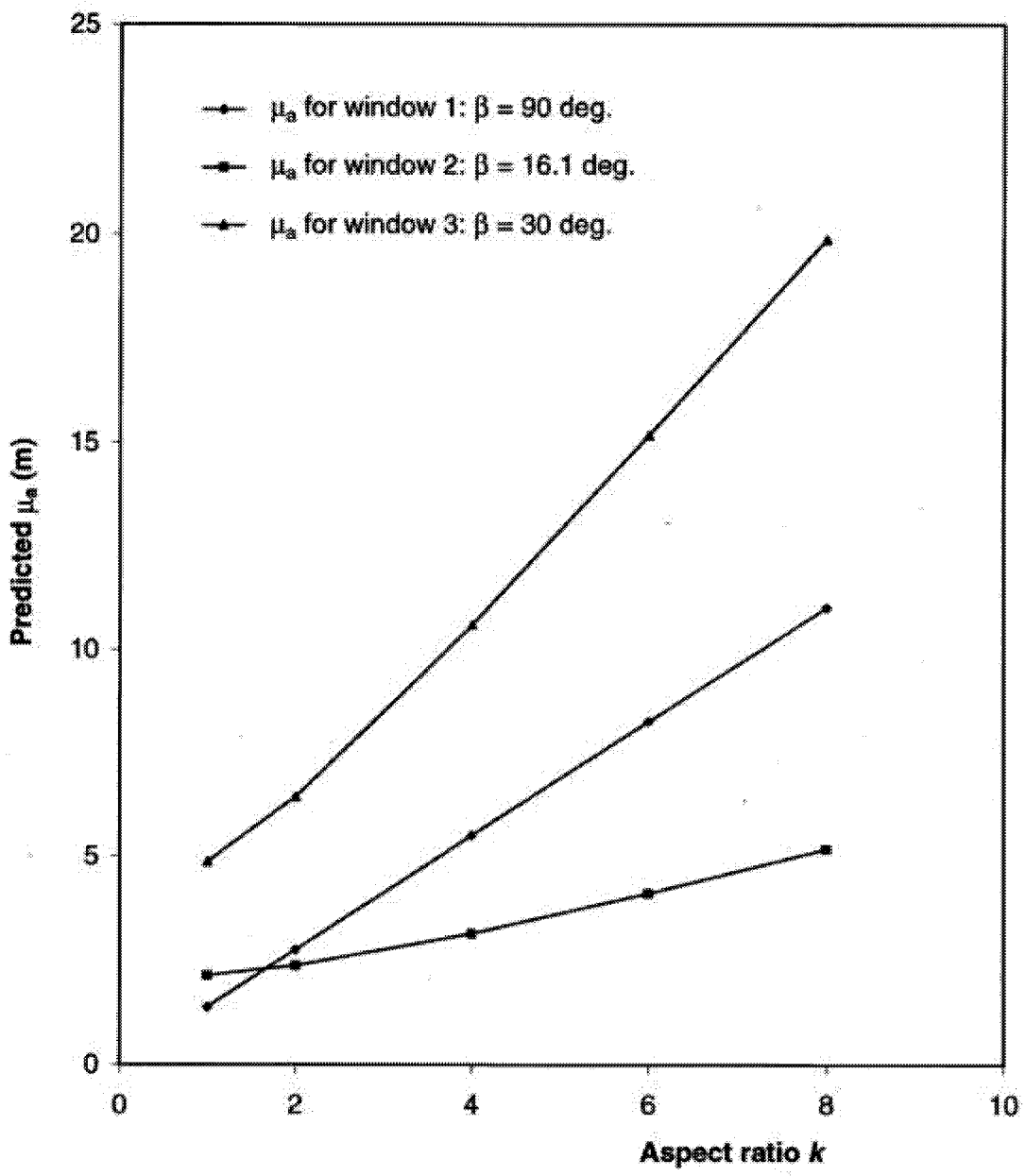

Figure 3-25 Variation of μ_a with aspect ratio k for assumed major axis orientation 1 (0°/0°): assuming a negative exponential distribution form of $g(a)$

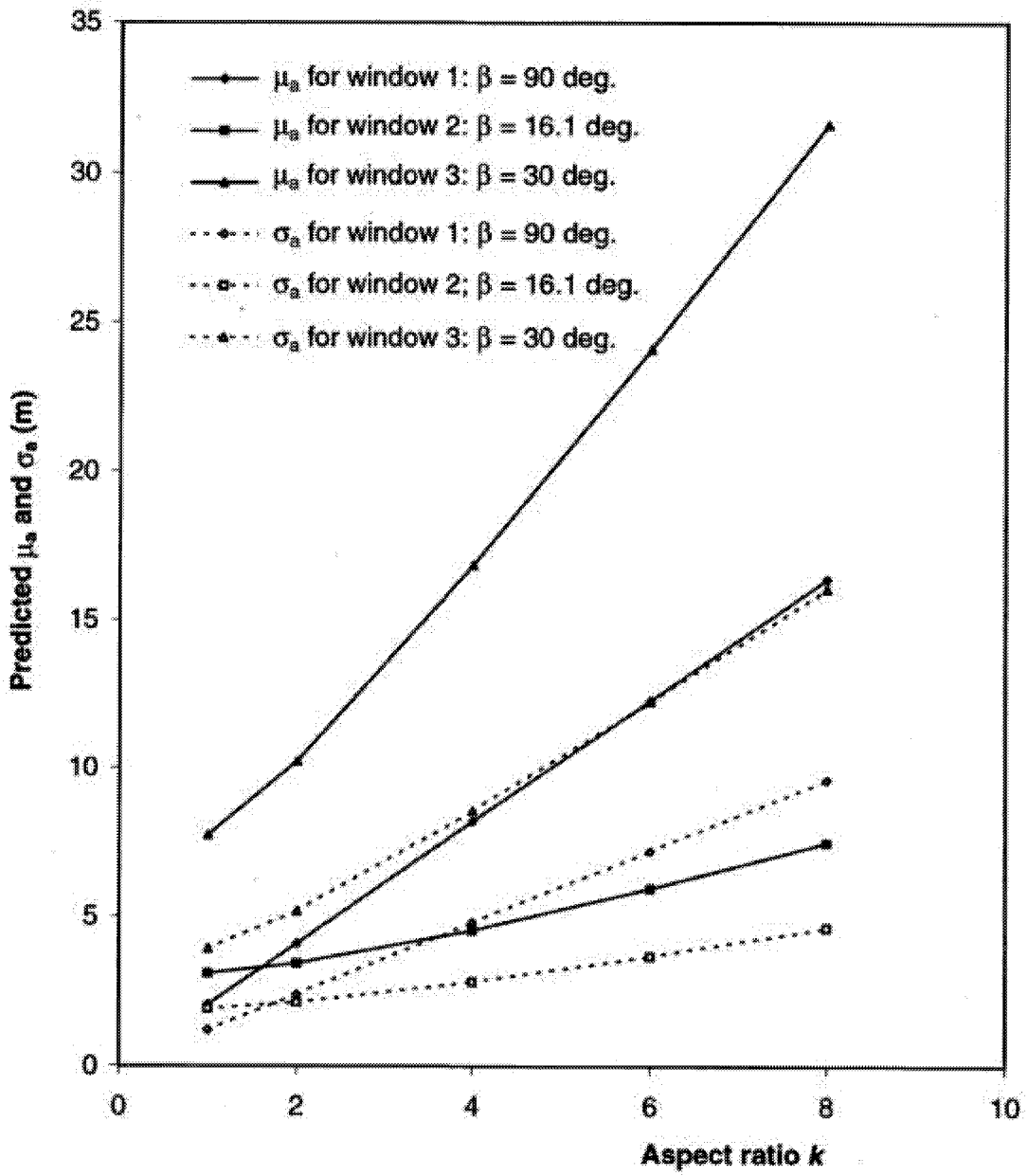

Figure 3-26 Variation of μ_a and σ_a with aspect ration k for assumed major axis orientation 1 (0°/0°): assuming a Gamma distribution form of *g(a)*

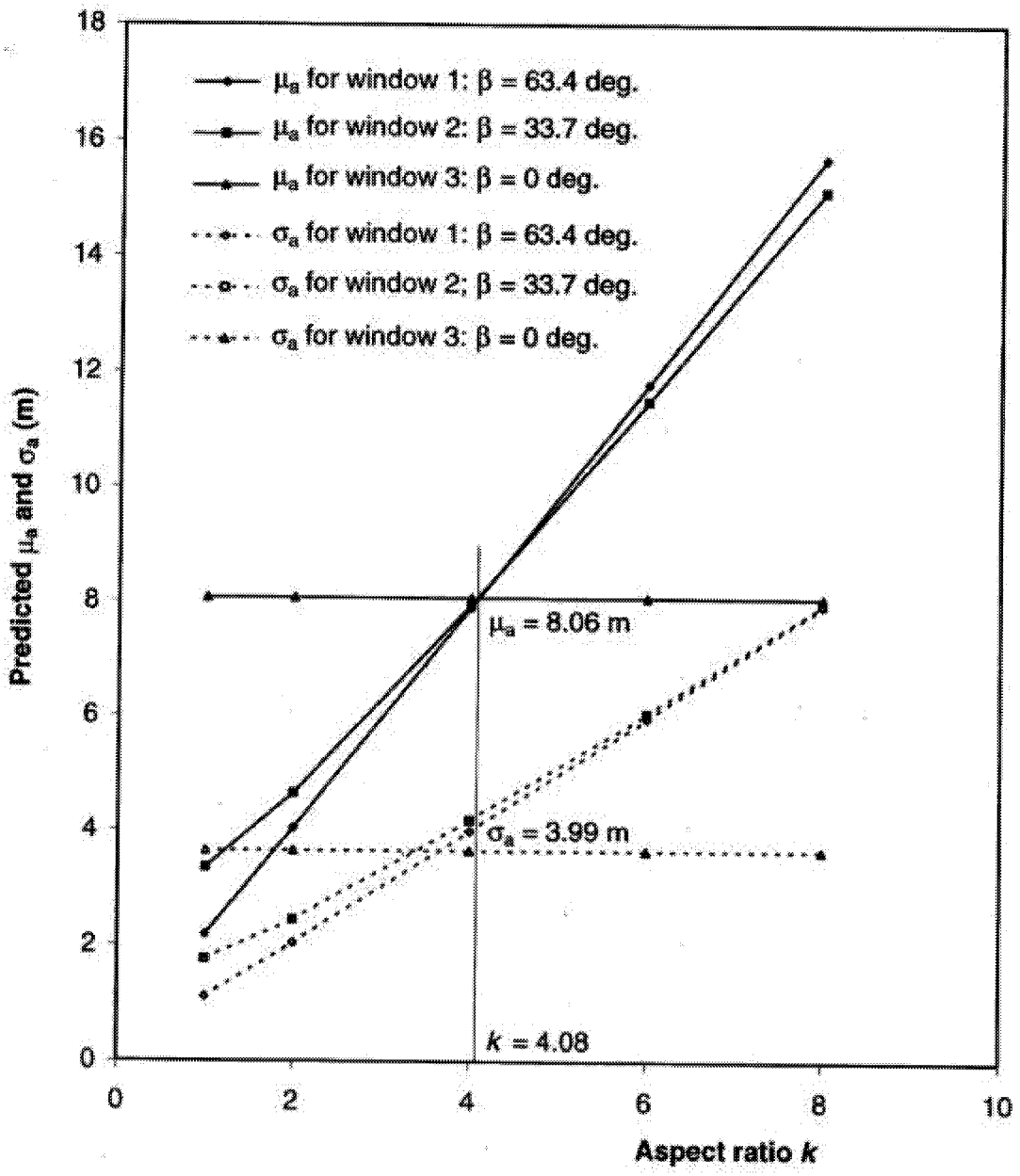

Figure 3-27 Variation of μ_a and σ_a with aspect ration k for assumed major axis orientation 2 (30°/0°): assuming a lognormal distribution form of a

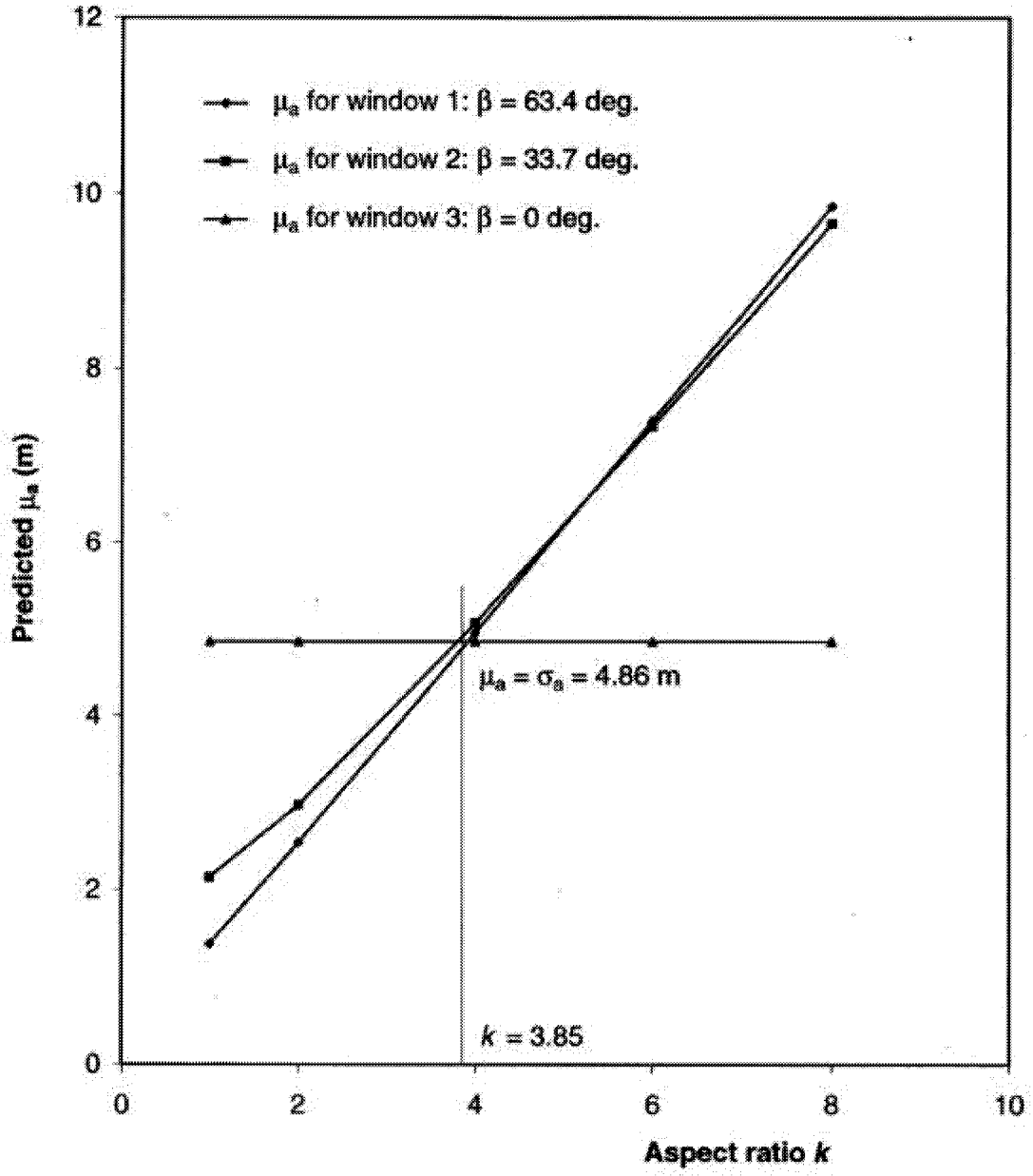

Figure 3-28 Variation of μ_a with aspect ration k for assumed major axis orientation 2 (30°/0°): assuming a negative exponential distribution form of a

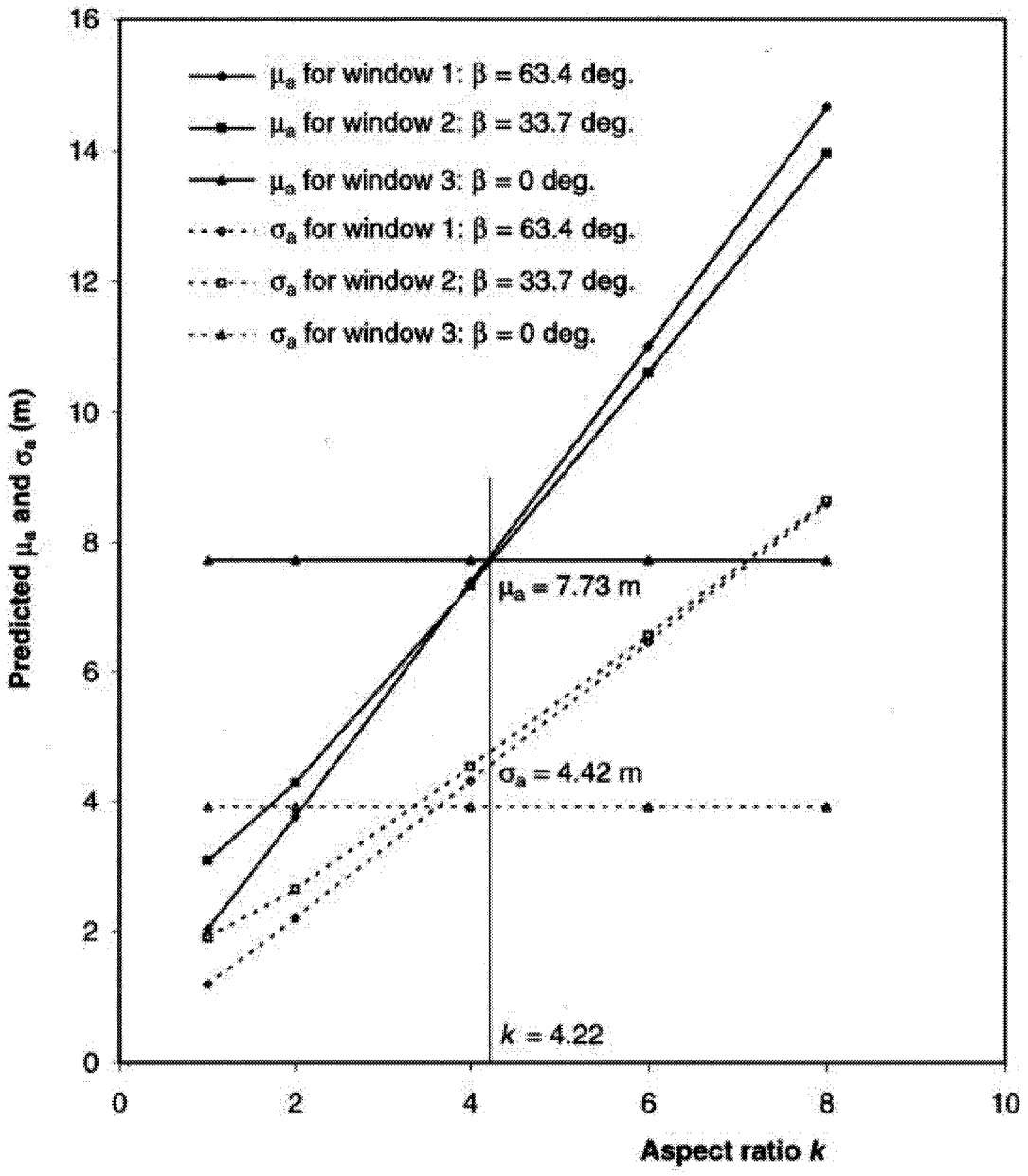

Figure 3-29 Variation of μ_a and σ_a with aspect ration k for assumed major axis orientation 2 (30°/0°): assuming a Gamma distribution form of a

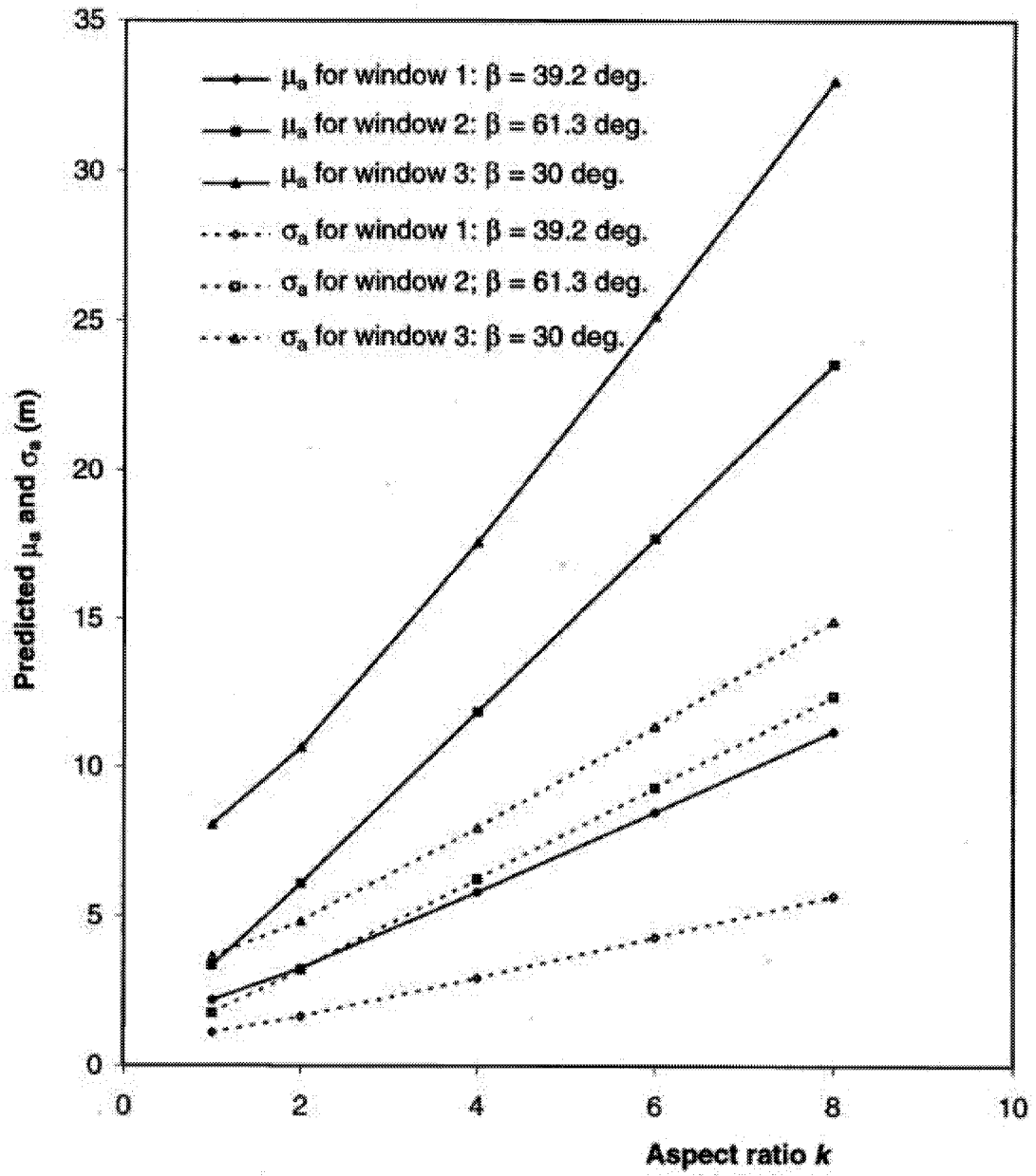

Figure 3-30 Variation of μ_a and σ_a with aspect ration k for assumed major axis orientation 3 (60°/0°): assuming a lognormal distribution form of a

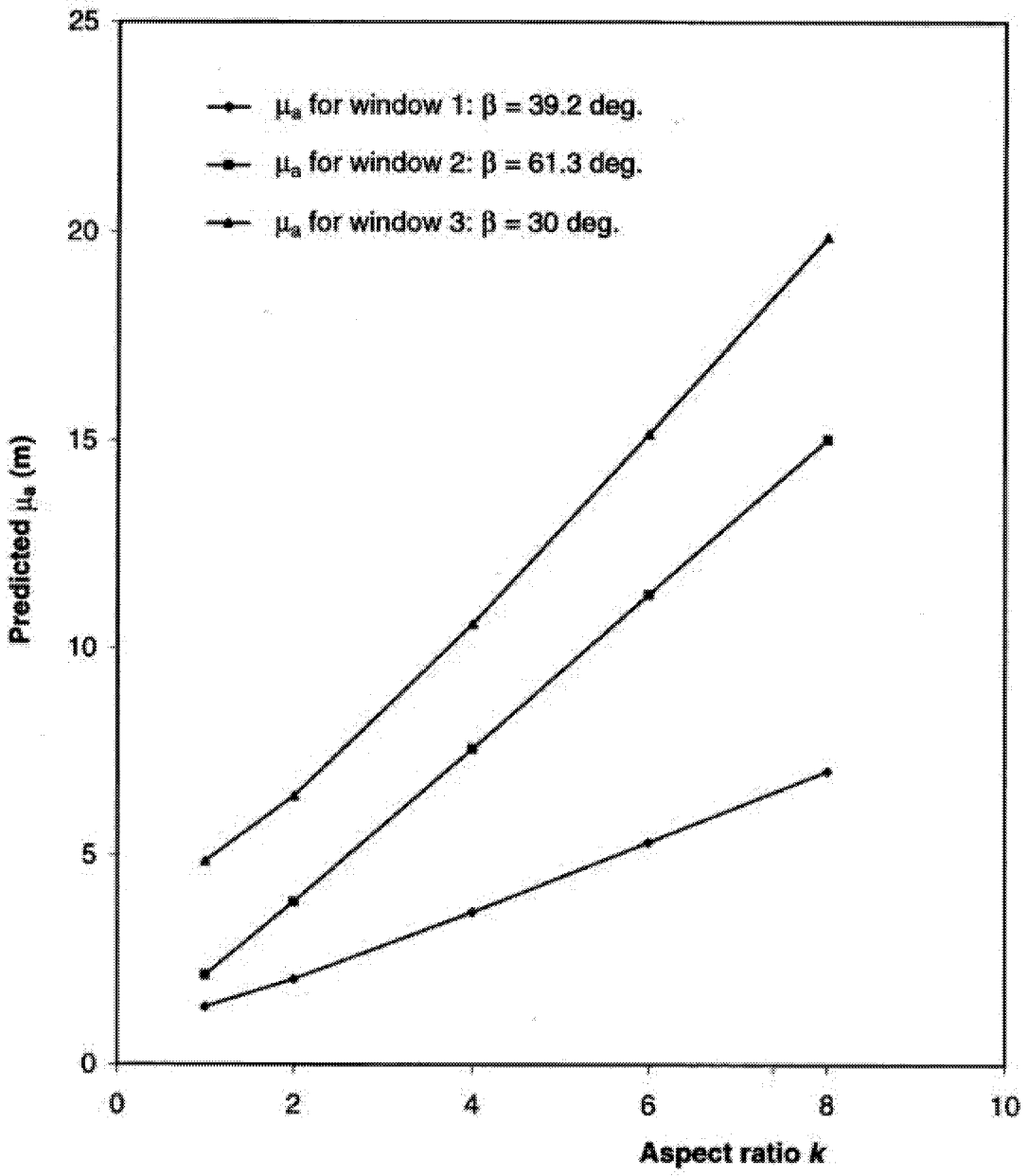

Figure 3-31 Variation of μ_a with aspect ration k for assumed major axis orientation 3 (60°/0°): assuming a negative exponential distribution form of a

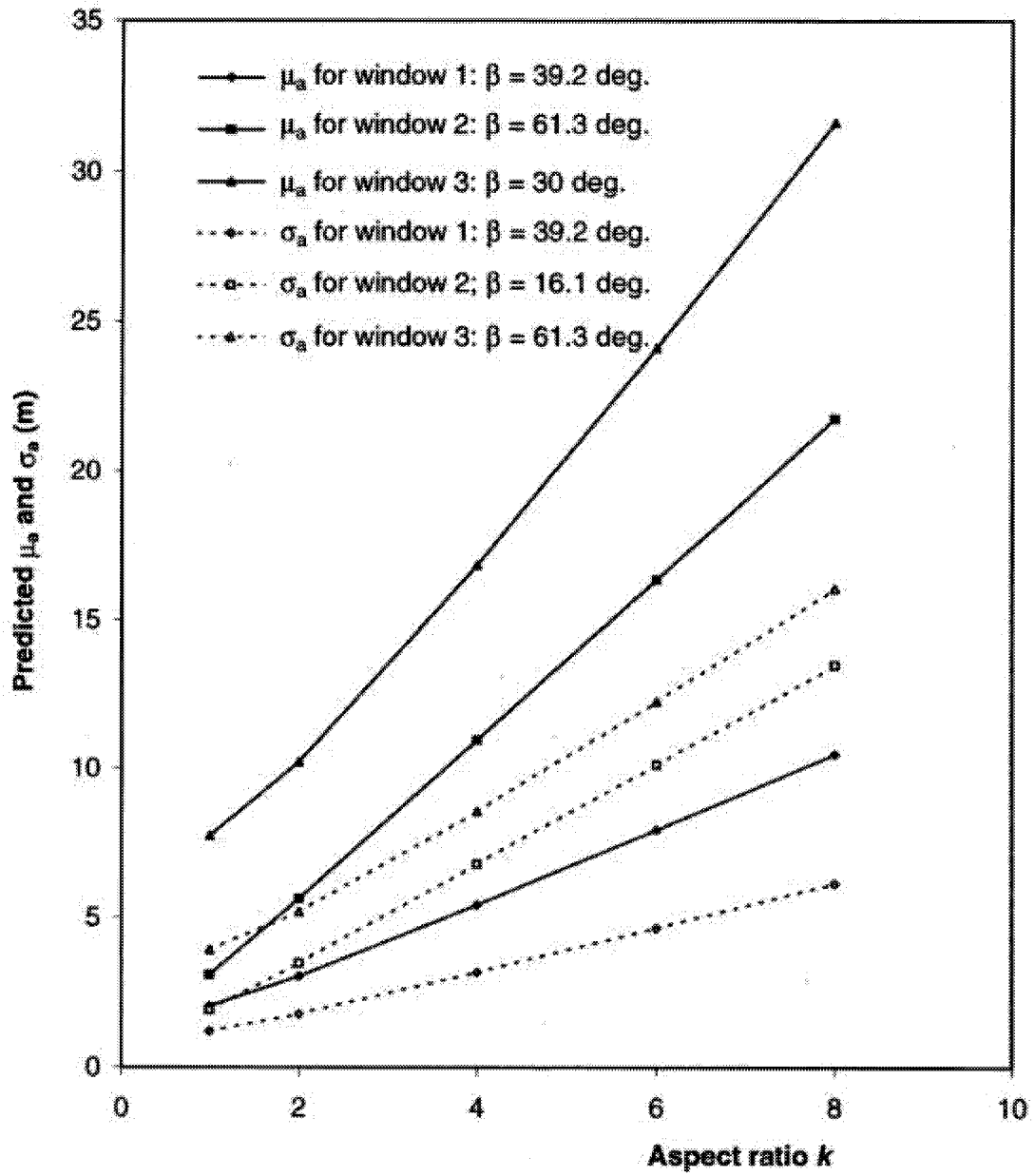

Figure 3-32 Variation of μ_a and σ_a with aspect ration k for assumed major axis orientation 3 (60°/0°): assuming a Gamma distribution form of a

Table 3-9 Assumed major axis orientations and their corresponding β values

Assumed major axis orientation (1)	β (°)		
	Window 1	Window 2	Window 3
0°/0°	63.4	33.7	0
30°/0°	90	16.1	30
60°/0°	39.2	61.3	30

Table 3-10 Predicted values of k, μ_a and σ_a at major axis orientation (30°/0°)

Assumed distribution form of $g(a)$ (1)	k (2)	μ_a (m) (3)	σ_a (m) (4)	Marks (5)
Lognormal	4.08	8.06	3.99	See Figure 3-24, Figure 3-27, and Figure 3-30[a)]
Negative exponential	3.85	4.86	4.86	See Figure 3-25, , Figure 3-28 and Figure 3-31
Gamma	4.22	7.73	4.42	See Figure 3-26, Figure 3-29, and Figure 3-32[a)]

a) The intersection point of μ_a curves is chosen to estimate k, μ_a and σ_a.

Since we have the results for three distribution forms of $g(a)$, what we need to do next is to find the best distribution form by checking the equality of equation (36) corresponding to each assumed distribution form of $g(a)$. For a lognormal distribution of $f(l)$, we have

$$\frac{16E(l^3)}{3\pi M^3} = \frac{16[(\mu_l)^2 + (\sigma_l)^2]^3}{3\pi M^3 (\mu_l)^3} \qquad \text{Equation 41}$$

Hence, using the data in Table 3-8 and Eq. (41), the values of $16E(l^3)/3\pi M^3$, for each sampling window, can be determined. The results are shown in Table 3-11 to Table 3-13 (column 2). The

left side of equation (36) can be obtained from Eq. (37), (38) or (39) and the corresponding data in Table 3-10. The results are also shown in Table 3-11 to Table 3-13 (column 6). Comparing the equality of both sides of Eq. (36) for each sampling window, we find that $g(a)$ can be best represented by the lognormal distribution, which is the actual distribution form of g(a).

In summary, the predicted major axis orientation, aspect ratio, and size distribution are:

- Major axis orientation = (30°/0°);
- $k = 4.08$; $g(a)$ = lognormal with $\mu_a = 8.06$ m and $\sigma_a = 3.99$ m
- which compare very well with the actual major axis orientation, aspect ratio and size distribution used in the simulations
- Major axis orientation = (30°/0°);
- $k = 4.0$; $g(a)$ = lognormal with $\mu_a = 8.0$ m and $\sigma_a = 4.0$ m

Table 3-11 Checking the distribution of $g(a)$ for sampling window 1 ($\beta = 63.4°$)

k (1)	M (1)	$\frac{16E(l^3)}{3\pi M^3}$ (2)	Assumed distribution form of $g(a)$ (3)	μ_a (4)	σ_a (5)	$\frac{E(a^4)}{E(a)}$ (6)	Recommended distribution form of $g(a)$? (7)
1	1.0	42.72	Lognormal	2.19	1.11	41.16	Yes
			Exponential	1.37	1.37	62.38	No
			Gamma	2.05	1.20	39.51	No
2	0.542	267.6	Lognormal	4.04	2.04	257.9	Yes
			Exponential	2.53	2.53	390.8	No
			Gamma	3.77	2.21	247.6	No
4	0.277	2001	Lognormal	7.89	3.99	1928	Yes
			Exponential	4.95	4.95	2921	No
			Gamma	7.38	4.33	1851	No
6	0.186	6666	Lognormal	11.79	5.96	6423	Yes
			Exponential	7.40	7.40	9733	No
			Gamma	11.02	6.46	6166	No
8	0.139	15729	Lognormal	15.70	7.93	15155	Yes
			Exponential	9.85	9.85	22967	No
			Gamma	14.67	8.60	14549	No

Note: The recommended distribution form of $g(a)$ corresponds to the case that columns (2) and (6) are the closest to each other.

Table 3-12 Checking the distribution of $g(a)$ for sampling window 2 (β = 33.7°)

k (1)	M (1)	$\frac{16E(l^3)}{3\pi M^3}$ (2)	Assumed distribution form of $g(a)$ (3)	μ_a (4)	σ_a (5)	$\frac{E(a^4)}{E(a)}$ (6)	Recommended distribution form of $g(a)$? (7)
1	1.0	169.1	Lognormal	3.35	1.76	162.9	Yes
			Exponential	2.14	2.14	234.8	No
			Gamma	3.09	1.91	155.5	No
2	0.721	451.0	Lognormal	4.65	2.44	434.6	Yes
			Exponential	2.97	2.97	626.4	No
			Gamma	4.29	2.66	414.8	No
4	0.422	2251	Lognormal	7.94	4.18	2169	Yes
			Exponential	5.07	5.07	3126	No
			Gamma	7.33	4.54	2070	No
6	0.291	6831	Lognormal	11.50	6.05	6582	Yes
			Exponential	7.34	7.34	9487	No
			Gamma	10.61	6.57	6282	No
8	0.221	15572	Lognormal	15.13	7.96	15004	Yes
			Exponential	9.66	9.66	21626	No
			Gamma	13.97	8.65	14322	No

Note: The recommended distribution form of $g(a)$ corresponds to the case that columns (2) and (6) are the closest to each other.

Table 3-13 Checking the distribution of $g(a)$ for sampling window 3 ($\beta = 0°$)

k (1)	M (1)	$\frac{16E(l^3)}{3\pi M^3}$ (2)	Assumed distribution form of $g(a)$ (3)	μ_a (4)	σ_a (5)	$\frac{E(a^4)}{E(a)}$ (6)	Recommended distribution form of $g(a)$? (7)
1	1.0	1663	Lognormal	8.06	3.65	1602	Yes
			Exponential	4.86	4.86	2749	No
			Gamma	7.73	3.92	1558	No
2	1.0	1663	Lognormal	8.06	3.65	1602	Yes
			Exponential	4.86	4.86	2749	No
			Gamma	7.73	3.92	1558	No
4	1.0	1663	Lognormal	8.06	3.65	1602	Yes
			Exponential	4.86	4.86	2749	No
			Gamma	7.73	3.92	1558	No
6	1.0	1663	Lognormal	8.06	3.65	1602	Yes
			Exponential	4.86	4.86	2749	No
			Gamma	7.73	3.92	1558	No
8	1.0	1663	Lognormal	8.06	3.65	1602	Yes
			Exponential	4.86	4.86	2749	No
			Gamma	7.73	3.92	1558	No

Note: The recommended distribution form of $g(a)$ corresponds to the case that columns (2) and (6) are the closest to each other.

3.2.1.10 Summary

The procedure to infer the major axis orientation, aspect ratio k and size distribution $g(a)$ (probability density function of the major axis) of elliptical discontinuities from trace length sampling on different sampling windows can be summarized as follows:

1. Sampling
   (a) Trace length: Use two or more sampling windows at different orientations to conduct trace (length) sampling. The sampling windows (planes) should be oriented such that significantly different mean trace lengths can be obtained from different windows (see Section 3.2.1.7).
   (b) Orientation: Use exposed rock surface or wellbore sampling so that the normal orientation of each discontinuity set can be obtained.

2. Conduct trace length analysis to estimate the true trace length distribution $f(l)$ on different sampling windows: μ_l, σ_l and form of $f(l)$ (see Section 3.2.1.7).

3. Infer the major axis orientation, aspect ratio k and size distribution $g(a)$ of discontinuities from trace length sampling on different sampling windows:
   (a) Assume a major axis orientation and compute the β value for each sampling window.

(b) For the assumed major axis orientation, compute μ_a and σ_a from μ_l and σ_l of each sampling window, by assuming aspect ratios k = 1, 2, 4, 6, 8 and lognormal, negative exponential and Gamma distribution forms of $g(a)$. The results are then used to draw the curves relating μ_a (and σ_a) with k, respectively, for the lognormal, negative exponential and Gamma distribution forms of $g(a)$ (see, e.g., Figure 3-24, Figure 3-25, and Figure 3-26).

(c) Repeat steps (a) and (b) until the curves relating μ_a (and σ_a) with k for different sampling windows intersect in one point (see, e.g., Figure 3-27, Figure 3-28, Figure 3-29). The major axis orientation for this case is the inferred actual major axis orientation. The k, μ_a and σ_a values at the intersection points are the corresponding possible characteristics of the discontinuities.

(d) Find the best distribution form of $g(a)$ by checking the equality of equation (36) (see Section 3.2.1.5). The k, μ_a and σ_a values found in Step (c) and corresponding to the best distribution form of $g(a)$ are the inferred characteristics of the discontinuities.

A general stereological relationship between trace length distributions and elliptical discontinuity size (expressed by the major axis length a of the ellipse) distributions for area sampling of discontinuities has thus been derived. Based on the general stereological relationship, an approach was developed for using the estimated true trace length distributions corresponding to different sampling windows to infer the major axis orientation, aspect ratio and size distribution of discontinuities. The validity of the developed method was checked by applying it to analyze data produced with simulations. In the simulations, discontinuities were generated and then sampling processes were simulated by using the FracMan code. The results show that the developed approach for inferring the major axis orientation, aspect ratio and size distribution of discontinuities can produce satisfactory results.

The effect of sampling plane orientation on trace lengths was investigated by using the derived stereological relationship between the trace length distribution and the discontinuity size distribution. The results show that the sampling plane orientation has an important effect on both the mean and standard deviation of trace lengths. If different sampling planes are used to collect trace (length) data, the sampling planes should be such oriented that significantly different mean trace lengths can be obtained from different planes.

3.2.2 Task 1.1.2 Fracture Shape Analysis

Research results have shown that the planar shape of discontinuities (or fractures) has a profound effect on the connectivity of discontinuities and on fluid flows (Petit et al. 1994; Dershowitz 1998). Consequently, it is important to know the planar shape of discontinuities when characterizing discontinuities in a rock mass. Since a rock mass is usually inaccessible in three dimensions, the real discontinuity shape is rarely known. Information on discontinuity shape is limited and often open to more than one interpretation (Warburton 1980a; Wathugala 1991).

Discontinuities can be classified into two categories: unrestricted and restricted. Unrestricted discontinuities are blind and effectively isolated discontinuities whose growth has not been perturbed by adjacent geological structures such as faults and free surfaces [see Figure 3-33(a)]. In general, the edge of unrestricted discontinuities is a closed convex curve. In many cases, the growth of discontinuities is limited by adjacent preexisting discontinuities and free surfaces [see Figure 3-33(b)]. Such discontinuities are called restricted discontinuities. One way to represent

restricted discontinuities is to use polygons, some of the polygon sides being those formed by intersections with the adjacent preexisting discontinuities and free surfaces.

In this discussion, only *unrestricted* discontinuities will be considered. First, a brief literature review about the shape of (unrestricted) discontinuities is presented, including the reported in situ data and the shapes assumed by different researchers. This followed by the analysis of the available data, which leads to the conclusion that the possible shape of discontinuities is more likely to be elliptical than circular.

3.2.2.1 Literature Review

In the past thirty years, a number of articles and reports have appeared discussing possible shapes of discontinuities.

3.2.2.1.1 In Situ Data about the Discontinuity Shape

Robertson (1970), after analyzing nearly 9,000 traces from the De Beer mine, South Africa, concluded that the strike trace length and the dip trace length of discontinuities have about the same distribution, possibly implying discontinuities to be equidimensional (circular). Figure 3-34 shows the strike and dip traces of a discontinuity.

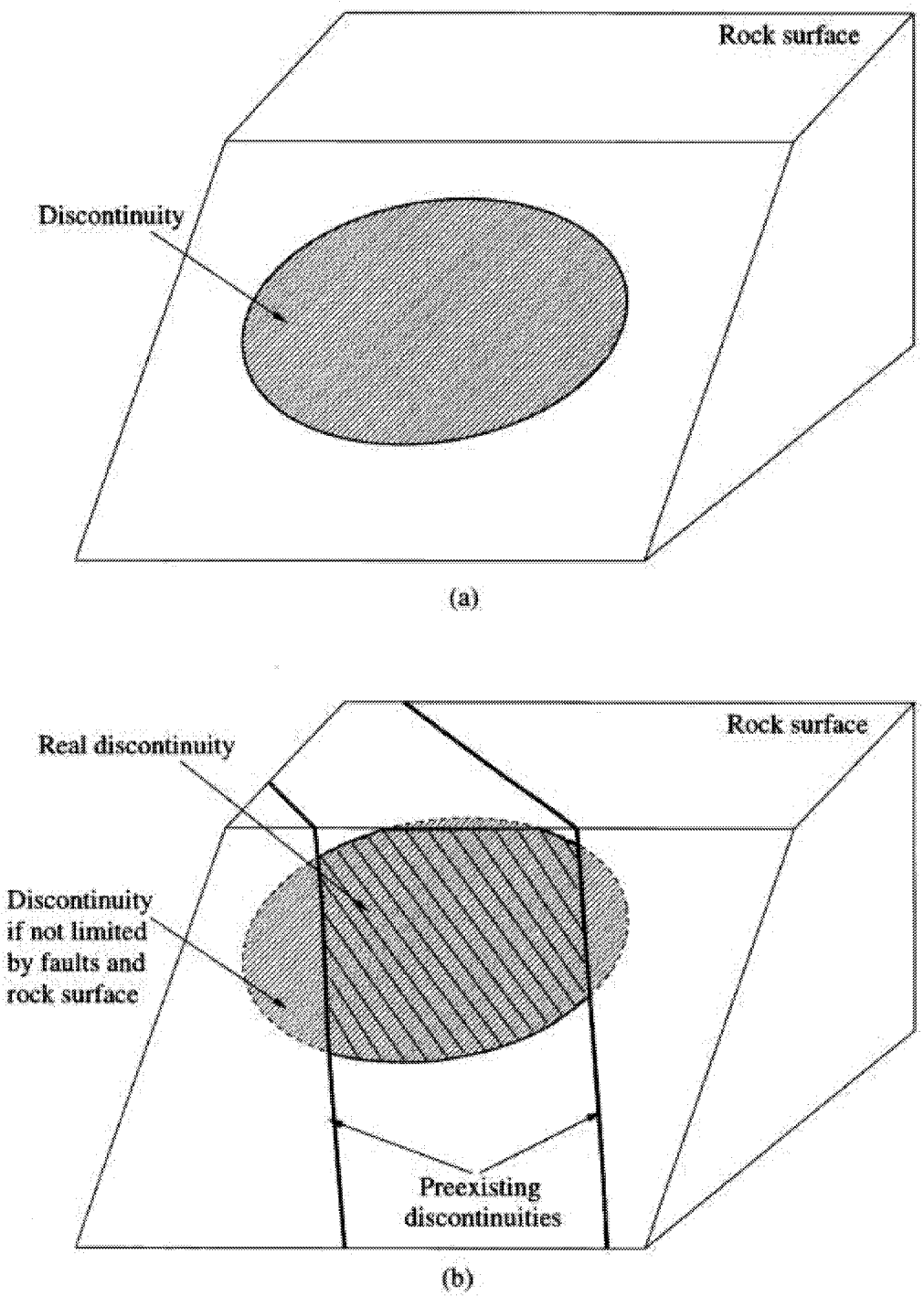

Figure 3-33 (a) An unrestricted discontinuity; and (b) A restricted discontinuity

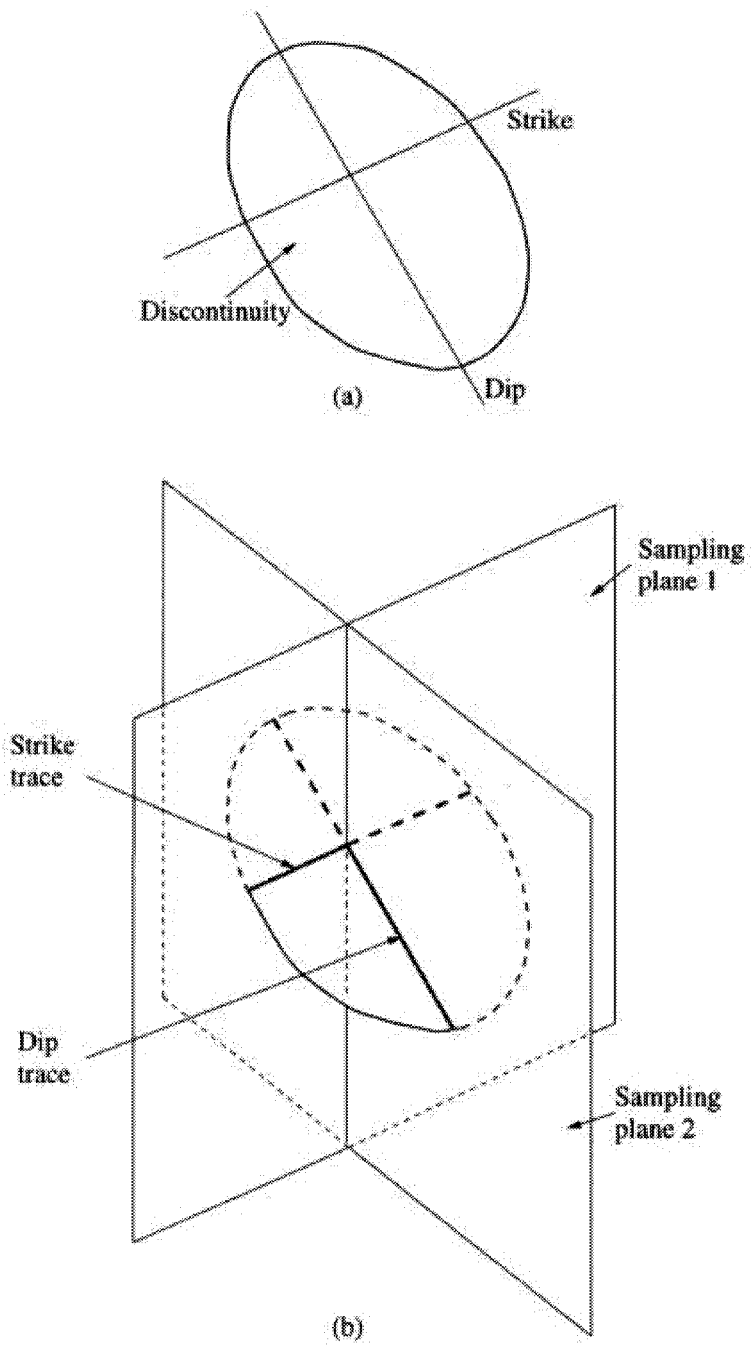

Figure 3-34 (a) Strike and dip of a discontinuity; and (b) Strike and dip traces

Bridges (1975) stated that "there is good evidence for" individual discontinuities to be taken to have a rectangular (elongated?) shape. However, no specific data can be found in the original paper to support this statement.

Barton (1977) presented a geotechnical analysis of rock structure and fabric at the C.S.A. Mine, Cobar, New South Wales. The country rock within the mine area is overwhelmingly composed of chloritic and quartzitic siltstone to slatey claystone. Based on observations of trace lengths along the strikes and dips of different rock exposures, Barton (1977) made an assumption of circular discontinuity shape.

Einstein et al. (1979) investigated discontinuities at a site in southern Connecticut. The country rock at this site is the Monson Gneiss, a thinly banded rock with feldspathic and biotitic layers. There are two major discontinuity sets at this site. Set 1 dips steeply to the southeast and Set 2 is nearly horizontal. Trace lengths of discontinuities were measured on both the horizontal and vertical surfaces of excavations. The results indicate that discontinuities are non-equidimensional (see Table 3-14).

Table 3-14 Mean of strike trace lengths and mean of dip trace lengths of two discontinuity sets (from Einstein et al. 1979)

Discontinuity Set #	Mean of strike trace lengths (ft.)	Mean of dip trace lengths (ft.)
1	28.3	16.1
2	25.2	21.1

According to Mostyn and Li (1993), McMahon (1982) used a dip length equal to 60% of the strike length for discontinuities in slope design. Since the original paper of McMahon (1982) is not published, it is not clear if McMahon based his assumption on in situ data.

Petit et al. (1994) presented results of a field study to determine the shape of discontinuities in sedimentary rocks. Pelites with isolated sandstone layers in the red Permian sandstones of the Lodeve Basin were studied. The exposed discontinuities (i.e., one of the discontinuity walls had been removed by erosion) appear as rough ellipses with a shape ratio L/H of about 2.0, where L and H are respectively the largest horizontal and vertical dimensions. For non-exposed discontinuities, the distributions of the dimensions of the horizontal and vertical traces were measured. The ratio of the mean L to the mean H of such traces is 1.9, which is very close to the L/H ratio of the observed individual discontinuity planes. This suggests that most of the discontinuities are elliptical with a shape ratio of about 2.0, independent of the discontinuity size.

Nicol et al. (1996) presented data about the shape of simple normal faults (see Figure 3-35 and Table 3-15). The results show that normal faults have an approximately elliptical shape with the major axis sub-horizontal. Aspect ratios of fault surfaces range from 1.0 to 3.4 with a mean of 2.15.

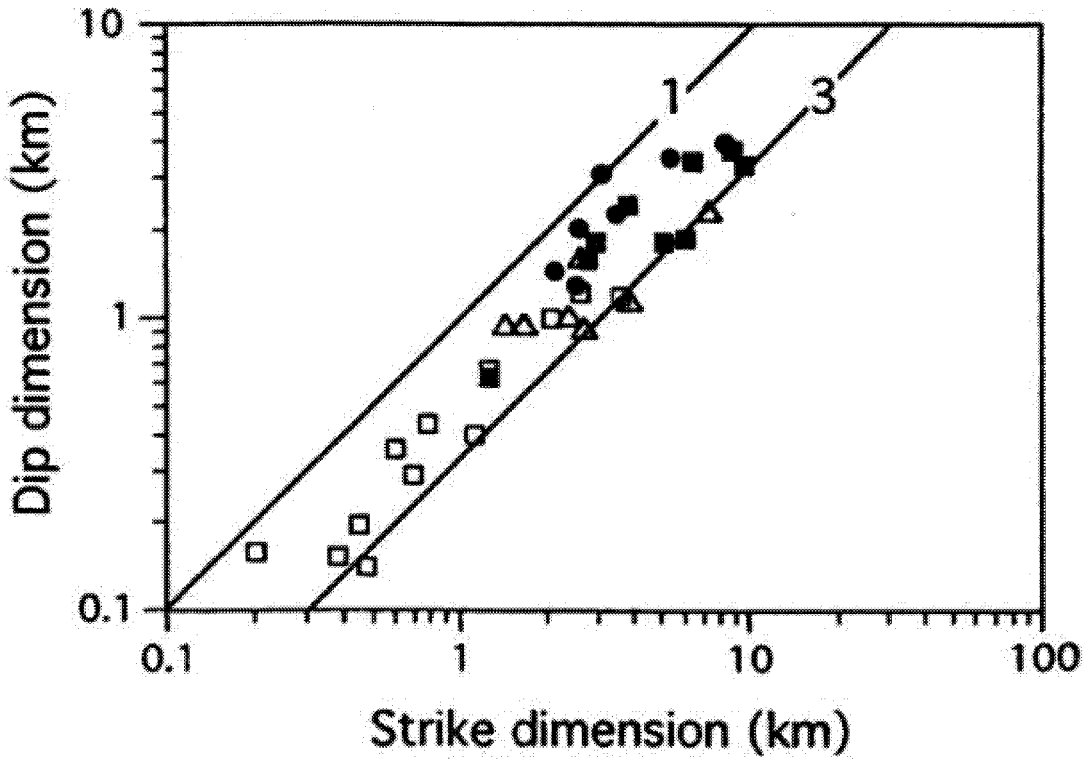

Figure 3-35 Dip dimension vs. strike dimension for nominally unrestricted faults from four regions (see Table 3-15) (from Nicol et al. 1996)

Table 3-15 Details of the four data sets plotted in Figure 3-35 (from Nicol et al. 1996)

Name and location	Lithologies	Number of faults	Aspect ratio (average)
Derbyshire Coal Mines, UK	Carboniferous sandstone, shale and coal	12	2.3
Timor Sea	Cenozoic limestone, claystone and sandstone	9	2.2
Gulf Coast	Late Miocene to recent sandstone with minor shales	7	1.6
North Sea	Jurassic sandstone and shales	7	2.4

Note: Data from the Derbyshire Coal field are from coal-seam plans, the remainder are from two- and three-dimensional offshore reflection seismic data sets.

3.2.2.1.2 Assumptions about the Discontinuity Shape by Different Researchers

Due to the mathematical convenience, many investigators assume that discontinuities are thin circular discs randomly located in space (Baecher et al. 1977; Warburton 1980a; Chan 1986; Villaescusa and Brown 1990; Kulatilake 1993). With circular discontinuities, the trace patterns in differently oriented sampling planes will be the same. In practice, however, the trace patterns may vary with the orientation of sampling planes (Warburton 1980b). Therefore, Warburton (1980b) assumed that discontinuities in a set are parallelograms of various sizes. Dershowitz et al. (1993) used polygons to represent discontinuities in the FracMan discrete fracture code. The polygons are formed by inscribing a polygon in an ellipse (see Figure 3-36). Ivanova (1995, 1998) and Meyer (1999) also used polygons to represent discontinuities in their discrete fracture code GeoFrac. It is noted that polygons can be used to effectively represent elliptical discontinuities when the number of polygon sides is large (say > 10) (Dershowitz et al. 1993).

3.2.2.2 Analysis of Existing Information on Discontinuity Shape

As seen from above, most of the researchers infer the discontinuity shape from the study of trace lengths in both the strike and dip directions (see Figure 3-34). The conclusion that discontinuities are equidimensional (circular) is drawn *only* from the fact that the average strike length of a discontinuity set is approximately equal to its average dip length. However, the average strike length of a discontinuity set being the same as its average dip length does not necessarily mean that the discontinuities of such a set are equidimensional; instead, there exist the following three possibilities:

a) The discontinuities are indeed equidimensional [see Figure 3-37(a)].

b) The discontinuities are non-equidimensional such as elliptical or rectangular with long axes in a single (or deterministic) orientation. However, the discontinuities are oriented such that the average strike length is approximately equal to the average dip length [see Figure 3-37(b)].

c) The discontinuities are non-equidimensional such as elliptical or rectangular with long axes randomly oriented. The random discontinuity orientation distribution makes the average strike length approximately equal to the average dip length [see Figure 3-37(c)].

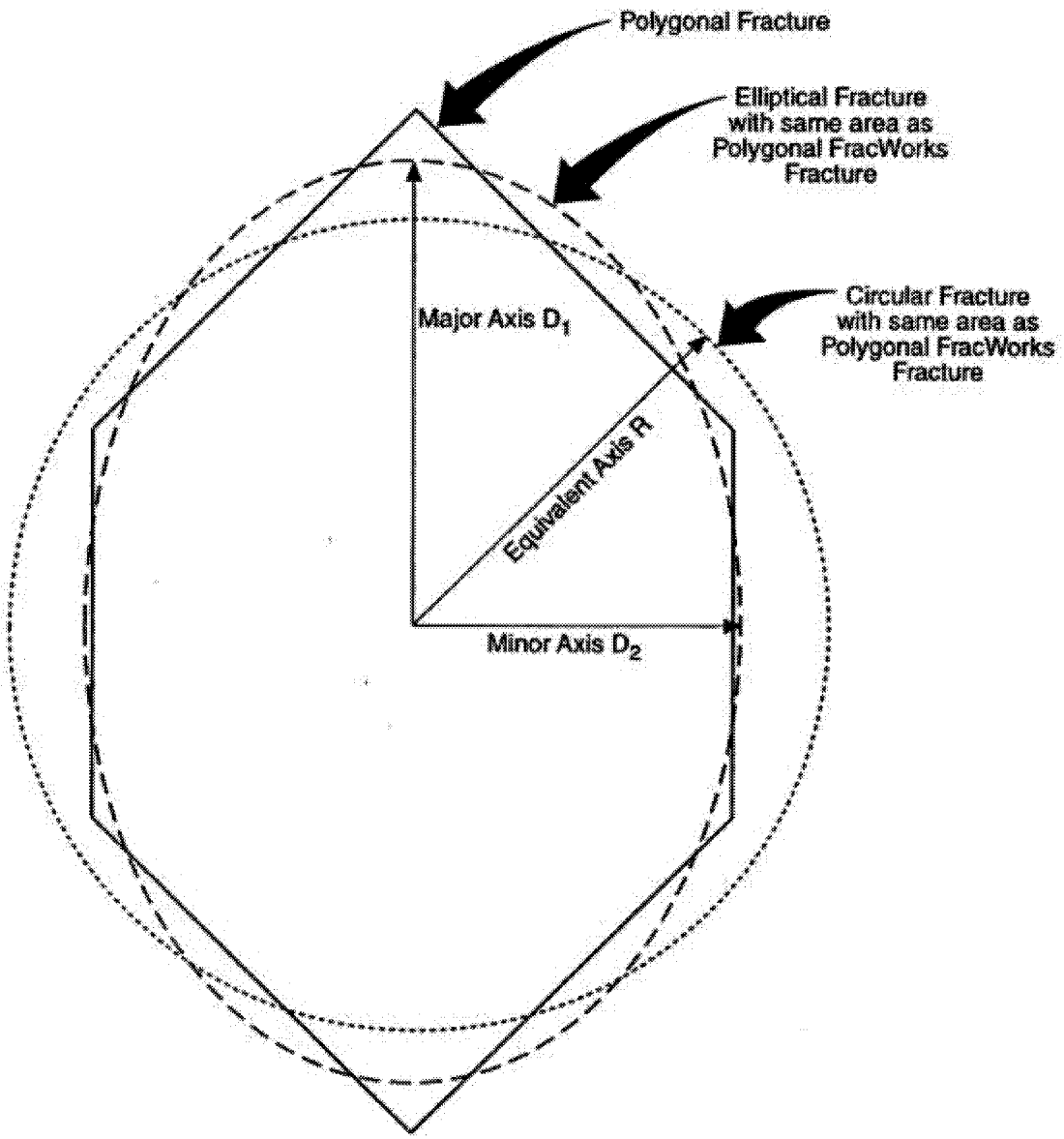

- Area of fracture is specified by equivalent radius R of circular fracture.
- Aspect Ratio a is defined as the ratio of major to minor axes for the elliptical fracture, $a=D_1/D_2$.
- Polygonal Fracture has same area and shape as elliptical fracture, with user specified number of sides. For a small number of sides, the aspect ratio for the polygon may be slightly smaller than for the equivalent elliptical fracture.

Figure 3-36 A polygon is used to represent an elliptical discontinuity (fracture) (from Dershowitz et al. 1993)

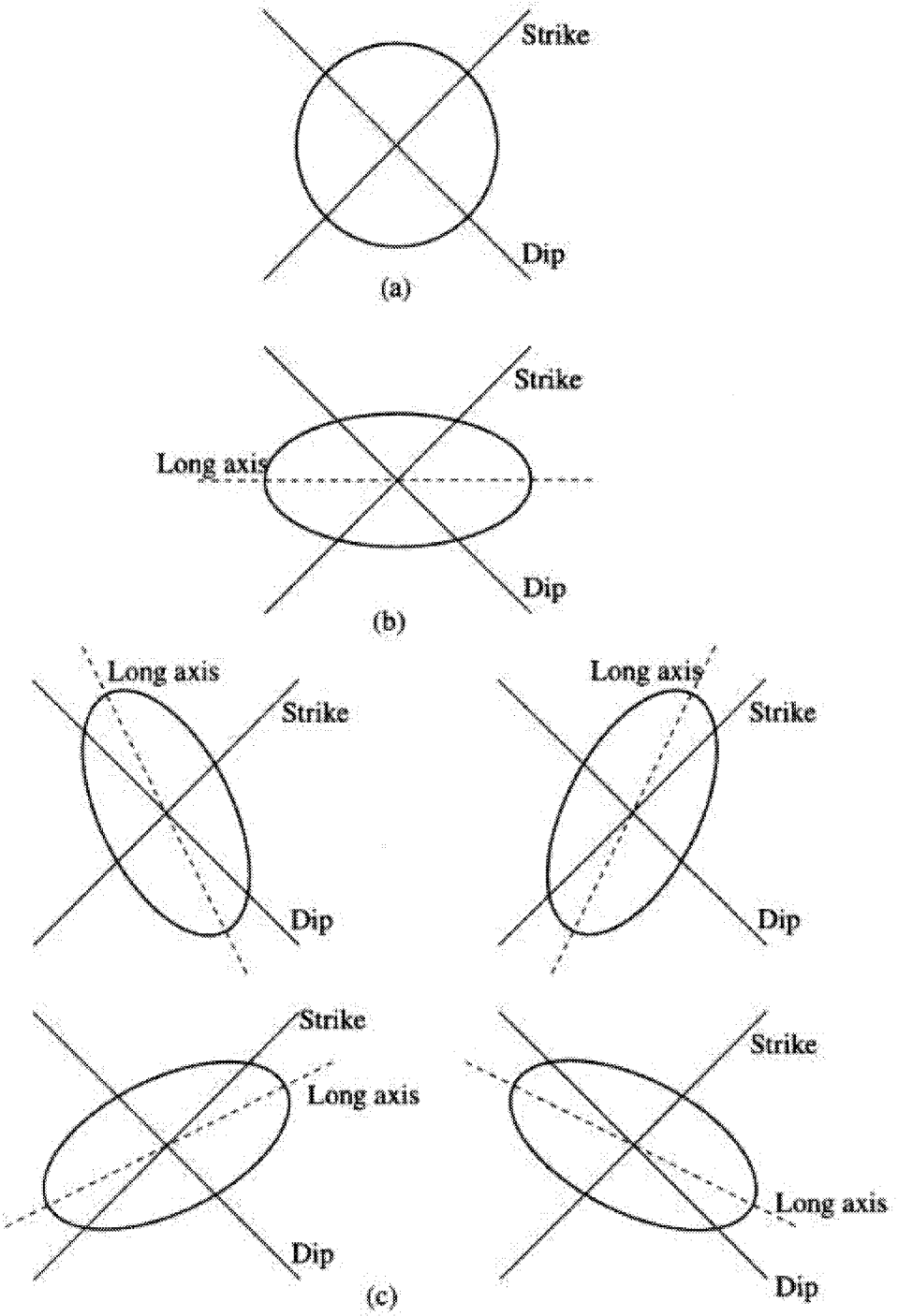

Figure 3-37 Three possible cases at which the average strike length is about equal to the average dip length: (a) Discontinuities are equidimensional (circular); (b) discontinuities are non-equidimensional (elliptical) with long axes in a single orientation. The discontinuities are oriented so that the average strike length is about equal the average dip length; and (c) Discontinuities are non-equidimensional with long axes such randomly oriented that the average strike length is about equal to the average dip length.

Therefore, the conclusion that discontinuities are equidimensional (circular) drawn from the fact that the average strike length of a discontinuity set is about equal to its average dip length is questionable. Investigators assume circular discontinuity shape possibly because of mathematical convenience.

On the other hand, if the average strike length differs greatly from the average dip length, the discontinuities are non-equidimensional. Since the reported exposed discontinuities (i.e., one of the discontinuity walls had been removed by erosion) appear as rough ellipses, it is appropriate to assume that discontinuities are elliptical.

Elliptical discontinuities can be effectively represented by polygons with a large number of sides. This may be one of the reasons why polygons are used to represent discontinuities in discrete fracture codes. Convenience of numerical analysis and ability to represent irregular discontinuities such as restricted discontinuities might be the other two reasons for using polygons to represent discontinuities in discrete fracture codes.

3.2.2.3 Summary and Conclusions

A brief literature review about the shape of *unrestricted* discontinuities was conducted, which included reported in situ data and the shapes assumed by different researchers. Analyzing this information one can state:

- The conclusion that discontinuities are equidimensional (circular) drawn from the fact that the average strike length of a discontinuity set is approximately equal to its average dip length is questionable. Investigators assume circular discontinuity shape possibly because of mathematical convenience.
- The possible shape of unrestricted discontinuities is more likely to be elliptical than circular.

3.2.3 Task 1.1.3 Application of Neural Nets to the Identification of Fracture Sets

3.2.3.1 Background

The key first step in the analysis of data from heterogeneous systems is to identify natural groups of data. Without first grouping the data for separate analysis, the variability in data values inherent in heterogeneous reservoirs unnecessarily reduces the spatial and statistical resolution of the data.

Any heterogeneous reservoir feature, such as fractures, laminations or shale lenses, has parameters that define it. More often than not, there may have been several depositional or tectonic events that have produced these features. Each event may produce features with different characteristics. This is often evident in fracture patterns where multiple fracture sets are developed, each with there own defining characteristics. Sometimes the differences are obvious, for example, when there are two sets formed at right angles to one another. Other times the differences are more subtle, for example, when orientations are highly overlapping, but other features like planarity, mineral infillings, surface roughness and size may be the parameters that distinguish one set from another. In this situation, it may be difficult for the geologist to easily evaluate the natural groupings in the data.

The identification of groupings or sets within heterogeneous data is often addressed by using a form of statistical cluster analysis. There are several different types of clusters:

- Disjoint clusters in which the populations of each cluster do not overlap at all;
- Overlapping clusters, in which feature properties overlap to a greater or lesser extent such that there is some ambiguity as to which cluster each feature belongs to; and
- Hierarchical clusters, in which members of one cluster simultaneously, include features of another cluster.

All three of these types of clusters can be expressed as "Fuzzy clusters" defined by a probability of membership in each cluster. This probabilistic concept of cluster membership was the foundation for the development of the NeurISIS 1.0 fracture set orientation algorithm (Dershowitz et al., 1996). The NeurISIS 1.0 algorithm used a "probabilistic neural network" to assign features to clusters based on their relative probability of membership, and then iteratively defined the clusters based on the statistics of their members. The weakness of the NeurISIS 1.0 algorithm is that it does not determine the initial fracture set definitions, relying on the user to provide the initial set definitions.

Other common clustering algorithms include: single-linkage methods (neighbor and dendritic), Ward's minimum variance, and Gower's medium method. These clustering methods were evaluated but failed to provide appropriate capabilities for fractured reservoir data. The appropriate clustering algorithm depends on a number of factors, including

- type of data,
- shape of the clusters,
- underlying probability distribution of the data,
- degree of heterogeneity, and
- degree of overlap.

Regarding data type, fracture data from heterogeneous reservoirs is generally a combination of four types of data:

- ordinal parameters, such as joint roughness classes,
- class parameters, such as type of fracture or mineralization,
- continuous parameters such as aperture and permeability, and
- vector parameters, such as orientation.

Very few common clustering methods can effectively use ordinal and class data; they are typically designed for using continuous variables only. Many of the common clustering methods make assumptions such as approximately equal covariance matrices and multinormality. Unfortunately, data typically associated with features in heterogeneous reservoirs is unlikely to satisfy these constraints. Probability distributions are frequently not normal, and covariance matrices are rarely approximately equal. It is not even clear what a covariance matrix of mineral fillings would be.

Thus, the clustering algorithm for heterogeneous reservoir fracture data must satisfy a number of requirements:

- ability to handle all four parameter types,
- freedom from restrictions of normality, and
- ability to function with varying covariance matrices.

One approach which satisfies these requirements is the family of neural networks termed "self-organizing" or "Kohonen" networks (Kohonen, 1988). During this project we developed the Kohonen networks for application to clustering of fracture data.

3.2.3.2 Kohonen Neural Network Algorithm

The topology of Kohonen networks consists of two layers, an input layer and an output layer. Each node in the input layer is connected to each node in the output layer by a connection with an associated weight.

A *slab* is a group of nodes with similar attributes. These attributes include parameters like the activation function, learning coefficient and momentum factor, as discussed later. All nodes in a slab receive their input from the same sources, be they other slabs or the initial input values, and they transmit their information to a common output destination. Figure 3-38 illustrates the basic Kohonen network topology.

The first step in application of the Kohonen network is to initialize the network by assigning values to the weights. These are typically random values selected in one of several ways depending upon the network analyst's preference, since there still remains much discussion as to the best way to assign these weights.

The next step is to train the network. This is done by using quantitative clustering criteria to measure how well the network is working in defining clusters. These "distance metrics" depend on the data being considered. Distance metrics for fracture data include Euclidean and Normalized. Both were evaluated, and as expected, Euclidean distance metrics outperformed normalized metrics.

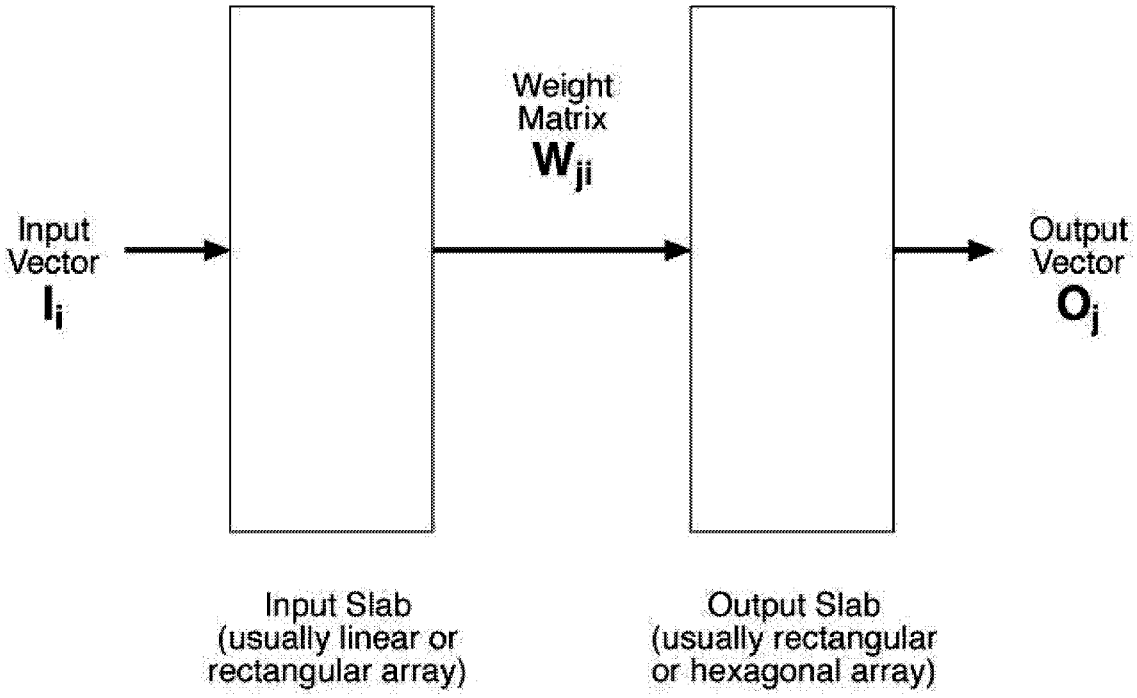

Figure 3-38 Self-Organizing (Kohonen) Network Model

Once the network distance metrics have been defined, the weights assigned to the Kohonen network are iterated until stable groups appear. This iteration proceeds as follows:

1. An input pattern is presented to the network, which can consist of geological attributes of each fracture and its orientation represented by the direction cosines of its normal vector.
2. Input patters are assigned to output nodes to which it is found to be closest in terms of the selected distance metric.
3. Once this winning output node has been selected, the nodes within a neighborhood of the winning node are adjusted to have similar properties.
4. This process is repeated, continuously reducing the learning rate and the neighborhood site until the calculated clusters or sets have stabilized.

The neighborhood starts off relatively large (although less than the number of output nodes). As training progresses, the properties of the output nodes tend to stabilize, and the neighborhood decreases along with the learning rate. Eventually, the neighborhood goes to 0, and only the winning node has its weight changed. At this point, the learning rate is also much smaller, and the clusters are as well defined, as they are likely to be.

3.2.3.3 Implementation for Heterogeneous Reservoir Data

The application of Kohonen networks to heterogeneous reservoir data requires conversion of fracture data to formats, which can be used to provide input to the networks. This is achieved by converting ordinal data to ranks and class data to presence/absence. For example, roughness

might have three classes: (1) smooth, (2) rough, or (3) very rough. A roughness-input variable would be assigned to the number 1, 2, or 3 depending on which class it belonged to. For class variables, such as mineral filling - calcite, the fracture would be assigned the value 0 or 1 to reflect absence or presence. As a final stage, all input data are normalized over their actual or theoretical range of values.

An example Kohonen network application is illustrated in Table 3-16. This test case consists of four types of properties: Vector data (orientation), ordinal data (planarity, opening), continuous data (size), and class data (filling).

Table 3-16 Example Dataset for Kohonen Network Demonstration

Set #	Orientation	Planarity	Filling	Size	Open/ Closed
1	Horizontal, Fisher Dispersion $\kappa = 10.0$	Smooth	Calcite	Normal, mean = 15, stdev = 2	Open
2	Mean Pole Trend, Plunge = (0,0) Fisher Dispersion $\kappa = 10.0$	Moderately Rough	Calcite	Normal, mean = 7, stdev = 2	Closed
3	Mean Pole Trend, Plunge = (0,45) Fisher Dispersion $\kappa = 10.0$	Rough	None	Normal, mean = 10, stdev = 3	Open

The example dataset was generated from the stochastic properties given in Table 3-16, using FracMan/FracWorks discrete feature network model (Dershowitz et al., 1998). The sets were defined with overlapping parameter distributions of, for example, orientation, size filling and openness. Figure 3-39 is a stereoplot of the three sets, showing the overlap in orientation distributions.

Three parameters must be specified to apply the Kohonen network for heterogeneous reservoir data. For the example network, the following parameters were specified as summarized in Table 3-17.

Table 3-17 Kohonen Network for Example Data Set

Parameter	Assumption	Basis
Number of Sets (Clusters)	3	Visual inspection of data
Initial Weighting of Neurons	Uniform Distribution U[0,1]	Lack of conditioning
Neighborhood Scale	2	
Learning Rate	0.6	
Distance Metric	orientation (vector data): euclidean distance on stereonet planarity (ordinal data) infilling (class data) size (continuous data) opening (ordinal data)	

All 600 fractures were correctly clustered by the net. The classification results maybe expressed as neuron values; the smallest value indicates the closest match to a cluster. For example, fracture #1 had values of 0.054, 1.888 and 3.303 for clusters #1, #2 and #3. The smallest value was for cluster #1, so that is the cluster or set to which it is assigned.

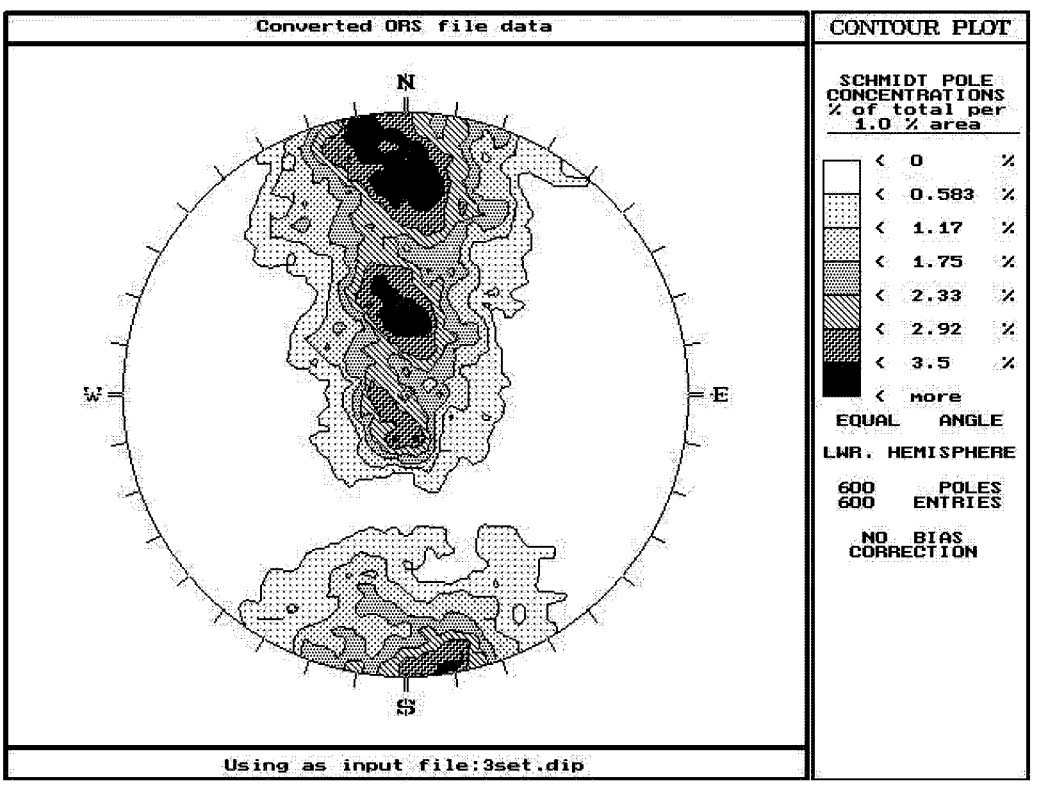

Figure 3-39 Contour Plot of Test Data with Three Fracture Sets

Figure 3-40 shows these neuron probability values for all 600 fractures in the example case. The separation between the three sets of points for the fractures 1-200 and 401-600 show that the net had little problem in distinguishing Set #1 from the other sets, or Set #3 from the other sets; the neuron values for each set are very different from each other. Set #2 is slightly different; while the net had no problem correctly clustering it, the neuron values for the two other sets are similar to each other. This suggests that the characteristics of Set #2 are intermediate between Set #1 and Set #3 (which is also seen by the intermediate position of neuron values for Set #2 for fractures 1-200 and 401-600). Set #1 is more unlike Set #3 than it is unlike Set #2.

3.2.3.4 Algorithm Demonstration, Yates Field Tract 17

The Kohonen neural network was applied using data from Tract 17 in the Yates Field, west Texas, one of the four project study site window areas. This data provides a rigorous test of a self-organizing network's ability to distinguish orientational sets in a complex data set. Figure 3-41 shows the stereoplot of joint orientations from three wells, YU1711, YU1755 and YU2511. An expert structural geologist (T. Cladouhos) was given the stereoplot and asked to identify sets based upon orientation. The geologist's picks are shown in Figure 3-42.

There were five sets identified by the geologist, labeled G1 through G5 on Figure 3-42.

A Kohonen network was applied to the orientation data. The parameters assumed for the Kohonen network are summarized in Table 3-18.

Table 3-18 Kohonen Network for Yates Tract 17 Data Set

Parameter	Assumption	Basis
Number of Sets (Clusters)	5	Structural geologist
Initial Weighting of Neurons	Uniform Distribution U[0,1]	Lack of conditioning
Neighborhood Scale	4	
Learning Rate	0.6	
Distance Metric	orientation (vector data): euclidean distance on stereonet planarity (ordinal data) infilling (class data) size (continuous data) opening (ordinal data)	

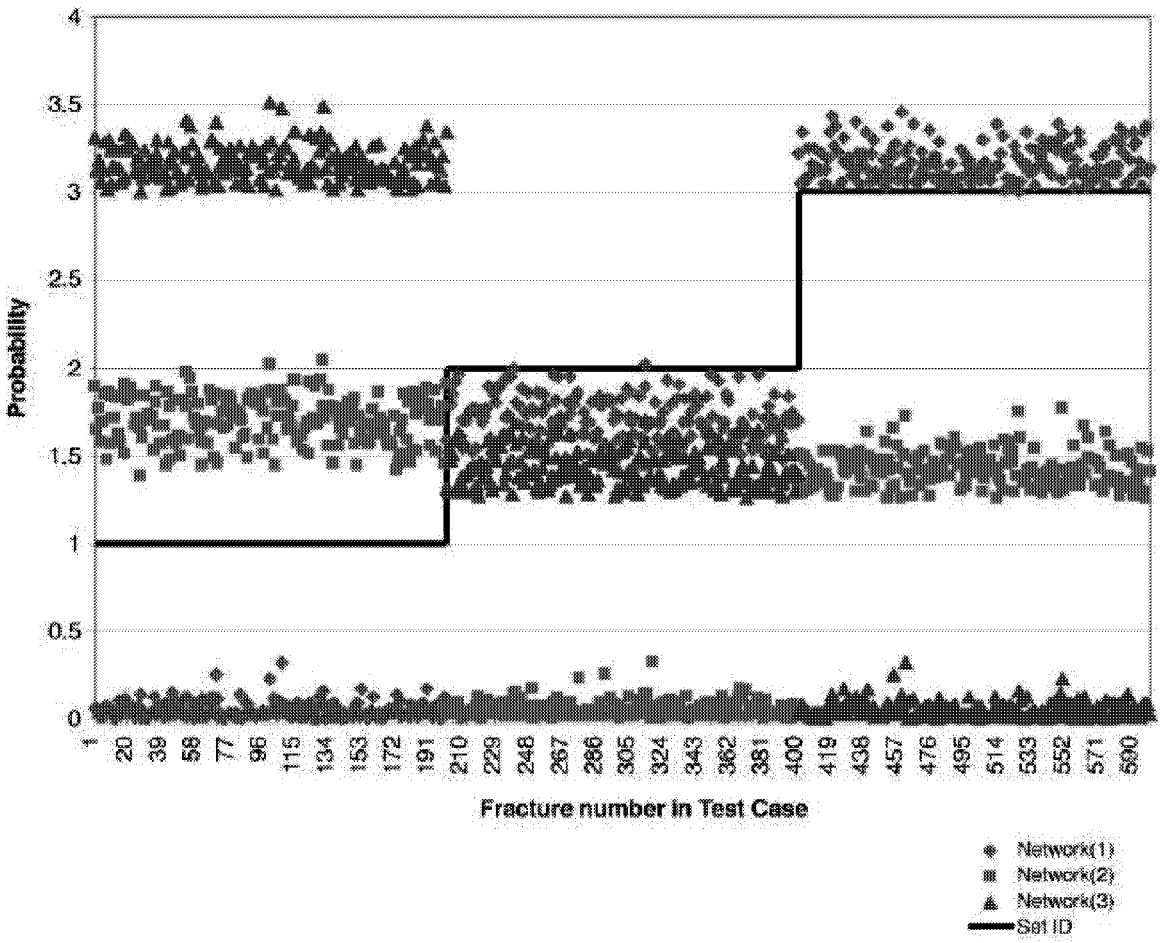

Figure 3-40 Neural Net Performance Results for 3 Set Test Case

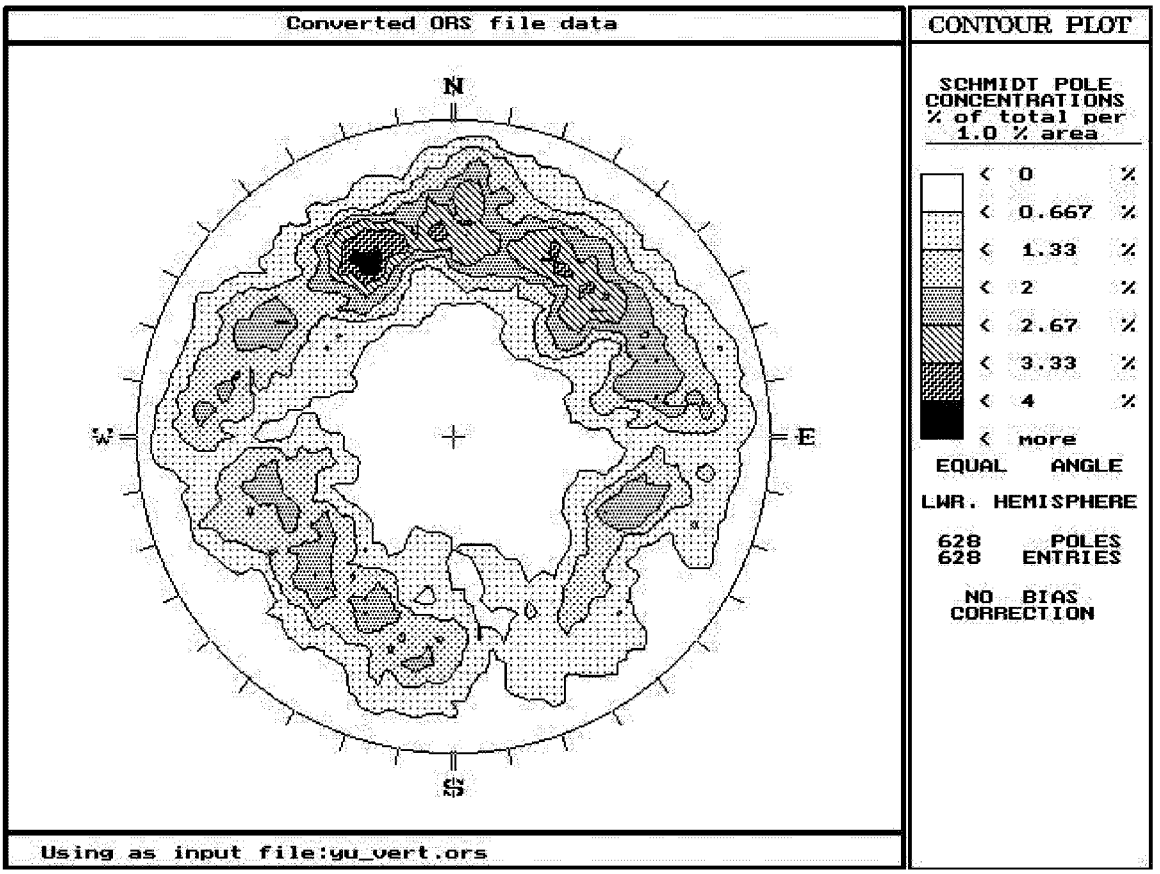

Figure 3-41 Contour Plot of Joint Orientations in Three Yates Wells

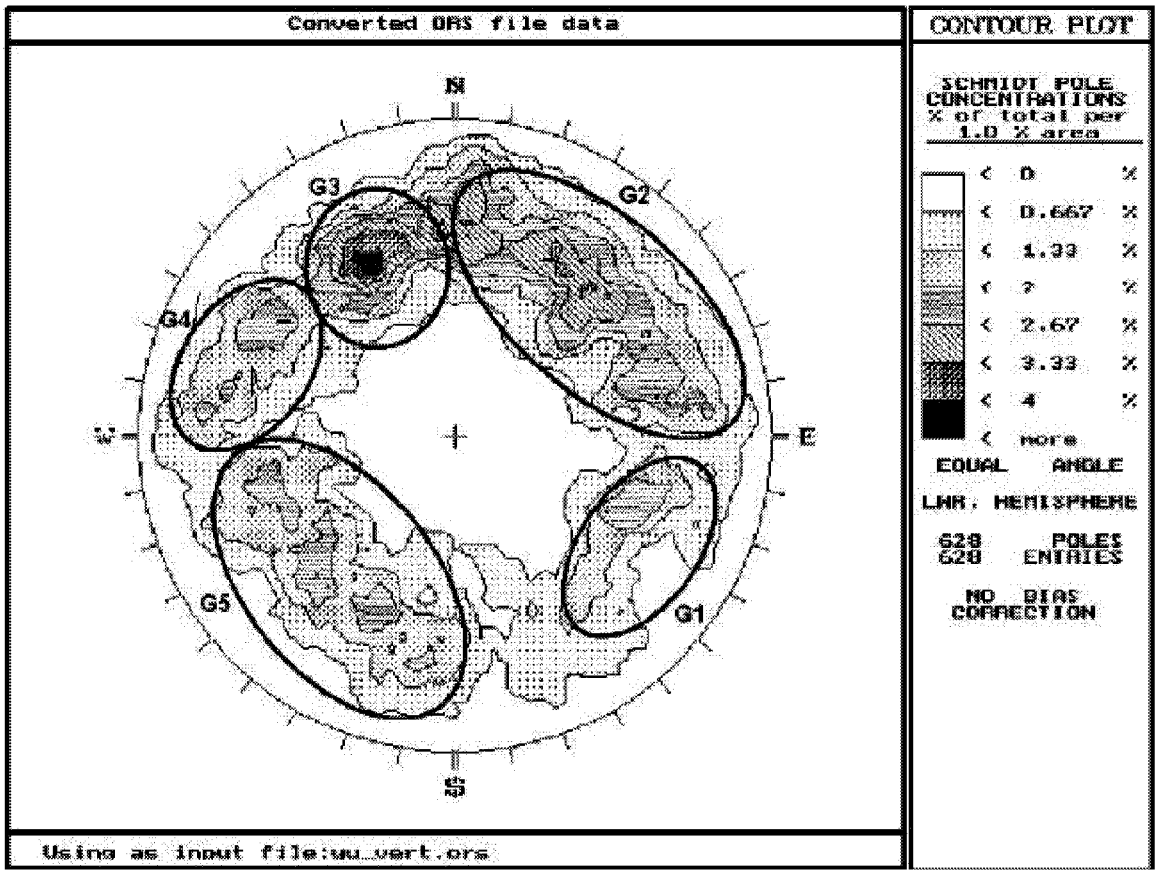

Figure 3-42 Contour Plot of Sets Identified by Structural Geologist

The five sets selected by the neural net are labeled as N1 through N5 in Figure 3-43.

The G sets and the N sets are very similar. G1 matches N1 exactly. The neural net made a slightly different selection of N2 and N3 versus G2 and G3. The region of the stereoplot covered by the combination of G2 and G3 is the same as that covered by N2 and N3. The difference is in the boundary between the two sets. The boundary between the G2 and G3 is approximately a few degrees west of north, while the boundary between N2 and N3 is about 20 degrees east of north. The difference is that the concentration of orientations represented by poles trending north is included with the N3 set by the neural network, but was included with the G2 set by the geologist.

Likewise, sets N4 and N5 cover the same region of the stereoplot covered by G4 and G5, the difference being where the boundary between the two sets is positioned. The boundary selected by the geologist was taken to be a few degrees south of due west, placing the concentration of poles trending around 250 degrees into G5. The neural net chose a boundary more to the southwest at around 240 degrees, moving this concentration of poles into N4.

Overall, the sets identified by the self-organizing neural net are very similar, but not identical to those picked by the geologist. The differences are minor, and would need to be resolved by either collecting additional parameter data or by considering other information on the tectonic or structural history of the reservoir. For example, the G3 set might have different sizes, fillings or roughness than the other fractures included in N3. Or it might be that the G3 fractures were in the orientation expected for a particular tectonic event, while the additional fractures found in N3 were not.

The fact that the geologist and the neural network came up with slightly different groupings is a useful result in itself. Just as two geologists might define sets differently, and thereby stimulate discussion, the network illustrates alternative interpretations and set definitions. The difference between the neural network's set identifications are useful for focusing further considerations as to the geological origins of each set.

3.2.3.5 Applications for Heterogeneous Reservoir Data

There are several potential applications of neural network technology to heterogeneous reservoirs. The first application is that described above: identification of clusters in the data in order to guide statistical analysis and to stimulate further investigations into the possible geological explanations of the groupings.

Another use of the self-organizing network analysis is as a classification tool for rapidly assigning additional data into the proper sets. This is particularly useful for mature reservoirs where there may be an abundance of data that can require a lot of time for a skilled geologist to classify. Once the self-organizing net has been trained on a small subset of data to the geologist's satisfaction, then the trained net can be used to automatically assign set probabilities to all the remaining data. The assignment is both quick and consistent, and does not require the time of a skilled geologist.

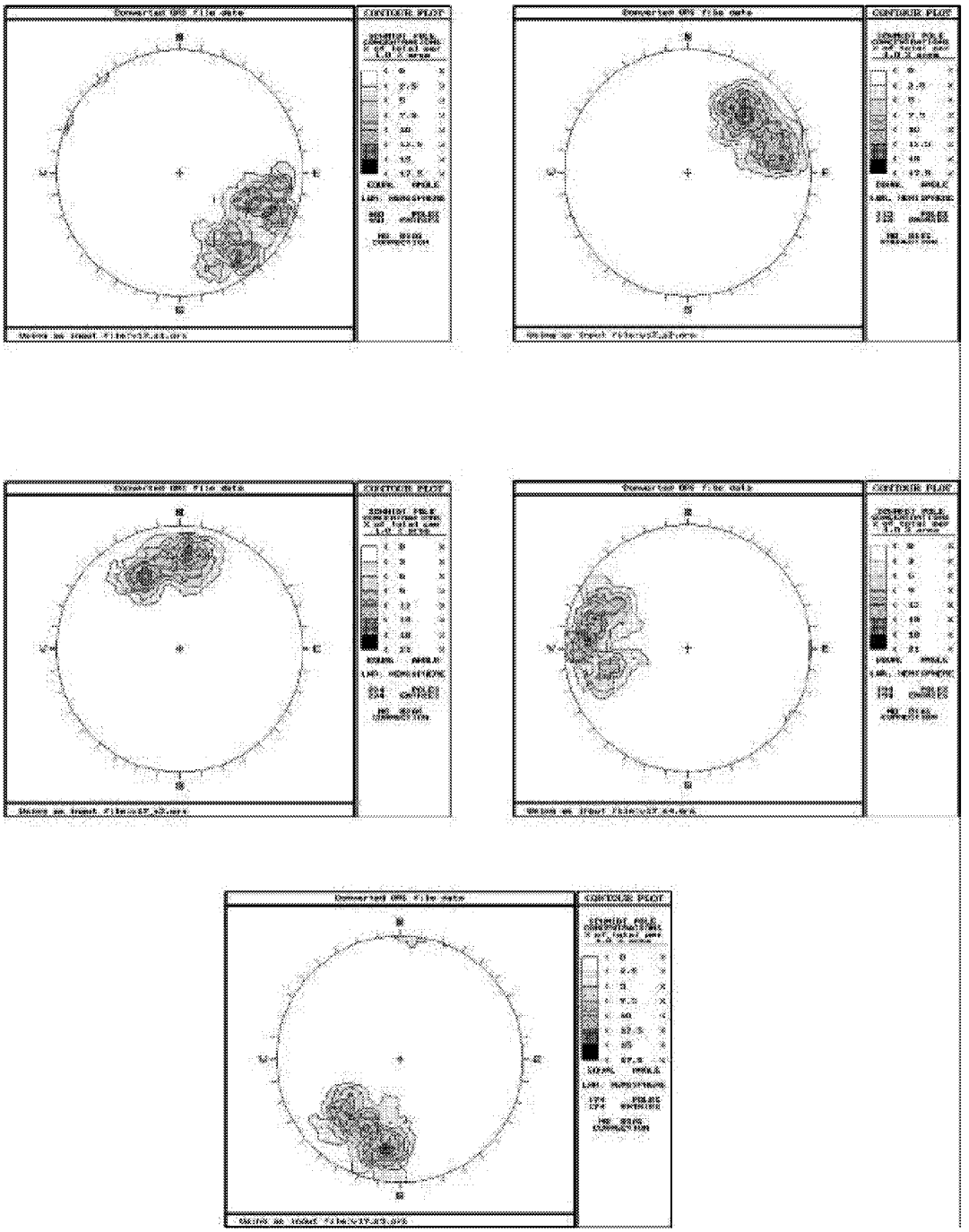

Figure 3-43 Contour Plots of Sets Identified by Neural Network

3.2.4 Task 1.1.4 Fractal Methods for Derivation of Fracture Statistics

Fractal methods are particularly useful for extrapolating information from the scale of measurement to scales at which measurements are difficult. During this project, we developed new and innovative approaches for use of fractal methods to extrapolate fracture size information from the scales of measurement such as VSP lineament to smaller scales, to provide useable fracture size distributions for DFN modeling.

Published methods to estimate fracture size combine Discrete Fracture Network (DFN) modeling with a forward modeling approach to match various statistical parameters of the 1D or 2D data (Dershowitz et al.,1998; La Pointe et al., 1993). While these methods are very general and powerful, they require sophisticated numerical simulations.

Many researchers who have analyzed fracture geometry in wells, outcrop, lineament maps or seismic profiles have concluded that individual fracture sets often exhibit Power Law or fractal characteristics for many of their parameters, including fracture size. If a fracture set does conform to a fractal size distribution model, then it is possible to derive a host of useful equations that relate statistics for the observed fracture trace lengths to the statistics that describe the unobserved three-dimensional parent fracture population, making numerical simulations unnecessary. The sections that follow detail the derivation of these equations, and illustrate through numerical DFN simulations that they provide accurate estimates of the parent fracture population size statistics.

3.2.4.1 Fractal Fracture Size Distributions

For the equations developed below, fractures are assumed to be planar and circular. The representation of fractures as circular discs, rather than as some other shape, is not a required assumption, but is convenient for the mathematical development presented in these sections. It turns out that the derived equations apply with minor modifications to fractures of other shapes, as discussed in Section 3.2.2.5.

It is also convenient to characterize fracture size by the effective radius of the fracture, since this parameter is often used in modeling simulations or engineering calculations. The effective radius of a fracture is defined as the radius of a circular fracture that has the same area as the actual fracture.

A group of fractures that have a Power Law or fractal radius distribution implies that the Complementary Cumulative Density Function (CCDF) of the fracture radii conforms to a power law. The CCDF is defined as the probability that a fracture radius is equal to or greater than a particular radius. Power Law distributions require the specification of a minimum value for their distributional mass and moments to be finite. The probability that a value is equal to or greater than the minimum value is 1.0, while the probability that the radius is greater than or equal to infinity is 0.0. The formal representation of the CCDF is given by Equation 42:

$$G(x) = \left(\frac{x_0}{x}\right)^D \qquad \text{Equation 42}$$

where x_0 is the minimum (radius) value,

x is any fracture radius between x_0 and ∞,

D is the exponent of fractal dimension, and

$G(x)$ is the probability that x is greater than or equal to x_0.

The Cumulative Density Function (CDF) of the three-dimensional radius distribution, is defined as:

$$F(x) = 1 - G(x) = 1 - \left(\frac{x_0}{x}\right)^D \qquad \text{Equation 43}$$

The Probability Density Function (PDF) defined as the derivative of the cumulative density function:

$$f(x) = \frac{\partial}{\partial x} F(x) = \frac{D x_0^{\,D}}{x^{D+1}} \qquad \text{Equation 44}$$

Note that the PDF and CCDF have a power law functional form, and so would plot as a straight line on doubly logarithmic axes, while the CDF does not have a power law functional form, and would not plot as a straight line on doubly logarithmic axes.

Statistical distributions can be characterized by their moments, such as their mean or standard deviation. Power law distributions differ from many common distributions, like the lognormal or the exponential, in that their moments are not. For power law distributions, the value of D governs whether a particular moment is finite or not, as is shown in this section. These considerations are important for using trace length data to infer the population characteristics of the parent fracture population.

The mean radius (μ) is defined as the expected value ($E[]$) of the radius distribution, or:

$$\mu = E[f(x)] = \int_{x_0}^{\infty} x f(x) \partial x \qquad (a)$$

$$= D x_0^{\ D} \int_{x_0}^{\infty} x^{-D} \partial x \qquad (b)$$

$$= \frac{D x_0^{\ D}}{1-D} x^{-D+1} \Big|_{x_0}^{\infty} \qquad (c)$$

$$= \frac{D x_0^{\ D}}{1-D} \left[\infty^{1-D} - x_0^{\ 1-D} \right] \qquad (d)$$

Equation 45

Now the term ∞^{1-D} will not vanish unless $D > 1.0$, which implies that the mean value is not finite unless $D > 1.0$. For $D > 1.0$, Equation 45d becomes:

$$\mu = \frac{D x_0^D}{D-1} x_0^{1-D}$$

Equation 46a

or

$$\mu = \frac{D x_0}{D-1}$$

Equation 46b

Equation 46b represents the expected value, or mean radius for the distribution for the case where $D > 1.0$.

The variance of a function is defined as:

$$\sigma^2 = \int_{x_0}^{\infty} f(x) * (x - \mu)^2 \partial x$$

Equation 47

where
$f(x)$ is the probability density function (pdf) for x,
μ is the mean or expected value of x, and
x_0 is the minimum value of x and
σ^2 is the variance.

As has been shown, the PDF of x for a Power law distribution is given by:

$$f(x) = \frac{D x_0^{\ D}}{x^{D+1}}$$

Equation 48

and the mean or expected value of the distribution is:

$$\mu = \frac{x_0 D}{D-1} \qquad \text{Equation 49}$$

So, inserting these two expressions into Equation 47 yields:

$$\sigma^2 = \int_{x_0}^{\infty} \left(\frac{D x_0^{\ D}}{x^{D+1}}\right) * \left(x - \frac{x_0 D}{D-1}\right)^2 \partial x \qquad \text{Equation 50}$$

Expanding the terms in brackets and bringing quantities not dependent upon x outside of the integration brackets yields:

$$\sigma^2 = D x_0^D \int_{x_0}^{\infty} \left[x^{1-D} - \frac{2 x_0 D x^{-D}}{D-1} + \frac{x_0^2 D^2 x^{-D-1}}{(D-1)^2} \right] \partial x \qquad \text{Equation 51}$$

Carrying out the integration produces:

$$\sigma^2 = D x_0^D * \left[\frac{x^{2-D}}{2-D} - \frac{2 x_0 D}{D-1} * \frac{x^{-D+1}}{1-D} + \frac{x_0^2 D^2}{(D-1)^2} * \frac{x^{-D}}{(-D)} \right]_{x_0}^{\infty} \qquad \text{Equation 52}$$

Now this quantity is finite iff $D > 2.0$. Thus,

$\forall D > 2.0,$

$$\sigma^2 = -D x_0^D * \left[\frac{x_o^{2-D}}{2-D} + \frac{2 x_0 D x_0^{-D+1}}{(D-1)^2} - \frac{x_0^2 D^2 x_0^{-D}}{D(D-1)^2} \right] \qquad (a)$$

$$= -D x_0^D * x_o^{2-D} * \left(\frac{1}{2-D} + \frac{D}{(D-1)^2} \right) \qquad (b)$$

Equation 53

or

$$\sigma^2 = \frac{x_0^2}{(D-1)^2} * \frac{D}{D-2} \qquad \text{Equation 54}$$

Since the standard deviation, σ, equals $\sqrt{(\sigma^2)}$, the standard deviation of the radius distribution is:

$$\sigma = \frac{x_0}{D-1} * \sqrt{\frac{D}{D-2}}$$ Equation 55

3.2.4.2 Trace Length Statistics

The traces observed on a planar surface, such as an outcrop, are biased in that larger fractures have a higher probability of intersecting the surface than do smaller ones. The solution to the problem of how the scaling properties of trace lengths relate to the scaling properties of the parent fracture radius distribution requires decomposition of the problem into two stages:

(a) The relation between the radius distribution of the parent fracture population and the radius distribution of the fracture population intersecting the trace plane; and

(b) The relation between the radius distribution of fractures intersecting a trace plane and the observed trace length distribution.

Section 3.2.4.3 analyzes the relation between the fracture and trace distributions.

3.2.4.3 Derivation of Size Distribution from Trace Data

La Pointe and Hudson (1985) showed that, for the assumption that fractures are circular, planar discs, the probability of a fracture intersecting a plane is linearly proportional to the fracture radius. In general, if the fracture is represented by any convex polygonal shape, the probability of the intersection is proportional to the dimension of the polygon parallel to the plane. For simplicity, we consider circular fractures in the following derivations.

Denoting the radius distribution of the parent fracture population by *f(x)* as in Equation 48, the radius distribution for fractures intersecting a plane is given by:

$$o(x) = xf(x) = D\left(\frac{x_0}{x}\right)^D$$ Equation 56

where
*o(x)*is the radius distribution of the intersecting fractures.

The above expression is not a proper probability distribution function, since it does not integrate to 1.0 between x_0 and ∞. A correction (*C*) must be made to insure that the total probability density equals 1.0:

$$C\int_{x_0}^{\infty} o(x) \equiv 1.0 \; or \qquad (a)$$

$$C\frac{Dx_0}{D-1} \equiv 1.0 \qquad (b)$$

$$C = \frac{D\text{-}1}{Dx_o} \qquad (c)$$

So

$$f_{int}(x) = \frac{D\text{-}1}{Dx_o} x f(x) \qquad (d)$$

or

$$f_{int}(x) = (D-1)\frac{x_0^{D-1}}{x^D} \qquad (e)$$

Equation 57

Now the CDF is the integral of the PDF, or:

$$F_{\text{int}}(x) = \frac{D-1}{Dx_0}\int_{x_0}^{x} f_{\text{int}}(x)\partial x \qquad (a)$$

$$= \frac{D-1}{Dx_0} * \frac{Dx_0}{1-D}\left[x^{1-D} - x_0^{\;1-D}\right] \qquad (b)$$

$$= -x_0\left[x^{1-D} - x_0^{\;1-D}\right] \qquad (c)$$

$$= \left(\frac{x_0}{x}\right)^{D-1} + 1 \qquad (d)$$

$$F_{\text{int}}(x) = 1 - \left(\frac{x_0}{x}\right)^{D-1} \qquad (e)$$

Equation 58

This implies that $G_{int}(x)$, the CCDF of the trace lengths, is:

$$G_{\text{int}}(x) = 1 - F_{\text{int}}(x) = \left(\frac{x_0}{x}\right)^{D-1} \therefore$$

Equation 59

Thus, if it were possible to plot the CCDF of the radii of the intersecting circular fractures, the slope of the line would be equal to slope for the true, three-dimensional radius distribution

It is straightforward to derive the expected value, or mean radius value for the intersecting fractures:

$$\mu_{\text{int}} = E[f(x)] = \frac{D-1}{Dx_0}\int_{x_0}^{\infty} x^2 f(x)\partial x = (D-1)x_0^{D-1}\int_{x_0}^{\infty} x^{1-D}\partial x \qquad (a)$$

$$= \left(\frac{(D-1)x_0^{\;2-D}}{2-D}\right) x^{2-D}\Big|_{x_0}^{\infty} \qquad (b)$$

$$= \left(\frac{(D-1)x_0^{\;2-D}}{2-D}\right)\left[\infty^{2-D} - x_0^{\;2-D}\right] \qquad (c)$$

$$= \left(\frac{(D-1)x_0^{D-1}}{2-D}\right)\left[0 - x_0^{2-D}\right] \qquad (d)$$

Equation 60

The equation above is finite iff $D>2.0$. So, for $D > 2.0$, the above equation becomes:

$$\frac{(D-1)}{(D-2)} x_0^{\;D-1} x_0^{2-D} \qquad (a)$$

$$\mu_{\text{int}} = \frac{x_0(D-1)}{D-2} \qquad (b)$$

Equation 61

The derivation of the variance of the radii of intersecting fractures can be simplified by making a simple variable transformation and considering the independence of D and x.

Let $D' = D - 1.0$ Equation 62

Then Equations 57e, 58e, 59a and 61b become:

$$f_{\text{int}}(x) = \frac{D' x_0^{\ D'}}{x^{D'+1}}$$ Equation 63

$$F_{\text{int}}(x) = 1 - \left(\frac{x_0}{x}\right)^{D'}$$ Equation 64

$$G_{\text{int}}(x) = \left(\frac{x_0}{x}\right)^{D'}$$ Equation 65

$$\mu_{\text{int}} = \frac{x_0 D'}{D' - 1}$$ Equation 66

These equations show that the statistical quantities associated with intersecting fracture radius distribution are identical in form to the three-dimensional radius distribution if the substitution $D' = D - 1$ is made in the three-dimensional radius formulae.

Because D' does not depend upon x, the variance (σ^2_{traces}) and standard deviation (σ_{traces}) for the intersecting fracture radius distributions will have the forms:

$$\sigma^2_{\text{int}} = \frac{x_0^2}{(D'-1)^2} * \frac{D'}{D'-2}$$ Equation 67

$$\sigma_{\text{int}} = \frac{x_0}{D'-1} * \sqrt{\frac{D'}{D'-2}}$$ Equation 68

where $D' = D - 1$.

This implies that the exponent for the radius distribution of fractures intersecting a plane can be used to calculate the correct three-dimensional radius distribution by simply adding 1.0 to the exponent, and statistics such as the mean and standard deviation of radius size can be calculated from the intersecting fracture distribution. Although the radius distribution of the intersecting fractures cannot be directly measured, it can be estimated from the trace length distribution as described in the next section.

Unfortunately, the radius of a fracture cannot be measured in outcrop, so it is impossible to compute the scaling properties of the intersecting fracture population. This is true whether the fracture sizes are fractal or follow any other distribution. However, it turns out that for the

fracture shape geometry often assumed for fractures, it is possible to derive relatively simple relations between the observed fracture trace length population and the radius distribution of the intersecting fractures. It turns out that the scaling properties of the radii of fractures intersecting a plane is identical to the scaling properties of the observed trace lengths!

As an illustration, consider a single circular fracture of radius R, oriented perpendicular to a trace plane. If the fracture intersects the plane, then the trace can vary in length from 0.0 to $2R$. As shown in Figure 3-44, the trace length can be expressed as a function of distance z between the fracture center and the trace plane, and the fracture radius, according to the equation:

$$T = 2\sqrt{R^2 - z^2} \qquad \text{Equation 69}$$

The mean observed trace length, T_μ is calculated as:

$$T_\mu = \frac{1}{R}\int_0^R 2\sqrt{R^2 - z^2}\,\partial z \qquad \text{Equation 70}$$

or, carrying out the integration,

$$T_\mu = \frac{\pi R}{2} \qquad \text{Equation 71}$$

Equation 71 is significant in that is shows that the mean observed trace length is equal to the radius multiplied by a constant. This means that the expected distribution of trace lengths is equal to the distribution of radii of the intersecting fractures multiplied by the constant $\pi/2$. In a log-log plot, multiplication of a power law function by a constant does not change its slope. This implies that the scaling exponent of trace lengths will be the same as the scaling exponent of the radius distribution of intersecting fractures. Moreover, the scaling exponent of the trace lengths will be equal to one less than the scaling exponent of the radius distribution of the parent fracture population.

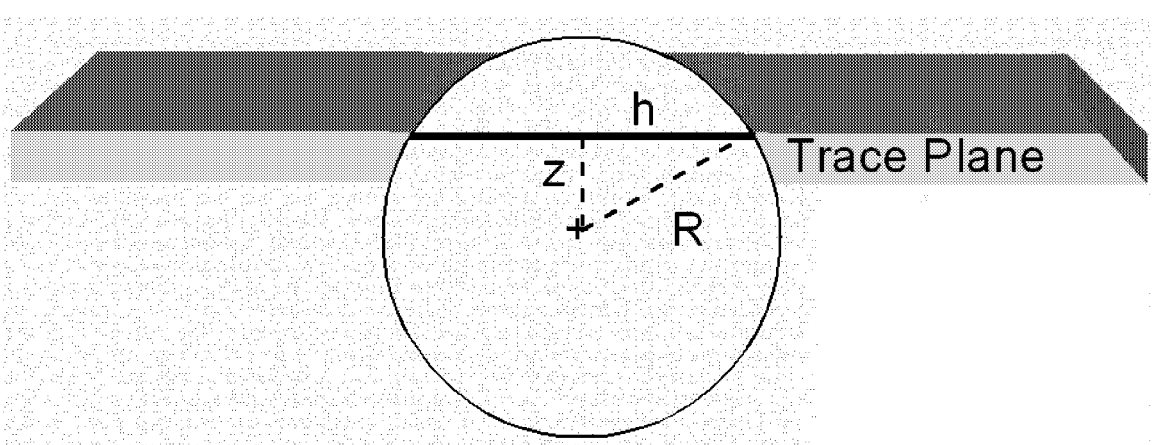

Figure 3-44 Fracture Intersection with Trace Plane

Now consider fractures of other shapes. For rectangular fractures in which at least two sides are parallel to the plane, the trace of an intersecting fracture will always be equal to the length of the side that is parallel. This type of fracture shape would represent a fracture that is confined between two bedding planes or terminates on the upper and lower surfaces of a mechanical layer. In this situation, the relation between the observed trace length and the intersecting fracture is:

$$T = L \qquad \text{Equation 72}$$

Where T is the observed trace length, and L is the length of the side that intersects the bedding or layer boundary. $T_\mu = T$, and so T_μ in Equation 72 is also directly proportional to R, as in Equation 71. The only difference is that the multiplicative constant is 1.0 instead of $\pi/2$. Thus, the scaling exponent for the trace lengths will also be equal to the scaling exponent of the intersecting fracture polygon radius (or edge length) distribution.

These two simple examples indicate that for any planar, anisotropic convex polygon, so long as one of its directions of anisotropy is parallel to the trace plane, the scaling exponent of the traces should be equal to the scaling exponent of the dimension of the intersecting fracture that parallels the trace plane. this, in turn, will be equal to the scaling exponent of the same dimension of the parent fracture population minus 1.0.

3.2.4.4 Verification of Fractal Algorithm for Fracture Size

Since it is not possible to verify the equations derived in Sections 3.1 and 3.2 from field data, as the three-dimensional fracture population cannot be observed directly or through others means, such as geophysics, numerical models of fractures were constructed for this purpose. These numerical models idealized fractures as planar polygons (Figure 3-45).

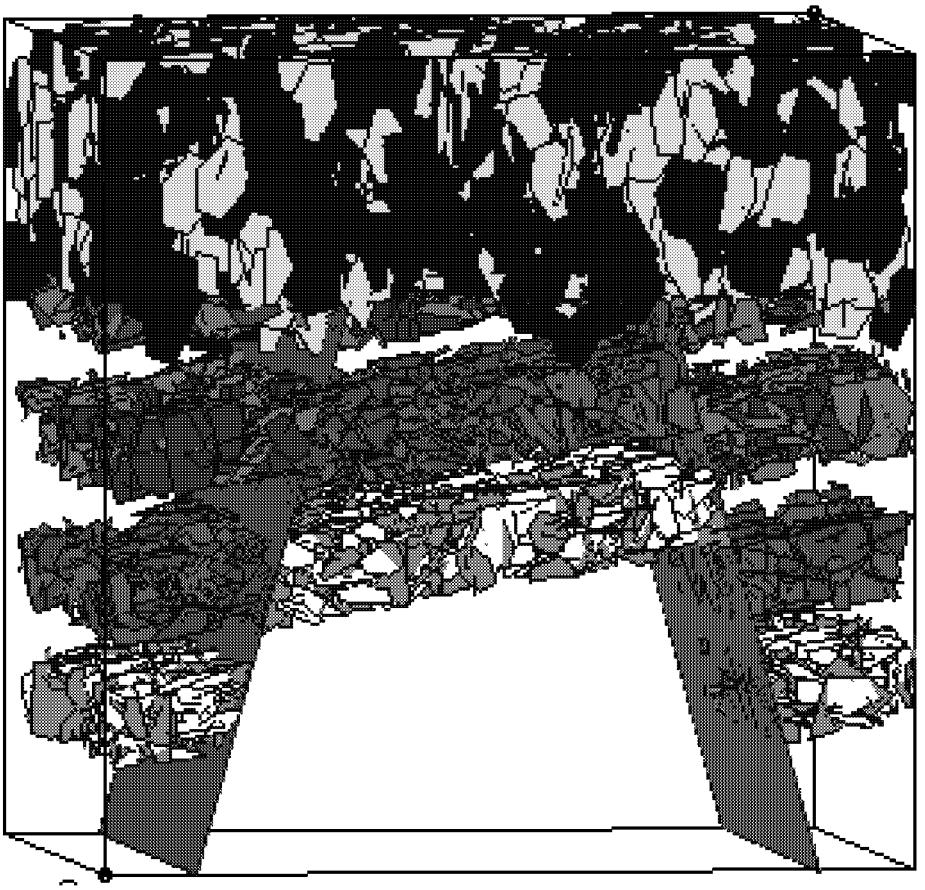

Figure 3-45 Example DFN Model for Size Analysis

The orientation of each fracture polygon, its size and location can be specified according to statistical distributions or constrained by lithology and structural development. Such models, which represent fractures as discrete objects, are commonly referred to as Discrete Fracture Network (DFN) models (Dershowitz et al., 1999).

Three DFN models were constructed to verify the equations. The models had different combinations of values of the exponent and minimum size, and also orientation. The parameter values are summarized in Table 3-19 below.

Table 3-19 Parameters used in simulations

Simulation #	D	Minimum Size	Orientation
1	3.5	1.0	Constant, (90., 0.)
2	2.5	5.0	Constant, (45., 45.)
3	1.5	0.5	Fisher, (0., 0.), $\kappa = 0.0$

All fractures were generated within a 100-m cube embedded with a larger 200 m cube in order to minimize truncation effects on observed trace lengths of fractures terminating against the outer surfaces of the model. 5000 fractures were generated in each model simulation. Locations were selected at random throughout the 100-m cube generation region.

After each simulation was created, a horizontal trace plane was inserted into each of the three models, and the traces saved in a file for subsequent trace length analysis. The names of the files containing the three-dimension DFN model, the trace plane results, and the horizontal plane sampling file are listed in Table 3-20.

Table 3-20 List of file names for verification tests.

Simulation #	3D DFN file	Trace Length File
1	Sim1.fab	Sim1.f2d
2	Sim2.fab	Sim2.f2d
3	Sim3d.fab	Sim3d.f2d
Trace Plane	Htplane.sab	

The first series of verification tests are on the 3D DFN model itself. Each simulation is created essentially through the generation of a uniformly random field of numbers over the interval (0,1), and then transformation of this field into a power law distribution through Gaussian anamorphosis. This procedure sets the cumulative probability of the uniform field equal to the cumulative probability of the power law distribution, or:

$$U = 1 - \left(\frac{x_0}{x}\right)^D, \; where\, U \in (0.0, 1.0) \qquad \text{Equation 73}$$

Solving this equation for x yields:

$$x = \frac{x_0}{(1-U)^{\frac{1}{D}}}$$ Equation 74

The resulting random realization of x will have a power law distribution characterized by Equations 42, 43, 44, 46b, and 57.

D and x_0 were estimated (denoted in Table 3-21 as D^* and x_0^*) through non-linear estimation of the CCDF function (Equation 44) for the radii of the 5000 fractures actually generated. In addition, the mean radius and the standard deviation of the radius distribution were estimated from Equations 46b and 55, respectively, from D^* and x_0^* for the cases where these moments were finite. These were then compared to the values actually calculated from the 5000 radius values for each of the fractures. The results shown in Table 3-21 verify that the simulation method produced three-dimensional fracture models with the desired power law characteristics, and that the mean and standard deviation of the radius distribution can be reliably estimated through Equations 46b and 55. Figure 3-46 shows the results of the non-linear fits for each CCDF.

Table 3-21 Verification of Fractal Fracture Size Algorithm

Simulation	**Specified D**	**Specified x_0**	**Estimated D (D^*)**	**Estimated x_0 (x_0^*)**
1	3.5	1.0	3.47	1.00
2	2.5	5.0	2.44	5.00
3	1.5	0.5	1.50	0.50
Simulation	**Predicted Mean**	**Predicted σ**	**Calculated Mean**	**Calculated σ**
1	1.40	0.62	1.40	0.57
2	8.48	8.20	8.47	6.29
3	1.49		1.47	

In Table 3-21, the standard deviations for Simulation 3 were not calculated since $D < 2.0$, which violates the constraint used to derive Equation 55.

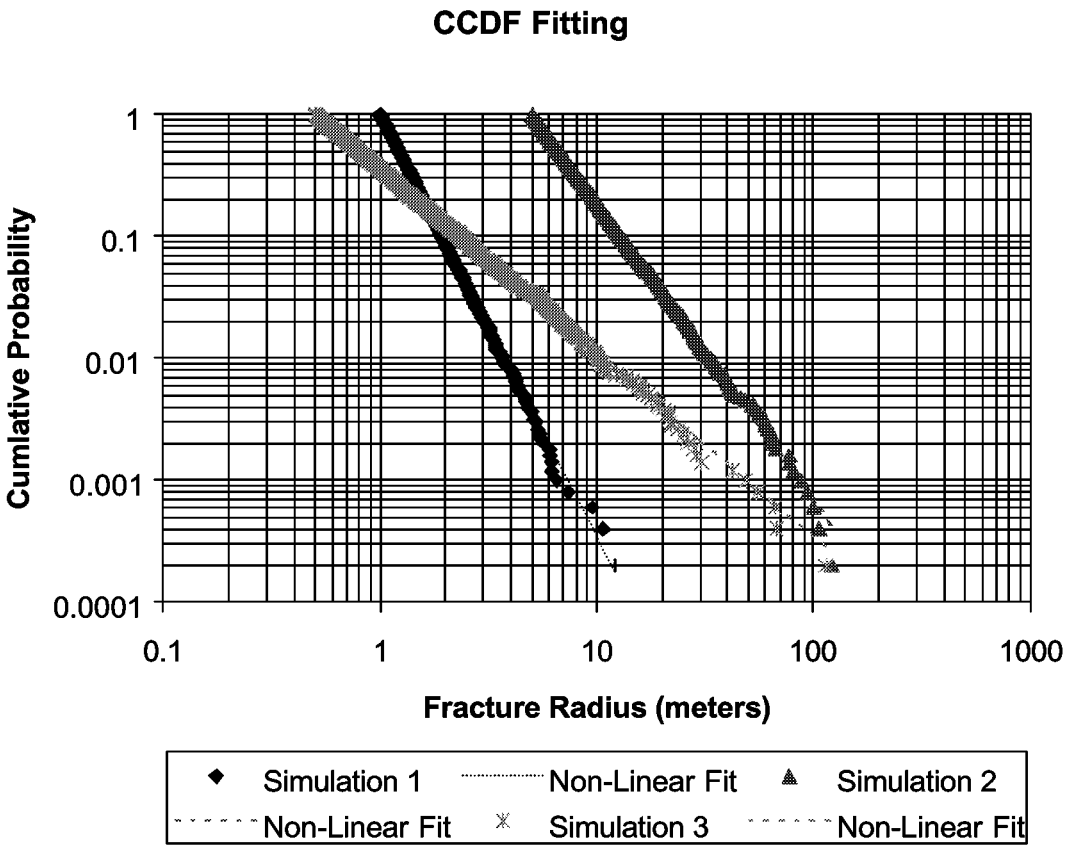

Figure 3-46 Complementary Cumulative Density Functions (CCDF) for Fracture Radius

The next stage in the verification process is to the trace length distributions using the files listed in Table 3-20. The scaling exponents of the trace length distributions are given in Table 3-23, and non-linear fits to the trace length distributions are shown in Figure 3-47.

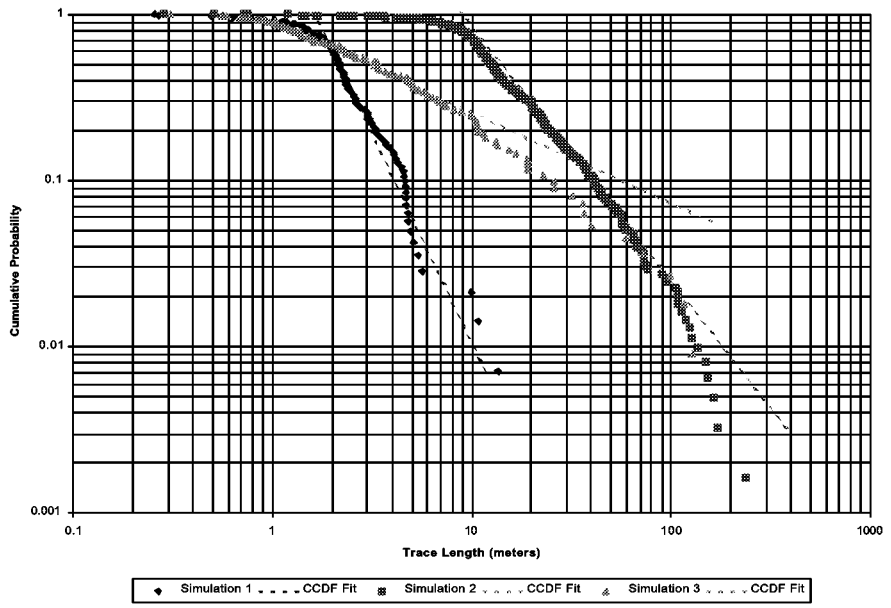

Figure 3-47 Fitted Trace Length Distributions

Table 3-22 Parameter values estimated for the observed trace lengths.

Simulation	D	x0	Mean
1	2.50	84.53	2.55
2	1.52	16218.1	20.32
3	0.54	31117.2	10.27

Table 3-23 Parameters for the radius distribution of fractures intersecting the trace plane.

Simulation	D	x_0	Mean	Mean Predicted From Mean Trace
1	2.51	1.00	1.67	1.62
2	1.48	5.02	12.85	12.94
3	0.51	0.51	7.15	6.54

In Table 3-22, the mean radius has been predicted from the mean trace length using Equation 71, which multiplies the mean trace length by $2/\pi$. A comparison of Table 3-22 and Table 3-23 shows that the trace length exponent and the radius exponent are in excellent agreement, and also that the mean radius is well-predicted from the mean trace length.

Equation 66 shows that the parameter, x_0, can be estimated from D and μ or σ. For Simulation 1, the only simulation in which both first- and second-order moments are finite (since $D > 2.0$), the values of D and μ can be used to estimate x_0:

$$x_0 = \frac{\mu(D-1)}{D}$$ Equation 75a

or

$$x_0 = \frac{1.62 * (2.50 - 1.00)}{2.50} = 0.972$$ Equation 75b

This is very close to the actual simulation mean of 1.00.

Since x_0 and D are now estimated for the radius distribution of fractures intersecting the plane, the values for the parent fracture population radius distribution are:

$$D_{fractures} = 2.50 + 1.0 = 3.50$$ Equation 76a

$$X_0 \text{ (fractures)} = x_0 \text{ (intersecting fractures)} = 0.972$$ Equation 76b

In turn, these values can be put into Equations 46b and 55 to compute the mean and standard deviation of the radius distribution of the parent fracture population:

$$\mu_{fractures} = \frac{0.972 * 3.50}{3.50 - 1.0} = 1.36$$ Equation 77a

$$\sigma_{fractures} = \frac{0.972}{3.50 - 1.00}\sqrt{\frac{3.50}{1.50}} = 0.59$$ Equation 77b

The actual values for the simulation are 1.40 and 0.57, respectively. This illustration shows that it is possible to make quite accurate predictions of the parent population from trace length data alone, and that the scaling exponent of trace lengths for a fractal fracture population is 1.0 less than the scaling exponent of the parent fracture radius distribution.

3.2.4.5 Fractal Fracture Size Distribution from Non-planar Surfaces

Natural objects, such as fractures, have been shown to have many fractal properties. However, these properties are typically sampled by methods that have a particular dimension. For example, wellbores or scanlines have a dimension of 1.0, since they are (if their width is neglected) line samples. Another typical sample is a surface, which may or may not be approximately planar. Examples include outcrops, underground exposures, lineament maps and two-dimensional seismic profiles.

The equations developed above were for perfectly planar surfaces. This section extends the equations in those sections to any general fractal or Euclidean sampling object. The basis for the method relies upon a theorem in topology (Mandelbrot, 1983) that states that the co-dimension of the intersection of two sets is equal to the sum of the co-dimensions of each set.

The theorem also extends to n sets. This theorem does not require the sets to be fractal, but certainly can be used for fractal sets.

The co-dimension of a set is denoted by C. The dimension of the set is denoted by D. Then, the co-dimension is related to the dimension as:

$$C = E - D \qquad \text{Equation 78}$$

where:

E is the Euclidean dimension of the space in which the sets exist.

For a volume of rock, $E = 3.0$.

Suppose a set of fractures has a dimension D_f. Then the co-dimension is:

$$C_f = E_3 - D_f \qquad \text{Equation 79}$$

where
E_3 is the Euclidean dimension of the embedding space, in this case, 3.0.

A plane within a volume has a dimension of 2.0, and a line has a dimension of 1.0. Thus:

$$C_{plane} = E_3 - 2.0 \qquad \text{Equation 80a}$$

$$C_{line} = E_3 - 1.0 \qquad \text{Equation 80b}$$

According to the theorem, the intersection of the fracture set and a plane has a co-dimension equal to the sum of the individual co-dimensions, or:

$$C_{traces} = C_{fractures} + C_{plane} \qquad \text{Equation 81}$$

which implies that:

$$C_{traces} = E_3 - D_{fractures} + E_3 - D_{plane} \qquad \text{Equation 82}$$

or

$$D_{traces} = E_3 - (E_3 - D_{fractures} + E_3 - D_{plane}) \quad \text{Equation 83}$$

or

$$D_{traces} = D_{fractures} + D_{plane} - E_3 \quad \text{Equation 84}$$

and, after inserting the numerical values for D_{plane} and E_3,

$$D_{traces} = D_{fractures} + 2 - 3 = D_{fractures} - 1 \quad \text{Equation 85}$$

Thus, the dimension of the trace plane pattern is equal to the dimension of the parent fracture population minus 1.0. A similar line of reasoning shows that the dimension of a line sample will be equal to the dimension of the parent population minus 2.0.

Note that Equation 76 is identical to Equation 62. In fact, Equation 75 could be re-written for a fractal sampling object of any dimension:

$$D_{traces} = D_{fractures} + D_{samplingobject} - E_3 \quad \text{Equation 86}$$

So, for example, assume that the traces were on a rough fractal surface whose dimension is $D = 2.5$. Then by substitution in Equation 78, the dimension of the traces is:

$$D_{traces} = D_{fractures} + 2.5 - 3.0 \quad \text{Equation 87}$$

or

$$D_{traces} = D_{fractures} - 0.5 \quad \text{Equation 88}$$

In this case, $D' = D - 0.5$, rather than $D - 1.0$ as in the case with a perfectly planar surface. This value of D' would be substituted into Equations 63 through 68 to compute the appropriate fracture radius statistics from the observed trace lengths.

3.2.5 Task 1.1.5 Transmissivity/Connectivity Analysis

This section describes the development of a new conceptual approach for understanding transmissivity, connectivity, and channeling in fractured rock.

Reservoir engineering generally understands fractures in terms of the hydraulic properties permeability (md), an aperture (m), and a porosity (-). Discrete fracture network (DFN) modeling, on the other hand, combines permeability, and an effective hydraulic aperture as a measure of the transmissive properties of the fracture (millidarcy-meters). Fracture storage properties are generally represented in DFN modeling in terms of the term storativity, which combines the effects of aperture, porosity, and compressibily. Storativity, *S(-)* is defined in terms of fracture aperture, e, the total compressibility, *C(1/Pa or 1/psi)*, fluid density and gravitational acceleration, ρg as:

$$S = \rho g e C n \qquad \text{Equation 89}$$

Transmissivity relates to the ke product by

$$T = \rho g \frac{ke}{\mu}. \qquad \text{Equation 90}$$

For parallel plate flow,

$$k = e^2/12 \qquad \text{Equation 91}$$

However, for most practical problems of reservoir engineering, it is better to allow a more general form of correlation between permeability and aperture,

$$k = A\, e^{B} \qquad \text{Equation 92}$$

where A and B are calculated based on field measurements and hydraulic tests. The transmissivity in petroleum units (millidarcy-meters) uses the equation for transmissivity above with the aperture value obtained from the storage calculation.

Fracture intensity can generally be expressed best as the two-dimensional fracture area per unit volume of rock. This measure we call P_{32} and it has measures of m^2/m^3 (i.e., m^{-1}). P_{32} is very important number of reservoir evaluation. When multiplied by aperture, P_{32} gives the total fracture porosity, n_{Total}, in a block of rock with a volume, V_{Total}, or:

$$n_{Total} = \frac{P_{32} \times e \times n}{V_{Total}} \qquad \text{Equation 93}$$

P_{32} information comes from several sources. One of the best sources is the frequency of conductive features along a well. These data come readily from PLT logs where the flow rates in the log go through sharp transitions every time the logging tool passes a significant conducting feature.

The frequency of conductors along a line sample, such as a well, relates to the intensity of fractures in the rock mass by a relationship to the fracture size. Fracture size is best estimated from rock exposures where flow can be observed. Lacking such information in a petroleum reservoir, fracture size may be estimated from censoring statistics in FMI logs (that is how often does one observe a fracture termination within the well bore wall). This approach has limited effectiveness, however, if one does not know which of the fractures one is observing in the FMI logs are conductive and which are not contributing to flow.

Flow dimensional analysis (Chakrabarty and Doe, 1999) has demonstrated that a full range of connectivities occur in fractured reservoirs – from 1-D channel flow to 2-D radial flow to fully connected 3-D flow (Figure 3-48). This dimensionality may change with distance from the well, and can frequently be seen in transient hydraulic responses. Fractures, for example, may intersect individual flow channels, providing a 1-D flow response. These 1-D channels may then intersect a large, well connected system of fractures resulting in an apparent 3-D network hydraulic response. Finally, this network may connect to a single, highly permeable layer or fault zone, providing a 2-D hydraulic response.

The success or failure of production wells can thus be a function of:

(a) Fracture Transmissivity – how much flow is directed to the well through the fractures intersecting the well

(b) Fracture Storativity – what is the storage capacity of the fracture network delivering oil to the well

(c) Fracture Porosity – what is the total volume of oil accessible for production within the fracture network

(d) Dimension of flow (1-D, 2-D, or 3-D) at connections to the well, beyond the well, and in the reservoir volume where the majority of oil is stored.

Conceptually, fracture transmissivity and storativity (porosity) can be understood as a combination of:

1. A fault plane or series of fault planes that are large, spatially extensive features, that have a medium level of permeability, but do not contain large storage volumes (Figure 3-49);
2. High permeability channels within these faults (Figure 3-50); and
3. Background fractures that contain most of the accessible storage within the model but have a low level of permeability (Figure 3-51).

In this concept, channels provide high permeability flows within the system, the fracture planes act as collection features, and the storage capacity is contained within the rock matrix and the porosity provided by background fractures.

Figure 3-52 through Figure 3-54 illustrate the differences in well performance depending on the interplay of well locations, channels, faults, and background fractures. In Figure 3-52, a single well is placed on a high permeability channel, and the fault plane transmissivity and storativity is minimized and the permeability of the channel is varied. This simulation does not include the fault plane, but does include the primary storage in the background fractures. In this case, the

permeability of the background fractures is of the same order as the total permeability of the channel, resulting in an apparent three dimensional flow response.

In Figure 3-53, the background fracture size was reduced so that the background fractures would provide primarily a storage rather than a flow effect, and the well was located on the fault plane, but off the channel. For the most part, the flow is two-dimensional with a slight opening up as the pressure field intersects the high permeability channel.

Figure 3-54 presents simulations in which the well connects only to the background fractures. These simulations show an initial closed boundary flow that evolves into two-dimensional flow as the pressure field interacts with the fault plane.

The above simulations demonstrate how fracture, channel, and fault elements combine to control the flow dimension seen in drill stem tests and production histories. This research has demonstrated the importance of understanding the pattern of transmissivity and storativity in each of the discrete feature porosities in order to understand the reservoir behavior and design appropriate IOR procedures.

3.2.6 Task 1.1.6 Fracture Correlations

As part of this project major statistical study was initiated for the correlations between fracture aperture, size, storativity, and transmissivity. The data for this study was obtained by reviewing over thirty sites in a wide variety of geologic settings. The data surveyed are summarized in Table 3-24.

Table 3-24: Correlation of Fracture Geometrical Hydraulic Properties

Site/Geology	Scale of Fractures (m)	Transmissivity (m^2/s)	Storativity (-)	Thickness or Aperture (m)
Persian Gulf/ Limestone	100 to 500	10^{-5} to 10^{-2}	10^{-3} to 10^{-2}	
S. Europe/ Dolomite	5 to 20	10^{-7} to10^{-5}	10^{-4} to 10^{-3}	10^{-3} to 10^{-1}
Äspö, Sweden Task 5 Area/ Granite	100 to 2,000	10^{-5} to 10^{-3}	10^{-3} to 10^{-1}	10^{-1} to 10^{0}
Äspö, Sweden TRUE-1 Area/ Granite	1 to 20	10^{-8} to 10^{-6}	10^{-5} to 10^{-3}	10^{-4} to 10^{-3}
Äspö, Sweden TRUE Block Scale Area/Granite	50 to 300	10^{-8} to 10^{-4}	10^{-5} to 10^{-2}	10^{-4} to 10^{-3}
SE Asia/ Granite	100 to 500	10^{-5} to 10^{-3}	10^{-3} to 10^{-2}	10^{-2} to 10^{0}
Wyoming/ Dolomite	10 to 100	10^{-5} to 10^{-3}	10^{-3} to 10^{-2}	10^{-3} to 10^{-2}
Wyoming/ Sandstone	5 to 100	10^{-5} to 10^{-3}	10^{-3} to 10^{-2}	10^{-3} to 10^{-1}
West Texas/ Dolomite	500 to 2,000	10^{-4} to 10^{-2}	10^{-2} to 10^{-1}	10^{-1} to 10^{0}
Finland/ Granite	5 to 500	10^{-8} to 10^{-5}	10^{-5} to 10^{-3}	
S. America/ Dolomite	1 to 50	10^{-5} to 10^{-4}	10^{-3} to 10^{-2}	
Sellafield, UK/ Tuff	10 to 200	10^{-8} to 10^{-6}	10^{-5} to 10^{-3}	10^{-4} to 10^{-3}
Puerto Rico/ Meta-sediments	10 to 100	10^{-6} to 10^{-2}	10^{-6} to 10^{-4}	10^{-4} to 10^{0}

These values given in Table 3-24 were derived from hydraulic tests including hydraulic interference, tracer transport, and transient well tests. Due to the confidential nature of many of the data sources, only overall ranges are provides, and no citations are given. Values for transmissivity, storativity, and transport aperture were generally used to build DFN flow models, which were then validated against large scale field measurements. In general, transmissivity, storativity, and aperture distributions were reported as lognormal.

The correlation between fracture size and transmissivity based on data from the Äspö Hard Rock Laboratory (HRL) is illustrated in Figure 3-55. Although there is an overlap in transmissivity values between different ranges and classes of features, a trend of increasing transmissivity with scale is apparent. The highest transmissivity values occur with the largest features occur and the smallest trasmissivities occur with the smallest fractures.

3.2.7 Task 1.2 Data Scaling Procedures

For conventional reservoir simulation, data scaling problems revolve around the problems related to simulator block scales. Blocks have scales of tens to hundreds of meters, unrelated to the scales at which data is measured in wells and geophysics. Scaling must therefore extrapolate grid cell properties from, for example, single well scales to interwell scales or from meter scales to hundred meter scales (Figure 3-55).

This necessity of scaling in continuum approaches is avoided in discrete features methods, since features of a wide range of scales can be modeled simultaneously. This approach is illustrated in Figure 3-57. At the scale of the wellbore, all fractures are modeled down to the scale of 0.5 meters. These are the fractures which would appear on fracture image logs, and would provide direct hydraulic connection for delivery of oil and other fluids to the well. At the scale of 100 meters around each well, the fractures from 05. to 100 meters are important, since they provide the primary connectivity and flow permeability. At reservoir scales, features smaller than approximately 10% to 20% of the distance can be treated as part of the background or matrix equivalent permeability/porosity, and only the larger fractures of over 50 to 100 meters need to be considered explicitly. The procedure for multi-scale modeling of discrete feature network models is described in Section 3.2.7.1.

Upscaling is also a consideration in converting between discrete feature network models and continuum approaches. In this form of upscaling, we are taking data from the scale of individual fractures, and taking it to the scale of continuum grid cells. This is described in Section 3.2.7.2.

Discrete feature network modeling frequently does require a particular form of data scaling developed in Section 3.2.7.3. This form of data scaling is necessary to interpolate between the limited ranges of scales addressed in particular data collection programs, and the full range of discrete feature scales necessary for discrete feature analysis.

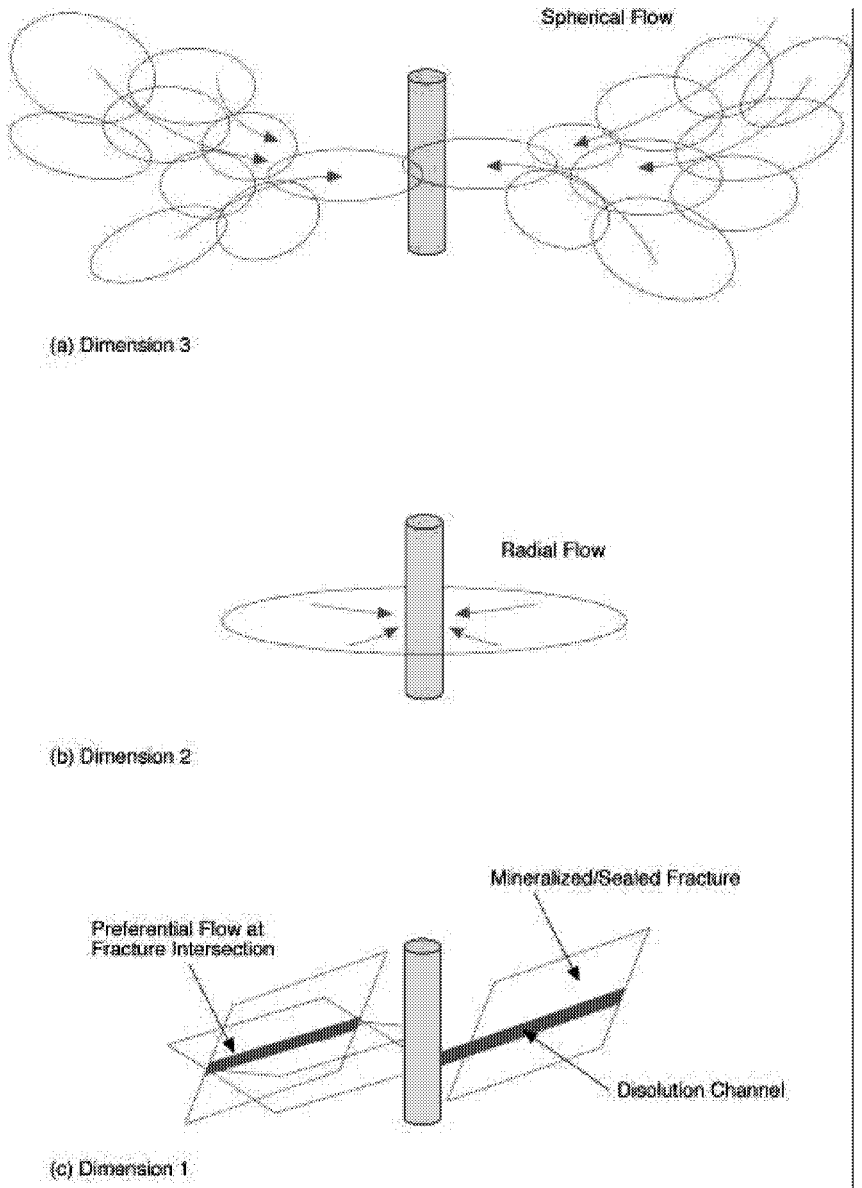

Figure 3-48 Flow Dimension

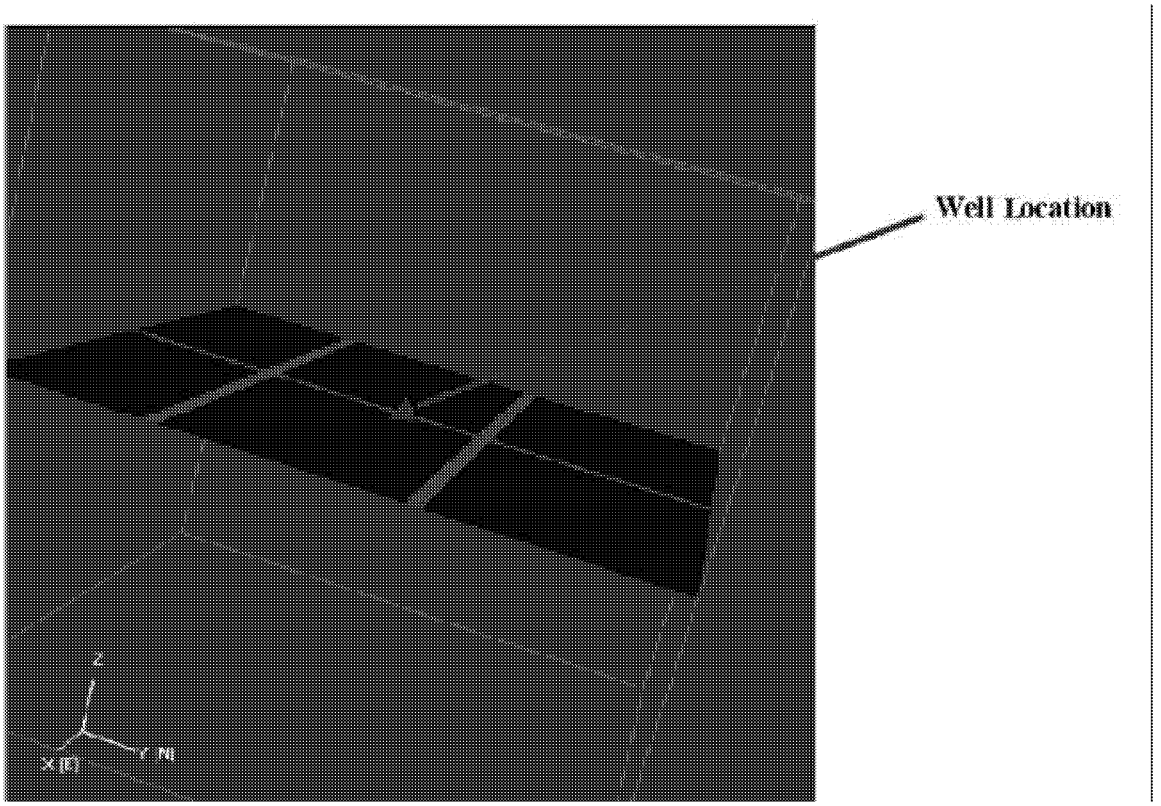

Figure 3-49 Channels in Fracture Plane

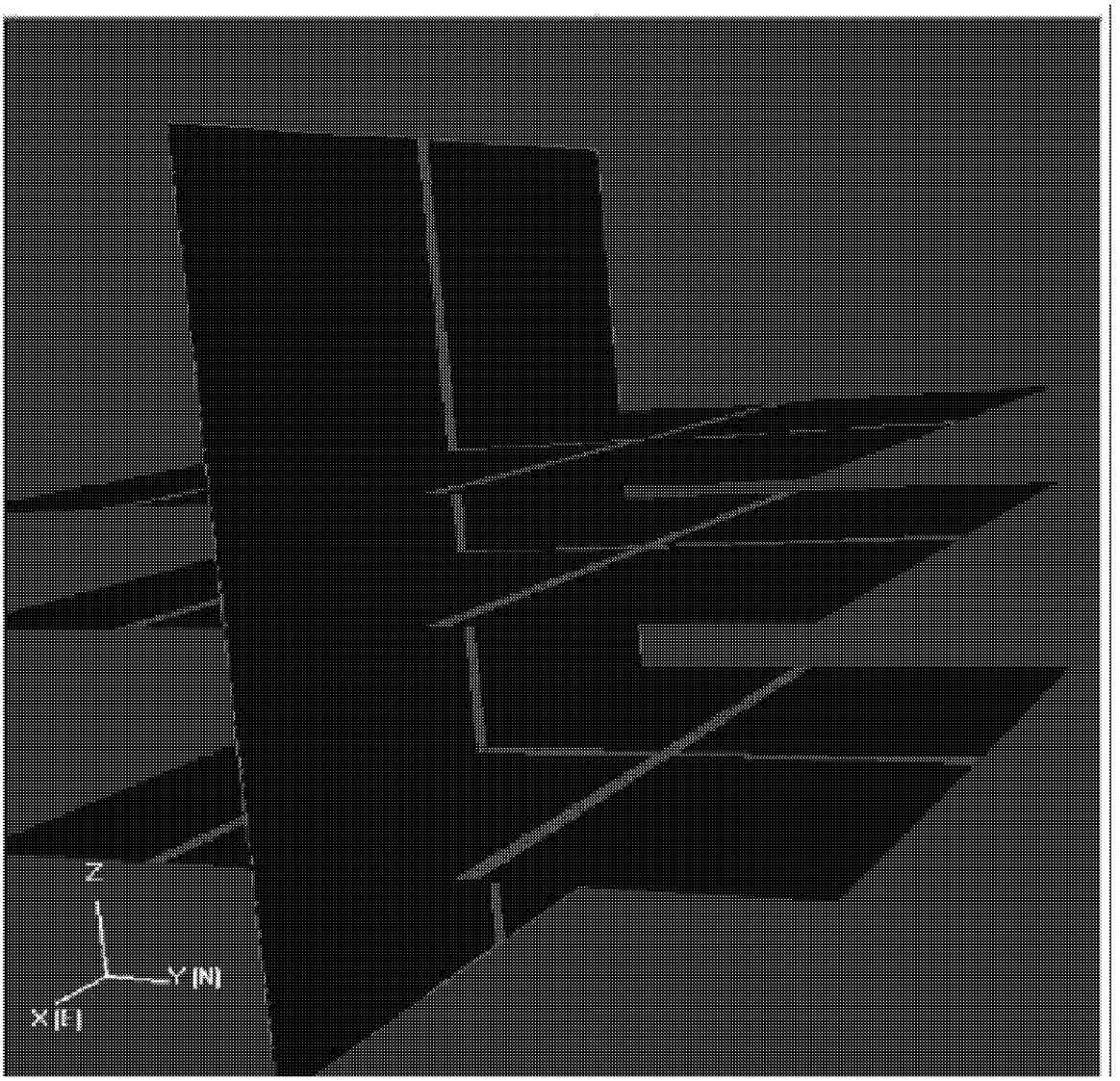

Figure 3-50 Channels in Faults and Fractures

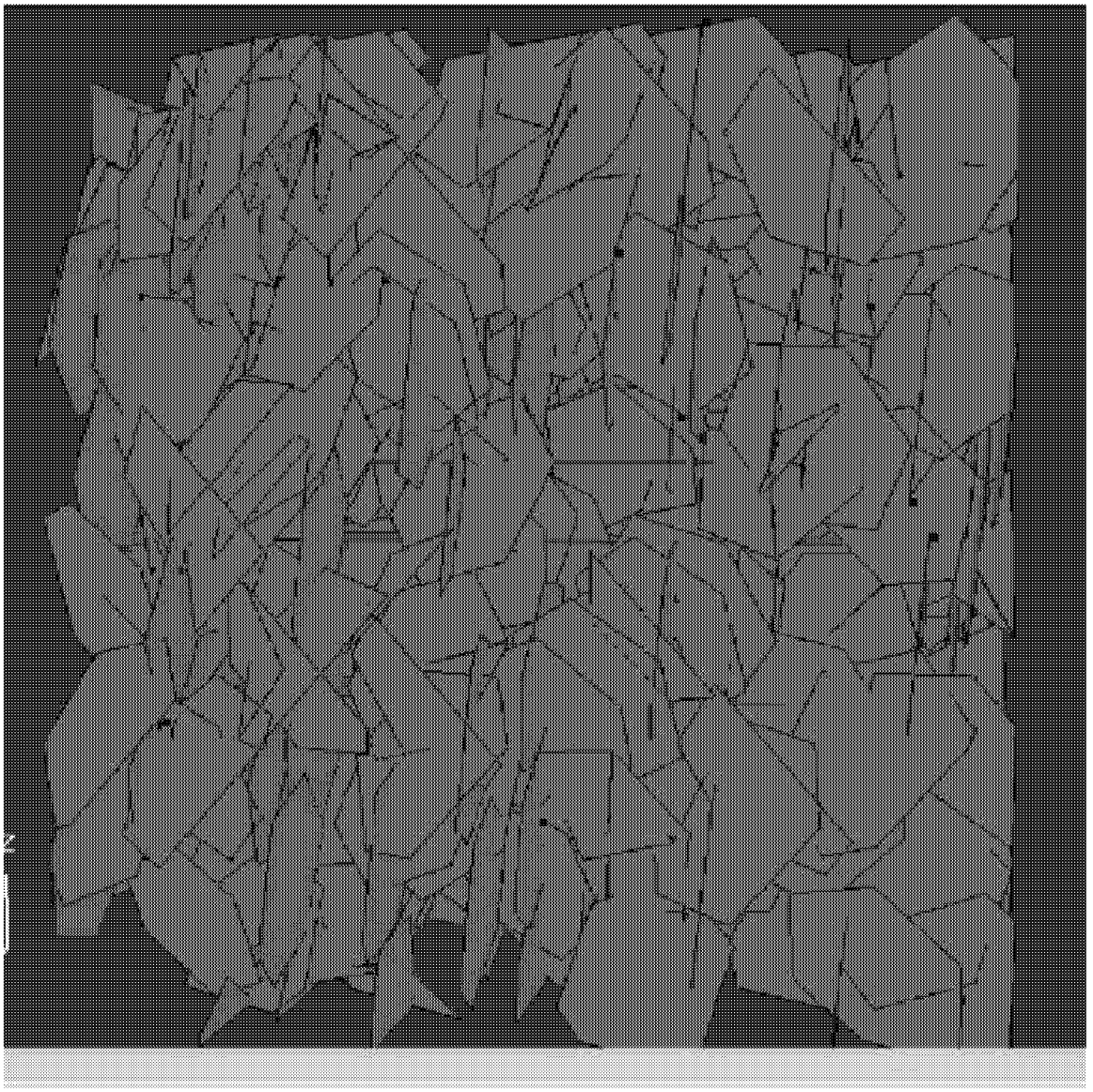

Figure 3-51 Background Fracture Porosity and Connectivity

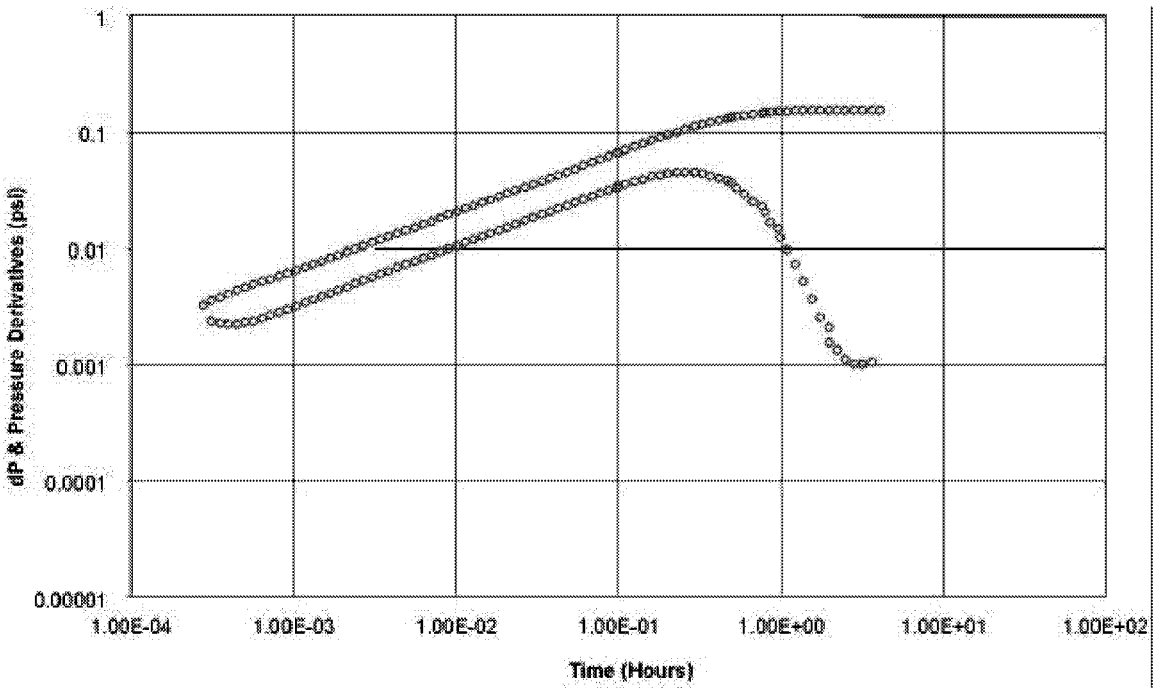

Figure 3-52 Productivity Test with Single Channel, Well on Channel

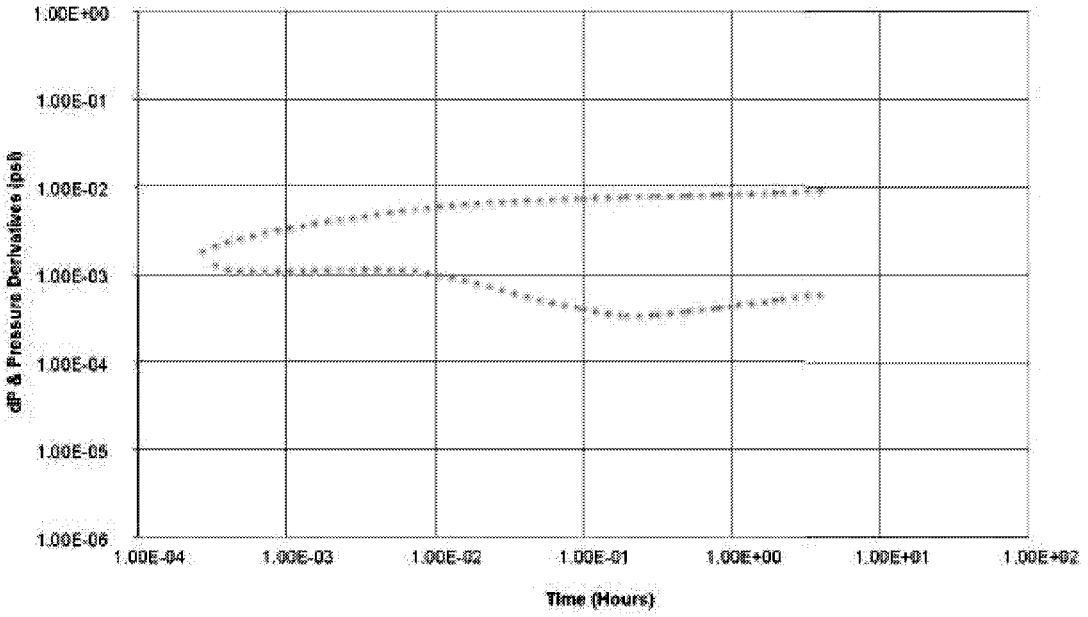

Figure 3-53 Production Test with Single Channel, Well on Fault

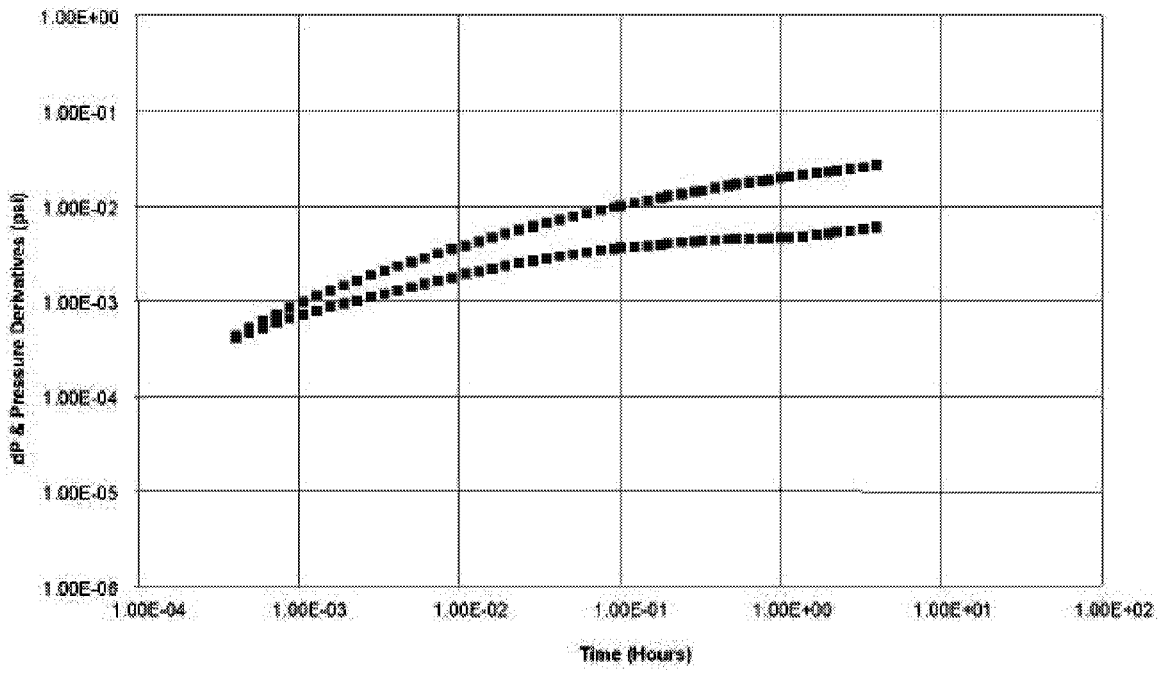

Figure 3-54 Production Test with Single Channel, Well in Background Fractures

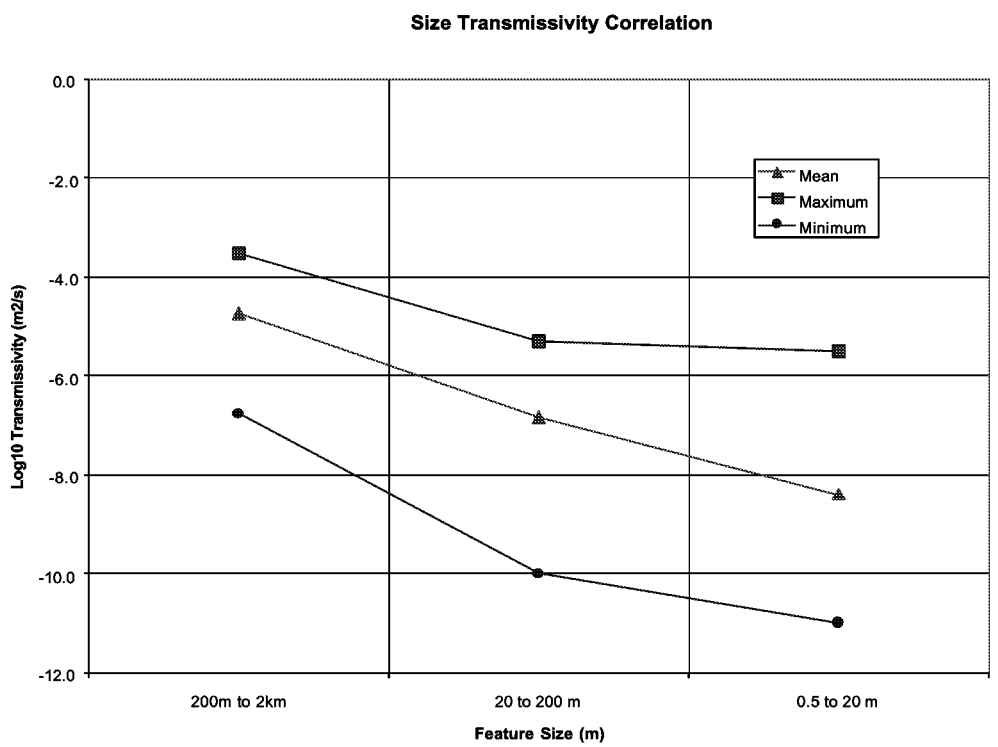

Figure 3-55 Size Transmissitivity Relationship at Äspö Sweden

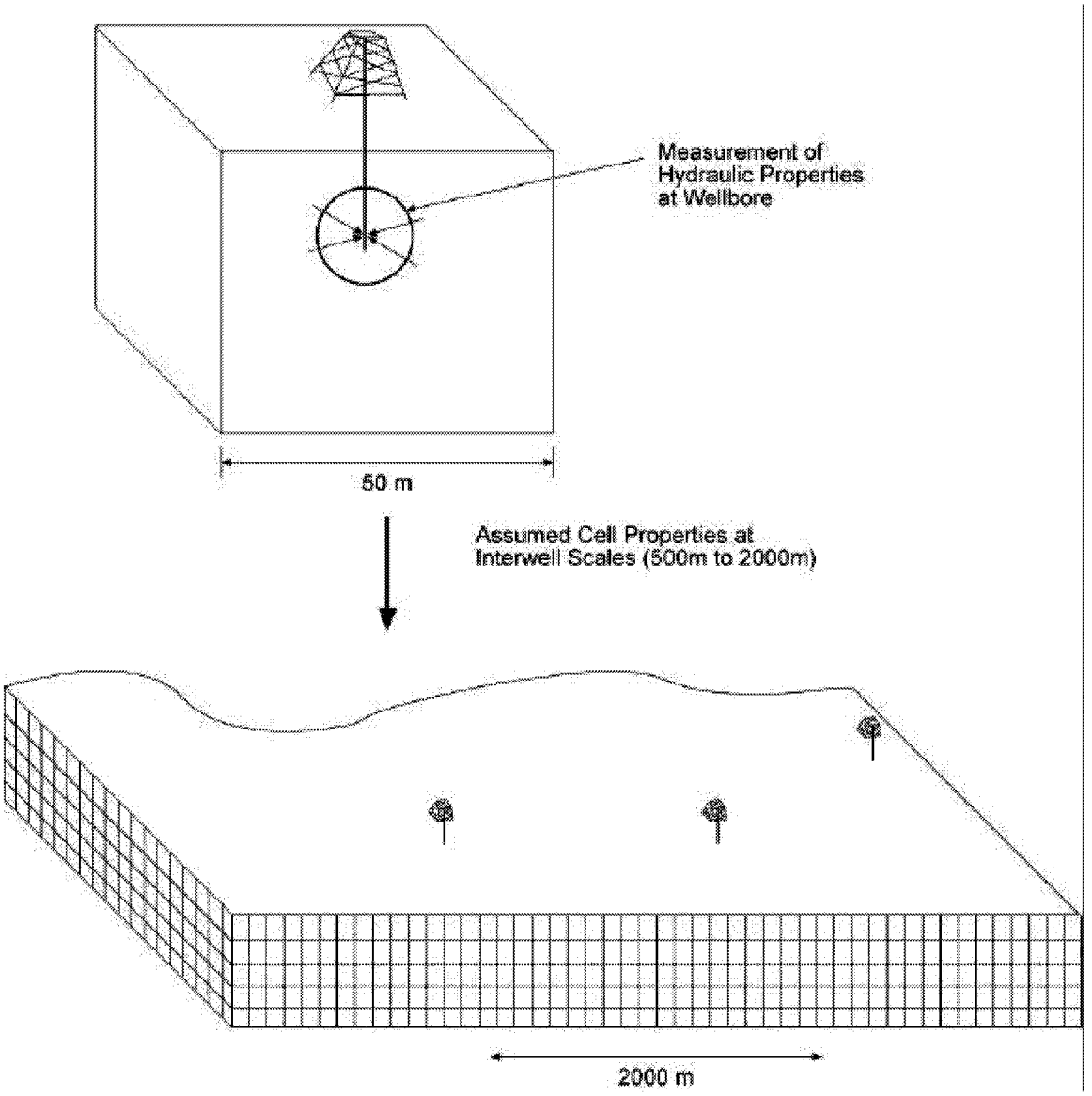

Figure 3-56 Data Scaling for Continuum Approaches

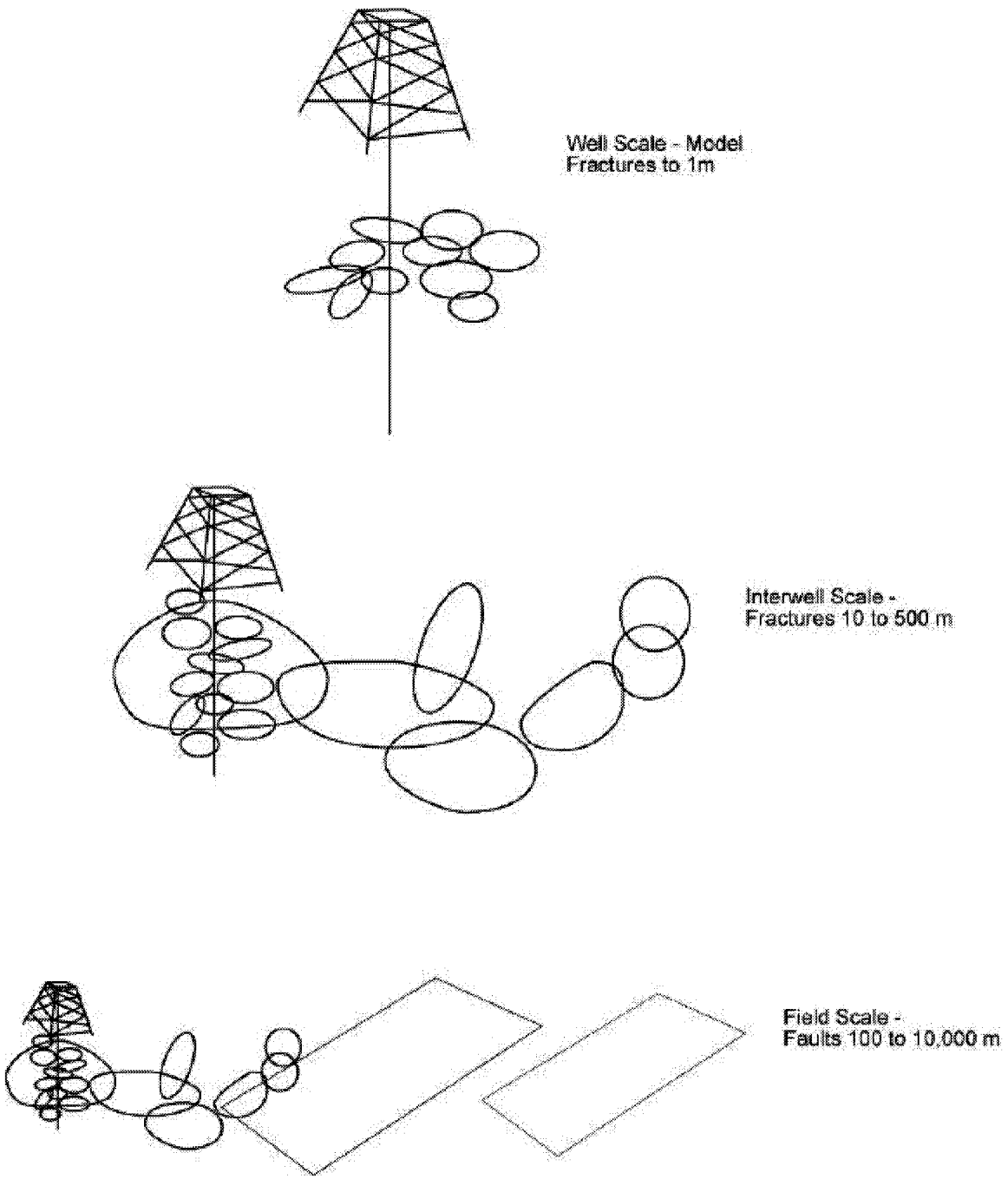

Figure 3-57 Multiscale Modeling with Discrete Fracture Networks

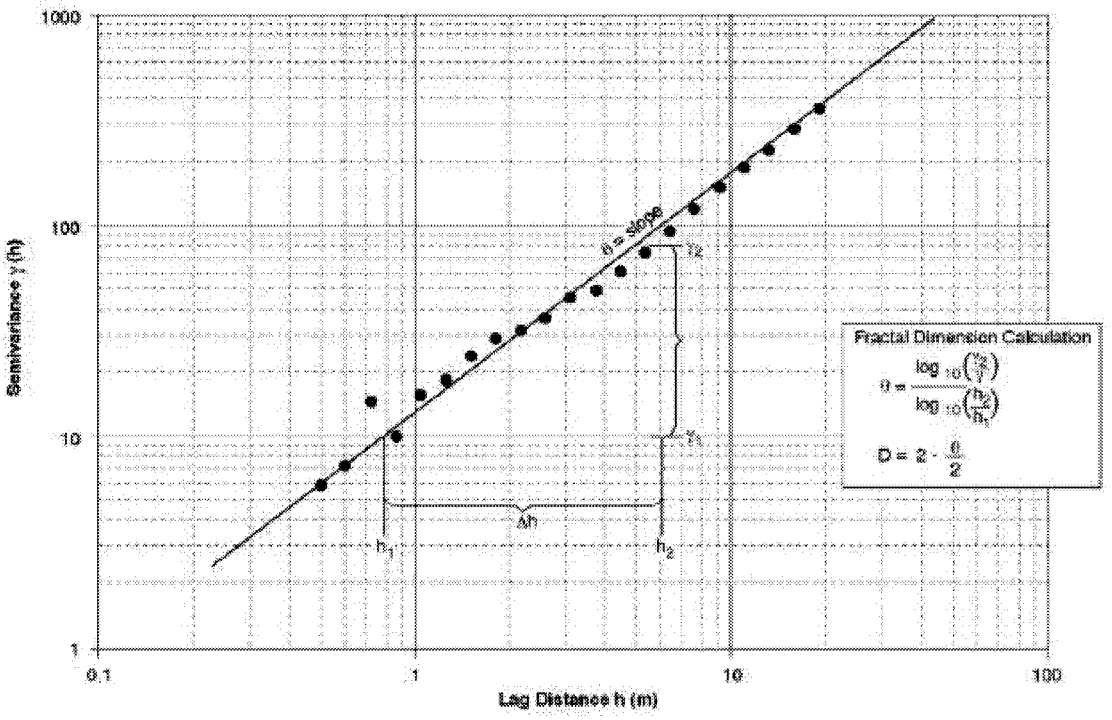

Figure 3-58 Fractal Dimension Calculation

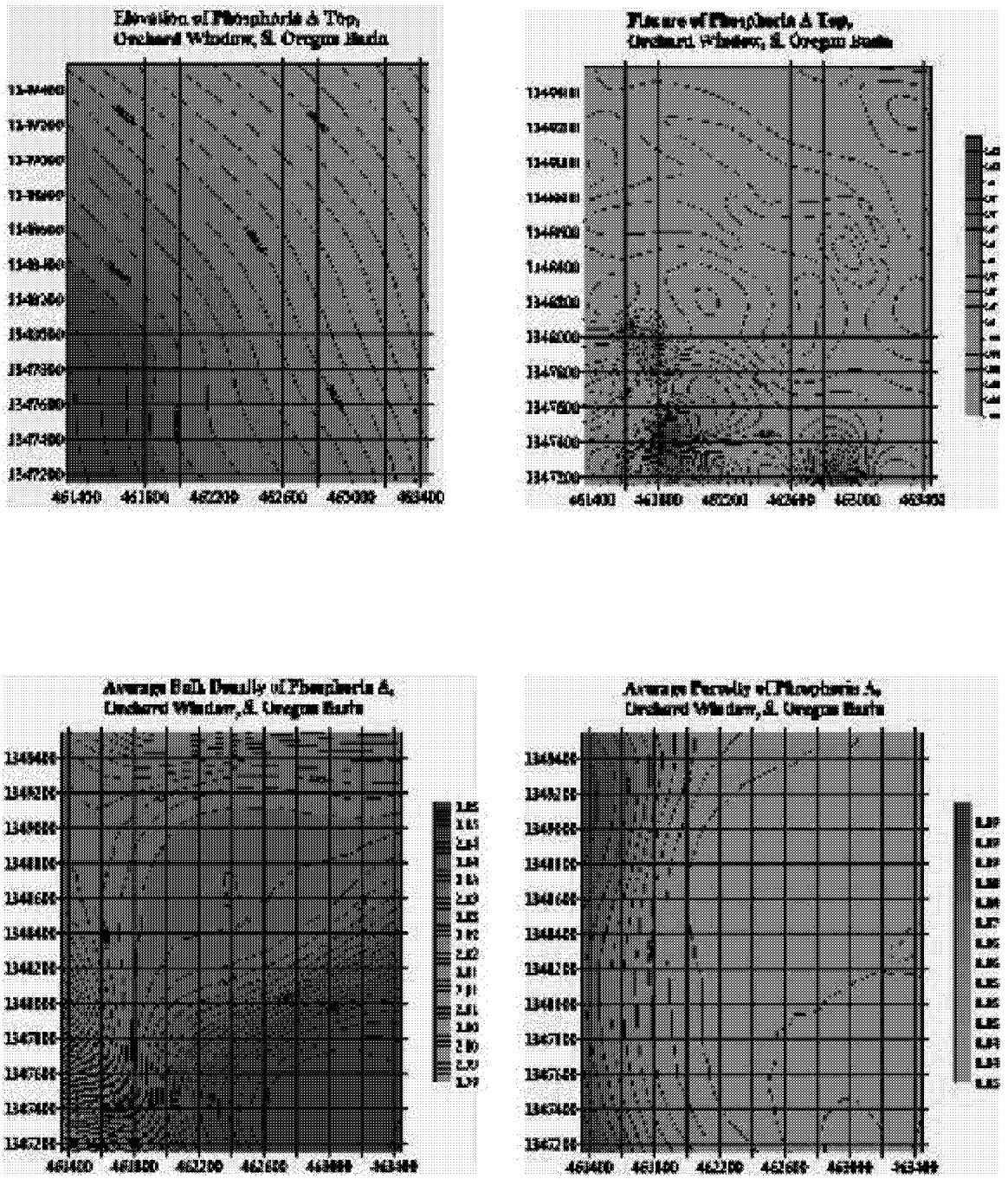

Figure 3-59 Example Strata model Data from South Oregon Basin

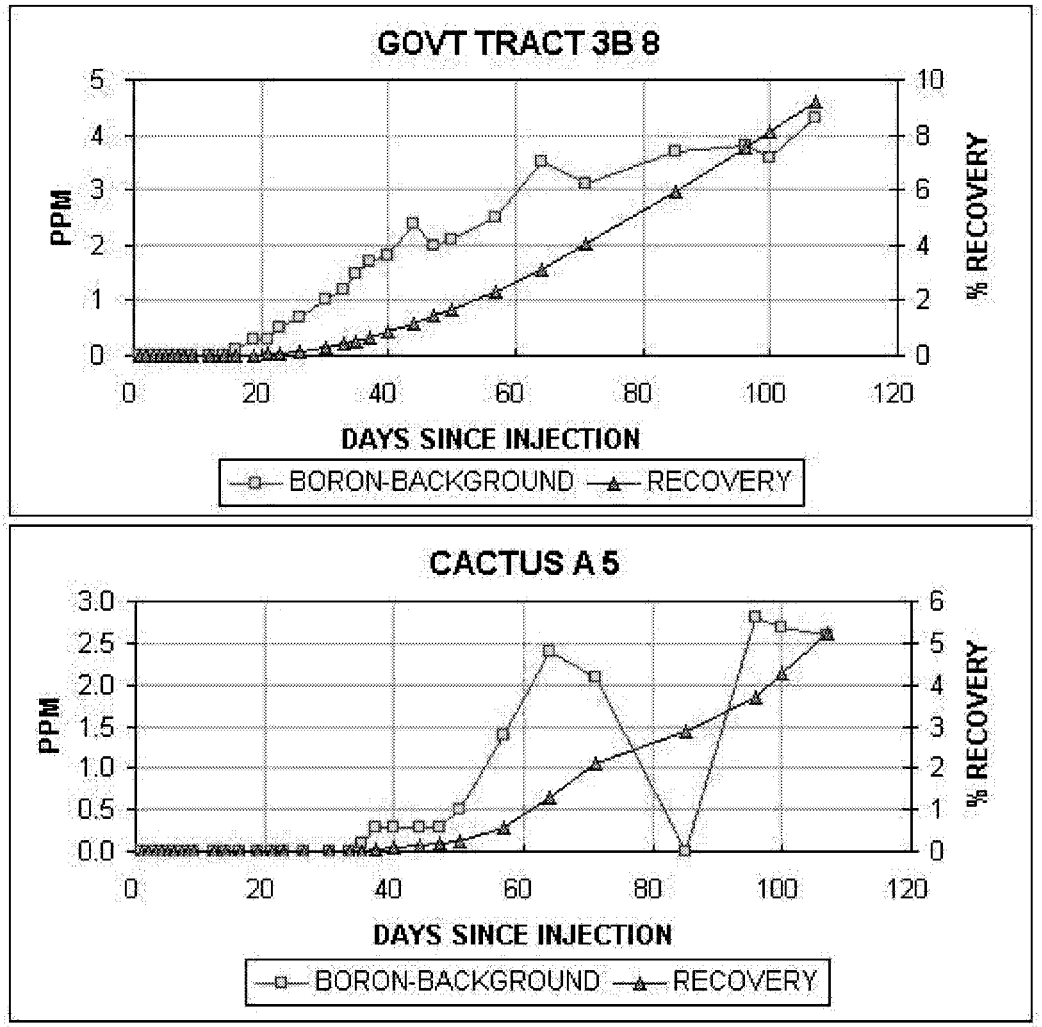

Figure 3-60 Example Tracer Breakthrough Curves from North Oregon Basin

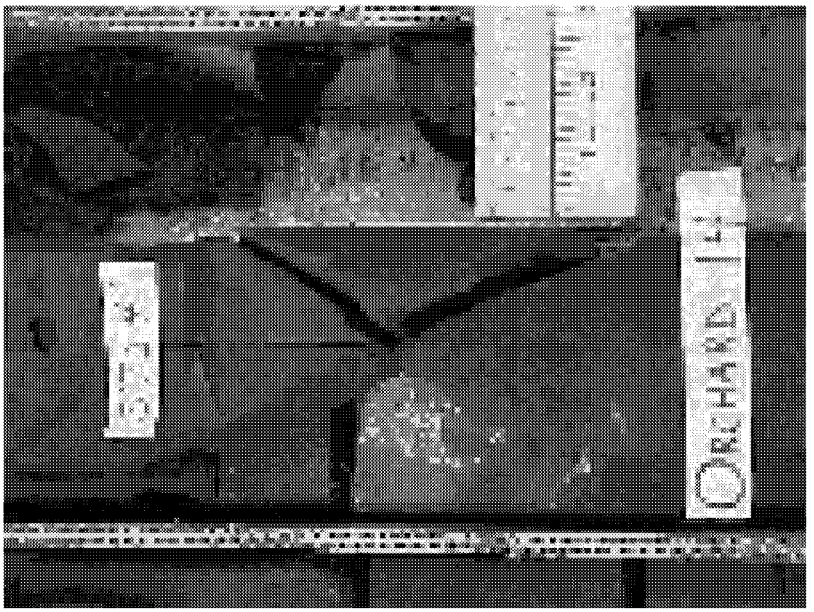

Figure 3-61 Cone Photos from Orchard 14, North Oregon Basin

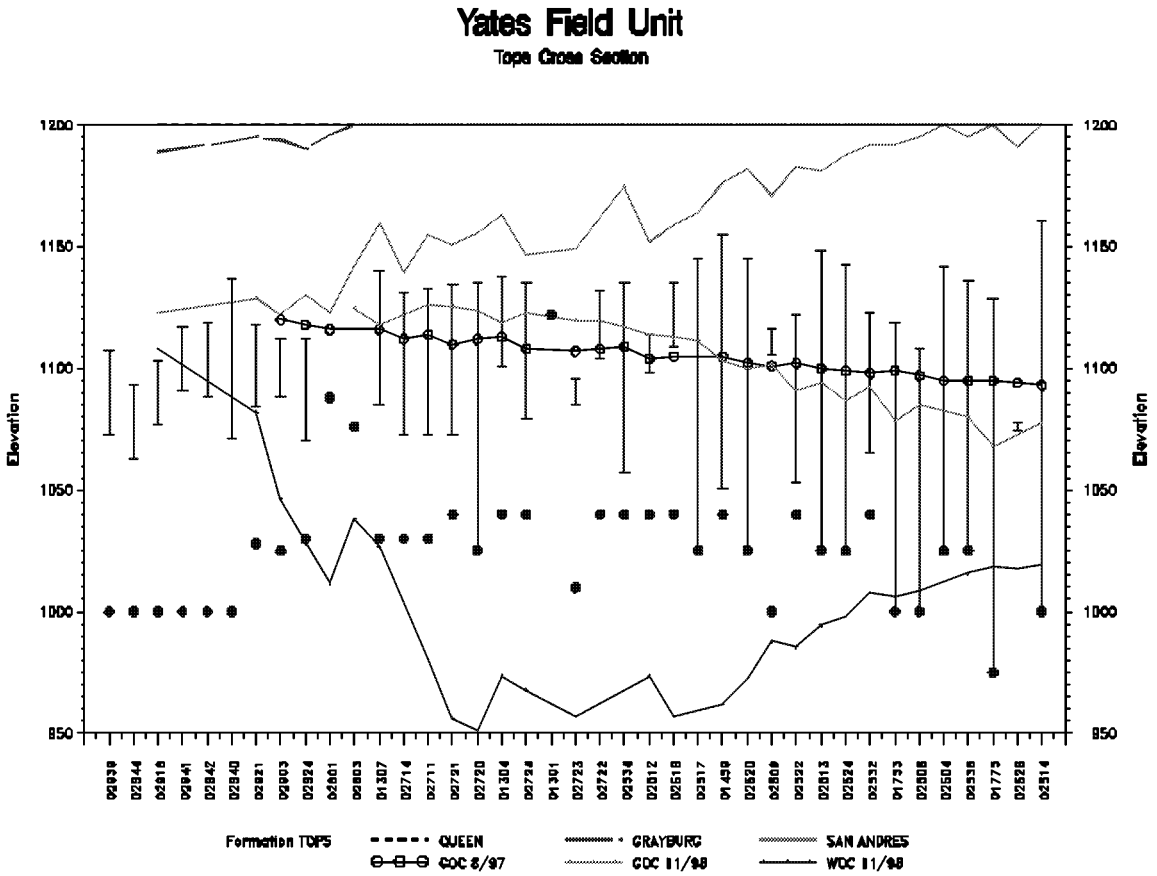

Figure 3-62 Yates Tops Cross Section

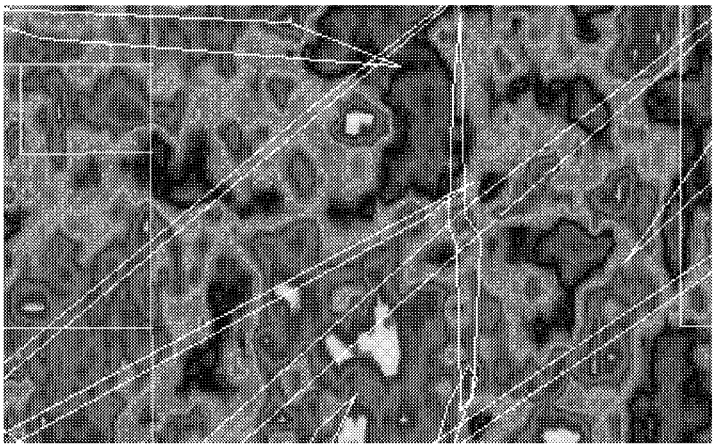

Figure 3-63 South Oregon Basin Seismic Lineaments

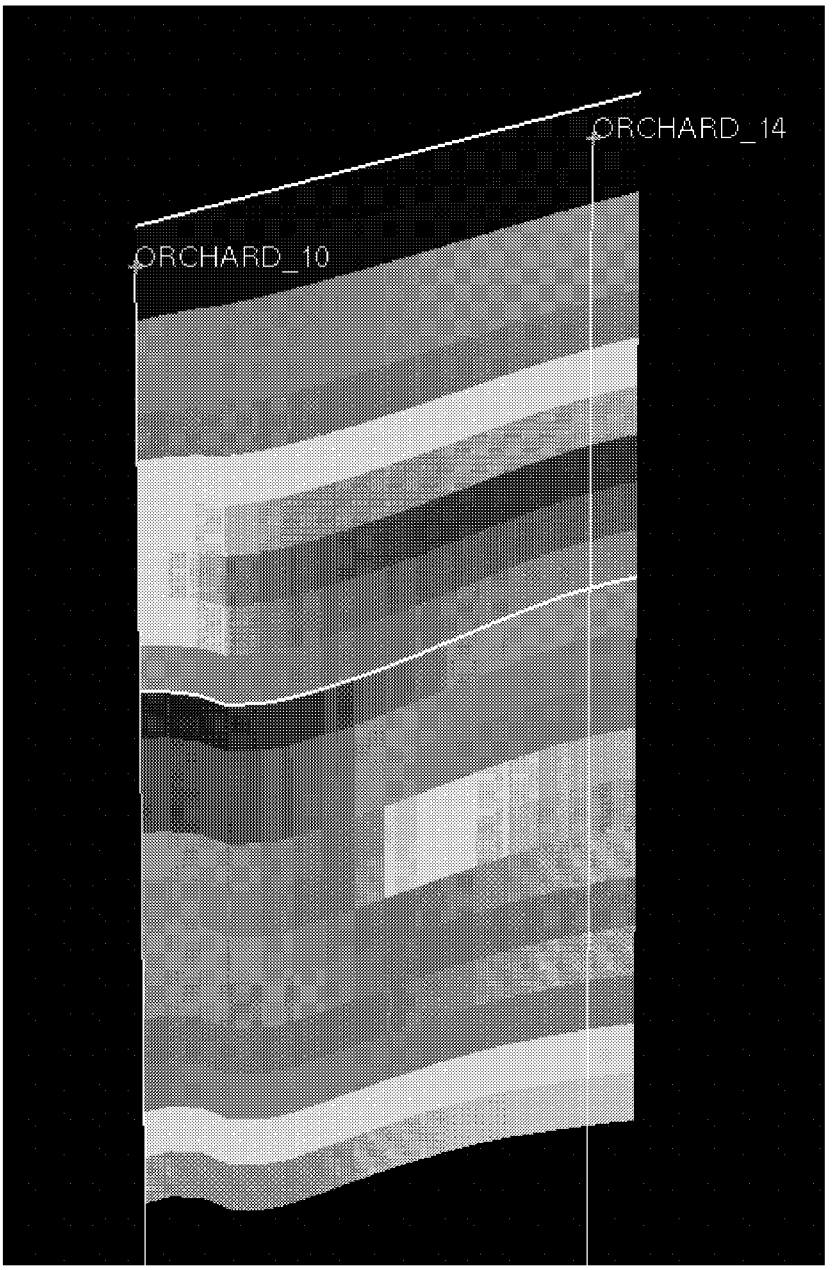

Figure 3-64 South Basin Geocellular ModelExample

3.2.7.1 Multiscale Modeling

Assuming a conductive fracture intensity P_{32} of 0.1 m^2/m^3, and a mean fracture area A_f of 10 m^2, the average 10 km x 10 km x 1 km reservoir volume V_r has on the order of 1 million conductive fractures.

$N_f = P_{32} V_r / A_f = 10^6$ fractures.

This number of fractures is well within the capabilities of DFN modeling software, which can currently handle on the order of 16 million fractures in production simulations. As a result, DFN models at the 10 km scale can directly incorporate fractures from the kilometer scale down to the meter scale throughout the reservoir model region. As a result, multiple scales of behavior can be modeled down to a 1 m scale features, even for models of 10 km scale. In contrast, continuum models at this scale would generally use cells of 50 to 200 m scale, requiring upscaling of well responses to obtain effective 50 to 200 m scale cell properties.

For larger scale models of 100 km x 100 km x 1 km, the number of fractures would increase correspondingly to 10^8, which does exceed current modeling capabilities and require some form of simplification. In addition 10^6 fractures is near the limit for single phase flow simulation, and significantly beyond the limit for multiphase flow simulation.

As a result, multiscale DFN modeling is frequently simplified by modeling only the fractures of concern at each scale. So, for the 100 km scale model, large scale flow would be influenced primarily by features of over 200 m. Within 100 m from each well, however, it is necessary to model fractures down to the meter or at least 10 m scale.

The strategy developed for multiscale DFN modeling is therefore as follows:

1. Establish the practical limit on the number of fractures to be modeled:
   - 2×10^7 for geometric simulations
   - 10^5 to 10^6 for single phase flow
   - 10^3 to 10^4 for multiphase flow
2. Determine the minimum fracture size (radius) necessary at each of the model scales
   - 1 to 10 m fracture radius near wells
   - 10 to 100 m fracture radius for the region between wells
   - 100 to 200 m fracture radius for the full reservoir volume
3. Determine the number of fractures which would be modeled in each of the model sub-regions, truncating the fracture populations by different minimum radius at each scale,
   $N_{total} = N_{well} + N_{interwell} + N_{reservoir}$
4. Adjust the model regions and cutoff sizes to be compatible with computational constraints
5. Implement the model
6. Carry out sensitivity studies to determine the influence of the fractures left out of the model for computational reasons, and make appropriate adjustments to fracture and rock matrix properties to account for these simplifications

Using this procedure, multiscale DFN modeling makes it possible to model the features of concern at each scale, without the need for upscaling approximations. Indeed, the level of detail in the DFN model can be as low as one meter, even for 100 km scale reservoir simulations. The level of error due to this multi-scale modeling procedure depends on the severity of the limitation of the number of fractures to be modeled, and the amount of the total permeability and porosity removed from the model. In general, this can be quantified by sensitivity simulations, and the

necessary permeability and porosity can be replaced to the model either by increasing effective matrix block properties, or by increasing the permeability and aperture of the fractures remaining in the model.

3.2.7.2 Data Scaling for Equivalent Continuum Modeling

There are two fundamental approaches for use of the DFN approach in data scaling for equivalent continuum models. In the first approach (Oda, 1994); Long (1983)) independent DFN models are developed for each grid cell, and these grid cell anisotropic permeabilities are then used directly in the EPM modeling. This approach is only accurate provided the gridding of the EPM model is of a scale significantly finer than the connectivity of the DFN model (Lapointe, 1995). Otherwise, the differences in connectivity between the DFN model and the corresponding EPM model will be severe. As a result, it is essential to carry out this type of data scaling at several levels of discretization to ensure that the resulting EPM model does not suffer from errors in connectivity.

The second approach recognizes the importance of connectivity as well as conductivity in DFN models. In this approach (Dershowitz et al., 1999), the connectivity of grid cells is calculated based on the DFN model, together with grid cell permeability tensors. This can be achieved either by providing explicit connections within the EPM model as in the "non-neighbor connections" feature of ECLIPSE (ECL, 1997), or by gridding the EPM model to accommodate the DFN features at scales important to the model (Svensson, 2000).

3.2.7.3 Data Scaling for Discrete Feature Network Modeling.

Oil reservoir fracture data are collected at two primary scales: the 0.1 meter well scale, and the 100 to 1000 meter geophysical and geological lineament scale. Occasionally trace map data is obtained at the 1 to 100 m scales. Data on fractures at different scales comes from data sets that best detect fractures over much narrower size ranges. For example, a lineament data based on air photos may not reliably detect fractures on the scale of hundreds of meters, while an outcrop study may only capture fractures on the scale of meters.

The key question in creating the fractures for the numerical simulations over the entire scale range of interest is whether there is a single population of fractures that is being sampled at different scales, or whether there are in fact multiple populations. The manner in which the simulations are prepared differs depending on which option is selected. In addition, there is probably greater uncertainty surrounding the model if there are different fracture populations at different scales.

The process for evaluating this issue is to examine the number of fractures greater than or equal to a specific size based on all of the data from the different sources. Since each data set may pertain to a region with a different area, the number of fractures must be normalized for the amount of area.

The common way for carrying out this normalization is to divide the number of fractures by the area covered by the data set (for example, Casting et al., 1996). This type of area normalization is essentially Euclidean, since it assumes that if the data set area were doubled, the numbers of fractures would also double. However, it may not always be the case that the number of fractures per unit area is modeled accurately by a Euclidean scaling process. For example, if the number of fractures scales as a fractal process, then an assumption of Euclidean scaling will lead to incorrect

area normalization. Thus, it is important to first evaluate the spatial scaling properties of each fracture set prior to the area normalization.

The spatial scaling analysis for fractally distributed discrete features can be carried out by computing the mass dimension for the data set at each site that contained the smallest traces. Other data sets that only contained larger traces have a greater *mass defect*, that is, the amount of fractures not present in the data set because they are below resolution or reporting limits is greater. Thus, the smallest possible error due to mass defects will be for the data set at the smallest scale.

The *Mass Dimension* of the fracture traces is given by:

$$N(L) = CL^{D_m} \qquad \text{Equation 94}$$

where L is the measurement scale;
C is a constant;
D_m is the fractal mass dimension; and
$N(L)$ is the number of fracture traces at a measurement scale L.

If the spatial intensity of fracturing scales in a Euclidean manner, then the mass dimension will be equal to 2.0.

The parameters of this equation can be estimated by counting the number of fractures in a circle of radius R, for different values of R and different locations (centerpoints) of the circle. Figure 3-58 illustrates how the mass dimension was calculated for the four example locations. The number of fracture traces contained within circles of different radii and centered at random locations in the trace map were plotted as a function of radius. Since multiple centerpoints were used, there are differences in the number of fracture traces for circles of the same radius value. The parameters are calculated through nonlinear regression of this data cloud.

Once the parameters have been estimated in this fashion, Equation 94 is used to estimate the number of fractures that would be expected in different size areas. The 1:20 000 scale map from which the mass dimension was estimated constitutes the reference area – 400 km^2. The number of fractures for a larger area, for example, the 1:50 000 scale maps that cover an area of 2500 km^2, is estimated by first computing the radius of a circle that would have the same amount of area, and then putting this radius value into Equation 94. In this example, the radius would be 28.21 km. The increase in the number of fractures from the 1:20 000 scale map, covering 400 km^2, to the 1:50 000 scale map that covers the larger area is thus given by:

$$N(28.21\,km) / N(11.28\,km) \qquad \text{Equation 95}$$

The number of fractures greater than or equal to a given trace length in the 1:50 000 scale map are divided by this ratio.

If the correction is based on the smallest area of any of the data sets, then the impact of this correction will be to increase the number of fractures than would otherwise be calculated from a simple Euclidean scaling correction for data sets measured over a larger area. Since the greatest impact is for the largest areas, which in these data sets, corresponds to the larger trace length sets, the impact of this correction reduces the value of the trace length size exponent relative to a simple Euclidean scaling. In terms of the properties of the fracture size distribution that results, a

fractal scaling correction predicts a higher percentage of large fractures relative to small fractures than would the Euclidean correction.

3.2.8 Task 1.3.0 Heterogeneous Reservoir Interdisciplinary Database

In this task, the project team developed a large data base of geological, geophysical, and reservoir engineering data for the heterogeneous reservoir project study sites. This data was provided by Marathon Oil company, and is posted on the project web site, http://heteroil.golder.com. These data posted to the web site is summarized in Table 3-25. Examples of data provided for the database by Marathon Oil is provided in Figure 3-59 through Figure 3-67.

Table 3-25 Heterogeneous Reservoir Interdisciplinary Database

	Yates Field, West Texas	Stoney Point, Michigan	North Oregon Basin, WY	South Oregon Basin, WY
Geological Background	X	X	X	X
FMI Data	X		X	X
Core Data	X	X	X	
Outcrop	X		X	X
Seismic		X	X	X
Geocellular Model	X	X		X
Tracer Test Results			X	X
Interference Tests	X			X

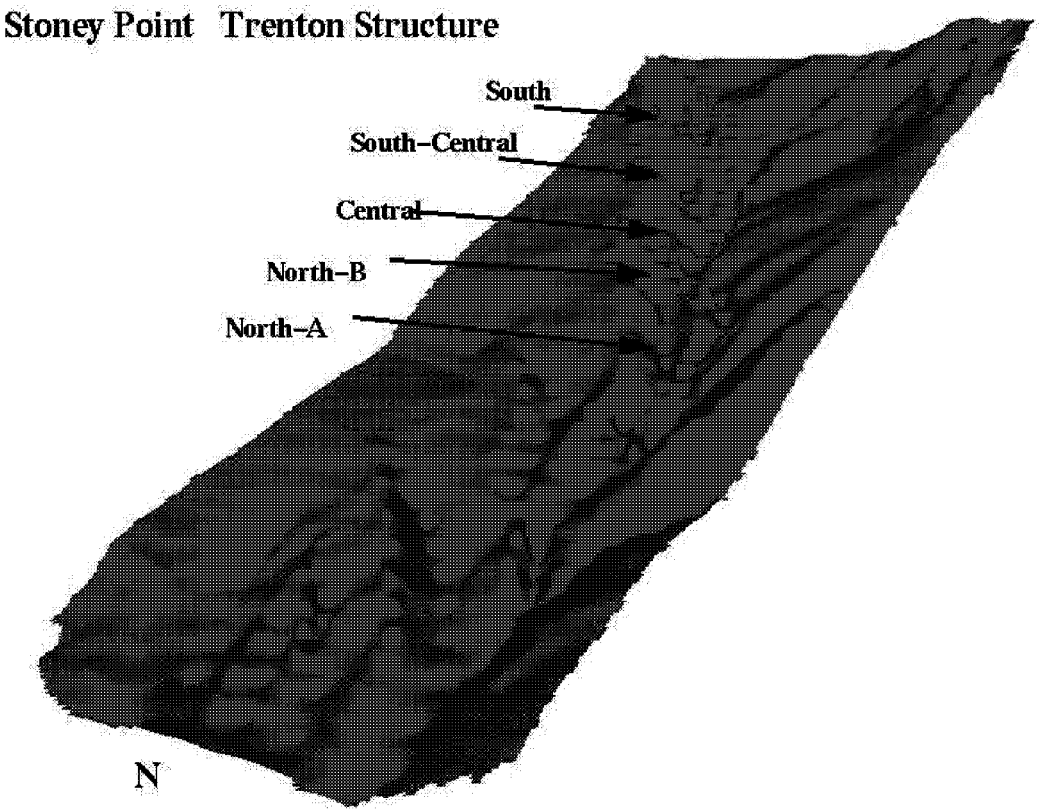

Figure 3-65: Stoney Point, Trenton Structure

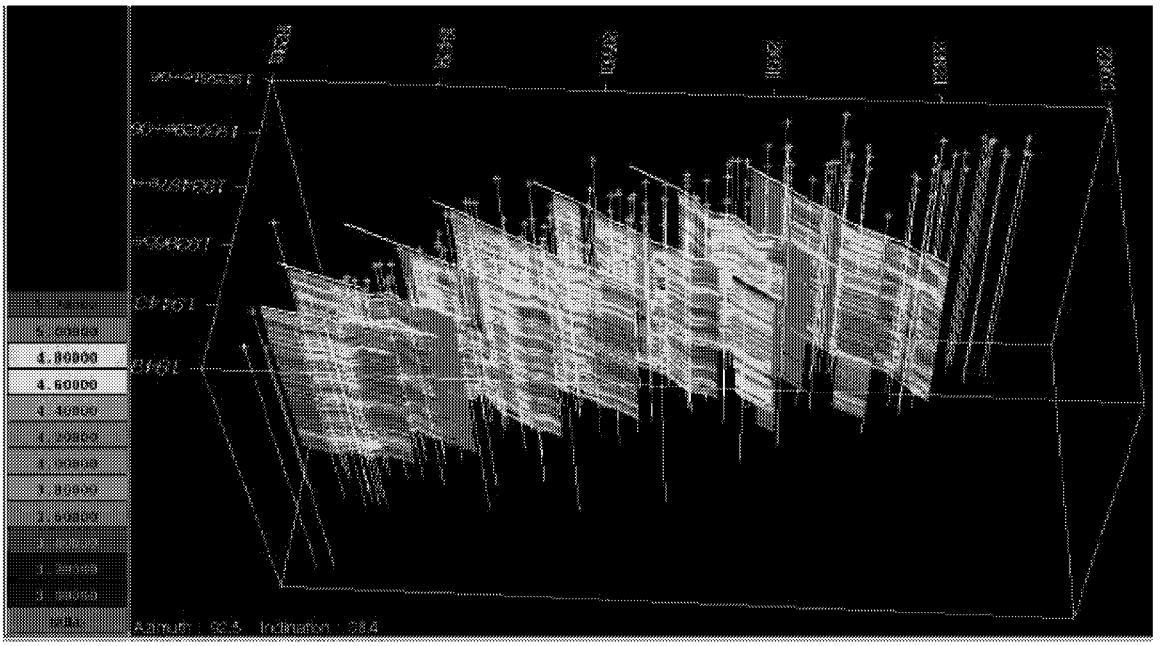

Figure 3-66: Stoney Point, Geophysical Cross Sections

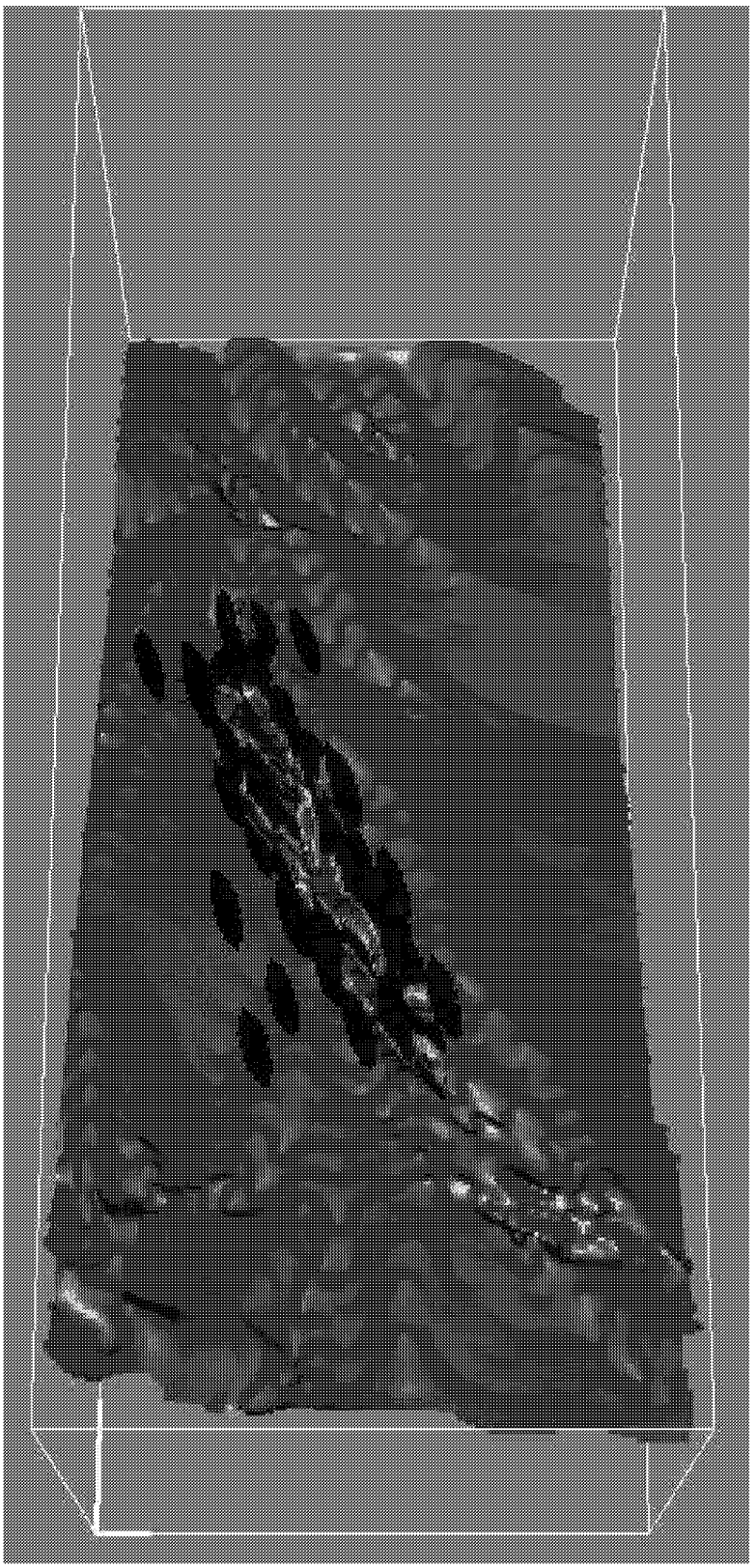

Figure 3-67: Stoney Point, Lost Circulation

3.3 Task 2: DFN Model Development

3.3.1 Task 2.1 DFN Model Approaches

The objective of this task is to document the DFN modeling approach by clearly describing each of the available DFN conceptual models, including pre-existing models and models developed specially for this project. There are three basic approaches to DFN modeling:

- Statistical Modeling, in which the spatial pattern is defined by stochastic processes
- Geocellular Modeling, in which the variation of parameter values in a three dimensional geocellular grid controls the fracture spatial pattern, and
- Geomechanical Modeling, in which fractures are generated based on geomechanical principles using fracture mechanics or approximate heuristics.

3.3.1.1 Statistical Models

The **Baecher model**(Baecher, Lanney and Einstein, 1978) was one of the first well-characterized discrete fracture models. In this model, the fracture centers are located uniformly in space, using a Poisson process and the fractures are generated as disks with a given radius and orientation. The enhanced Baecher model (Dershowitz et al, 1988) extended the Baecher model by providing a provision for fracture terminations and more general fracture shapes. The BART (Baecher Algorithm, Revised Terminations) model generalizes the Baecher model further by allowing termination modes which result in non-uniform fracture locations. The Enhanced Baecher and BART model utilize fracture shapes which are generated initially as polygons with three to sixteen sides. These polygons can be equilateral (aspect ratio of one) or elongate, with the aspect ratio (major to minor axis size and orientation).

In the Enhanced Baecher Model, termination is specified as termination probability P[T|I], the probability that a fracture will terminate at a pre-existing fracture, given that it intersects a fracture. In the Enhanced Baecher Model, all fractures are generated from center locations distributed uniformly in space. In the BART model, termination is assigned not by termination probability, but by termination percentage T%. In the BART model, 1-T% fractures are generated based upon uniformly located fracture centers. T% fractures terminating at intersections are then generated from locations uniformly located on the surfaces of existing fractures. These locations are not the fracture centers, but rather the location at which the fracture termination occurs.

Periodic Models are useful for describing regularly spaced or periodic fracture patterns. Periodic fractures may occur with a constant fracture spacing or a spacing distribution, which follows some other simple, deterministic function with stochastic variations. In periodic models, the fracture location is generated serially, with every fracture generated directly from the previous fracture based on a specified direction and spacing. This approach has been found to be particularly useful in carbonate and sandstone reservoirs.

The **"Nearest Neighbor"** model is a simple, non-stationary model in which fracture intensity varies with distance from specified features.

$P_{32}(x_i,y_i,z_i) = f(d_{ij})$

where d_{ij} is the distance of point from the selected features. The function $f(d_{ij})$ has been implemented using exponential and power functions (Dershowitz et al., 1998). The "Nearest Neighbor" model has been found to be useful in modeling fractures related to faults and folds and a number of sedimentary processes.

In the **Fractal Model** fractal patterns may be either "self-similar" (topologically identical at different scales) or "self-affine" (topologically similar but anisotropically distorted at different scale). Fractal fracture patterns can be generated in three ways:

- Utilize a recursive generation scheme which produces fracture patterns at one scale, then superposes them at different scales (with self-affine distortion if appropriate) to directly produce a fractal pattern;
- Generate fractures according to a process such as "Levy-Flight" which has been shown mathematically to produce fractal patterns; and
- Generate fractures using non-fractal processes, then test the resulting patterns to determine whether the resulting pattern is fractal.

The Levy-Lee fractal fracture model utilizes the second of the above approaches and is based upon "Levy Flight" (Mandelbrot, 1985). The Levy Flight process is a type of random walk, for which the length L of each step is given by the probability function of D, the fractal mass dimension of the point field of fracture centers and Ls, the distance from one fracture to the next for the previous step in the generation sequence. For D=0, the distribution of the step length is uniform, such that there is no clustering or heterogeneity. For large D, there is a very low probability of large steps and therefore fractures are formed close to each other in concentrated clusters.

The Levy-Lee fractal model requires derivation of a dimension D for the three-dimensional process of fracture centers from the two-dimensional pattern of fracture traces. Dershowitz et al. (1988) present a derivation to convert the fractal mass dimension of points on a plane to the dimension of points in three-dimensional space required for fracture generation. This derivation indicates that the three-dimensional fractal process should be generated using a fractal dimension one greater that the dimension calculated for the two-dimensional trace plane.

For this analysis, it might be tempting to utilize the fractal box counting dimension calculated for the Enhanced Baecher model. However, the box fractal statistic calculated as part of the Baecher analysis is only applicable to patterns which are "self-similar", which means that the patterns are topologically identical at different scales. Many fracture patterns are "self-affine" rather than "self-similar", since they are topologically similar, but undergo an anisotropic distortion with scale.

The **3D Box Fractal Model** is a simple method used to generate a self-similar three-dimensional discrete fracture simulation. It is used only to create a simulation in which the fracture intensity scales in a self-similar, isotropic manner. The FracWorks implementation of this method requires the user to provide a value for the Box fractal dimension, which will be a real number between 0.0 and 3.0. The generation region is divided into an assemblage of grid cells. Each grid cell is assumed to be a cube with an edge length equal to 1/64 of the generation region edge length. The algorithm conceptually implements the following procedure, although in practice, some properties of the recursive nature of the described process have been exploited to greatly speed up the algorithm.

In the initial stage, the generation region is idealized as a box of dimension 1.0 by 1.0 by 1.0. Next, each edge of the box is divided into two, so that there are now 8 sub-cubes comprising the original box. From the specified fractal box dimension Db, we can compute the number of boxes that contain one or more fractures.

As the size becomes smaller, the number of filled boxes increases. If every box contained one or more fractures at every box size, then Db would be equal to 3.0. This is the largest possible value for the fractal dimension. For values less than 3.0, not all of the boxes will necessarily contain fractures at all levels of box discretization.

Because of the recursive nature of the algorithm, the location of these filled boxes is not random. As a result, the number of filled boxes at any level of aggregation conforms to a power law and is fractal. Fractures are generated only in those 6208 boxes designated as filled until the global fracture intensity P_{32} is reached.

The **Geostatistical Variogram Method** varies fracture intensity and other properties according to a geostatistical variogram (Journel and Huijbregts, 1978). The variogram is a function, which relates the similarity of values at different locations to the distance *h* between those locations. Geostatistical semivariograms are defined by function $\gamma(h|a,C)$where h is the lag distance, a is the range or correlation length, C is the sill, and $\gamma(h)$ is the semivariance. Semivariograms may be either exponential, spherical, Gaussian, power-law (fractal), null, or deWijs. Geostatistical models generally require stationarity – that is, the expected value and variance (standard deviation) of the variable being modeled must be independent of its location, or at least any trend must be separated out and dealt with outside of the geostatistical algorithm.

Geostatistical models are implemented by calculating the variogram from available data. The spatial pattern can then be generated from the variogram definition using an algorithm such as Turning Bands (Journel, 1974).

The **Fractal POCS algorithm** (Projection On Convex Sets) is a general procedure for generation of stochastic fields according to constraints such as spatial correlation which can be represented mathematically as convex sets (Malinverno and Rossi, 1994). The constraints are enforced on the interpolation by projecting these convex sets in an interative fashion. Five constraints are imposed in the generation of POCS stochastic fields of fracture centers or surface points: 1. Known data is honored. This is known as Set P, for "Point". The constraint is that the final data set will have values F(xi, yi, zi) at points i = 1 to N. In this way, the final simulation matches observations on trace planes or in wells. 2. Self-affine spatial correlation is honored. This is known as Set S, for "Spectrum". The way in which this constraint is applied involves mathematical operations on the amplitude of Fourier spectrum of the data. 3. The mean value of the data is preserved. This is known as Set M, for "Mean." 4. The values of the data set are bounded. This is known as Set B, for "Bounded." For example, it is not meaningful to have negative fracture intensity or transmissivity. 5. The energy of the data is preserved. This is known as Set E, for "Energy". Energy in this context is defined as the sum of the value-squared at all points.

In order to create a POCS stochastic field of fracture intensities, it is necessary for the user only to specify constraints (1) and (2). The algorithm automatically computes the mean value of the data used in constraint (1) and also the energy of the data used for constraint (1). The algorithm then conditions the spectrum for constraint (2) based upon a parameter, termed, derived from a spectral density plot of the known data points and from an anisotropy function describing the relative strengths of spatial correlation in three orthogonal directions. The factor is linearly related to the fractal dimension, D. The fractal dimension of a self-affine process relates to according to

a relation defined in terms of fractal dimension Ds, Euclidean dimension E, sometimes represented by the variable n, which is the exponent of the corresponding one-dimensional power spectral density.

The parameter has been the source of much confusion in the literature (for example, see Goff, 1990 and Huang and Turcotte, 1990). A one-dimensional self-affine process has a power spectrum proportional to f-b, where f is the frequency. An n-dimensional process has a power spectrum proportional to f 1-b-n (Huang and Turcotte, 1990). The fractal dimension, for 1-, 2- and 3-dimensional processes are given in Table 3-26.

Table 3-26 POC Dimensions

E	Ds	b Range	Ds Range
1	(5-b)/2	[1-3]	[1-2]
2	(8-b)/2	[2-4]	[2-3]
3	11-b)/2	[3-5]	[3-4]

The POCS algorithm requires the user to provide values for anisotropy parameters Ax, Ay, and Az. Only the relative magnitudes are important, although the values must be positive. Negative or zero values make no physical sense and produce a warning message. The program also produces warning messages if the value of D specified is not within the range[3.0 - 4.0]. Although the factor and not the fractal dimension, is used internally to control the spatial correlation structure, the program computes this from the user-specified value of D.

The impact of anisotropy for any simulation depends upon the fractal dimension and the constraint data. For low fractal dimensions, the simulation becomes more obviously layered at lower anisotropy ratios. Also, if the constraint data has inherent larger-scale anisotropy, then the layering will become more readily apparent at both higher value of fractal dimension and lower anisotropy ratios.

3.3.1.2 Geocellular Models

Stochastic process, geostatistical, and fracture models attempt to apply a single, unifying set of simple parameters to describe the three dimensional pattern of discrete features within a statistically homogeneous region. In contrast, Geocellular models are based on the assumption that the underlying spatial pattern parameters change in space, such that different sets of parameters are required at every point in space. This is particularly attractive when there is a geological or stratigraphic model to provide the basis for DFN modeling.

In statistical approaches models such as the Baecher model, the probability of fracture centers is equal at each point in space. However, there are not fractures at every point in space - rather the intensity varies continuously from locations containing many fractures to locations with none. Expressing this as a geocellular model, each cell might be assigned a set of parameters expressing:

- the number of fractures,
- the percentage of the fractures within the cell which continue to neighboring cells,
- the orientation distribution of the fractures ,
- the distributions and correlations of geometric, hydraulic, and mechanical properties ,
- the percentage of the fracture terminations which are terminations at intersections.

In this way, the exact same model generated using the Baecher or Bart approach could be generated using a detailed geocellular approach. However, the amount of data necessary to achieve the same model through a geocellular approach is significantly greater than that needed in the Baecher model. In addition, while the actual fracture model varies continuously in space, the geocellular model varies by steps given by the grid refinement of the geocellular model. With coarse grids, the results might not be as good as could have been achieved using the standard Baecher model.

3.3.1.2.1 Fracture Generation

Fracture generation from geocellular models has two stages. In the first stage, the model must chose which cell to generate the fracture from, and the second stage is to chose the parameters of fracture generation based on the values found in the cell.

The cell selected for fracture generation is generally based on a "potential field" describing the relative likelihood of fracture generation from each cell. This potential can be expressed statistically based on the relative intensity in each cell, or it can be based on the location of previously generated fractures, as in the nearest neighbor and Levy-Lee models. The fracture generation "potential field" represents the probability that a fracture will be generated in a given cell, relative to the likelihood of other cells.

Once the cell is selected, the fracture geometric, hydraulic, and mechanical properties need to be assigned. For each parameter, which is not assigned in the cell, the parameters can be obtained from the defaults for the fracture set. For example, the fracture size might be assigned from the set size distribution. For parameter values assigned on a cell-by-cell basis, the fracture parameters can be set from values or distribution parameters for the cell. For example, the fracture orientation might be obtained from distribution parameters stored in the cell.

3.3.1.2.2 Geocellular Grid Preparation

The most common approach for preparation of a geocellular grid is to start with an existing three-dimensional geocellular model such as StrataModel, GeoFrame, EarthVision, ARC/Info, or EVS. In these models, every point in space is assigned to a cell. The cells in turn have spatial volume coordinates, and one or more properties. Each of these cell properties can then be linked to the fracture generation parameters of intensity, orientation, size, etc, and the fracture hydraulic or mechanical properties.

3.3.1.2.3 Potential Fields

Potential fields for fracture generation are used to determine the percentage of fractures, which are generated in each cell. Potential fields are defined for each set separately, and can be based on:

- rock type, where different rock types have different fracture intensities,
- geophysically derived fracture porosity, where greater porosity presumably implies greater fracture intensity,
- structural curvature, bed thickness, and other geometric properties of the stratigraphic model,
- geometry and intensity of fractures from previously generated sets, and
- calculated stress field.

Rock type is used to define fracture potential based on geological evidence, which indicates greater fracture intensity in particular rock types. Where only a few rock types with relatively large regions are involved, it is frequently preferable to define a generation region corresponding to each rock type, avoiding the use of more complex geocellular approaches.

Fracture Porosity information is commonly available from geophysical density measurements. Geophysical measurements provide total porosity. Fracture porosity is then calculated by subtracting the average rock porosity from the total porosity. Fracture porosity results from a combination of fracture size, intensity, and thickness. This needs to be taken into consideration when defining relative fracture potential based on porosity measurements.

Structural and Stratigraphic Geometry provide geologically based methods for defining fracture intensity. For example, certain sets have highest intensity close to faults, while other sets have highest intensity near the maximum curvature of folds. Similarly, some fractures have the highest intensity in thin beds, while others may have the highest intensity in beds dipping at a certain angle. For each of these cases, the fracture potential for each cell can be calculated by examining the structural and stratigraphic geometry in the vicinity of the cell.

Previous Fracture Sets clearly affect the geometry and occurrence of fractures in subsequent sets. Statistical approaches such as the "Nearest Neighbor" approach provide methods to generate fractures correlated to previously generated fractures. However, with the geocellular approach, rules can be used to generate fractures with any desired intensity relationship to previously generated fractures - with higher or lower densities near or far from particular sets, or particular sized or oriented fractures.

Stress Fields together with material properties control fracture occurrence and geometry. However, the actual stress field existing at the time of fracturing is rarely known, such that assumed stress fields based on numerical modeling or paleo-stress interpretations and interpolations must be used instead. When appropriate paleo-stress field information is encoded to the geocellular grids, this information can be used directly to generate fracture relative intensities using rules to relate the stress field to occurrence of fractures from particular sets.

3.3.1.2.4 Orientation Fields

Orientation fields describe the orientation (tangent), elongation, and curvature of fractures as they are generated. Orientation is generated in cells rather than larger "generation regions" when the orientation of particular sets varies in space. This is typically important where the orientation is defined relative to for example fold or fault surfaces or stratigraphic boundaries.

Specification of orientation fields is generally done by defining two vector directions, generally a pole and a transverse direction. The orientation for features generated in that cell can then be

defined relative to those vector directions. For example, the mean fracture pole might be defined as 45 degrees from the mean pole specified in the geocellular data.

The vector direction contained in the geocellular model is typically based on:

- structural curvature,
- bed thickness,
- position within structural features such as faults,
- orientation of fractures from previously generated sets, and
- calculated stress field.

Structural Curvature controls fracture orientation in two ways. First, fractures within structural members are frequently oriented relative to those features, rather than in absolute coordinates. Second, the fracture orientation can depend on the location within the structural feature. For example, tension fractures located near the top of synclinal folds, and conjugate shears located within fault zones.

Bed Thickness affects the occurrence of many fracture sets and therefore the orientation of fractures within the set. For example, in thin beds, fracturing may be restricted to orientations defined by the bed orientation, while through going fractures and fractures in thicker beds are oriented Thick fractures may have fractures oriented

Structural Position within stratigraphic layers also can influence fracture orientation, since different orientations can be preferred at different locations within a structural member. For example, the center of a particular stratum might contain fractures oriented according to a global mean pole, while fractures closer to the edge of the structure are increasingly controlled by the structural curvature...

Previous Fractures can influence fracture orientations in the same way as structural curvature and structural position. Fractures close to previously generated fractures may tend to have similar orientation, or conjugate orientations, or some other relationship.

Calculated Stress Field at different stages in time are particularly attractive for defining fracture orientations, since fractures are formed with respect to principal stress orientations: at $\pm(45-\phi/2)$ with respect to shear fractures, perpendicular to the minor principal stress for tensile fractures, and parallel to the major principal stress for compressive fractures (if such a thing exists). The key in this case is the availability of stress tensors describing the state of stress when the fractures were formed.

3.3.1.2.5 Size Fields

Fracture size for stochastic fractures is defined by a distribution of mean fracture equivalent radius. The size distribution can vary in space for much the same reasons that intensity and orientation vary. In particular, bedding thickness and stress fields can have significant influences on the local fracture size distribution parameters. Where this is the case, this can be dealt with by defining size distribution parameters on a cell by cell basis with a geocellular-based model.

3.3.1.3 Geomechanical Models

Geomechanically based DFN models are derived by simulating the physics of fracture propogation, fault movement, and other processes of structural geology. The geomechanical approach is attractive for a number of important reasons:

- the fracture patterns in geomechanically based models are constrained to be physically possible
- qualitative information on geological and stress history can be used to develop quantitative realizations for the fracture pattern
- quantitative information on rock mechanical properties can be used to support fracture realizations
- hypotheses concerning reservoir stress/strain history can be tested by comparing the measured fracture patterns against theoretical patterns based on principles of fracture generation and propagation
- spatial heterogeneity and non-stationarity in fracture geometry and properties can be defined in terms of the stress-strain history at different locations in the rock.

There are two basic approaches for geomechanical modeling: forward modeling, and reverse modeling. In forward modeling, initial mechanical conditions are assumed, and stress boundary conditions are applied. Fracture propagation is then simulated one fracture at a time, and each fracture is generated in a mechanical environment including the influence of pre-existing fractures. This approach has been developed over the last 20 years by Ingrafia (2000) and others. In the reverse modeling approach, a series of displacements, erosions, and strains is applied to reverse the process from the current deformed state to an original undeformed state. This process is referred to as "palenspastic reconstruction" (Midland Valley, 2000). Fractures can then be generated according to rules related to the stress-strain history for each location within the rock.

3.3.1.3.1 Geomechanical Forward Models

Geomechanical forward models simulate the process of fracture generation in continuous and discontinuous materials, using the principles of fracture propogation. The geomechanical forward modeling approach began with the idealized analytical solutions of Griffith (1921). The Griffith crack represents the propogation of a single idealized elliptical fracture in a simple tensional stress regime.

If all fractures were Griffith cracks, the development of three dimensional DFN models would only require an understanding of the stress history boundary conditions which formed those cracks. However, actual rock fracture formation is:

a) a combination of tension, shear, compression modes

b) occurs within rock materials which combine elastic, brittle, granular, and plastic behaviors

c) occurs in heterogeneous materials with distinct boundaries between zones, and

d) occurs within a complex stress field resulting from the interaction of multiple pre-existing fractures

e) is frequently subject to displacement or strain as well as stress boundary conditions

The combination of a) through e) above with the frequently complex stress history of fracture formation over geologic time makes forward modeling of fracture formation quite challenging. Until recently, forwarding modeling for generation of fracture patterns was not tractable. Over the past five years, fracture mechanics simulation has advanced to the point where it is possible to generate fracture patterns reflecting many combinations of a) through d) above.

Of particular interest is the work of Carter, Wawrzynek, and Ingraffea (2000) and the Rock Fracture Group at Cornell University. In their research, the boundary element method (BEM) code FRANC3D has been developed for arbitrary, non-planar, three dimensional fracture nucleation and propagation. FRANC3D is able to model propagation, interaction, and/or coalescence of multiple fractures, fracture propagation across material interfaces and intersecting fractures, and fracture bifurcation. FRANC3D can model fracture propogation for multiple, non-planar, arbitrary shaped fractures. For a given initial fracture geometry, FRANC3D calculates the 3D stress field to determine the stress intensity factors, and then extends the fractures along those "crack fronts." Because of this approach, FRANC3D can simulate realistic 3D fracture shapes, including en-echelon, curving, and stepping fractures. FRANC3D calculates "crack fronts" using elastic plane strain assumptions. FRANC3D is solved primarily using finite element methods, although boundary element formulations are also possible.

While FRANC3D is only above to handle a limited number of fractures at this time, it is possible to foresee the extension of these capabilities over the coming decade to generation of networks of thousands of fractures. At present, FRANC3D can be used to generate networks of tens of fractures. Even within this limitation, however, FRANC3D is useful to derive distributions for fracture size, fracture orientation, and fracture spatial distribution. In addition, FRANC3D simulations can provide the basis for extrapolation of fracture patterns using geocellular approaches by defining the correlations between cell locations and fracture geometric and mechanical properties.

FROCK is program similar to FRANC3D, developed by Chan and Einstein. (1991). FROCK uses a displacement discontinuity method (DDM) in which the boundaries of the continuum are discretized into small elements. The advantages of the DDM are that it only requires discretization at the boundaries of the continuum. FROCK calculates stresses around the "crack tip" and uses tensile and shear criteria to determine where fracture propagation should occur. The shape of the fracture propagation region is approximated as a cylinder with the center at the tip of the flaw, and with dimensions defined by the radius, ro, which depends on the material and on the loading mode. Tensile fractures are propagated in the direction perpendicular to the maximum tensile tangential stress, and when this stress reaches a critical value which is material dependent. Shear fractures are propagated in a direction in which the absolute value of the shear stress attains a maximum. It will propagate when the maximum shear stress reaches a critical value which is also material dependent. FROCK uses three parameters to describe fracture propagation:

- the critical tensile strength,
- the critical shear strength, and
- the radius of the assumed cylindrical fracture propogation region (assumed to be a function of the loading mode (uniaxial, biaxial compression, tension) as well as with the material.

FROCK has been verified against a variety of analytical solutions (Chan and Einstein, 1991). However, it is limited to two dimensions, and can therefore be used only to derive qualitative information about fracture spatial pattern, intensity, and orientation. in 3D.

Beyond computational constraints, the approach used by FRANC3D and FROCK is limited by the underlying assumption of small strain, elastic continuum mechanics. As a result, FRANC3D and FROCK can not be used to model fractures generated with respect to faults with throws of hundreds of meters or processes such as block rotation and kinematics.

The kinematic or particle mechanics approach (Potyondy, Cundall and Lee, 1996) avoids the small strain elastic assumption limitations inherent in continuum mechanics approaches such as those used by FRANC3D and FROCK. In the particle mechanics approach, the rock mass is represented as a set of particles with varying degrees of connection or bonding. Fractures and fracture propogation are represented as breakage of these bonds. Displacement and rotation within a particle mechanics model is limited only by kinematics. The particle mechanics approach has been implemented in the PFC3D (Potyondy, Cundall and Lee, 1996) and has also been implemented by Mühlhaus, Sakaguchi and Wei (1997) at CSIRO in Australia. Using the particle mechanics approach it is theoretically possible to generate fracture patterns with unlimited numbers of interacting fractures, obtaining spatial distributions of size, intensity, and orientation directly from the stress history and material properties. The primary limitation of particle mechanics codes is that they require the use of empirical parameters to describe the particles and bonds which are modeled – there is no direct relationship to measured rock properties. However, if a particle mechanics model can be calibrated to observed fracture patterns and assumed stress histories, that model could potentially be used to extrapolate the full three dimensional spatial distribution of fracturing. Particle mechanics codes can in theory model large displacements, rotations, and distortions.

Beyond purely mechanistic geomechanical models such as those described above are the empirical rule-based geomechanical fracture generators such as those of Swaby and Rawnsley, (1996) and Cacas (1999). In this approach, fractures are generated according to empirical rules which relate the fracture patterns to geocellularly or spatially defined "potential fields", and then generate the fractures relative to those "potential fields". For example, the Swaby and Rawnsley model uses the following empirical rules for fracture propagation:

- the probability that a fracture will grow into a particular cell is defined by an empirical "propagation potential" and "impedance potential" defined on a geocellular basis
- the direction and distance that the fracture will propagate given that it propagates in a given cell is given for that cell based on cell attributes
- fracture propagation is prevented in defined zones surrounding previously defined fractures based on stress relief assumptions
- cell attributes are updated based on the fractures existing at the end of a given time step

An example empirical geomechanical forward model from the Swaby and Rawnsley model is provided in Figure 3-77. Empirical geomechanical models have the potential to be extremely powerful fracture generators, capable of generating mechanically realistic patterns of hundreds of thousands of fractures for varying scales. The potential of the empirical geomechanical forward modeling approach is limited only by the ability to define reasonable empirical fracture propagation rules and implement them in a computationally efficient manner.

3.3.1.3.2 Geomechanical Reverse Models

Geomechanical Reverse Models, also referred to as "Palinspastic Reconstruction" Models reverse structural displacements, deformation, and rotations to return a known structural geology to an assumed original condition. Major development of the palinspastic approach is described in Suppe (1983, 1985, 1989), Suppe et al. (1990), and Mitra (1986, 1989, 1990).

The technology of palinspastic reconstruction is approximately twenty years old, and has matured to the point at which it is a commercially available technology. The two leading software packages for palinspastic reconstruction are 3Dmove by Midland Valley (Figure 3-78) and Geosec3D by Paradigm (Figure 3-79).

Since palinspastic reconstructions work from known structural geology, at a level of detail which includes measured or at least inferred displacements. Where the structural geology is known in detail, there is no need to implement stochastic or extrapolated structural models – the fracturing can be modeled as deterministic ! The primary use of these models is therefore to define the undetected structures which would be necessary to make the known structural deformations kinematically possible. As such, geomechanical modeling is a method for interpolation from known structures to the smaller or less readily detected features. It is also a method for verification of interpreted structural features and displacements, determining whether there is a series of structural events which could have produced the structural features as interpreted.

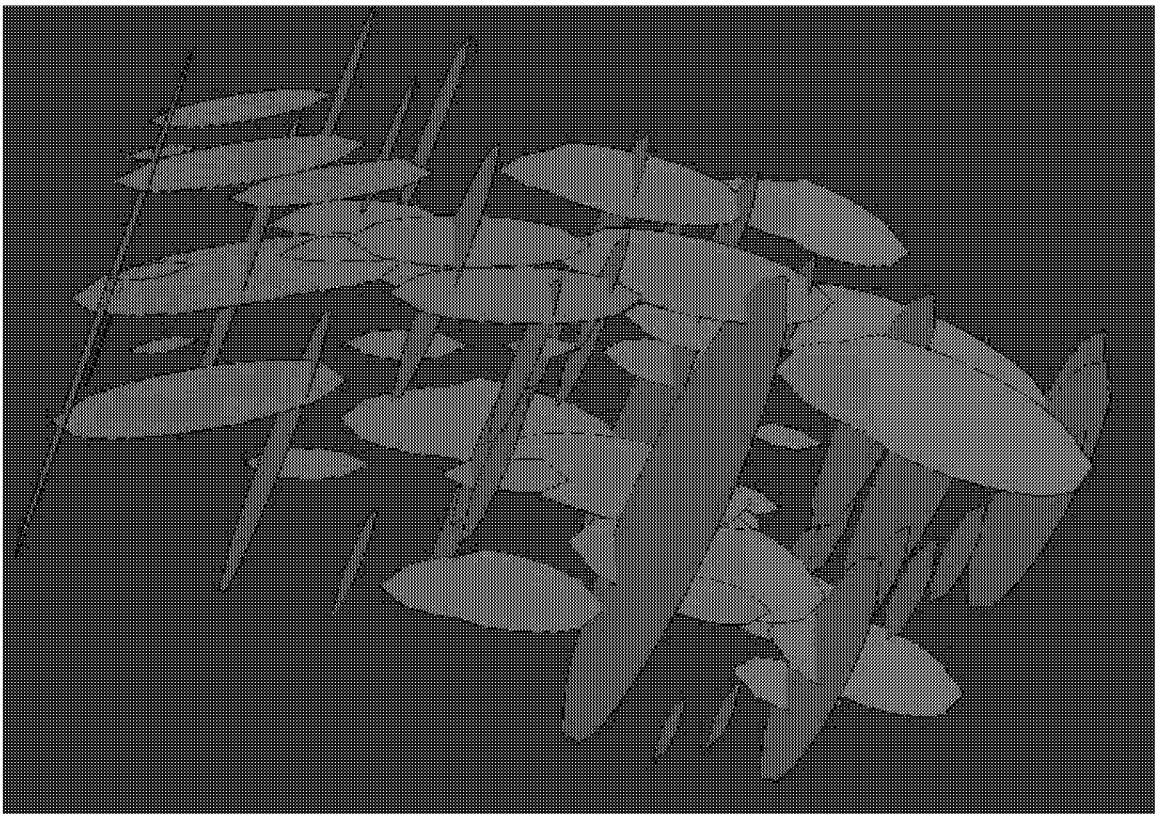

Figure 3-68 Fracture Growth Model (after Swaby and Rawnsly, 1996)

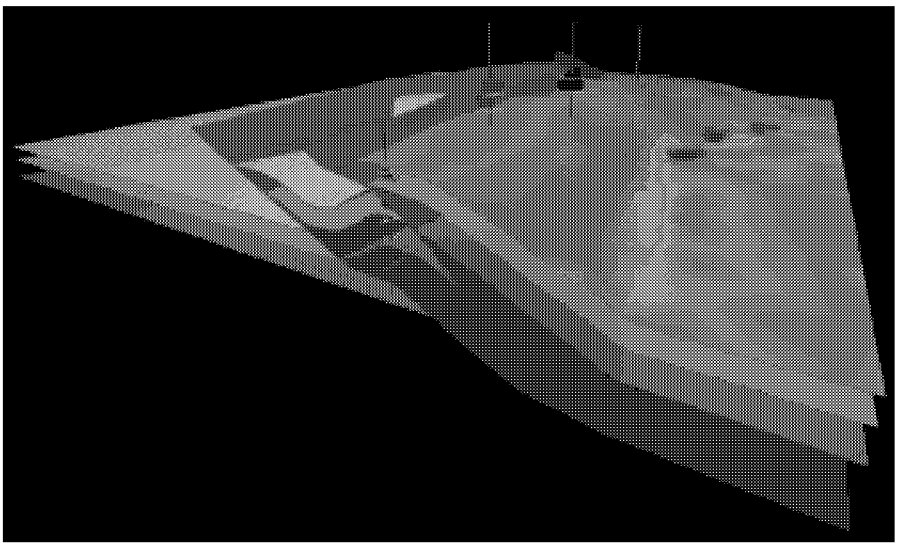

Figure 3-69 3Dmove Palinspastic Reconstruction (Midland Valley, 2001)

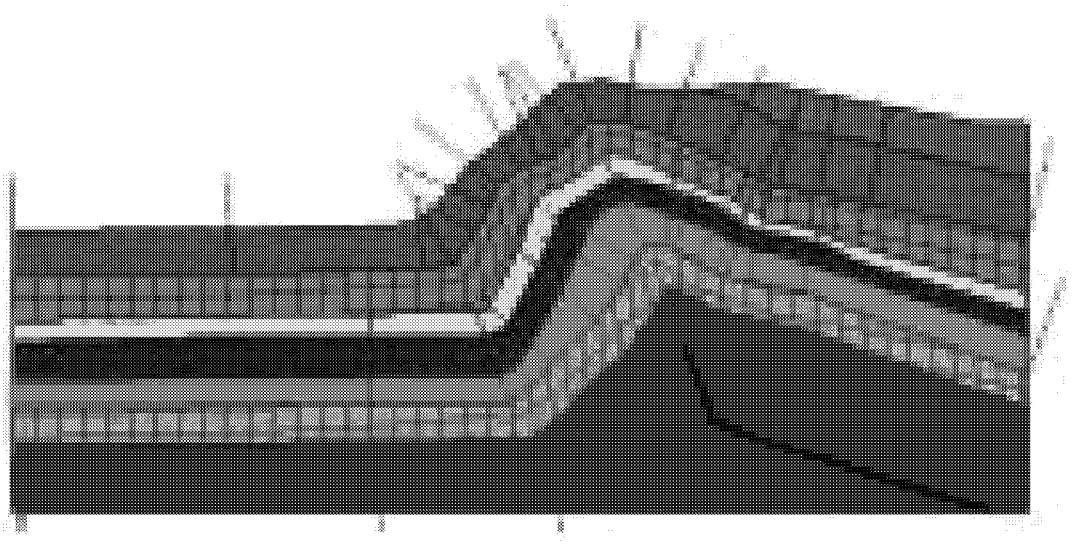

Figure 3-70 Goesec2D Palinspasic Reconstruction

Hermanson , J., LaPointe, and Eiben (2001) developed an approach to use palinspastic reconstruction to generate 3D discrete fracture networks. Palinspastic reconstruction models produce a series of strain fields for each stage of structural deformation (Figure 3-80). Each of these strain fields represents a combination of elastic strain within the rock mass, displacement on existing fractures, and formation of new fractures. Hermanson et al. (2001) use these strain fields to derive compatible or physically possible 3D fracture populations in terms of location, size, and orientation distributions (Figure 3-81).

3.3.2 Tasks 2.2, 2.3, and 2.4 Site DFN Model Development, Implementation, and Validation

In these tasks, preliminary DFN models were built for each of the project study sites. These models were subsequently superceded by models developed within Task 3 and Task 4, and are therefore not described here. For more information on the preliminary model versions, please refer to the progress reports listed in Table 2-1. Preliminary DFN models for the project study sites are illustrated in Figure 3-83 through Figure 3-85.

3.4 Task 3: Reservoir Improvement Strategy

In Task 3, the project team developed procedures to improve reservoir productivity and recovery, with specific applications to project study sites.

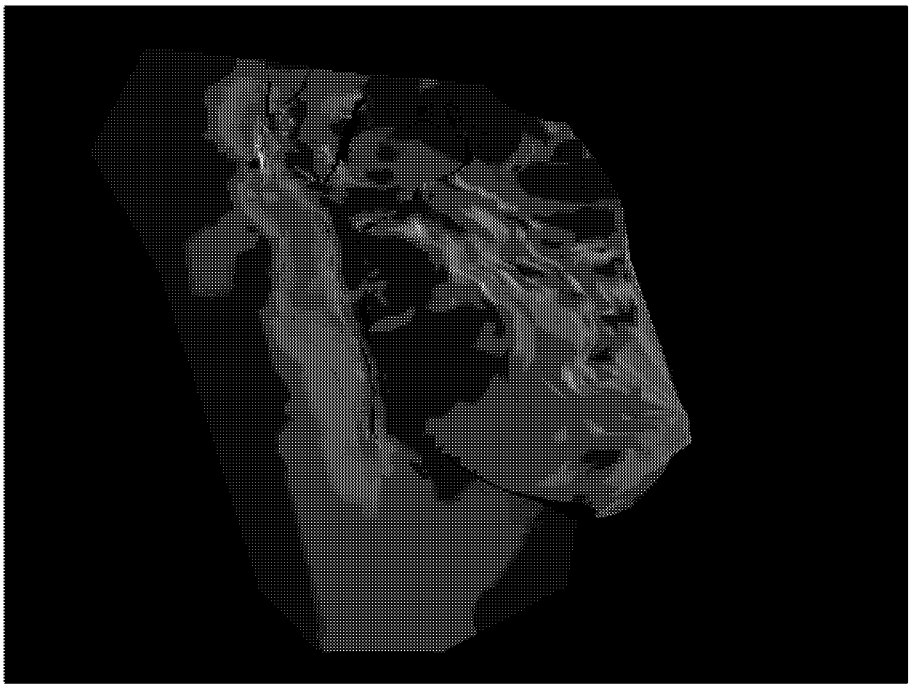

Figure 3-71 Strain Fields for Fracture Generation

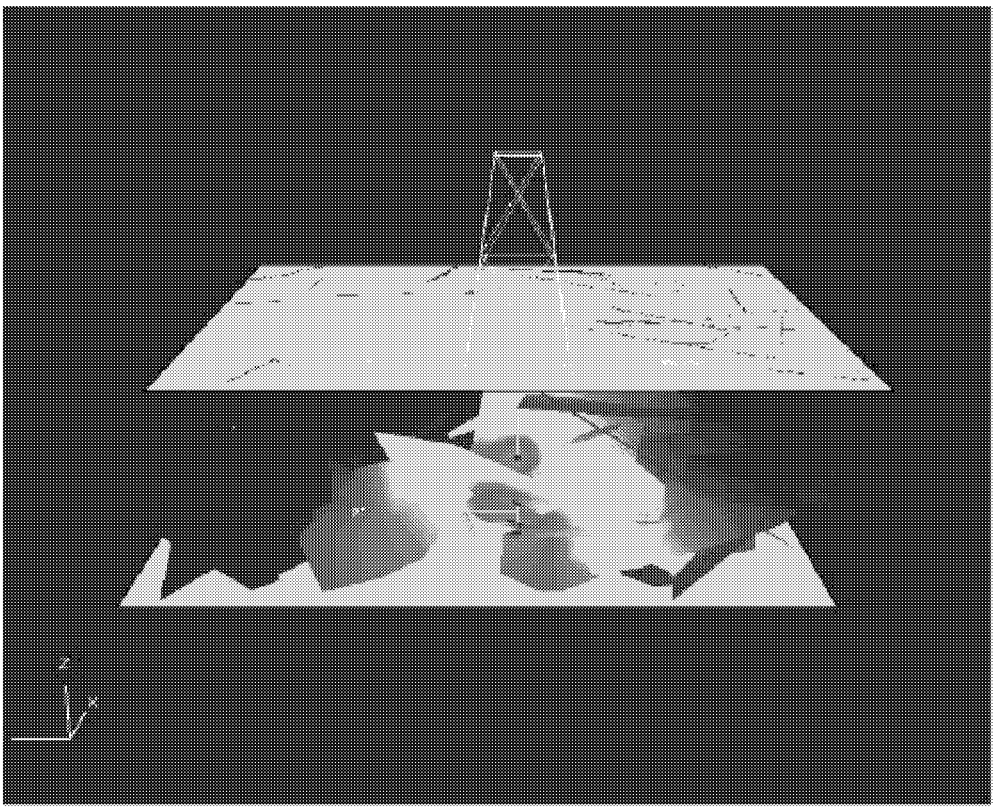

Figure 3-72 Geomechanical Modeling of 3D Fracture Populations

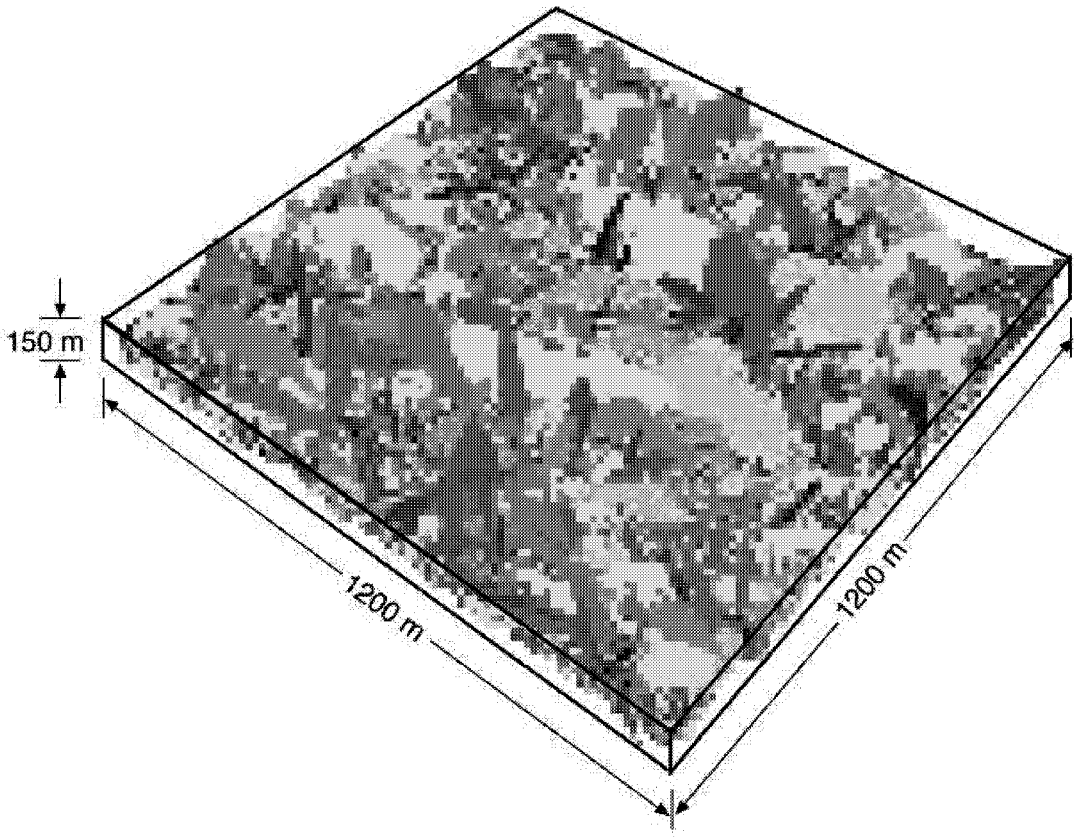

Figure 3-73 Preliminary Yates DFN Model

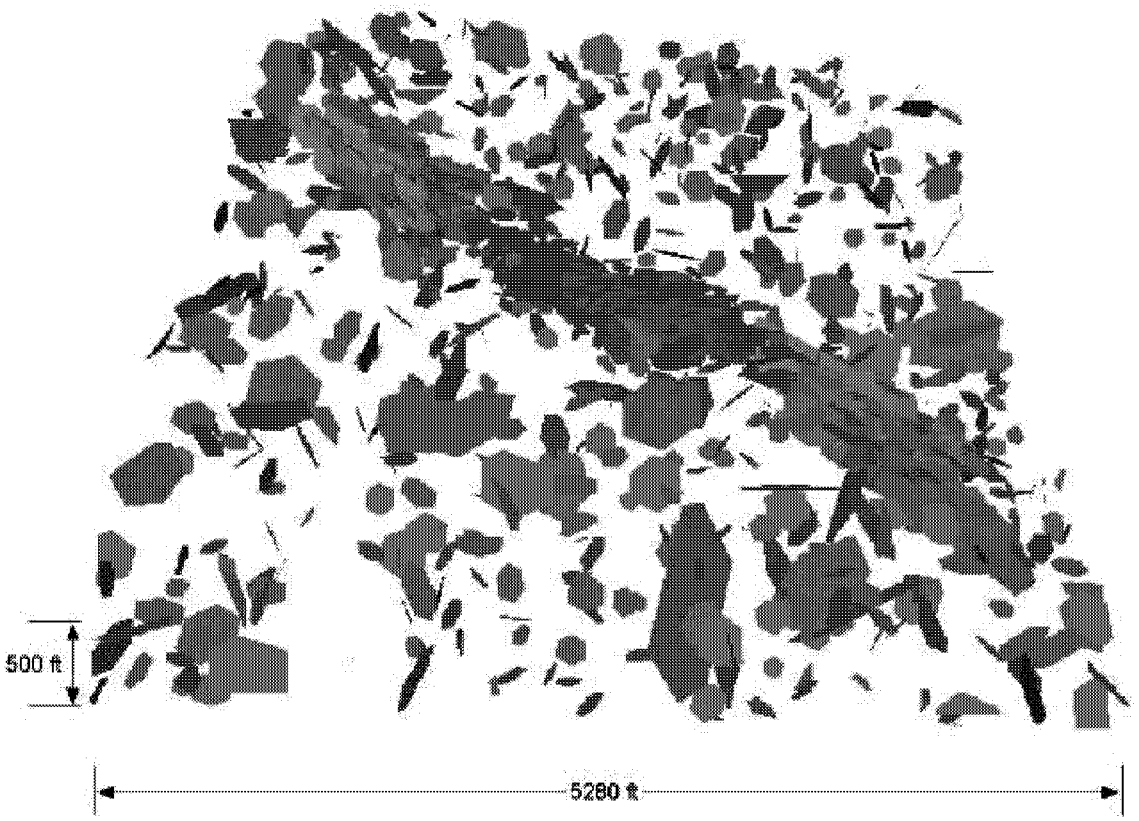

Figure 3-74 Preliminary Stoney Point DFN Model

Figure 3-75 Preliminary North Oregon Basin DFN Model

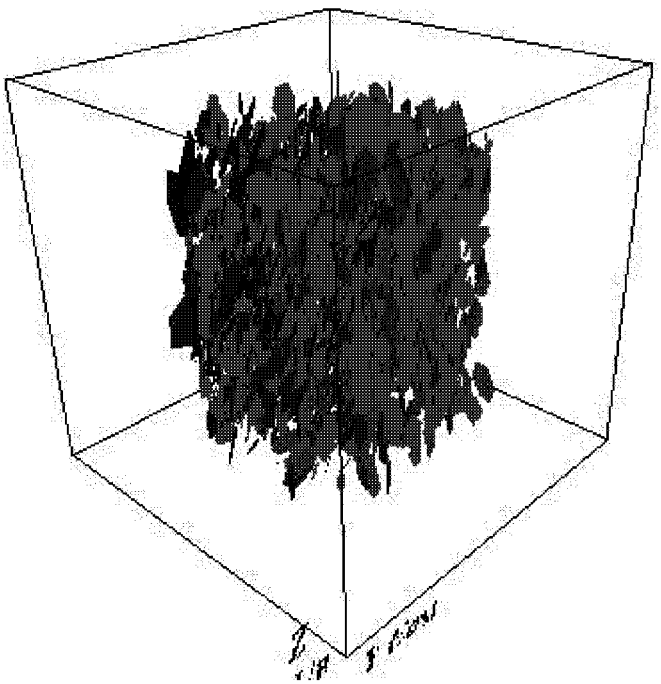

Figure 3-76 Preliminary South Oregon Basin DFN Model

Particular emphasis was placed on the use of the following DFN tools:

- **Pathways Analysis**: Graph theory analysis of the connectivity structure of the discrete conductive and storage features to identify connected well intervals, and to target injection and withdrawal rates for steam, water, oil, and gel as appropriate
- **Compartmentalization Analysis**: Analysis of connected network geometry and tributary drainage volumes
- **Block Size Analysis**: Derivation of dual porosity parameters based on discrete feature geometry
- **Flow Modeling**: Single phase flow modeling for derivation of flow rates and pressure responses
- **Transport Modeling**: Quantification of flow pathways by particle tracking methods.

Reservoir improvement strategies were developed for each of the sites in three stages: preliminary strategy development, DFN model development, and strategic plan. These are described below for each of the study sites.

3.4.1 Task 3.1. Strategic Plan: Yates Field Reservoir Improvement

The focus of efforts to improve production in the Yates field is on improving oil mobility to the producing intervals. Since oil is delivered to the wells primarily through the fracture network, the DFN approach has considerable potential to provide this support.

The strategic plan for the Yates field is as follows:

1. Oil mobility to the producing intervals needs to be improved. The DFN Modeling approach will support this through improving the understanding of pathways for injected surfactants, and how these pathways relate to the pathways for surfactant imbibition to the rock matrix, and pathways for oil delivery to production intervals
2. Improve the placement of producing intervals (strategic completion) to maximize the volume of oil accessed by the wells and minimize connectivity to sources for water.

3.4.1.1 Surfactant Flood DFN Analysis

Surfactant flood is important because it facilitates increased delivery of oil from the rock matrix through the fracture network to the production wells: DFN analysis an be used to address the following aspects of surfactant flood design:

- circulating optimum concentration of surfactant in water into the fractures,
- transfer of the surfactant from the fractures into both the less-directly-connected fractures and formation matrix pores,
- the chemical EOR mobilization of oil from the matrix into the fractures, and
- the capture of oil from the fracture network.

Procedures were developed to extend the investigation of flow from the wellbores to the matrix pore volume by way of water-filled fractures in the thick water-invaded fracture network and oil flow from this zone to accumulate in the oil column of the fracture network for capture of the mobilized oil. Two styles of chemical application are addressed;

1. the surfactant has been applied to treat production wells where the chemical is intended to circulate into the water invaded fractures and stimulate water imbibition into the matrix, and
2. injection of surfactant into openhole completions deep in the formation where the surfactant is intended to replace formation water along fracture flow paths to nearby producers.

Optimum application of these treatments depends on appropriate injected surfactant concentration and total volume to adequately treat the formation matrix exposed along the connected fracture network. This requirement encourages quantitative assessment of the variation in fracture network connectivity as formation character and deformational strains vary across the field. The tool for this assessment is DFN modeling. A DFN realization of a 125-foot thick water invaded interval of a fracture network is provided as Figure 3-77a. The largest inter-connected cluster of fractures is provided as Figure 3-77b. Note that many of the remaining fractures form only small clusters with small associated matrix volume.

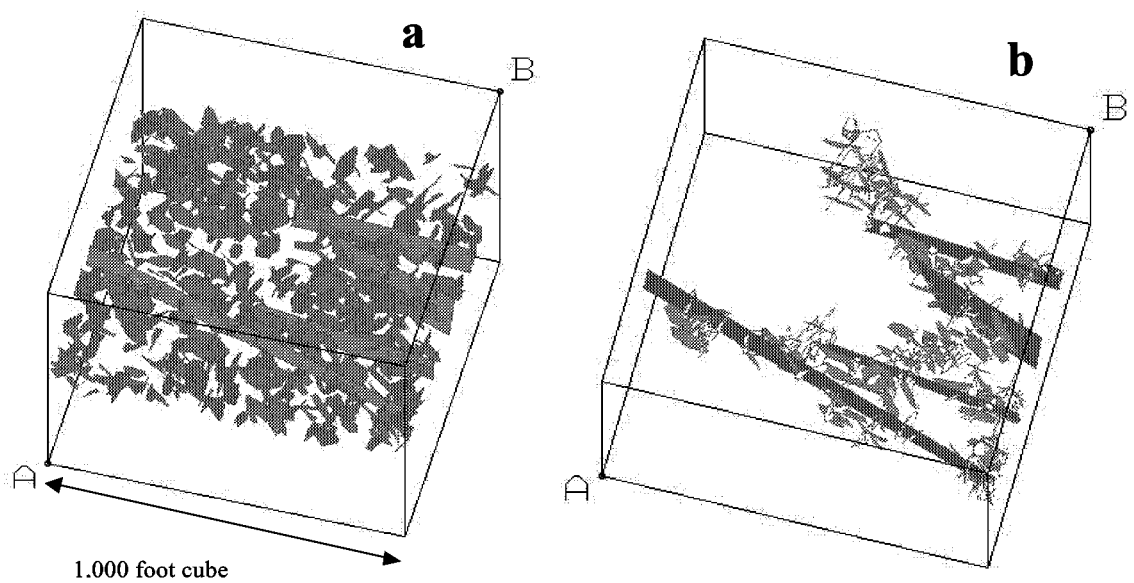

Figure 3-77 DFN Model Illustrating Surfactant Imbibition

Past production and injection completion performance can serve as an indicator of probable associated fracture cluster area to guide selection of wells for the various style treatments. The treatment types are conceptually illustrated in Figure 3-78. The production well treatment would treat fracture communicated matrix surfaces extending away from the well in varying directions. As the well is returned to production following a brief shut in period, any oil liberated by the stimulated Imbibition of water would be available along fractures that are well-connected to the

producer. This contrasts with the sustained injection style application in which the surfactant propagates into the fracture network away from the application point and selectively advances toward fracture-connected producers. The most locally intense treatment is at the point of application. Near an offsetting producer, chemical dosage may be minimal and only along a single fracture pathway leading to it. Oil mobilized by the process will be difficult to capture and account to the process. Figure 3-79 and Figure 3-80 provide graphs of tested or metered response to the two styles of treatments.

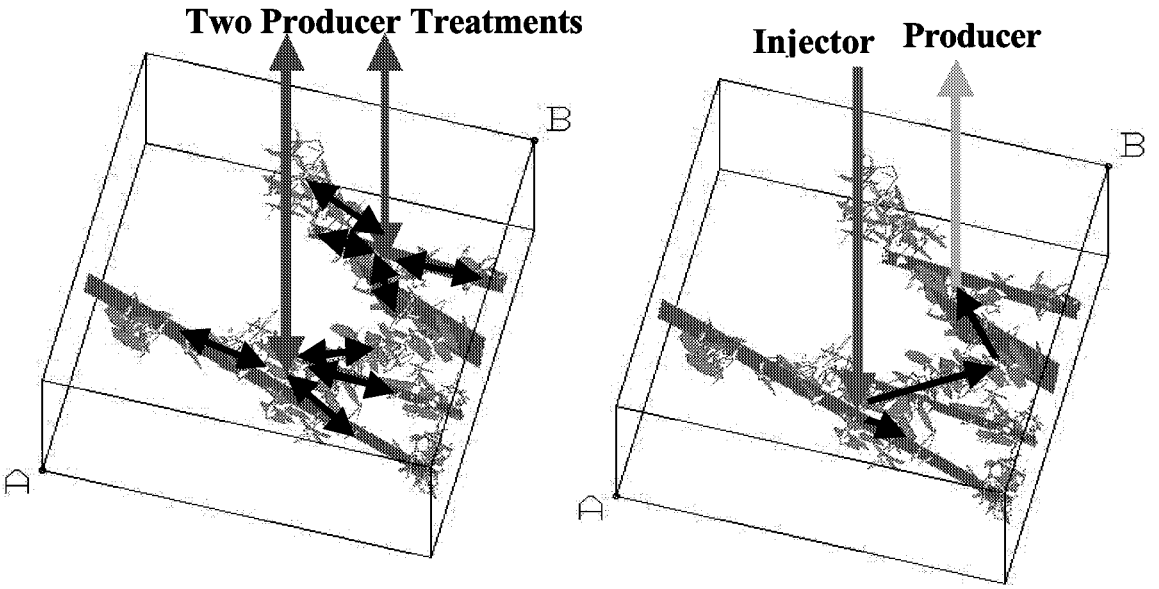

Figure 3-78 Surfactant Injection Strategies

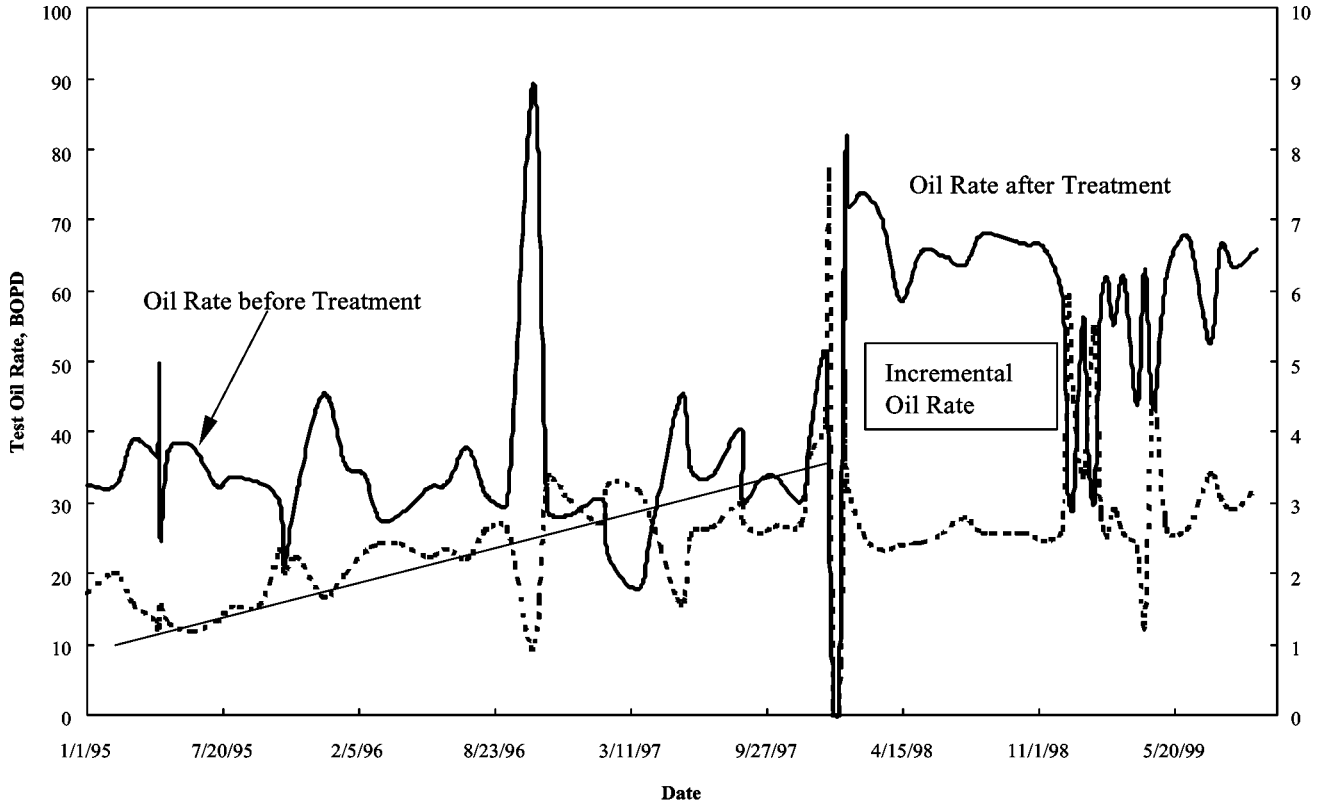

Figure 3-79 Well 2913 was treated with surfactant late in 1997 and responded with stimulated liquid productivity and reduced water-oil ratio (WOR) after recovery of treatment fluid. The stimulated fluid productivity has been maintained while the WOR has resumed an upward trend.

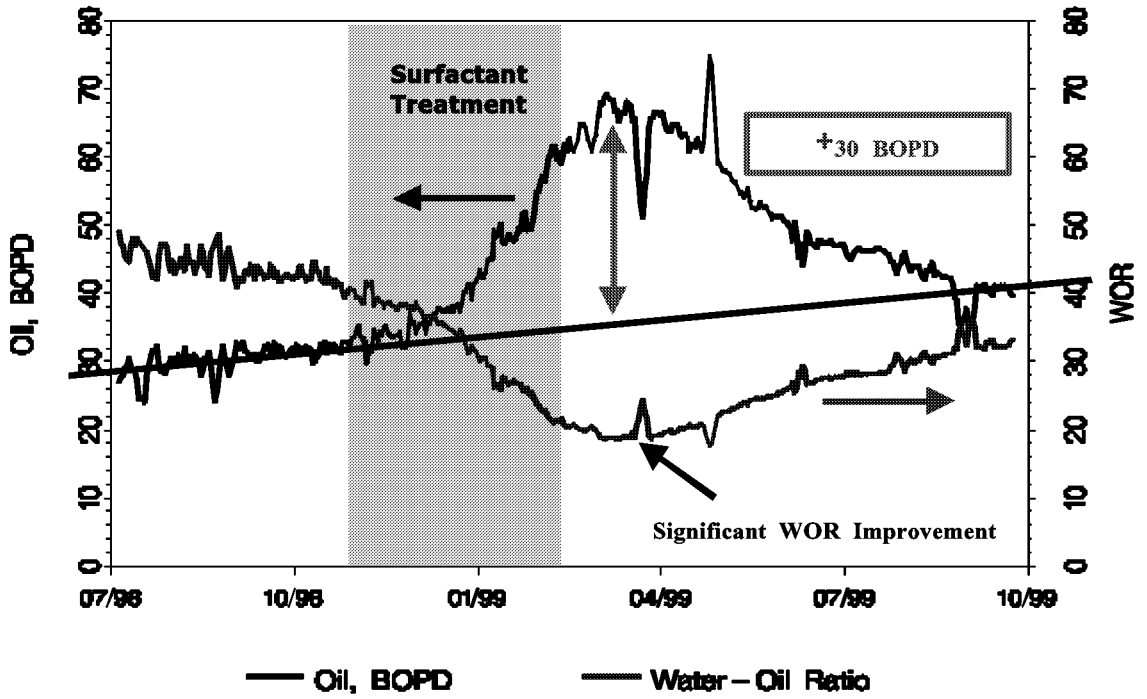

Figure 3-80 Response to injection over one mile away is observed almost immediately at a well which is producing at an elevation over 100 feet above the fracture flow feature taking the surfactant in the injection well

Field response to surfactant application has been economically encouraging even without the benefit of dosage optimization. Therefore, field testing is continuing while flow characterization/DFN modeling improves and quantification of chemical transfer from the fractures into the matrix continues. This quantification includes a number of parameters that can be mathematically related for solution of the transfer along an idealized planar surface.

3.4.1.1.1 Analytical Development

In order to optimize surfactant design, a mathematical model and its analytical solution are presented in this paper. The model relates the fracture area treated by surfactant with the injection rate, volume and concentration and fluid and permeable medium properties. The effects of fluid convection and dispersion on treated fracture area are also discussed.

During initial injection, the surfactant solution is first mixed with fluid in the fracture system. The mixing depends on the injection rate, fracture pore volume and permeability. The mixed solution then advances through the fracture system and diffuses into matrix. This process depends on the chemical properties of surfactant solution, formation water and formation rock. The fluid in the fracture system will also percolate into matrix and transport surfactant molecules. The fluid transport from fracture to matrix is controlled by the pressure gradient distribution in the reservoir and matrix permeability. For simplicity, The fracture system is conceptualized as a vertical plane (Figure 3-81). The surfactant is injected at one end of the fracture. The fluid convection into matrix from the fracture is assumed to be steady-state flow with constant flux over the fracture

surface. To model the surface area treated by surfactant, the surfactant transfer into matrix is investigated.

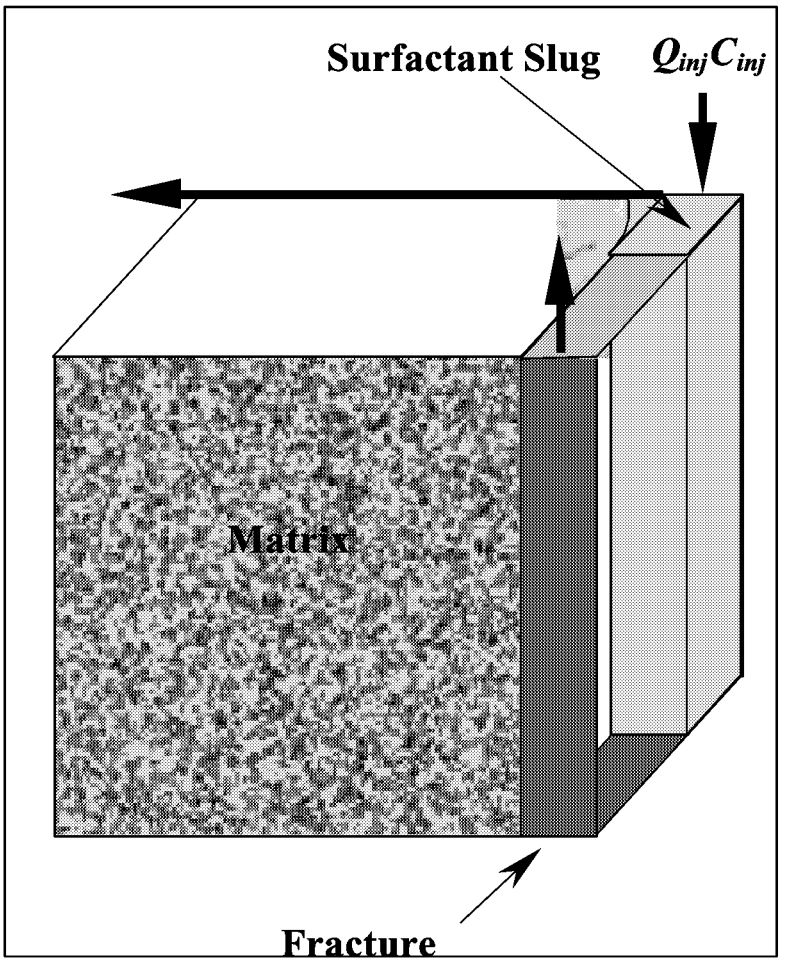

Figure 3-81 Conceptual Fracture Model

Let the surfactant with concentration C_o be in contact with fracture surface at time zero. It is assumed that the surfactant concentration in the matrix is initially zero and remains zero at an infinite distance from the fracture surface. The mathematical model for material balance and boundary conditions of the convection and diffusion processes can be described as (Lake, 1989),

$$K_l \phi \frac{\partial^2 C}{\partial x^2} - u \frac{\partial C}{\partial x} = \phi \frac{\partial C}{\partial t}$$ Equation 96

$$C(0,t) = C_o$$ Equation 97

$$C(x,0) = 0$$ Equation 98

$$\lim_{x \to \infty} [C(x,t)] = 0$$ Equation 99

Where C is surfactant concentration. It is a function of location and time. u is fluid convection velocity from fracture to matrix. ϕ is matrix porosity. K_l is longitudinal dispersivity coefficient. For one-dimensional flow, K_l is given by Lake (1989),

$$\frac{K_l}{D} = C_1 + C_2 \left(\frac{|v| D_P}{D} \right)^{\beta}$$ Equation 100

Where D is the effective binary molecular diffusion coefficient between the miscible displacing and displaced fluids. C_1, C_2 and β are properties of the permeable medium and the flow regime. For very slow flows, the second term in Equation 5 is negligible.

The partial differential of surfactant concentration with respect to distance, x, after taking Laplace transform on Equations 1 through 4 with respect to time is given by Eq. 6,

$$\left. \frac{\partial c(x,s)}{\partial x} \right|_{x=0} = \frac{C_o}{s} \left(\frac{u - \sqrt{u^2 + 4 K_l \phi^2 s}}{2 K_l \phi} \right)$$ Equation 101

This equation will be used in the following section to obtain fracture area treated by a surfactant slug.

The surfactant transfer rate by both convection and diffusion can be calculated as,

$$q_d = u C_o \delta_\lambda(t) - K_l \phi \left. \frac{\partial C(x,t)}{\partial x} \right|_{x=0}$$ Equation 102

Due to surfactant transfer into matrix and dispersion at the front of the surfactant solution, the surfactant concentration in the fracture is not constant. Figure 3-83 shows a typical surfactant concentration profile in a fracture.

For simplicity, the surfactant concentration behind the front of surfactant slug is considered to be constant (Figure 3-83). Using a similar method proposed by Marx(1959) and Carter (1957) in their reservoir heating project and fluid loss optimization of hydraulic fracturing, the surfactant material balance in the fracture system can be described as:

Surfactant Injected = Surfactant diffusion and convection into matrix + surfactant slug advance in fracture

We can then derive Eq. 8:

$$Q_{inj}C_{inj} = 2n\int_0^t \left[uC_o\delta_0(t-\lambda) - \phi K_l \left.\frac{\partial C(x,t-\lambda)}{\partial x}\right|_{x=0} \right]\left(\frac{dA}{d\lambda}\right)d\lambda$$

$$+ n\phi_f w_f C_o \frac{dA}{dt} \qquad \text{Equation 103}$$

where Q_{inj} and C_{inj} are injection rate and injection concentration. A is single side fracture surface area treated by surfactant and is a function of time and other parameters such as injection rate fracture and matrix permeability, and *etc*. ϕ_f and w_f are fracture porosity and width. n is the number of fractures connected to the wellbore. λ is the time when the fracture surface is exposed to surfactant. Solving this mathematical system results in Eq. 9:

$$A(t) = \frac{(M+K)L}{4MK^2}\left\{e^{[4MK]\,t} erfc\left[(M+K)\sqrt{t}\right] - 1\right\}$$

$$- \frac{L\sqrt{J}}{K} terfc\left(\sqrt{Jt}\right) + \frac{L\sqrt{t}}{K\sqrt{\pi}} e^{-Jt}$$

$$+ \frac{(M^2+K^2)L}{4MK^2\sqrt{J}} erf\left(\sqrt{Jt}\right) \qquad \text{Equation 104}$$

where

$$J = \frac{u^2}{4K_l\phi^2} \qquad \text{Equation 105}$$

$$M = \frac{\phi\sqrt{K_l}}{\phi_f w_f} \qquad \text{Equation 106}$$

$$K = \sqrt{M^2 + J - \frac{u}{\phi_f w_f}} \qquad \text{Equation 107}$$

$$L = \frac{Q_{inj}C_{inj}}{2nC_o\phi_f w_f} \qquad \text{Equation 108}$$

For a special case when the fluid convection from fracture to matrix is ignored, Equation 6 becomes

$$A(t)=\frac{L}{2M^2}\left[e^{(2M)^2 t}erfc\left[(2M)\sqrt{t}\right]+\frac{4M}{\sqrt{\pi}}\sqrt{t}-1\right] \qquad \text{Equation 109}$$

For another special case when the molecular diffusion into matrix is neglected, Equation 6 becomes,

$$A(t)=\frac{L\phi_f w_f}{2u}\left(1-e^{-\frac{2ut}{\phi_f w_f}}\right) \qquad \text{Equation 110}$$

3.4.1.1.2 DFN Model Validation

To verify the analytical model, a conceptual surfactant flooding simulation model is setup using a commercial simulator. The model is 600 ft x 116.06 ft x 100 ft with a grid dimensions of 117 x 117 x 1 (Figure 3-83). The fracture is located along the central line parallel to the model edge of the longer side (Figure 3-82). The fracture permeability is 5 darcy and the porosity is 0.99. The fracture is 600 ft long and 0.06 ft wide. The matrix permeability is 100 md and porosity is 0.15. Two wells are located at each end of the fracture. One well is a producer and the other is an injector. To ensure constant flux of fluid convection into the matrix from the fracture, a constant flux aquifer is attached along the two longer edges of the model. The aquifer efflux is 5.6146E-5 ft/day, which is the same as the flux of fluid convection from fracture to matrix. The diffusion coefficient is 1.8E-5 ft^2/day for the simulation model. The injection rate is 20 STB/day and the production rate is 18.8 STB/day. The simulation has an initial 100-day period to establish steady-state flow. The surfactant solution is then injected with a concentration of 2 lb/BBL.

The fracture surface area swept by surfactant solution with a concentration greater than 1.0 lb/BBL is output for different time steps. The results are plotted in Figure 3-84 along with those calculated from the analytical model. A dispersion coefficient of 12 times that of the molecular diffusion coefficient is used in the analytical calculation. The adjustment needed here accounts numerical dispersion and macro dispersion due to convection. This ensures that dispersion caused by fluid flow and mixing is dominant in this case (Lake, 1989). The overall results show a good agreement. The deviation around 40 to 50 days is caused by surfactant break through. Therefore, the fracture area treated in the simulation model is limited to 60,000 ft^2.

Figure 3-85 shows an analytical calculation demonstrating the effects of convection rate on the treated fracture area. We can see that at early time, the effect is negligible. As treatment time increases, the treated fracture area decreases with the increase of convection rate. After 50 day's of treatment with 20 STB/day and 2 lb/BBL of dilute surfactant injection, the difference of the treated fracture area is as large as 3,000 square feet with convection rate varying from 1.0E-5 to 1.5E-4 ft/day.

Figure 3-86 shows the effects of molecular diffusion coefficient on the treated fracture area. The pattern is similar to the effects of fluid convection into matrix on the treated fracture area. At early time the effect is negligible. As treatment time increases, the treated fracture area decreases with the increase of molecular diffusion.

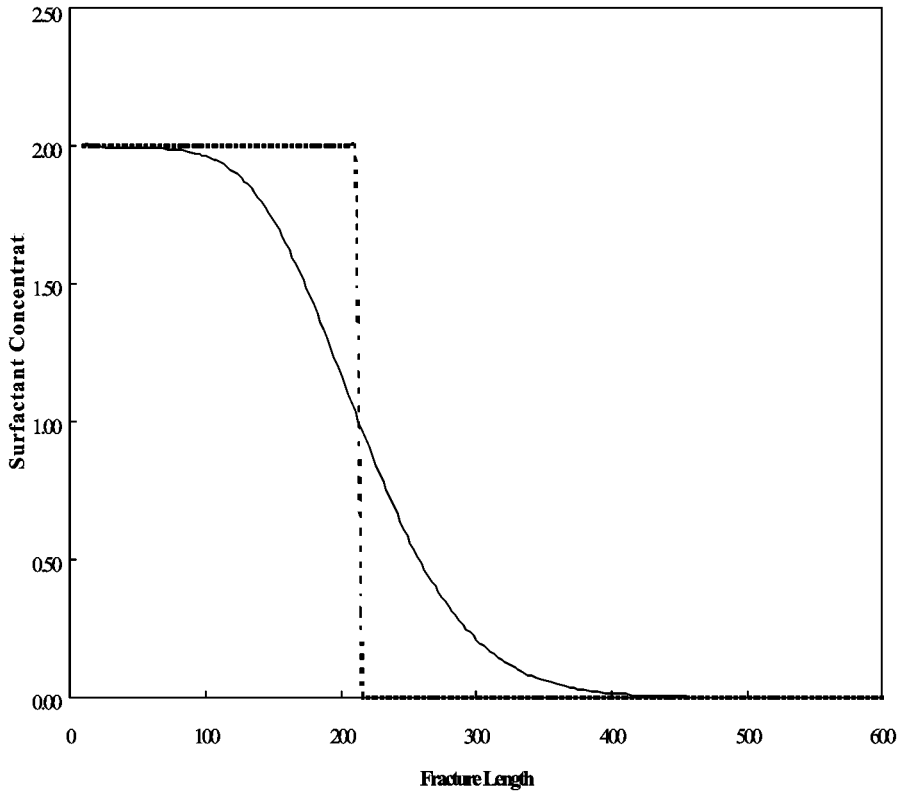

Figure 3-82 Surfactant Concentration Profile in Fracture

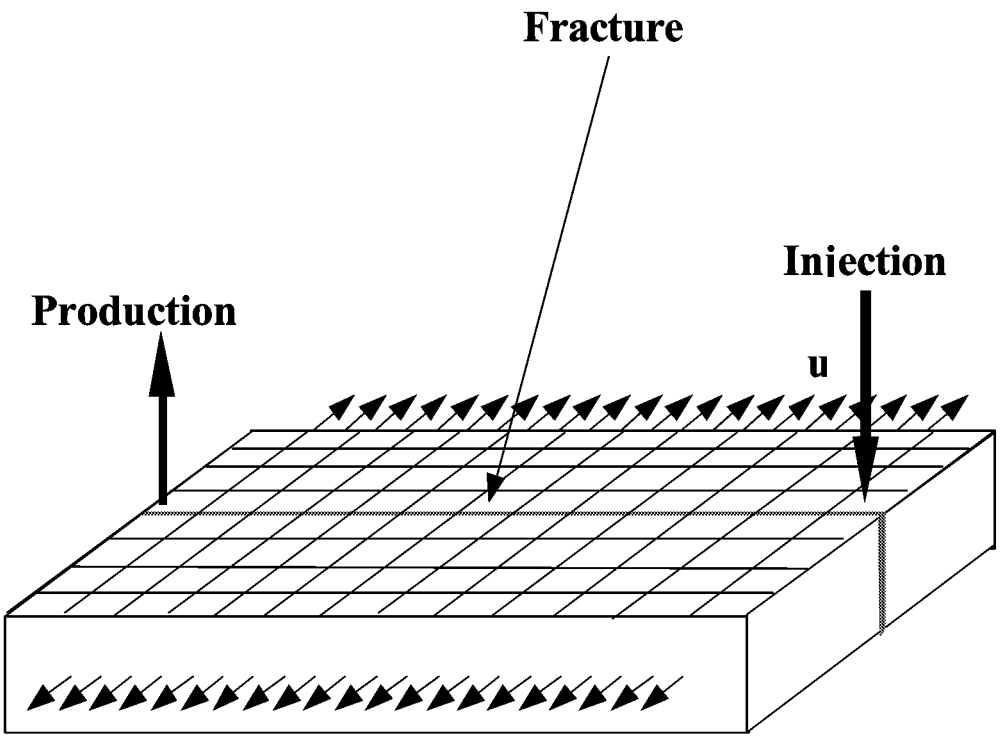

Figure 3-83 Schematic View of Reservoir Model

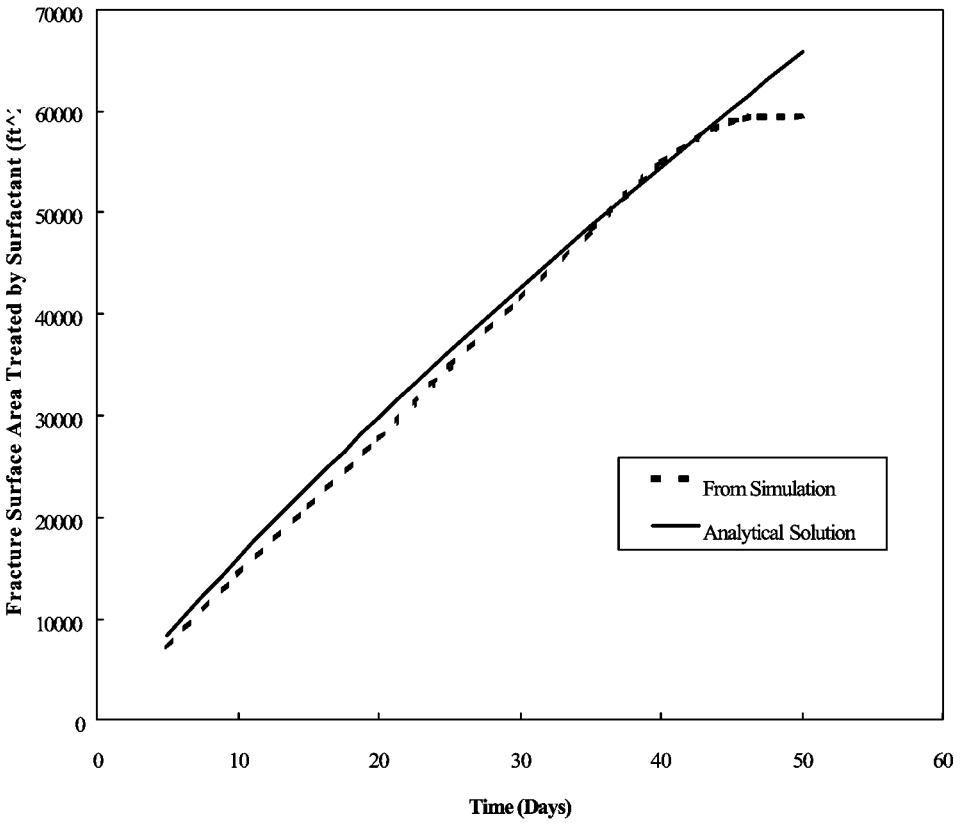

Figure 3-84 Comparison of Results from Simulation and Analytical Model

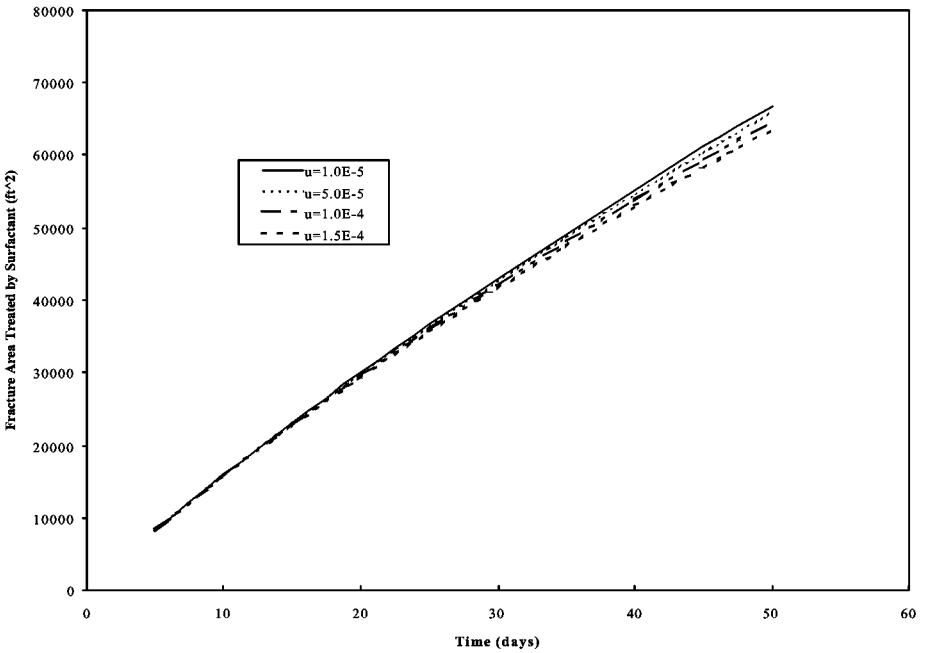

Figure 3-85 Effects of Convection Rate on Fracture Area Treated

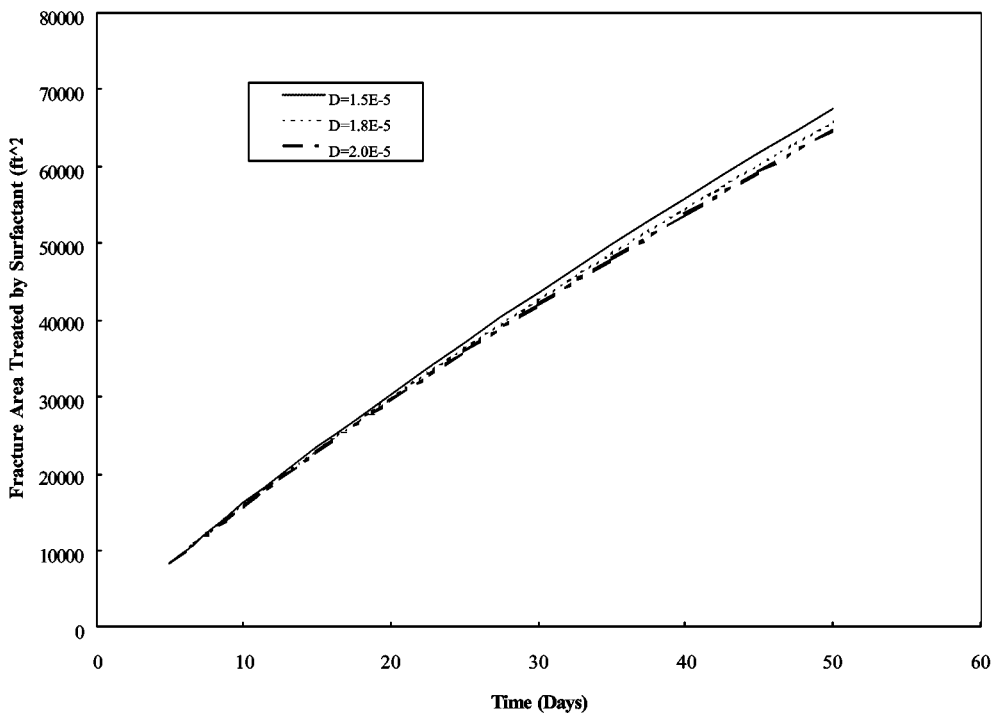

Figure 3-86 Effects of Molecular Diffusion on Fracture Area Treated

3.4.1.2 Strategic Completion DFN Analysis

The DFN Model described above in Section 3.4.1 was used to evaluate strategic completion for the 8 wells At the end, this produced about 80 DFN models for the of deepening candidate wells 1304, 1307, 14A1, 1495, 1663, 177,3 2513, and 2722. The purpose of the analysis is to determine which DFN model parameters can be used as indicators for prioritizing strategic completion candidates. The indices considered were:

- Conductive fracture frequency P_{10} (1/m), which indicates the frequency with which conductive fractures intersect the different wells considered. In theory, higher P_{10} could correlate with better production. However, past studies have universally demonstrated poor correlation to transmissivity, and is not expected to be a good predictor of production
- Compartment statistics of volume and projected area, which measure the distribution of connected fracture porosity within the reservoir volume adjacent to the well.
- Matrix block statistics, which measure the distribution and shape of the reservoir matrix which feeds oil to the wells through the fracture network.

Figure 3-87 and Table 3-27 summarize the conductive fracture frequency statistics for each of the eight wells evaluated. Based on these simulations, the mean conductive feature intersection intensity for the most heavily fractured well (W1307) is almost twice as great as that for the least heavily fractured well (W1773). However, this inter-well variability is still within one standard

deviation for the variability between realizations for a single well. As a result, it is unlikely that conductive intensity will be a good predictor for production.

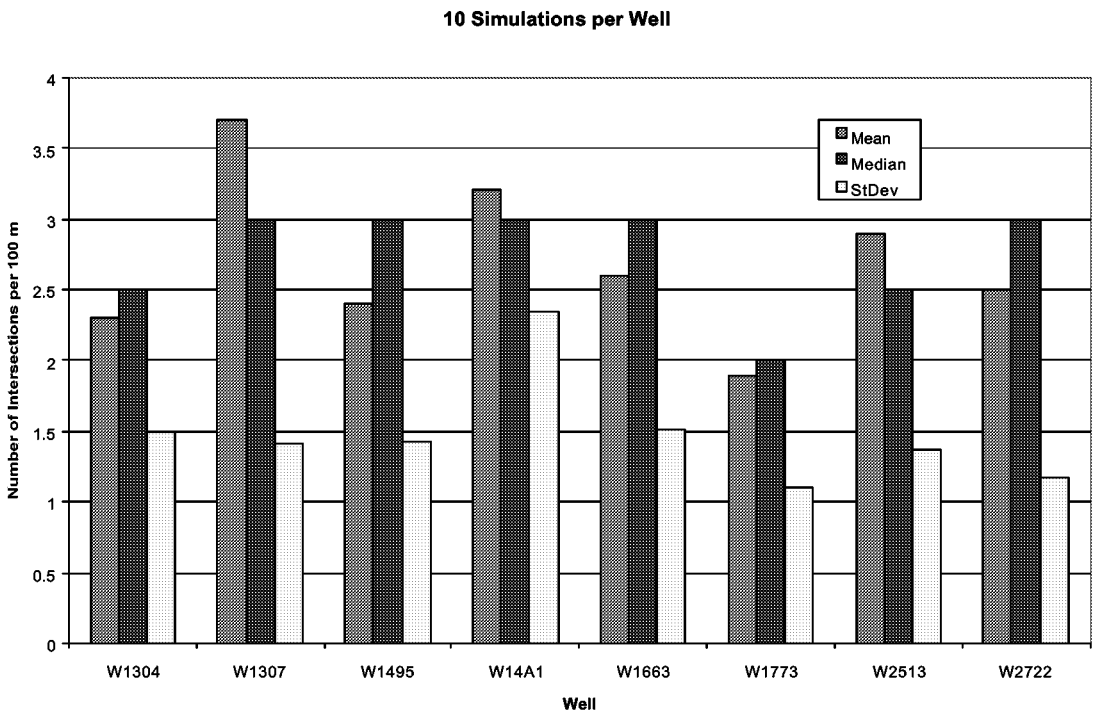

Figure 3-87 Intersection Statistics for Deepening Candidate Wells

Table 3-27 Summary of Intersection Simulations, Yates Deepening Candidates

	Intersection Intensity P_{10} from Simulations (Conductive fracture intersections per 100 m)				
Well	Mean	Median	StDev	Min	Max
W1304	2.3	2.5	1.5	0	4
W1307	3.7	3	1.4	2	7
W1495	2.4	3	1.4	0	4
W14A1	3.2	3	2.3	0	8
W1663	2.6	3	1.5	1	6
W1773	1.9	2	1.1	0	3
W2513	2.9	2.5	1.4	1	5
W2722	2.5	3	1.2	1	4

Compartment statistics were analyzed using the methods of LaPointe et al. (1998). For all of the wells analyzed almost the entire reservoir volume in the well vicinity s part of a single large compartment. As a result, the differences between the connectivity of the different well locations is defined by the differences between the compartments which are not part of this single large compartment. Compartment volume statistics were therefore calculated for those compartments of volume less than 50 million m^3, and compartment area statistics were calculated for those compartments of projected area less than 200,000 m^2.

Table 3-28 and Table 3-29 and Figure 3-88 and Figure 3-89 summarize the results of ten realizations of compartment analysis for well deepening candidate W1304. The projected area and volume vary significantly between realizations. However, the distributions are consistently skewed, with the vast majority of compartments much smaller than the mean, and only a very few compartments of volumes of the same order as the largest compartments. As illustrated in Figure 3-88 and Figure 3-89, the distributions for compartment volume and projected area are both well matched by lognormal distributions. This indicates that in any case there are a significant number of smaller compartments, which should drain relatively quickly, with a few larger compartments, which will provide long-term production.

Table 3-28 Compartment Projected Area Statistics, Well W1304

	Compartment Volume m^3 (Cutoff 50 million m^3)				
Realization	Min	Max	Median	Mean	StdDev
0	3.6	120065.9	323.0	3732.9	14436.9
1	5.9	44668.7	554.0	2655.7	6092.3
2	9.8	187956.6	360.8	6140.8	21802.6
3	4.6	219962.5	362.8	5783.3	24169.4
4	9.3	169452.0	459.8	4246.7	17800.4
5	1.4	19204.0	734.3	2066.4	3957.3
6	5.6	115737.5	533.0	3927.5	11843.8
7	5.9	113578.4	346.3	2754.0	11740.2
8	3.6	21459.8	296.9	1679.1	3511.8
9	8.8	214933.7	460.8	6503.6	23095.5
Mean	5.8	122701.9	443.2	3949.0	13845.0
StdDev	2.7	75718.6	135.1	1720.1	7778.6

Table 3-29 Compartment Projected Area Statistics, Well W1304

	Compartment Projected Area m^2 (Cutoff 200,000 m^3)				
Realization	Min	Max	Median	Mean	StdDev
0	4.3	3130.6	78.3	220.3	443.4
1	3.9	1255.8	115.5	209.2	255.7
2	4.5	3650.6	87.6	308.2	583.7
3	3.3	4431.9	97.6	263.3	535.8
4	5.3	3976.8	106.6	239.2	465.0
5	3.7	2102.4	121.8	210.0	305.7
6	3.9	3343.6	111.9	260.4	434.6
7	3.2	3045.0	76.9	187.8	364.5
8	2.7	1443.7	90.6	163.8	236.4
9	3.6	1527.3	94.1	201.9	301.5
Mean	3.9	2790.8	98.1	226.4	392.6
StdDev	0.7	1133.6	15.5	42.1	118.5

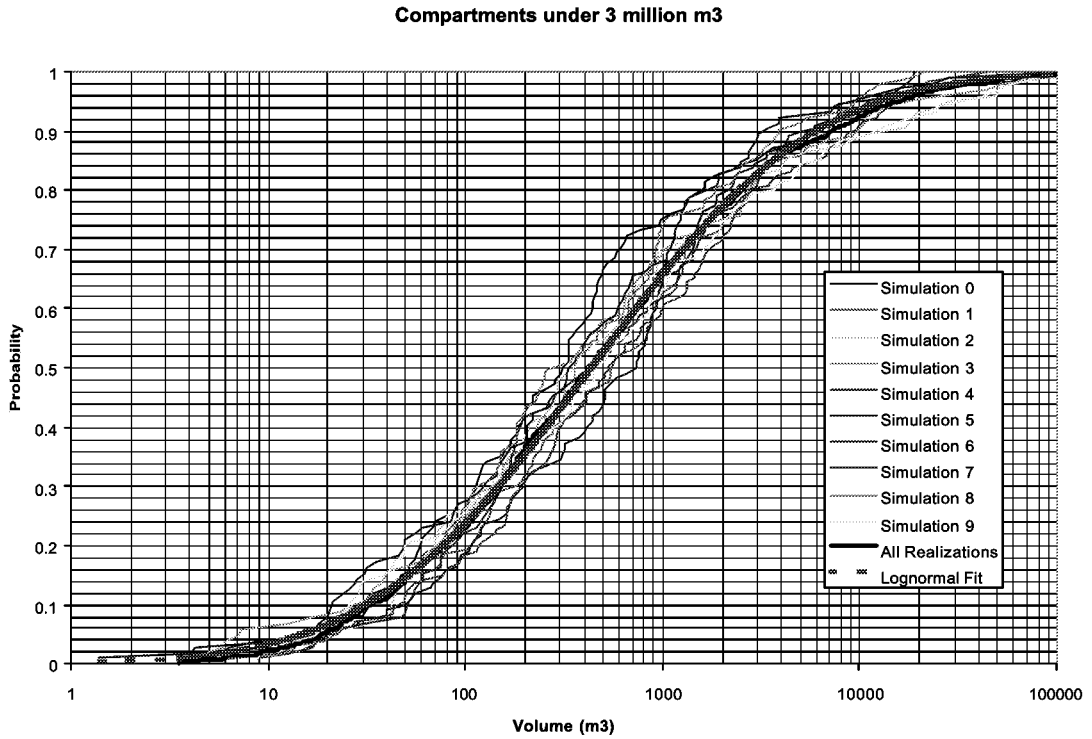

Figure 3-88 Compartment Volume Distribution, W1304

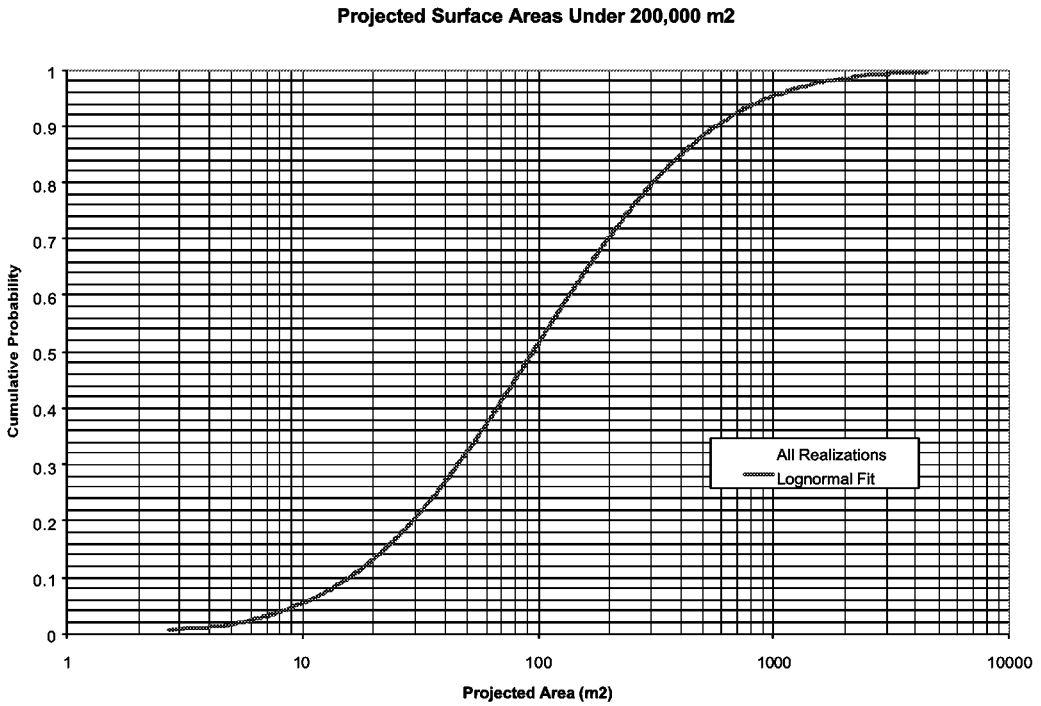

Figure 3-89 Compartment Projected Area Distribution, W1304

Table 3-30 and Table 3-31 and Figure 3-90 and Figure 3-91 present the compartment volume and projected area statistics for all ten realizations of the eight deepening candidate wells considered. Significant differences in compartment statistics are evident between the wells. In terms of compartment volume (Figure 3-90), well 2722 has the smallest median internal compartment volume, while wells 1663 and 1773 have the largest. This could imply that 2722 has the least amount of reservoir volume tied up in sub compartments, which could drain poorly, reducing production and recovery. Wells 1663 and 1773 have the largest median compartment volume, implying the least amount of reservoir volume isolated in sub-compartments. The difference between the worst case and the best case is on the order of a factor of 3. Results of comparable when expressed in terms of projected area (Figure 3-91).

Table 3-30 Compartment Volume Statistics, Yates Deepening Candidate Wells

WELL	Compartment Volume m^3 (Cutoff 50 million m^3)				
	Min	Max	Mean	StDev	Median
1304	1,274	219,963	37,621	52,983	17,648
1307	1,747	760,502	70,740	140,494	16,928
14A1	584	284,088	41,103	60,138	13,247
1495	1,496	349,058	37,507	64,049	16,511
1663	1,638	110,669	34,188	33,054	19,809
1773	1,214	376,169	37,125	57,620	18,871
2513	2,257	19,033,830	472,060	2,775,766	14,297
2722	1,242	1,028,226	42,131	144,423	13,141

Table 3-31 Compartment Projected Area Statistics, Yates Deepening Candidate Wells

WELL	Compartment Projected Area m^2 (Cutoff 200,000 m^3)				
	Min	Max	Mean	StDev	Median
1304	4431.9	100.5	1197.1	1116.3	879.7
1307	10400.5	120.1	1629.5	2035.6	938.8
14A1	7079.5	68.9	1424.6	1634.4	825.7
1495	4701.3	187.3	1238.9	1083.9	832.6
1663	3475.0	189.7	1286.5	839.2	995.9
1773	9586.3	119.1	1329.7	1404.7	953.8
2513	93618.8	158.1	3462.8	13649.3	826.6
2722	9329.2	157.1	1082.1	1385.7	716.6

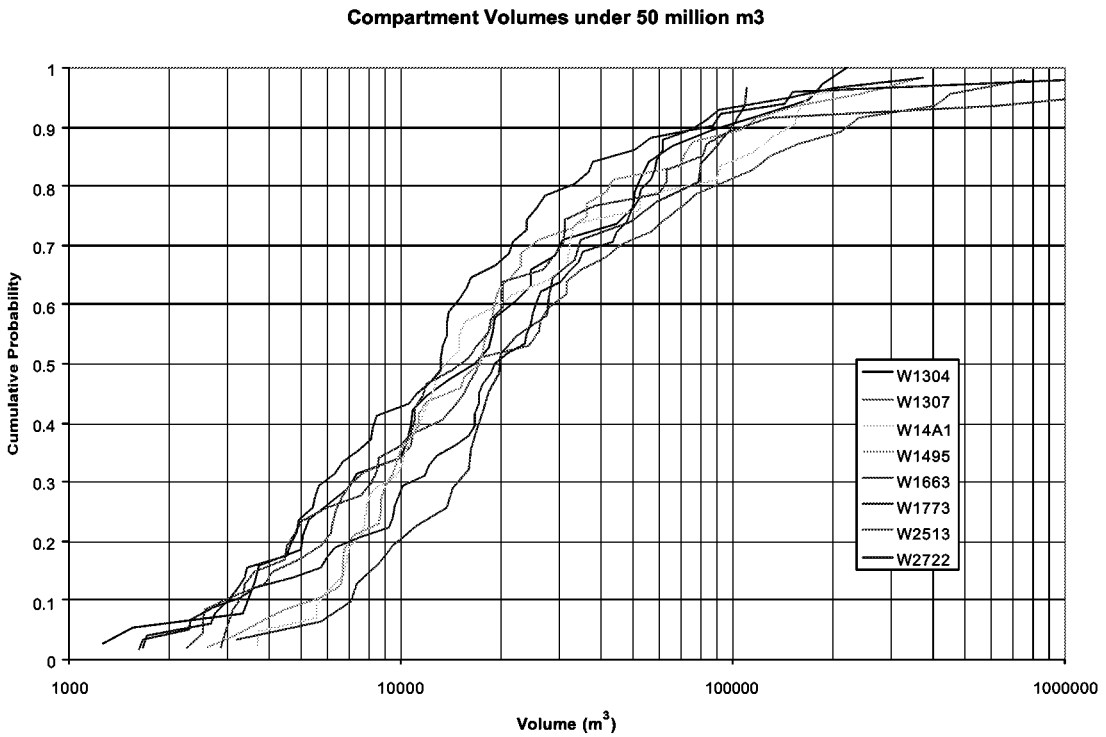

Figure 3-90 Compartment Volume, Yates Deepening Candidates

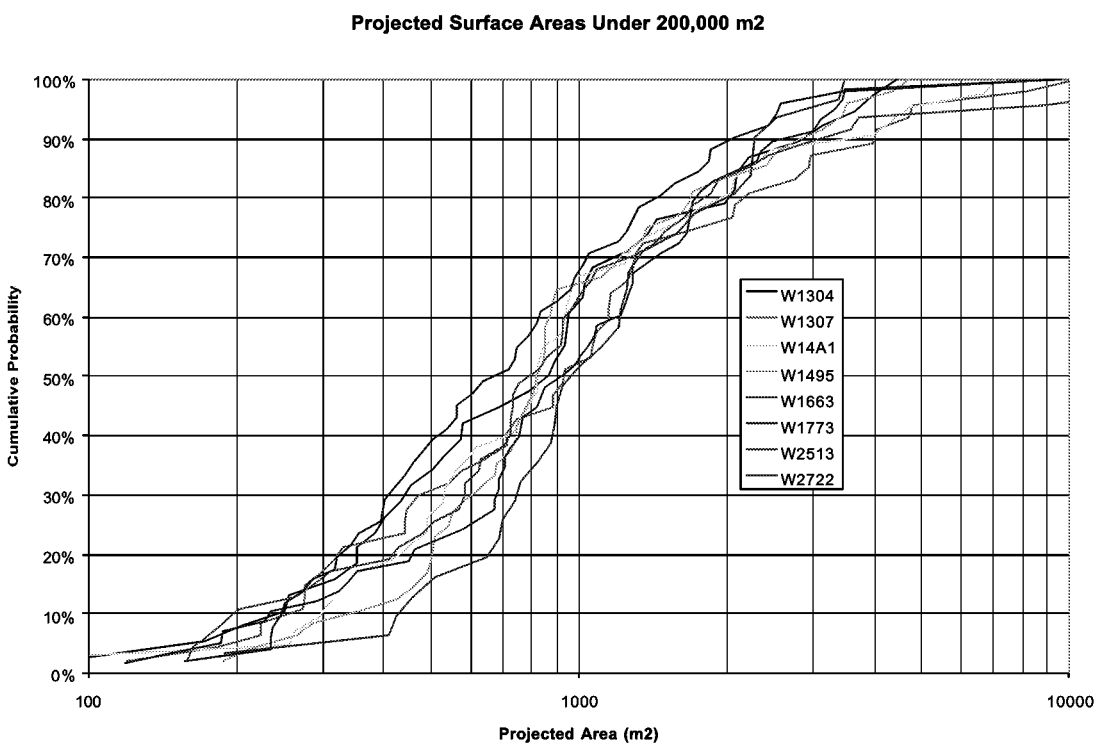

Figure 3-91 Compartment Projected Area Distribution, Yates Deepening Candidates

Fracture geometry also influences matrix block geometries, which can have a profound influence on fractured reservoir production. The Yates DFN model was used to calculate:

- matrix block volume;
- "sigma factor", the ratio of the matrix block height to the horizontal cross-sectional area; and
- matrix block aspect ratio.

Matrix block statistics are summarized in Table 3-32 through Table 3-37.

Table 3-32 Matrix Block Volume Statistics

	Min	Max	Mean	StDev	Median
1304	0.000	477,638	19,778	42,856	4,850
1307	0.366	889,569	25,175	65,258	5,379
14A1	0.033	419,962	20,636	41,943	4,891
1495	0.047	961,745	23,966	58,473	5,243
1663	0.082	1,378,270	22,274	60,639	4,889
1773	0.009	691,748	22,278	51,717	5,341
2513	0.133	13,380,090	301,526	1,076,394	13,507
2722	0.492	1,580,614	21,680	57,086	5,482

Table 3-33 Matrix Block Sigma Factor Statistics

	Min	Max	Mean	StDev	Median
1304	0.00223	192,353	8,459	34,730	0.517
1307	0.00142	250,663	6,022	22,007	0.499
14A1	0.00238	66,085	9,278	32,844	0.545
1495	0.00143	316,251	7,512	32,020	0.528
1663	0.00133	137,237	7,468	36,710	0.529
1773	0.00187	2,422,107	100,861	554,222	0.501
2513	0.00141	18,110	7,261	30,642	0.498
2722	0.00127	340,082	260	8,680	0.322

Table 3-34 Matrix Block Z/X Ratio Statistics

	Min	Max	Mean	St.Dev	Median
W1304	0.0000	6059.7	13.94	182.45	1.20
W1307	0.0005	22256.0	20.76	466.75	1.44
W14A1	0.0003	2337.4	12.08	85.50	1.49
W1495	0.0004	18022.1	19.03	384.54	1.51
W1663	0.0007	3907.2	13.41	121.74	1.43
W1773	0.0003	4074.3	13.25	113.31	1.47
W2513	0.0003	3493.6	9.85	122.48	0.66
W2722	0.0001	8751.2	15.57	197.69	1.50

Table 3-35 Matrix Block Aspect Ratio Z/Y Statistics

	Min	Max	Mean	St.Dev	Median
W1304	0.0019	881.8	6.35	30.07	1.373
W1307	0.0001	9746.8	12.69	199.78	1.631
W14A1	0.0002	592.0	8.40	33.36	1.576
W1495	0.0004	5066.2	11.18	115.98	1.486
W1663	0.0008	1253.6	10.20	54.83	1.728
W1773	0.0000	5940.8	13.91	152.80	1.497
W2513	0.0007	2743.6	9.95	88.73	1.234
W2722	0.0001	1351.4	8.29	39.02	1.475

Table 3-36 Matrix Block Aspect Ratio X/Y Statistics

	Min	Max	Mean	St.Dev	Median
W1304	0.0001	631.4	6.15	26.91	1.187
W1307	0.0001	4177.5	10.10	126.31	1.096
W14A1	0.0010	1771.2	6.80	55.95	1.016
W1495	0.0004	1490.9	8.13	59.13	0.982
W1663	0.0005	2381.5	9.47	81.43	1.169
W1773	0.0002	6633.6	11.92	159.33	1.052
W2513	0.0001	73448.0	113.07	1601.47	1.887
W2722	0.0001	1330.7	6.02	40.61	0.985

Table 3-37 Ratio of Block Height to Horizontal Area

	Min	Max	Mean	St.Dev	Median
W1304	8.71E-05	1089.14	1.94	24.98	0.080
W1307	1.52E-05	1317.36	2.19	29.23	0.100
W14A1	5.70E-06	694.57	3.02	28.66	0.099
W1495	2.13E-05	3921.90	4.42	90.09	0.091
W1663	2.68E-05	990.07	2.77	28.22	0.101
W1773	2.48E-05	722.27	2.10	20.04	0.096
W2513	5.56E-06	453.21	1.37	0.034	14.78
W2722	3.02E-06	486.51	1.81	0.098	13.55

As shown in Figure 3-92 and Figure 3-93, the rock block volume distributions are similar for wells 1304, 1307, 14A1, 1495, 1663, and 2513. Well 1773 has significantly larger mean and standard deviation of rock block volume, while well 2722 shows significantly smaller mean block volumes. The larger block size of well 1773 might indicate lower initial production, while the smaller block volume of well 2722 might indicate better sustained production. As indicated by the median block size of under 1 m^3, the vast majority of blocks for all wells are extremely small for all well regions.

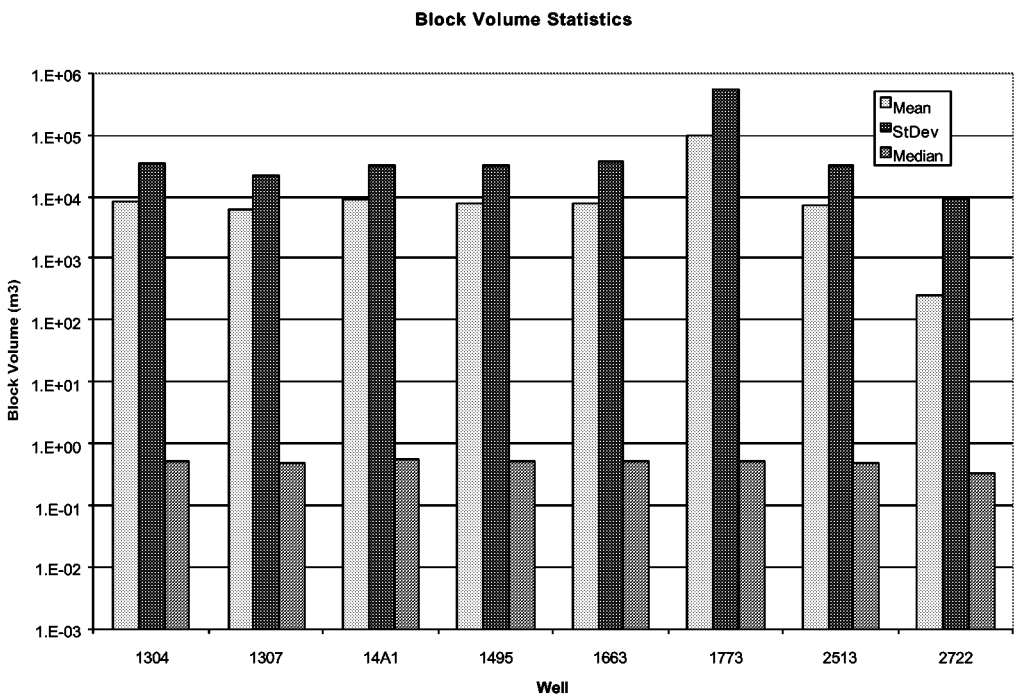

Figure 3-92 Block Volume Statistics

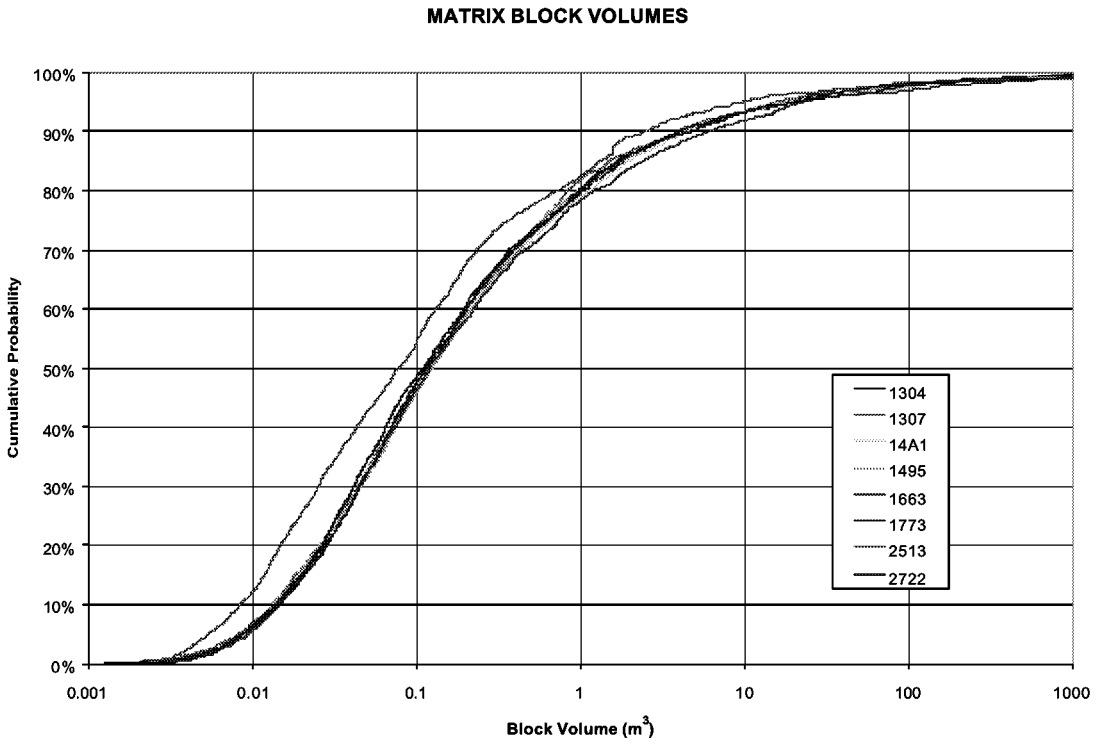

Figure 3-93: Block Volume Distribution

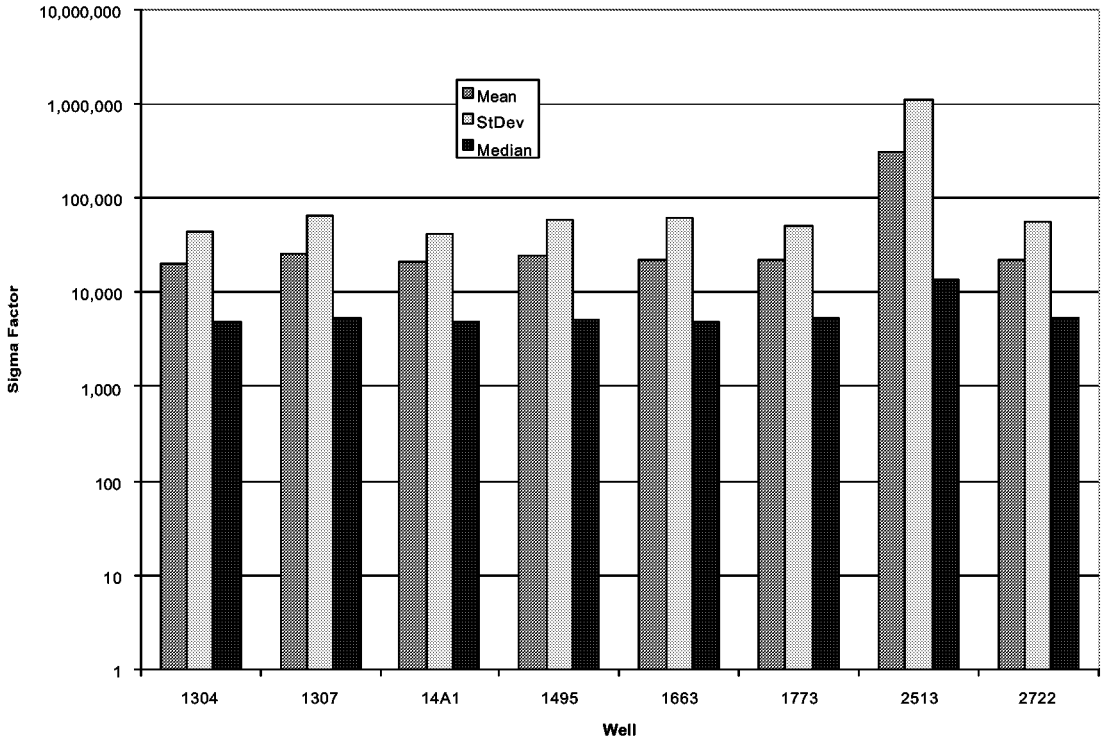

Figure 3-94 Block Sigma Factor Statistics

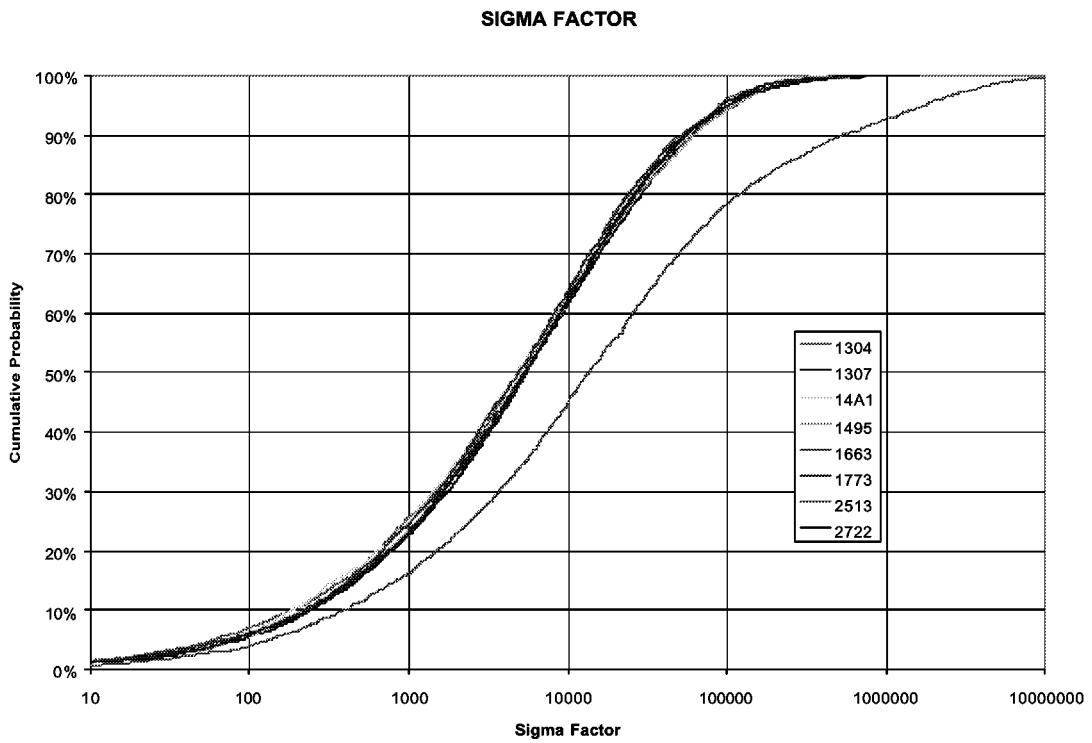

Figure 3-95 Block Sigma Factor Distributions

The rock block sigma factor statistics (Table 3-33, Figure 3-94, and Figure 3-95) are very similar for all wells except for 2513. For most of the wells, the sigma factor follows a roughly normal distribution with a mean of approximately 8,000. In contrast, well 2513 has a mean sigma factor of 100,000 which implies that well 2513 may have lower initial production, and probably should not be high priority for strategic completion.

Median rock block aspect ratios are shown in Figure 3-96. These values were calculated by comparing the X, Y, and Z dimensions for 2500 blocks calculated in the vicinity of each of the eight wells. The ratio of height to either X or Y horizontal extent varies from 1.2 to 1.6. In general, the ratio is higher for Z/Y than for Z/X, implying that the Y dimension is the smallest. For most of the wells, this is confirmed by the ratios for X /Y which are slightly larger than 1.0. The exception is well 2513, in which the X dimension is about twice the Y dimension. At the same time, the Z/X ratio for this well is much smaller than for any other wells, implying that X is much larger than Z. Together, these ratios suggest that the block shape around 2513 is different from the shape for the other wells. The blocks around 2513 have a much greater extent in the X direction.

The distribution of aspect ratio for well W1304 is illustrated in Figure 3-97. Well 1304 is typical of the block shapes in most of the other well regions. In Figure 3-88, the aspect ratios Z/X, Z/Y, and X/Y all appear to follow a lognormal distribution, with a large range. This implies that although the median aspect ratio may be near one, the actual block shapes are more like match

sticks, with one dimension much larger than the other dimensions. This is confirmed by examining the minimum and maximum aspect ratios in Table 3-34, Table 3-35, and Table 3-36.

The ratio of block height to horizontal area is given in Table 3-37, and Figure 3-98 and Figure 3-99. If we assume that the base of the matrix block can be represented as a square, then values of this ratio close to 0.1 implies a block that is equant in all directions (a sugar cube). Value lower than 0.1 imply a horizontal extent greater than the vertical height. The median statistics suggest this approximately equant shape.

The median block shape for all of the wells except 2513 are fairly consistent and roughly equant, while the vast majority of blocks have Z dimensions either much larger or much smaller than their horizontal dimension. . The mean values, which are more impacted by outliers, vary from 2.0 to 4.5. These suggest matrix blocks that are 10 or 20 times as high as they are wide, and resemble matchsticks. The median block for well 2513 is shorter by a factor of three relative to its height when compared to the other blocks. Interestingly, well 1495 has a considerably larger variability of block shape than the other wells, with a standard deviation and maximum aspect ratio three times larger than that for the other wells. This is seen in the mean aspect ratio (Figure 3-98).

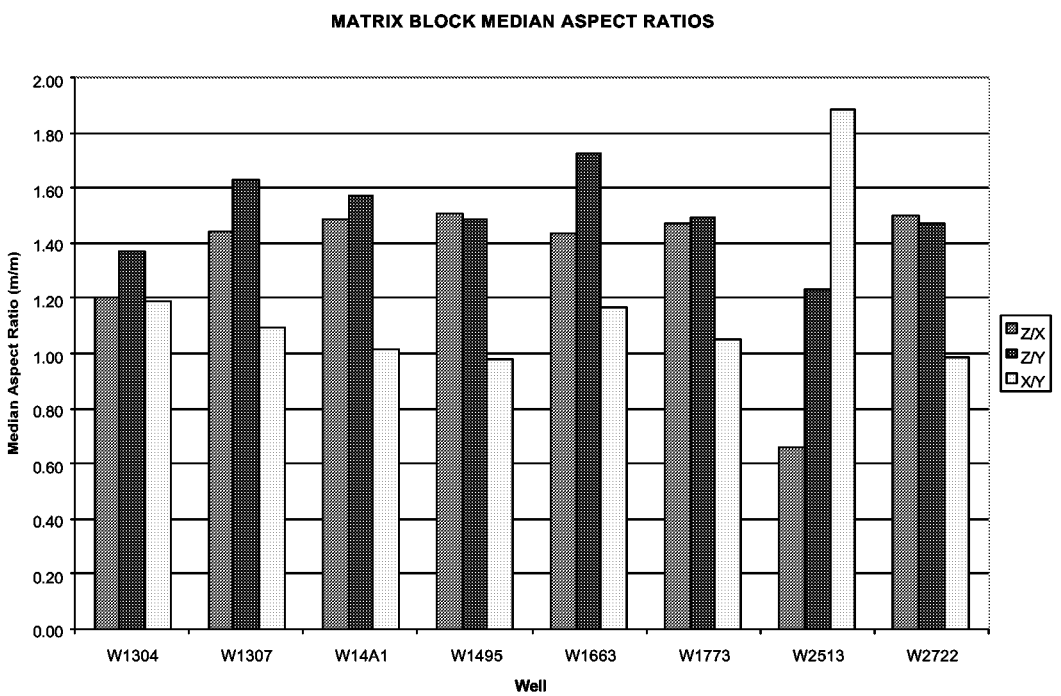

Figure 3-96 Median Block Aspect Ratio

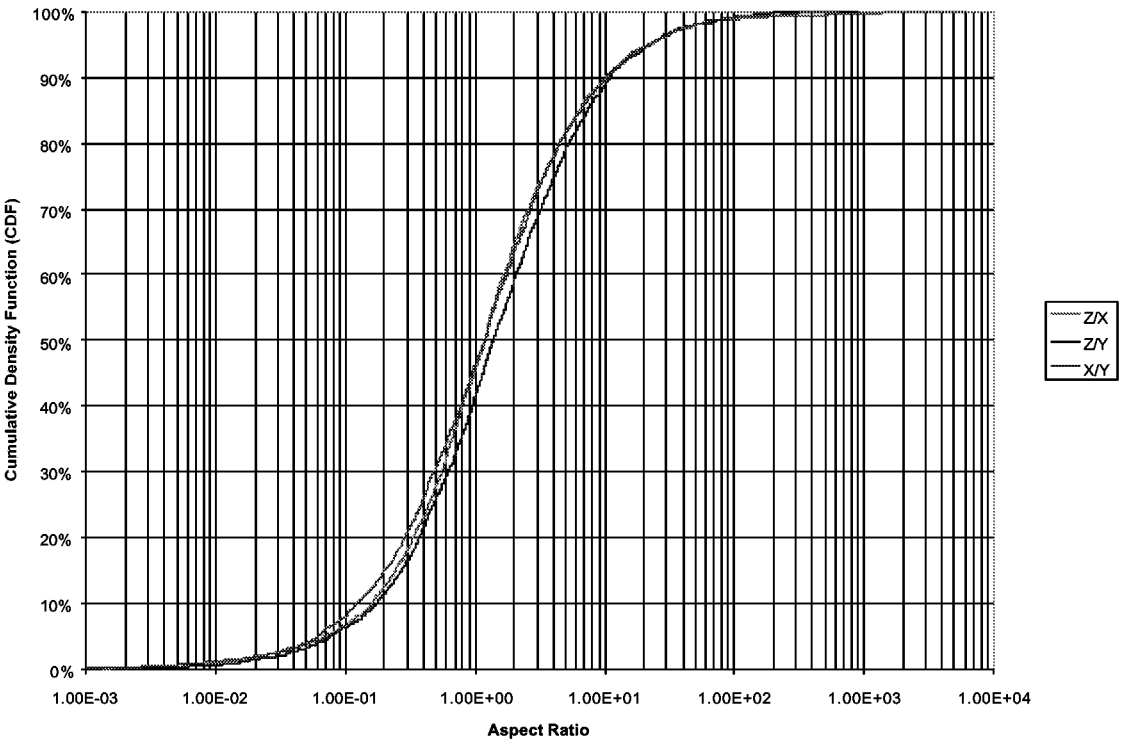

Figure 3-97 Distribution of Block Aspect Ratio

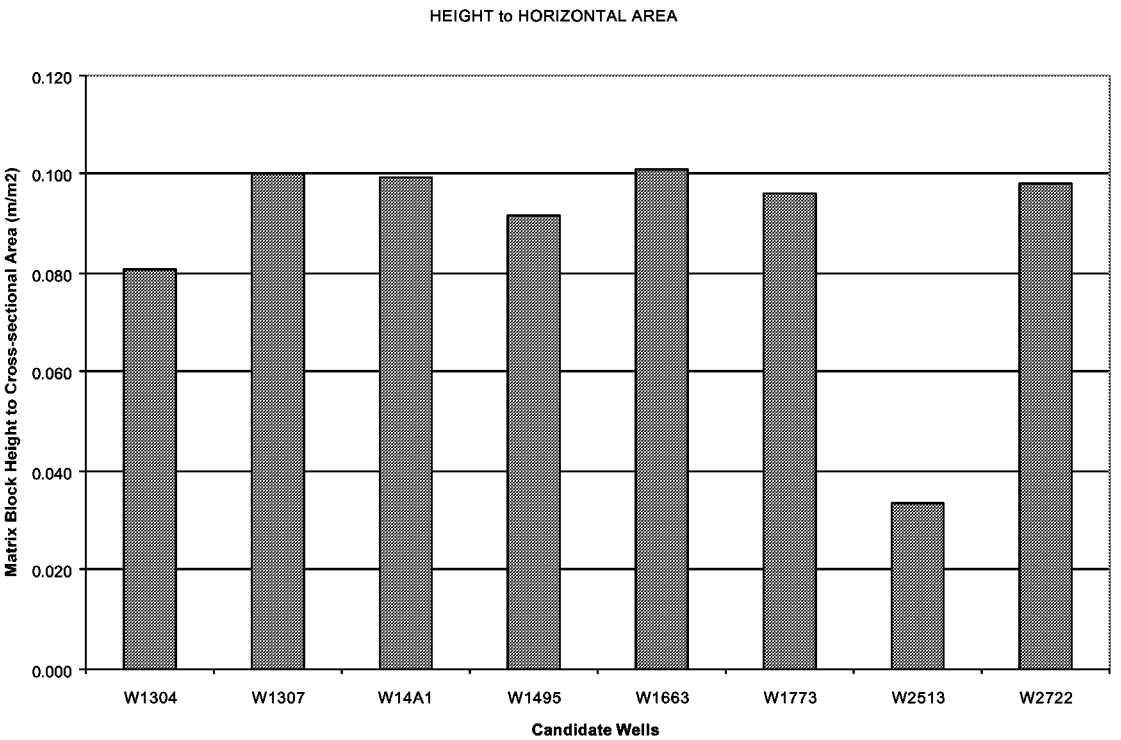

Figure 3-98 Median Ratio of Height to Horizontal Area

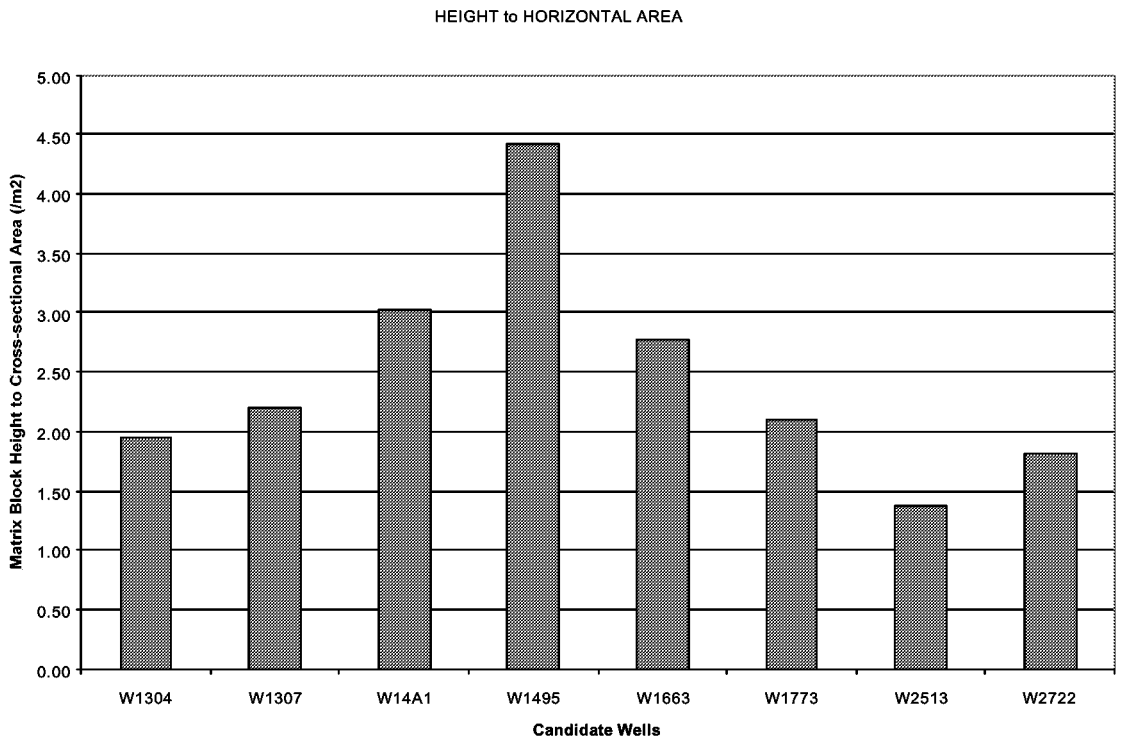

Figure 3-99 Mean Ratio of Height to Horizontal Area

3.4.2 Task 3.2 Strategic Plan, Stoney Point Reservoir Improvement

3.4.2.1 Strategic Placement and Water Control

Production problems at Stoney Point are mostly related to lack of understanding of the gas-water-oil contacts within compartments, and particularly the tendency for water breakthrough from overlying strata resulting in high water cuts within the reservoir production wells. The strategy developed for the Stoney Point field was therefore to use the DFN models to determine the sources and connectivity for oil and water phases, and the variation in connectivity within the reservoirs with depth, so that connectivity to overlying aquifers can be minimized.

3.4.2.2 DFN Analysis for IOR Strategic Plan

During this project work was initiated on implementation of Discrete Fracture Network modeling to support IOR strategies for Stoney Point. As part of this effort, compartment volumes and tributary volumes were calculated for the models. This was done using the program FraCluster, which was developed under previous DOE funding (Dershowitz et al., 1998).

A compartment is a region connected by a network of fractures. Relevant information that can be calculated about a compartment are its volume, surface area, and area projected on to a horizontal plane. Tributary volume analysis is a geometric calculation of the volume accessed by a well or set of wells in a fractured reservoir (Figure 3-100). Two different methods provide a maximum and minimum estimate of the volume.

- Hull volume is the volume contained in a convex hull surrounding a fracture network connected to the well. This is a maximum volume because it can include large blocks of matrix between fractures.
- Fracture thickness volume is the volume of a one-meter slab around each fracture connected to the well.

The results of the compartment size and area analysis for the Stoney Point field are shown in Figure 3-101 through Figure 3-103. As shown graphically in Figure 3-101a, at high fracture intensities the fractured reservoir defined by a convex hull includes all three portions of the structural model, from the northern fault through the step-over to the southern fault. This is likely to be too well connected compared to the real reservoir characteristics of Stoney Point. The medium (Figure 3-101b) and lower (Figure 3-101c) intensity models more closely represent the reservoir structure as indicated by reservoir development and well tests. The number of compartments and their projected areas and volumes are graphed in Figure 3-102 and Figure 3-103 and listed in Table 3-38. This analysis shows that at the lowest fracture intensity (0.001) five small compartments form, while at an intensity one order of magnitude higher, one very large compartment forms.

The well configuration shown in Figure 3-104 was assumed for the tributary volume calculations. Vertical wells are 200-m long and spaced 200 m apart (equivalent to about a 10 acre well spacing). Horizontal wells are 50 long and have the same spacing. The graph in Figure 3-105 and Table 3-39 show the insensitivity of the modeled reservoir to well orientation; in only one case did the SE horizontal well intersect fewer compartments than the vertical well. Much more important than well orientation is fracture intensity. Figure 3-106 also clearly demonstrates the importance of fracture intensity for well success. In the top frame 9 out of 12 wells successfully connect into a fracture network. In the bottom frame only four out of 12 simulated wells were successful.

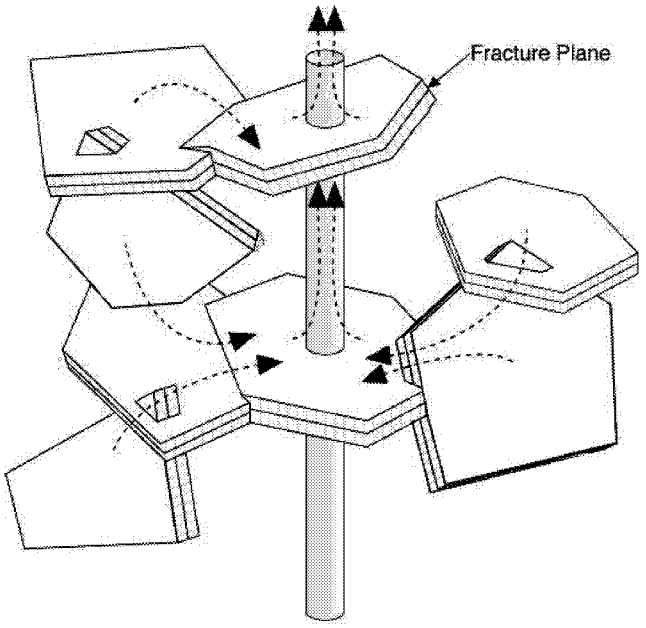

a) Slab Algorithm

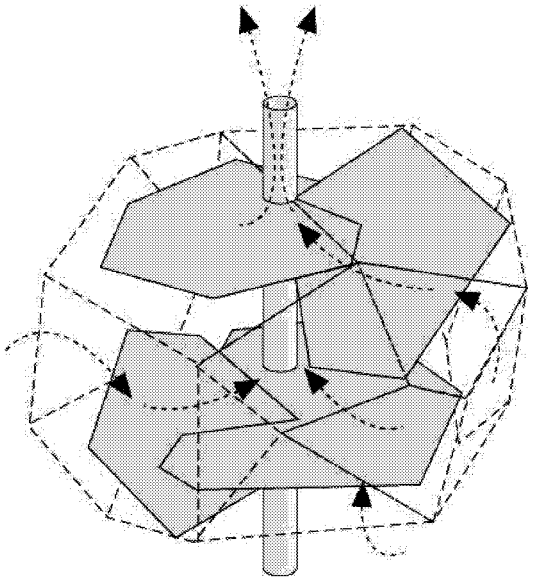

b) Convex Hull Algorithm

Figure 3-100 Tributary Drainage Volume Algorithms

Table 3-38 Compartment Area and Volume Analysis, Stoney Point

Projected Compartment Areas (m^2)					
P_{32}	# Compts.	Average	Std. Dev.	Minimum	Maximum
0.01	1	9.12e+5	0	9.12e+5	9.12e+5
0.005	2	4.68e+5	3.35e+5	1.3e+5	8.1e+5
0.0025	4	1.95e+5	2.21e+5	5.6e+4	5.8e+5
0.001	5	8.76e+5	3.19e+4	4.1e+4	1.4e+5
Compartment Volumes (m^3)					
P_{32}	# Compts.	Average	Std. Dev.	Minimum	Maximum
0.01	1	1.39e+8	0	1.39e+8	1.39e+8
0.005	2	6.81e+7	5.18e+7	1.6e+7	1.2e+8
0.0025	4	2.95e+7	3.62e+7	6.9e+7	9.3e+7
0.001	5	1.07e+7	4.33e+6	3.8e+6	1.7e+7

Table 3-39 Tributary Volume Analysis, Stoney Point

Vertical Well Tributary Volumes (m^3)					
P_{32}	# Compts.	Average	Std. Dev.	Minimum	Maximum
0.01	1	1.39e+8	0	1.39e+8	1.39e+8
0.005	2	6.81e+7	5.18e+7	1.67e+7	1.2e+8
0.0025	1	9.21e+7	0	9.21e+7	9.21e+7
0.001	2	1.01e+7	9.9e+5	9.03e+6	1.12e+7
NE Horizontal Wells Tributary Volumes (m^3)					
P_{32}	# Compts.	Average	Std. Dev.	Minimum	Maximum
0.01	1	1.39e+8	0	1.39e+8	1.39e+8
0.005	2	6.81e+7	5.18e+7	1.67e+7	1.2e+8
0.0025	1	9.21e+7	0	9.21e+7	9.21e+7
0.001	2	1.01e+7	9.9e+5	9.03e+6	1.12e+7
SE Horizontal Wells Tributary Volumes (m^3)					
P_{32}	# Compts.	Average	Std. Dev.	Minimum	Maximum
0.01	1	1.39e+8	0	1.39e+8	1.39e+8
0.005	1	1.2e+8	0	1.2e+8	1.2e+8
0.0025	1	9.21e+7	0	9.21e+7	9.21e+7
0.001	2	1.01e+7	9.9e+5	9.03e+6	1.12e+7

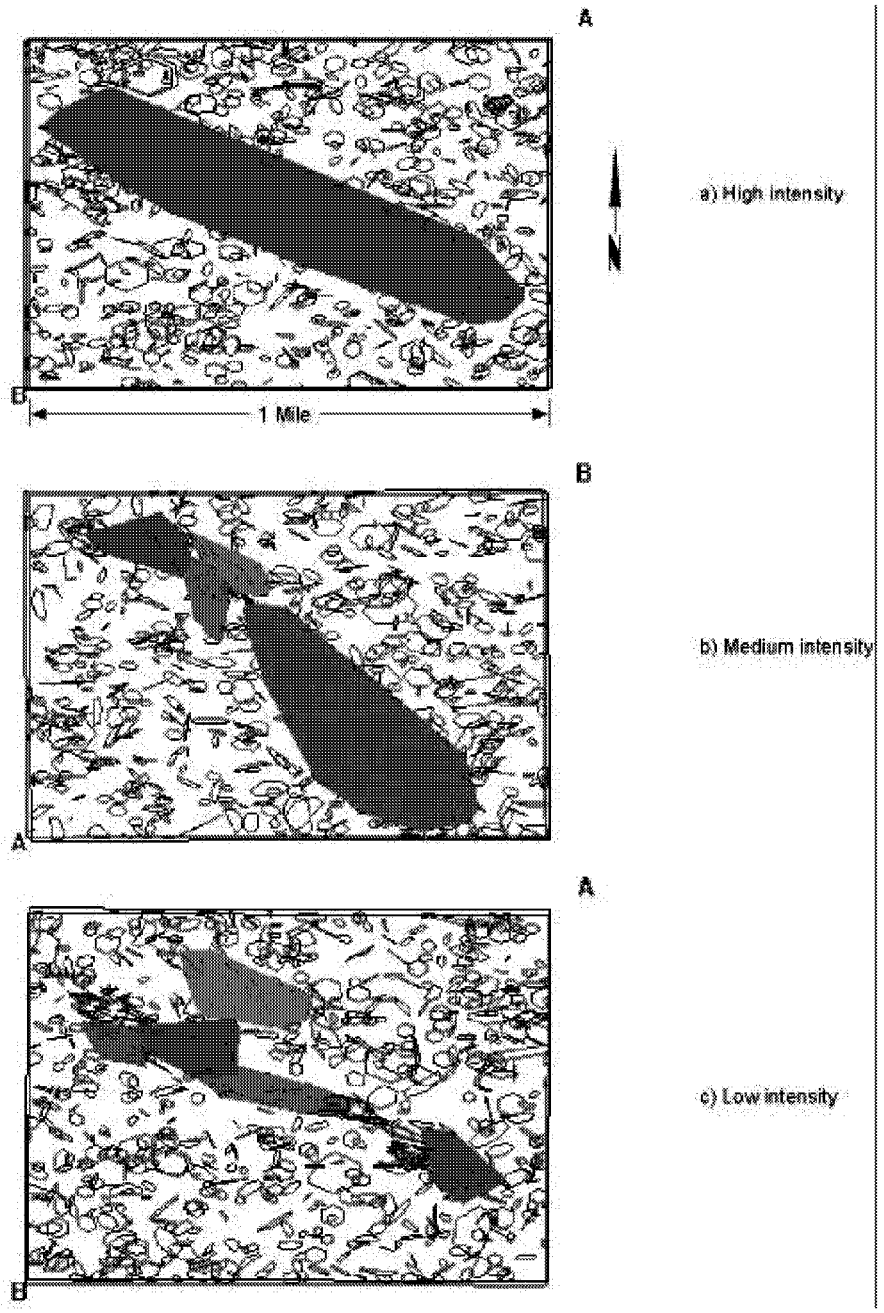

Figure 3-101 Compartments in Stoney Point DFN

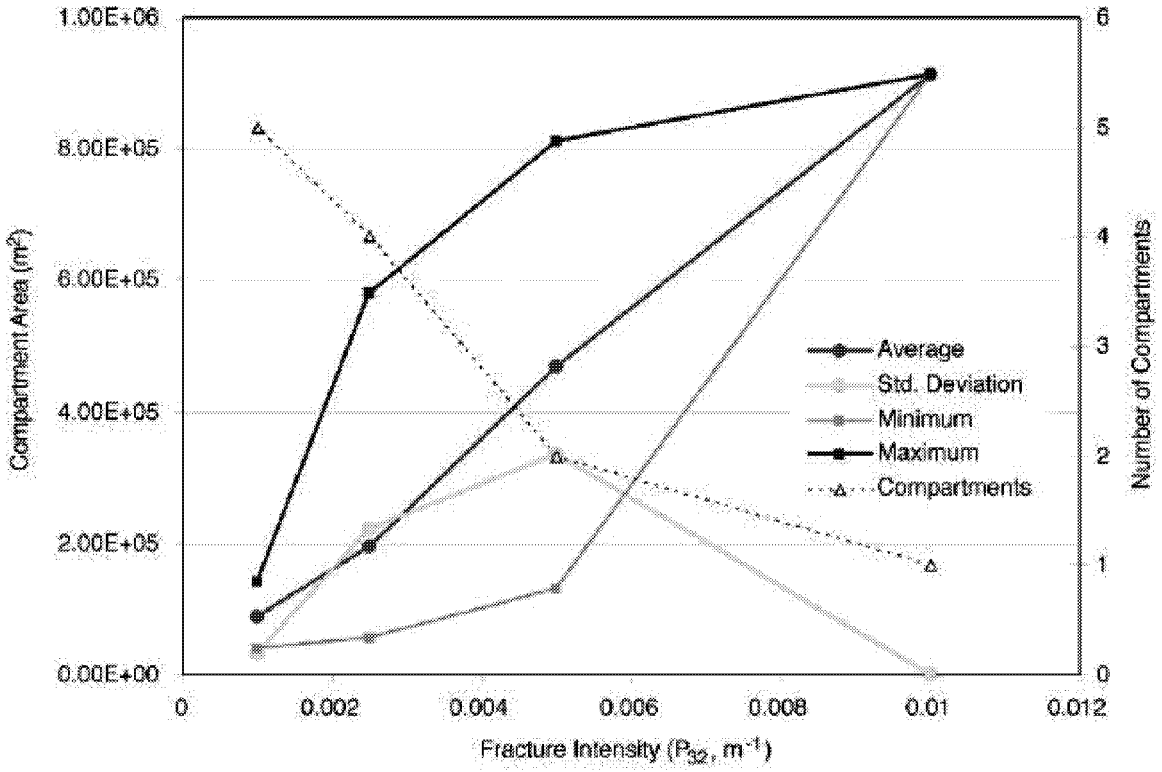

Figure 3-102 Projected Areas of Compartments

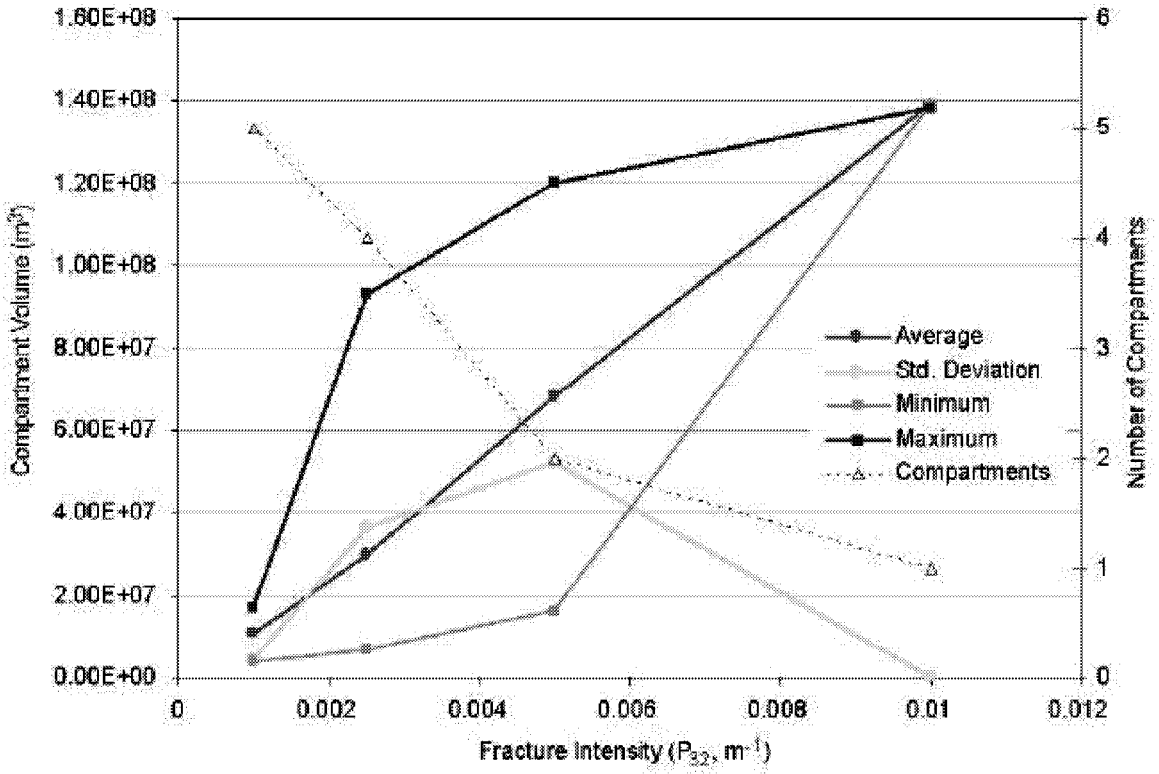

Figure 3-103 Volumes of Compartments in Stoney Point Model

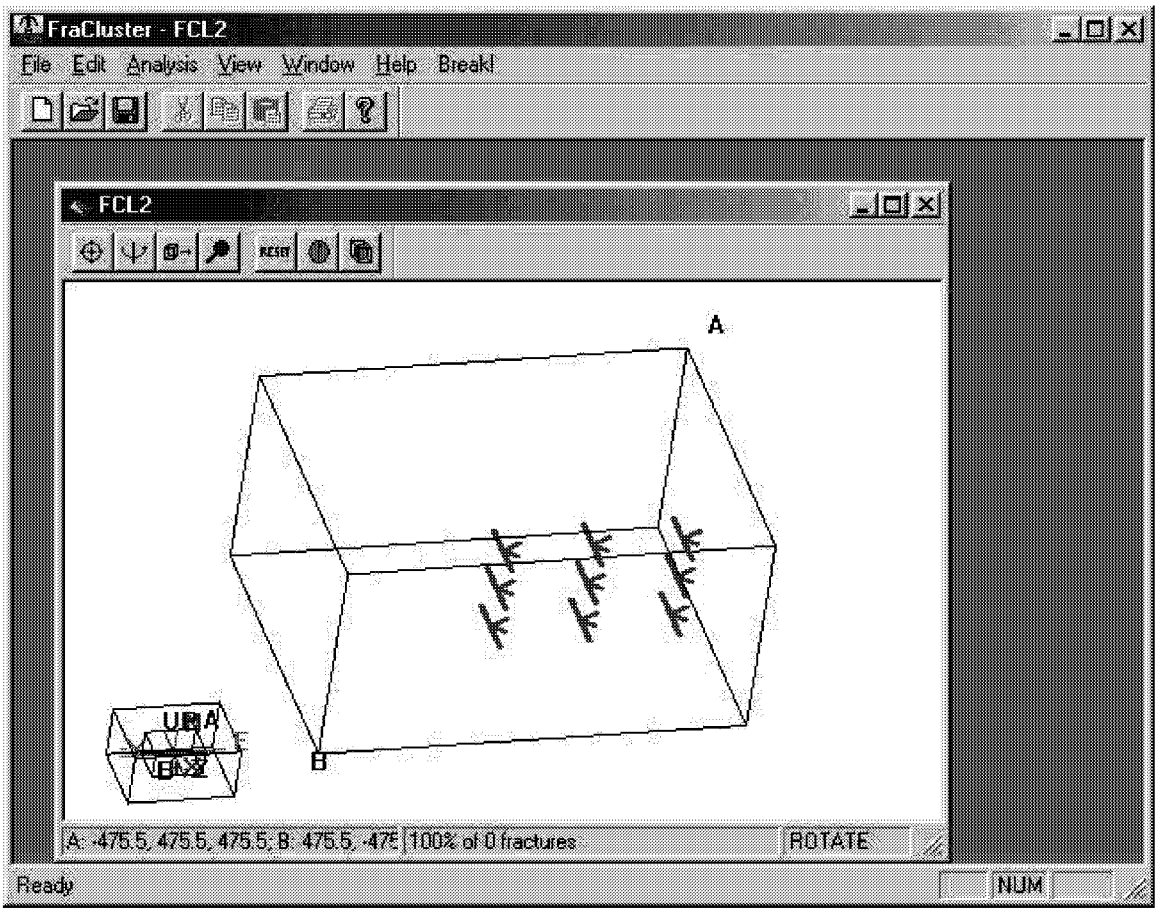

Figure 3-104 Well Configuration for Tributary Volume Analysis of Stoney Point Model

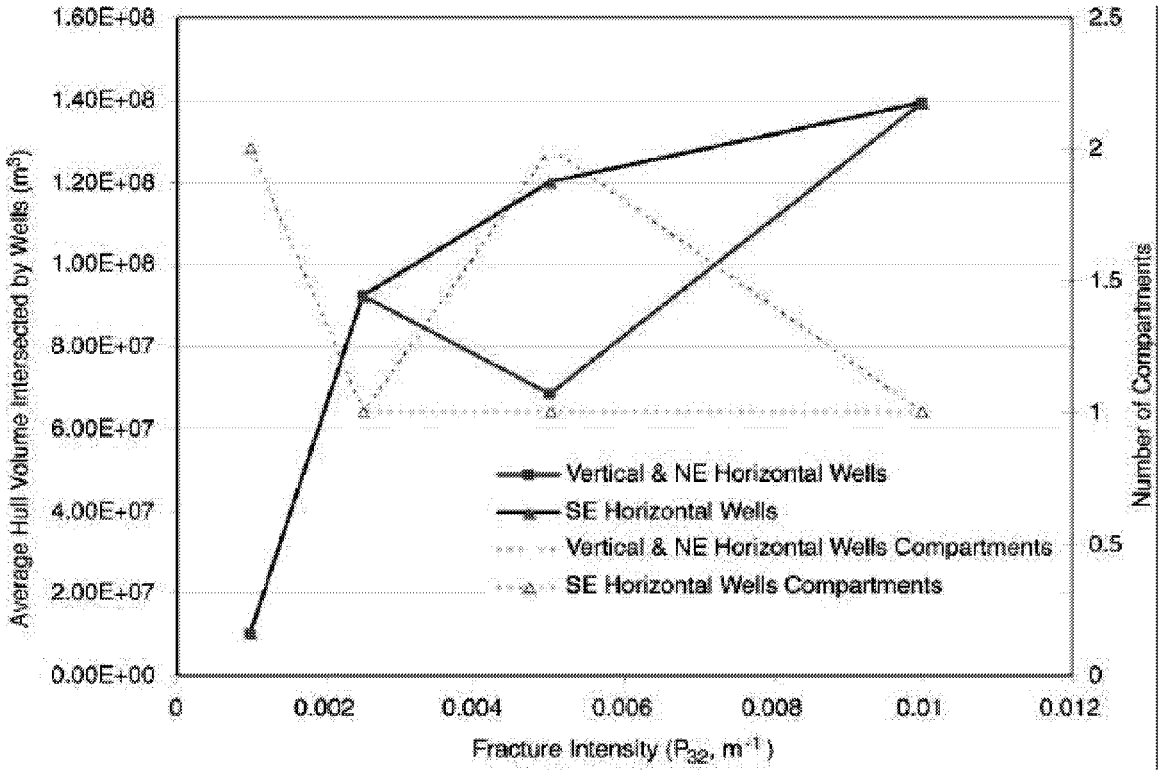

Figure 3-105 Tributary Volumes of Stoney Point Model

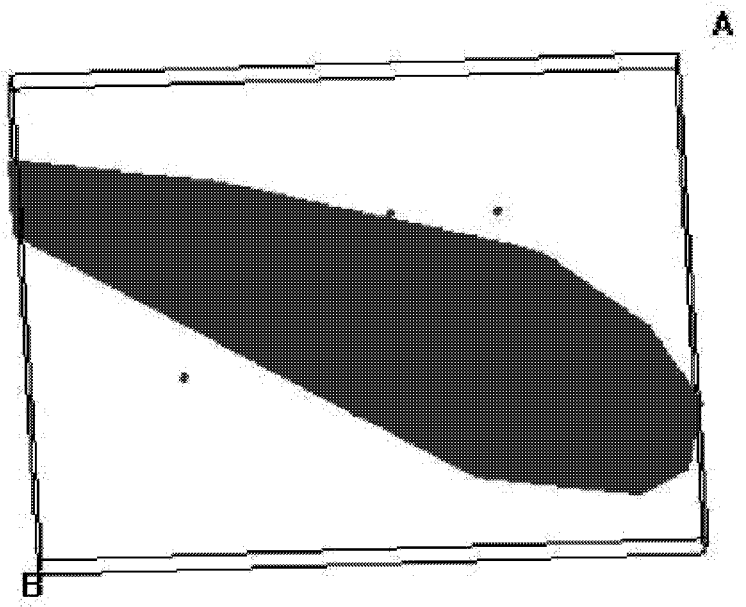

a) Medium intensity

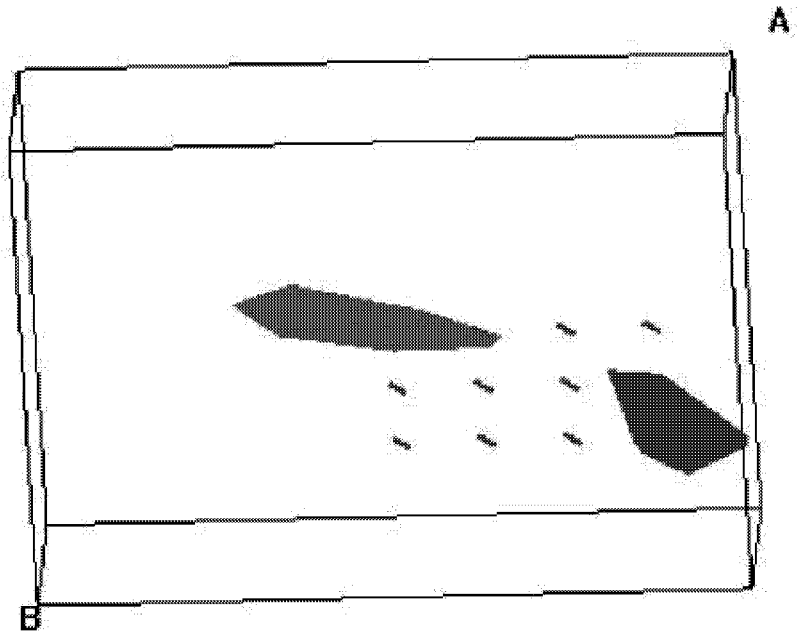

b) Low intensity

Figure 3-106 Well Pattern and Tributary Volumes Intersected in Stoney Point Model

3.4.3 Task 3.3 Strategic Plan: South Oregon Basin Reservoir Improvement

3.4.3.1 DFN Strategy for IOR

The IOR issue at South Oregon Basin relates to bypassed oil in the uppermost Phosphoria. Oil saturation in the upper Phosphoria is 80% whereas in the lower part of the formation saturation is as low as 30-40%. The perceived connectivity problem in the upper Phosphoria (B. Curran, pers. comm.) is that the pores are unconnected except by fractures. The engineering solution to this problem is more strategic well placements.

In the first progress report (Dershowitz, 1999) Golder identified that the primary tasks for South Oregon Basin would be "carrying out compartment and tributary volume calculations including a range of oriented well locations." Table 3-40 lists these engineering questions and the respective DFN solutions as well as other possible questions and solutions that we anticipate will be addressed in the future.

Table 3-40 IOR Engineering Issues, South Oregon Basin

Engineering operation or question	**DFN tool**
Well orientation and placement to maximum horizontal connection	Compartment and tributary volume calculations in FracCluster
Surface area to volume for gel (WALRUS) treatment	
What is the flow dimension of the fracture network in the Phosphoria?	Flow dimensional analysis
Can tracer tests which show NNE permeability trends be used for model calibration?	Flow solution and particle tracking in MAFIC

3.4.3.2 DFN Analysis for Strategic Plan

Strategic plan DFN modeling for the South Oregon Basin concentrated on the development of approaches for simulation of gel treatments. Discrete fracture network models can be used to directly model this entire process. First, the DFN model is derived and implemented based on site characterization data. The procedures for this are described in Dershowitz (1995). For the South Oregon basin, this model needs to combine

- deterministic features, including seismically detected structures and stratigraphic contacts,
- conditioned fractures, such as features identified in flow and FMI logs, and
- stochastic features, based purely on statistical information.

The region being modeled for assessment of gel treatment is illustrated in Figure 3-107. This figure includes an overlay of seismic features and structural contours.

The total volume of gel which can be taken by the grout injection at Connaghan 13 will be estimated by network analysis of the fractures intersecting the well. (Figure 3-108). In this

analysis, a graph theory search is used to search back into the fracture network from the well. The gel injection propagates into the fracture network according the heuristic rules which consider the fracture aperture, pressure, and phase composition of the fractures. The gel injection into the well proceeds until the gel reaches a prescribed limit. This provides an estimate for the gel injection volume to be expected.

The effect of gel treatment on the reservoir hydraulics is analyzed using a combination of flow modeling and pathways analysis. The permeability of each of the elements containing gel is set to zero as illustrated in Figure 3-109. This re-directs the pathways for water breakthrough to the production wells. The effect of gel treatment on production can be assessed by calculating the water saturated pathways to the production wells before and after the gel treatment.

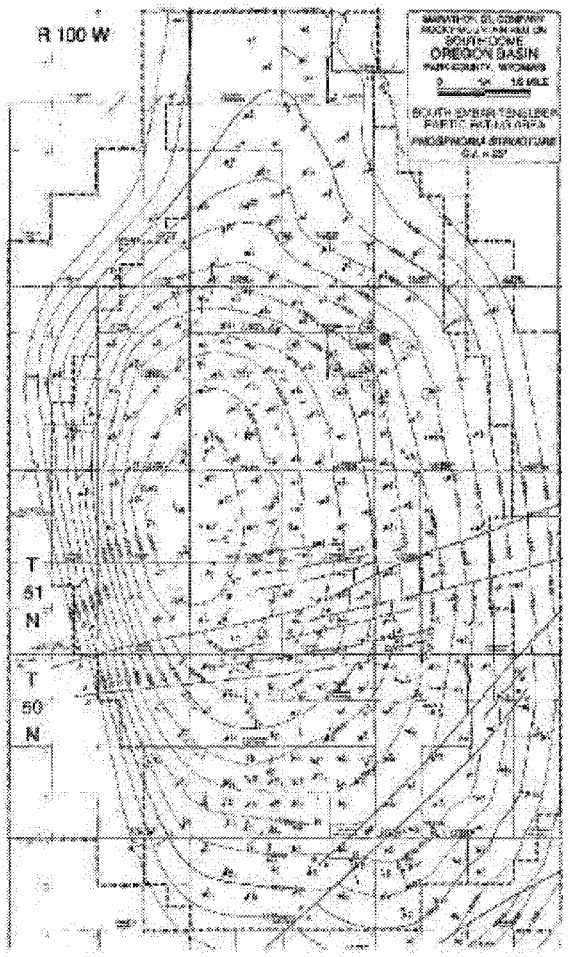

Figure 3-107 South Oregon Basin Gel Treatment Analysis Region

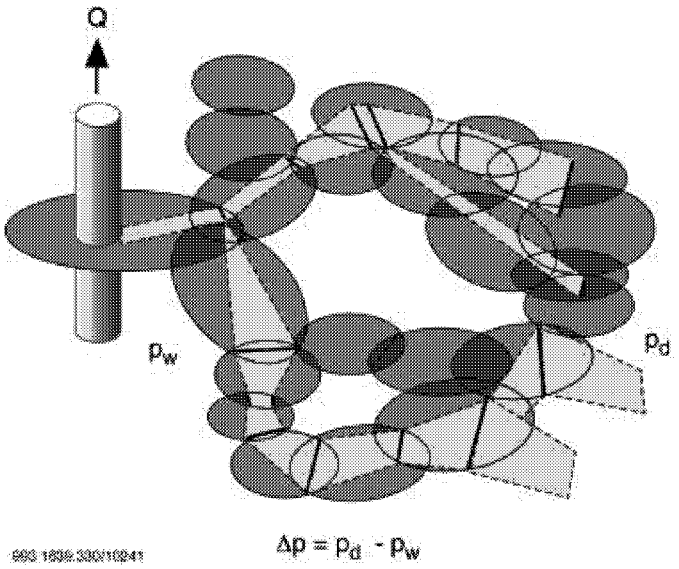

Figure 3-108 Network Analysis for Gel Treatment Design

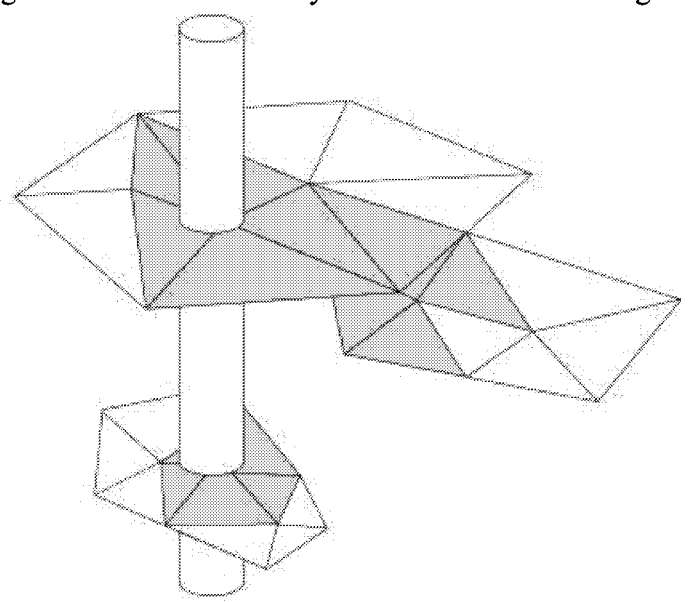

Figure 3-109 Gel Injection into Fracture Network

Connectivity analyses were carried out using the DFN model developed above. These models focused on the "percolation threshold", which defines the transition in connectivity with increases in fracture intensity. Results of this compartmentalization analysis are shown in Figure 3-110 and summarized in Table 3-41. At low fracture intensities (P_{32}<0.2 m^{-1}), the fractures do not connect into any significant compartments. At high fracture intensities (P_{32}>0.4 m^{-1}), the fractures connect the entire volume around the well. The transition from unconnected fractures to fully connected fractures is called the percolation threshold. For the South Oregon Basin Phosphoria model, this occurs near 0.3 m^2/m^3.

Table 3-41 Compartment Area and Volume Analysis, South Oregon Basin

Projected Compartment Areas (m^2)					
P_{32}	# Compts.	Average	Std. Dev.	Minimum	Maximum
0.2	5	482	343	180	1000
0.3	16	471	403	120	1500
0.4	10	680	1170	110	3848
0.6	2	1984	2636	120	3848
0.8	2	1984	2636	120	3848
Projected Compartment Volumes (m^3)					
P_{32}	# Compts.	Average	Std. Dev.	Minimum	Maximum
0.2	5	13100	13000	2600	35000
0.3	16	12700	16800	1500	56000
0.4	10	32000	78400	1100	269392
0.6	2	135246	189711	1100	269392
0.8	2	135396	189499	1400	269392

In order to assess the importance of well orientation on fracture volumes intersected, three wells were simulated: a SE-trending horizontal well, a NE-trending horizontal well, and a vertical well. The results of the tributary volume analysis are shown graphically in Figure 3-111and Figure 3-112, and are summarized in Figure 3-113 and Table 3-42. At low fracture intensity (P_{32}=0.2 m^{-1}) there are five compartments formed in the region surrounding the wells; however, none are intersected by the three perpendicular wells. In one instance in Figure 3-110, the well intersects the convex hull of a fracture network, but no fracture in that network intersects the well. If this geometry were the case in a real well, induced fracturing would prove very successful by making the connection to the fracture cluster. At a slightly higher fracture intensity (P_{32}=0.3 m^{-1}), large, vertical NE-SW trending compartments are formed. Because of their orientation, the SE-NW horizontal well, intersects the greatest fracture volume (Figure 3-113). The lower half of Figure 3-59 shows the difference between the hull volume and slab volume methods of calculating tributary drainage. The hull volume could be used to calculate the total oil accessible to a well. The flow from the matrix blocks into the fractures would depend upon the matrix permeability (due either to connected pores or microfracturing). The fracture slab volume is roughly 10% of the hull volume (Figure 3-113). This volume would correspond to the volume of injected fluids necessary for tracer tests and gel treatments. Table 3-43 summarizes the preliminary conclusions, which can be drawn from the cluster analysis of the Phosphoria formation at South Oregon Basin.

Table 3-42 Tributary Volume Analysis, South Oregon Basin

Vertical well Tributary Volumes		Hull volumes				Volumes from fracture thickness			
P_{32}	# compts.	mean	stdev	min	max	mean	stdev	min	max
0.2	0								
0.3	1	50100	0	50100	50100	6190	0	6190	6190
0.4	2	134000	133000	1100	270000	26000	25600	40000	62000
0.6	1	397000	0	397000	397000	112000	0	112000	112000
0.8	1	420000	0	420000	420000	150000	0	150000	150000
H1 well Tributary Volumes		Hull volumes				Volumes from fracture thickness			
P_{32}	# compts.	Mean	stdev	min	max	mean	stdev	min	max
0.2	0								
0.3	3	30000	17200	7900	51000	4430	1820	1900	6300
0.4	2	134000	133000	1100	270000	26000	25600	40000	62000
0.6	1	397000	0	397000	397000	112000	0	112000	112000
0.8	1	420000	0	420000	420000	150000	0	150000	150000
H2 well Tributary Volumes		Hull volumes				Volumes from fracture thickness			
P_{32}	# compts.	mean	stdev	min	max	mean	stdev	min	max
0.2	0								
0.3	1	50100	0	50100	50100	6190	0	6190	6190
0.4	1	267000	0	267000	267000	51500	0	51500	51500
0.6	1	397000	0	397000	397000	112000	0	112000	112000
0.8	1	420000	0	420000	420000	150000	0	150000	150000

Table 3-43 Implications of Tributary Volume Analysis, South Oregon Basin

Question	**Answer**	**Uncertainties or assumptions**
Does the Phosphoria break into compartments at the well scale?	Yes, if conductive fracture intensity is less than 25% of the geologic intensity (P_{32}<0.4 m^{-1})	Fracture size
Minimum volume of surfactant to inject?	~1,000,000 gallons 264* m^3	P_{32}=0.3 m^{-1} and assuming 1 m penetration around each fracture

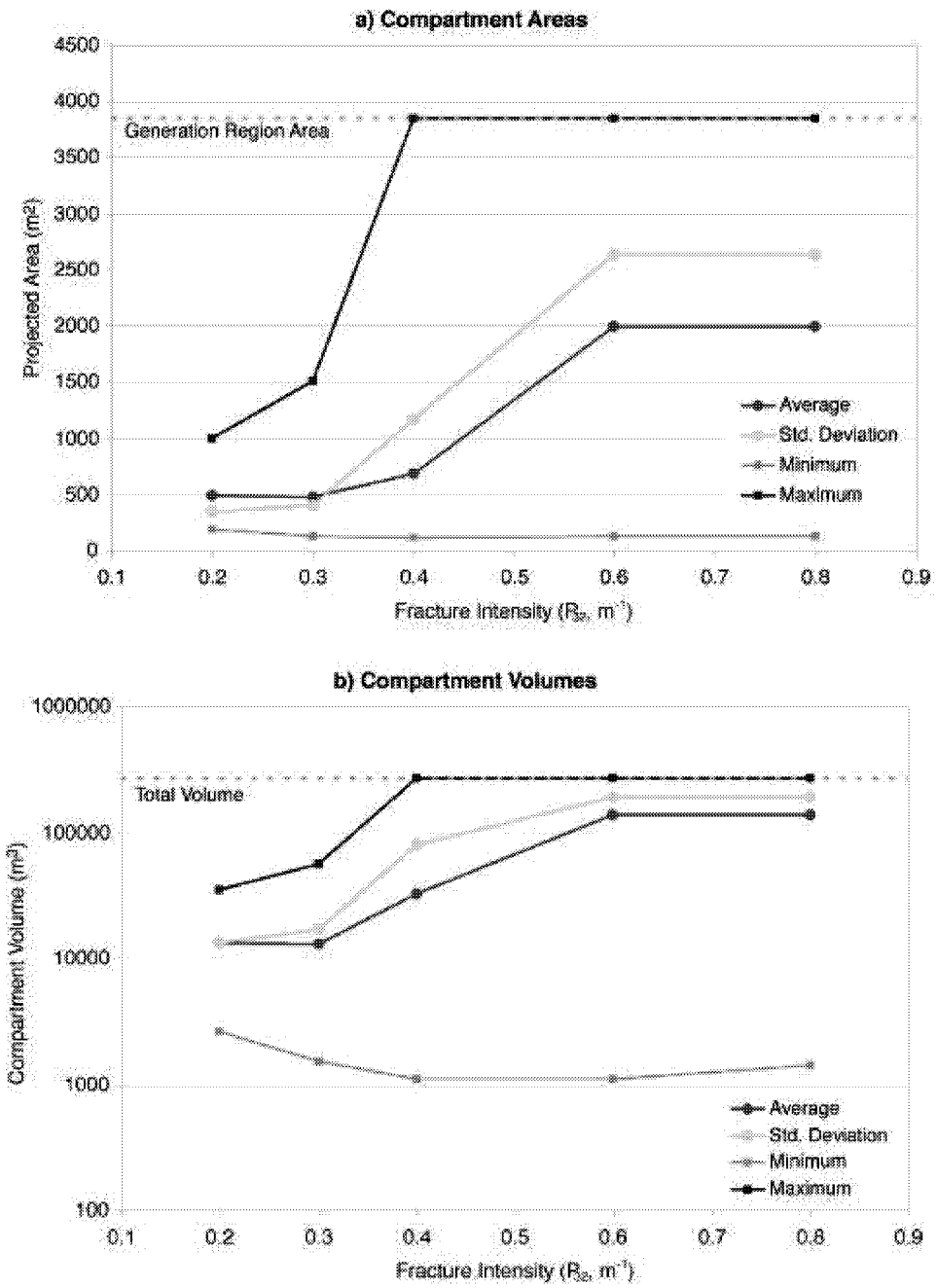

Figure 3-110 South Oregon Basin Compartmentalization Analysis

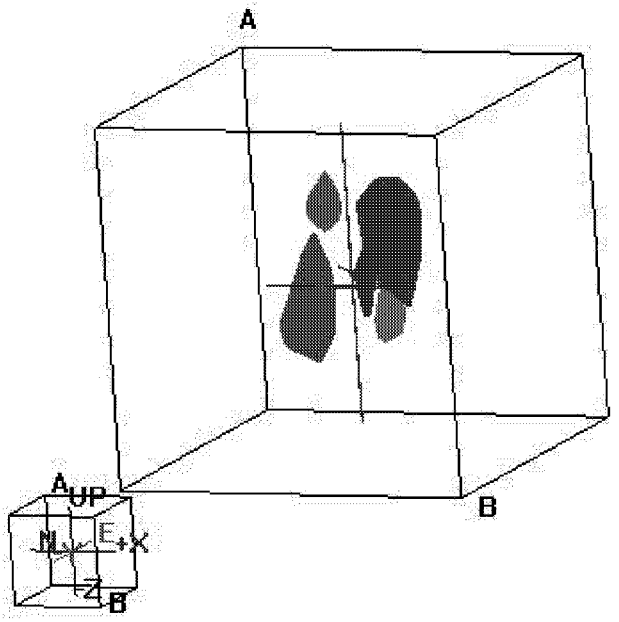

Figure 3-111 Tributary Volumes in South Oregon Basin Model for P_{32} = 0.2 Model

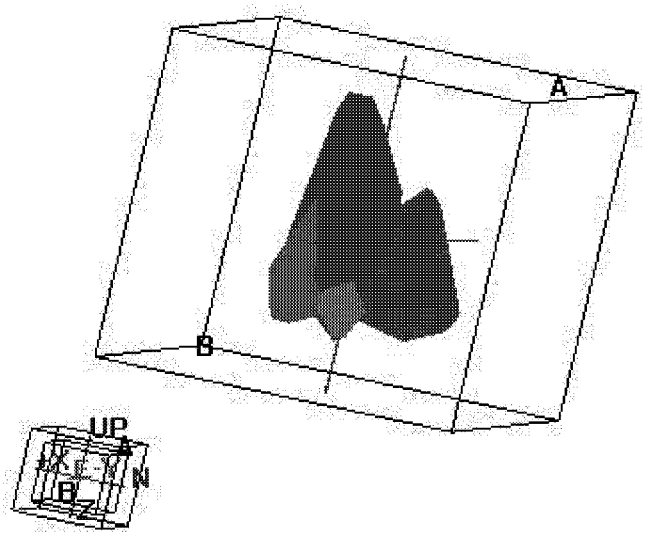

Figure 3-112 Tributary Volumes in South Oregon Basin Model for P_{32} = 0.3 Model

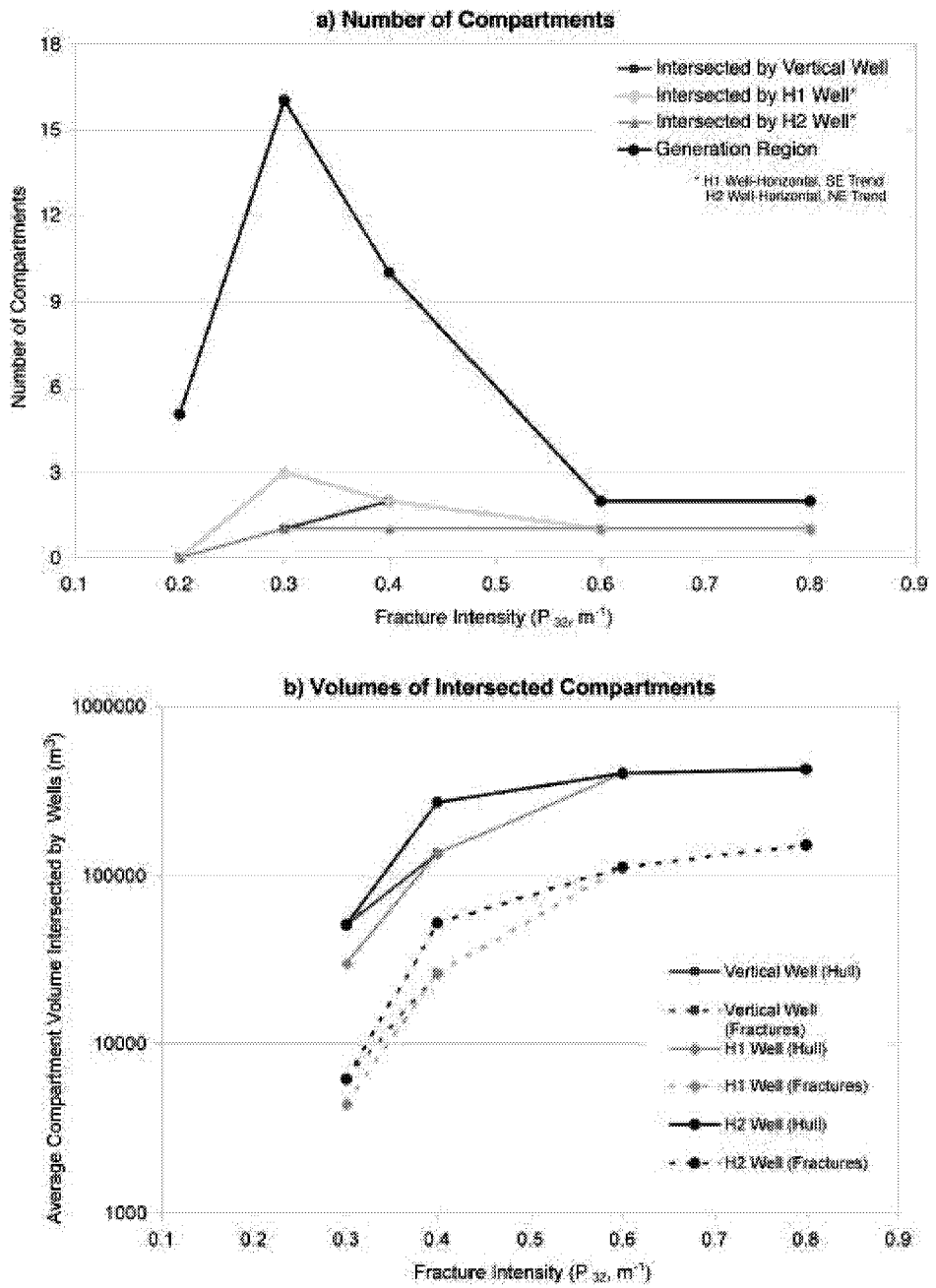

Figure 3-113 South Oregon Basin Tributary Volume Analysis

3.4.4 Task 3.4 Strategic Plan : North Oregon Basin Reservoir Improvement

Water injection is being used extensively in the North Oregon Basin Tensleep study site. The DFN model of the North Oregon basin will be used to evaluate the possible pathways for water migration from the Sidney #20 "C" zone horizontal well into the reservoir and affecting offsets (Figure 3-114). Results from this DFN modeling will be compared to field measurements to determine whether the DFN model is successful in assessing the well-connected high-conductivity fracture clusters.

The strategic plan for the North Oregon Basin will also include analysis of hydraulic compartment connectivity to specific wells to evaluate gel-squeezes of injectors vs. producers and the utility of horizontal wells in the Tensleep formation.

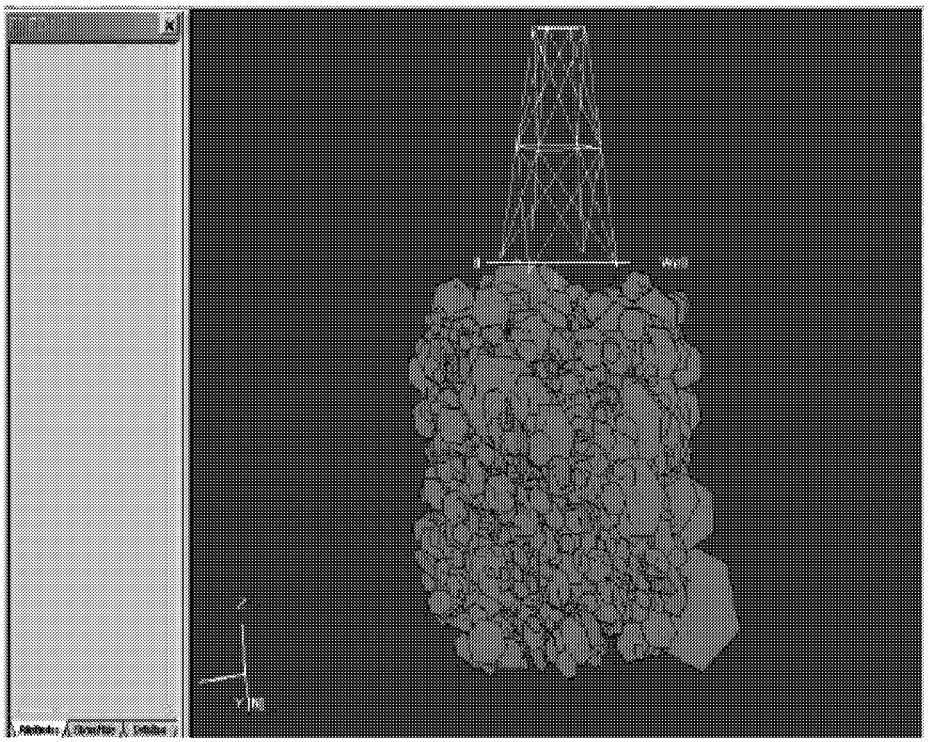

Figure 3-114 Tensleep Formation Water Injection DFN Study.

3.4.4.1 Gel Treatment DFN Analysis

The IOR issues at the North Oregon Basin relate to bypassed oil in the "ABC" sandstones of the upper Tensleep. Dolomite intrabeds, water-filled fractures, deformation bands, and dune cross-bedding all create horizontal compartments in the upper Tensleep reservoir (Table 3-44). Breaches of the horizontal compartments occur where fracturing in the dolomite intrabed between the C and D sandstone allows communications across the dolomites. These vertical connections allow coning from the lower Tensleep, which has a much higher, water-cut than the upper Tensleep. Engineering solutions to these problems are (Dershowitz et al. 1999);

- Targeting of water injection for waterfloods,
- Horizontal drilling to connect low recovery portions of the reservoir, and

- Gel placement to reduce water cycling.

Table 3-44 IOR Engineering Issues at North Basin

IOR Problem	DFN Strategic Plan
Fractures in dolomites connect upper and lower Tensleep	Calculate pore volume and connectivity of lower and upper Tensleep for gel treatment design
Baffles due to crossbedding and deformation bands create compartments in ABC Tensleep sands	Determine optimal drilling directions to connect compartments
Water-filled fractures create compartments	

Like the South Oregon Basin DFN model of the Phosphoria formation the preliminary DFN model of the Tensleep formation at North Oregon basin was used to evaluate compartment size and locations distributions, and to calculate tributary volumes for specific well patterns. These results can be used to estimate the at-well connectivity of the reservoir and the volumes of water or gel injection necessary to achieve IOR objectives.

The results of the compartment area and volume analyses are illustrated in Figure 3-115 and summarized in Figure 3-116 and Table 3-45. Like the South Oregon Basin Phosphoria model, the percolation limit of the North Oregon Basin Tensleep model occurs near 0.3 m^2/m^3. Unlike the Phosphoria model, compartments in the Tensleep are horizontal due to the dolomite layering, rather than vertical.

Figure 3-117 and Figure 3-118 illustrate tributary drainage volumes for different well configurations. Figure 3-117 shows tributary volumes for a NE trending horizontal well, and Figure 3-118 shows tributary drainage volumes for a system of vertical and horizontal wells. Figure 3-119 and Table 3-46 summarize the results of this analysis. The shape and size of these wells can be used to assist in the design of strategic completions and well locations.

Table 3-45 Compartment Area and Volume Analysis, North Oregon Basin

Projected Compartment Areas (m^2)					
P_{32}	# Compts.	Average	Std. Dev.	Minimum	Maximum
0.2	7	204	146	77	550
0.4	32	339	352	67	1400
0.6	6	882	1790	49	4900
0.8	1	4900	0	4900	4900
Projected Compartment Volumes (m^3)					
P_{32}	# Compts.	Average	Std. Dev.	Minimum	Maximum
0.2	7	1490	1320	520	4600
0.4	32	3240	4280	340	16000
0.6	6	26200	57400	120	156000
0.8	1	156000	0	156000	156000

Table 3-46 Tributary Volume Analysis, North Oregon Basin

SE Horizontal well Tributary Volumes		**hull volumes**				**volumes from fracture thickness**			
P_{32}	number of	mean	stdev	min	max	mean	stdev	min	max

	compartments								
0.2	0								
0.4	3	9100	4550	4400	15000	2010	1170	920	3700
0.6	1	154000	0	154000	154000	48400	0	48400	48400
0.8	1	156000	0	156000	156000	60200	0	60200	60200
NE Horizontal well Tributary Volumes		**hull volumes**				**volumes from fracture thickness**			
P_{32}	number of compartments	mean	stdev	min	max	mean	stdev	min	max
0.2	0								
0.4	3	6150	4180	530	11000	1270	743	220.	1900
0.6	1	154000	0	154000	154000	48400	0	48400	48400
0.8	1	156000	0	156000	156000	60200	0	60200	60200
Vertical well Tributary Volumes		**hull volumes**				**volumes from fracture thickness**			
P_{32}	number of compartments	mean	stdev	min	max	mean	stdev	min	max
0.2	0								
0.4	1	15300	0	15300	15300	3640	0	3640	3640
0.6	1	154000	0	154000	154000	48400	0	48400	48400
0.8	1	156000	0	156000	156000	60200	0	60200	60200

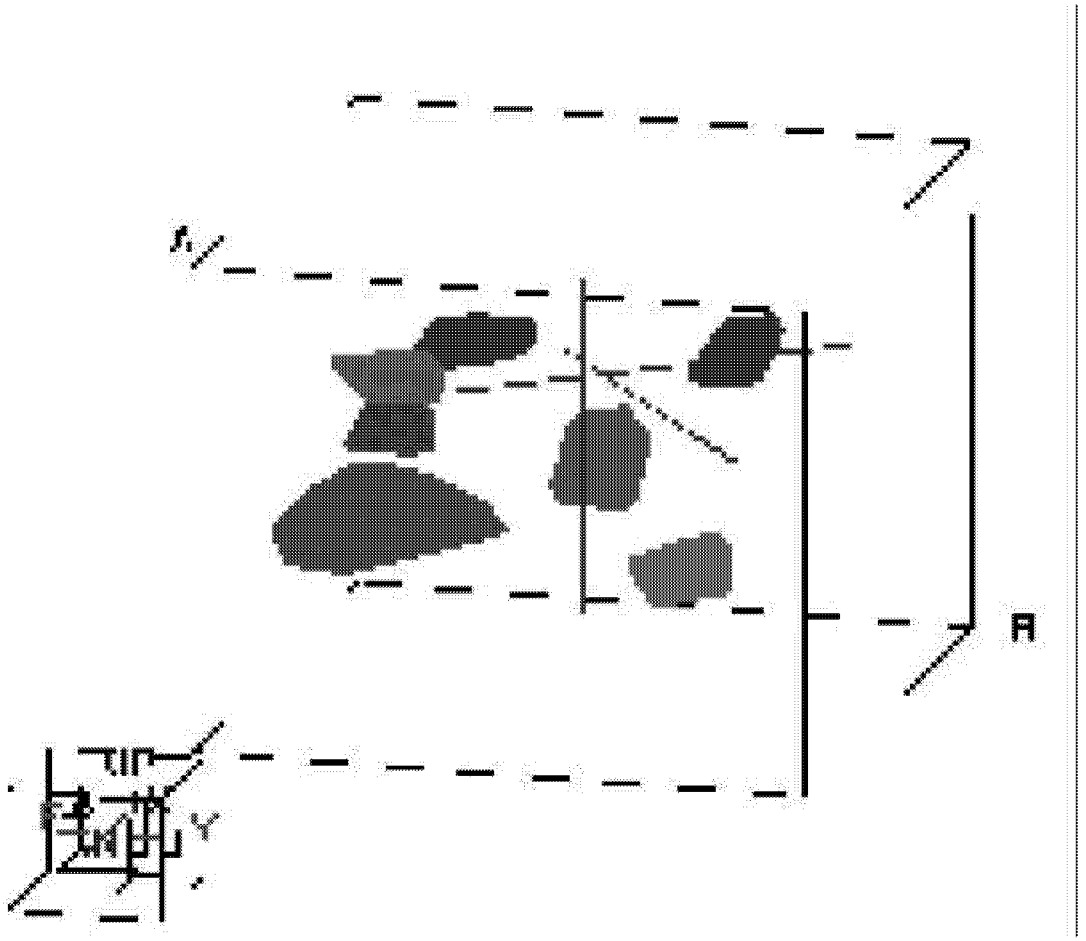

Figure 3-115 Compartments in North Oregon Basin Model with P_{32}=0.2

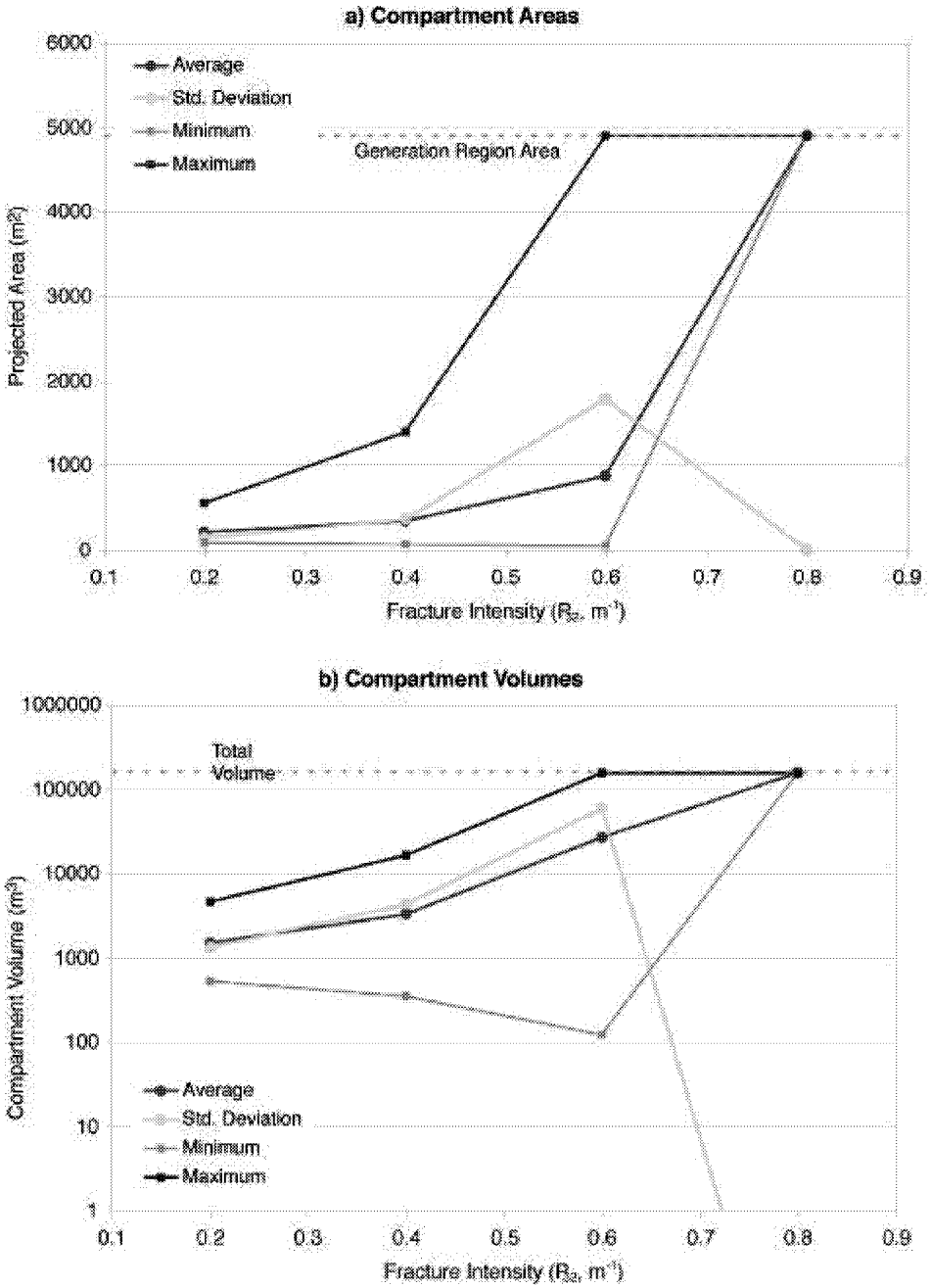

Figure 3-116 North Oregon Basin Compartmentalization Analysis

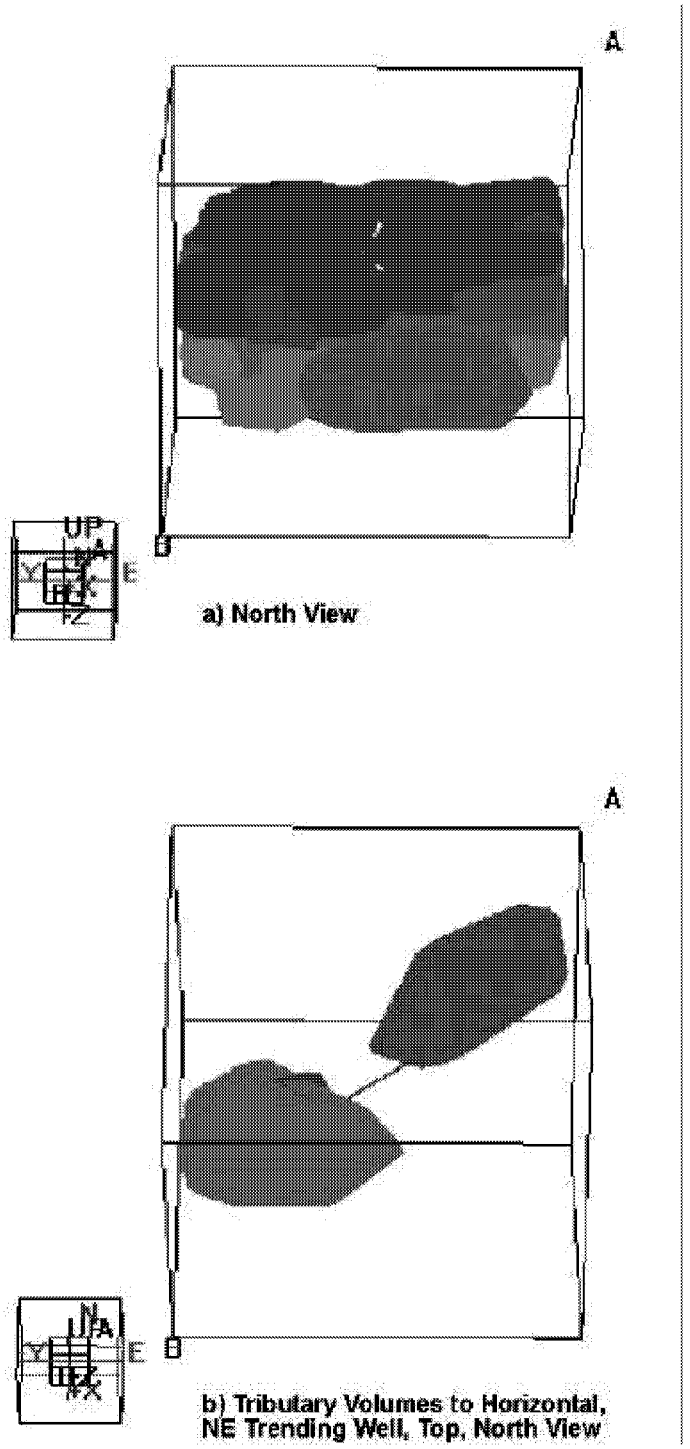

Figure 3-117 North Oregon Basin Model with P_{32} = 0.2

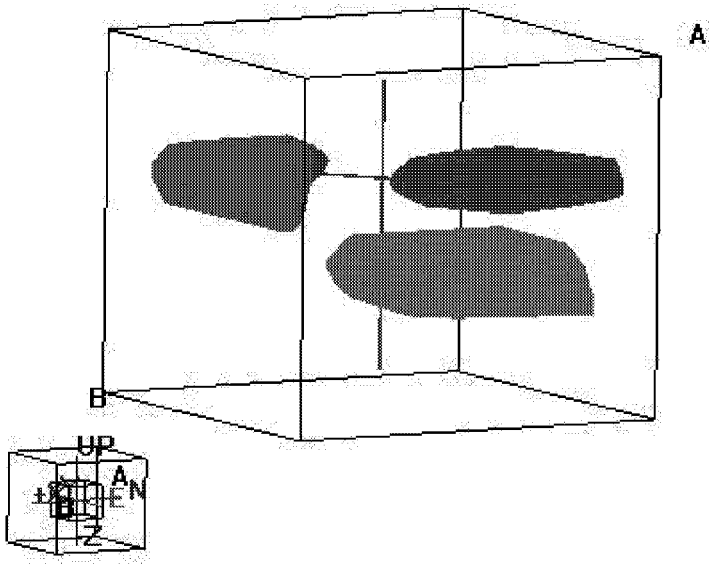

Figure 3-118 Side View of Tributary Volumes of Vertical and Horizontal Wells in North Oregon Basin Model with $P_{32} = 0.2$

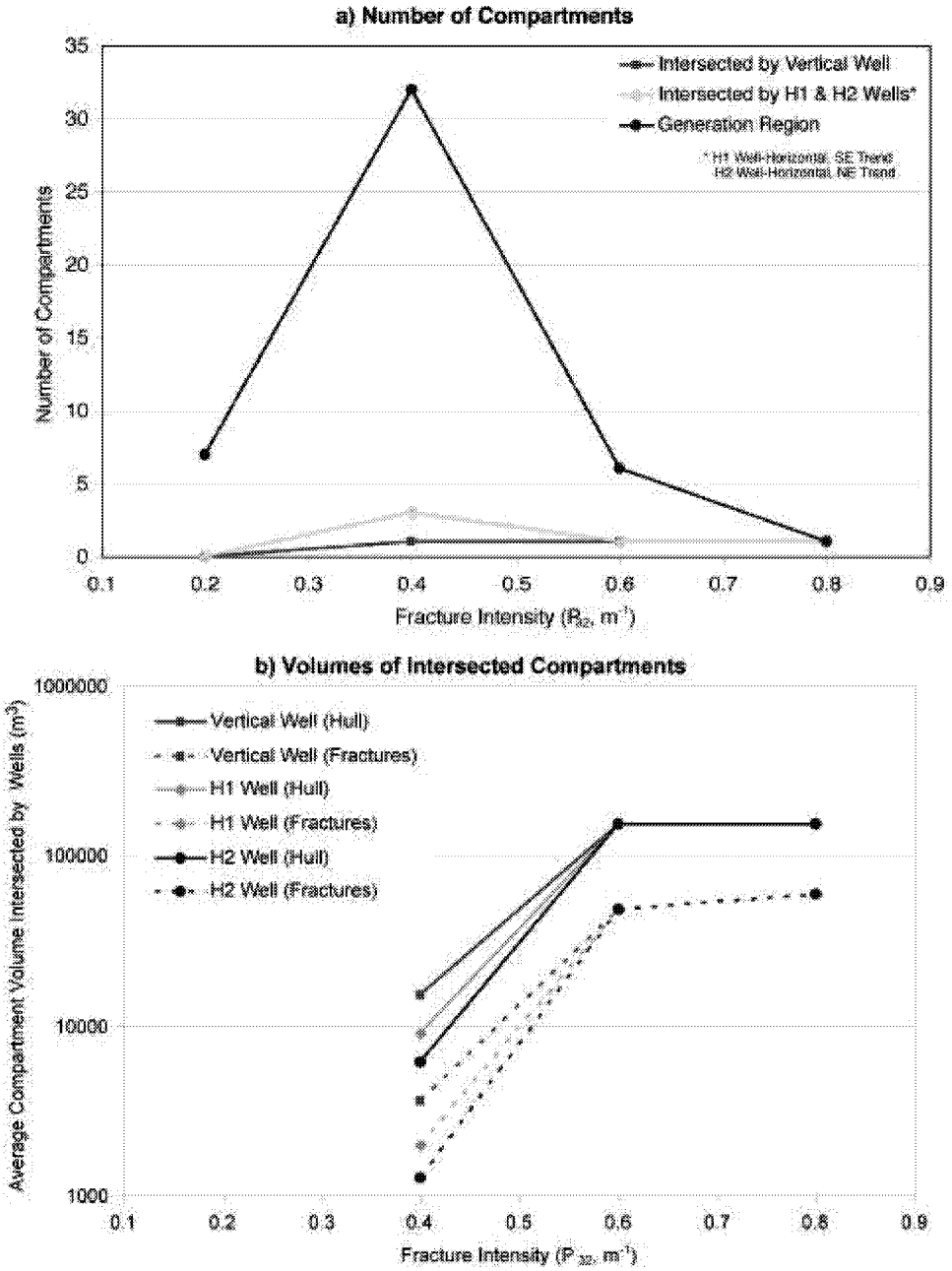

Figure 3-119 North Oregon Basin Tributary Volume Analysis

Table 3-47 summarizes the preliminary conclusions, which can be drawn from the cluster analysis of the North Oregon Basin.

Table 3-47 Implications of Tributary Volume Analysis, North Oregon Basin

Question	Answer	Uncertainties or assumptions
Does the Tensleep break into fracture compartments at the well scale?	Yes, if conductive fracture intensity is less than 75% of the geologic intensity (P_{32}<0.6 m^{-1})	Fracture size
What is the best well orientation to minimize gel volume?	NE Horizontal	
What is the minimum volume of surfactant to inject?	~340,000 gallons 264 gallons/m^3	P_{32}=0.4 m^{-1} and assuming 1 m penetration around each fracture

3.5 Task 4: Application Tasks

3.5.1 Task 4.1 Reservoir IOR Demonstration, Yates Field

3.5.1.1 Introduction to Strategic Completion Analysis

An extensive study was carried out to support the use of strategic completion for IOR in the Yates field. The goal of this study is to help identify possible areas where new completions might yield the best production. A part of the strategy to delineate promising areas involves estimation of what areas appear to have fracture characteristics favorable to production. Five wells in the Tract 17 area (1304, 1307,1495, 2513 and 2722) have production information that can be compared to fracture network characteristics. This makes it possible to look for a relation between fracturing and favorable production characteristics.

However, even if a useful predictive relation is found, there needs to be a method of evaluating whether this relation is likely to hold elsewhere in the field. A necessary, though not sufficient, condition for the relations to persist throughout the area of interest is that the controls on matrix block parameters are similar. For example, it may be that in the five test wells, low values of block height to block width ratios are generally due to increased spacing of subvertical fractures, and not due to a decrease in subhorizontal fracture spacings. However, in some areas of the field, it might be found that low values of block height to block width are strongly correlated with decreased subhorizontal fracture spacings. In this case, it would be riskier to assume that the production characteristics related to low block height to block width ratios in the five test wells would also correspond to the low values of the ratio in this other area.

A way to evaluate whether the matrix block characteristics that appear to be associated with desirable production characteristics in the five test wells are generally seen in the surrounding areas is to explore the statistical correlation structure of the matrix block parameters for the five-well test set and for the full well test set. For example, a high negative correlation between block height to width ratio to vertical fracture spacing in the test set would be compared with the full

well set results. If a similarly high negative correlation were found, then the assumption would be that the reasons for low ratio were the same, and the production characteristics associated with this ratio could be inferred with some confidence. If, on the other hand, the correlation in the full test set was not significant with vertical fracture spacing, but positively correlated with the spacing of one or more subvertical fracture sets, then this would indicate that inference of the production characteristics associated with block height to block width ratio is more uncertain.

3.5.1.2 Strategic Completion Modeling

The strategic completion modeling carried out using the Yates Field Tract 17 DFN Model, developed during the first half of 2000, was adapted to support IOR activities. The parameters for this model are summarized in Table 3-48.

To obtain a statistical understanding of the connectivity pattern of the field, 100 realizations were run. Each of these model realizations was processed to obtain the spatial distribution of matrix block shape parameters. It is hoped that the correlation between these matrix block shape parameters and the well test results will provide a basis for strategic completion design.

The matrix block shape parameters are listed in Table 3-49.

The values for each parameter are calculated from fracture spacing histograms calculated in three orthogonal directions for the region measuring 100 m by 100 m in horizontal extent centered on each well. The spacing histograms are computed by projecting lines through the DFN model, and recording the intersection points to each successive fracture. The intersection points are used to determine the spacing values.

The lines are located with uniform probability throughout the DFN model region. One hundred lines were generated for each direction for each model. This typically produced spacing histograms for each direction consisting of hundreds of spacing values. To compute the various matrix block shape parameters shown in Table 3-49, uniformly random draws were made from each relevant spacing distribution. For a particular DFN model, this procedure made it possible to calculate, through random sampling, a distribution of values for each matrix block shape parameter. As a result, it was possible to calculate various statistical parameters from the results. These consisted of the minimum and maximum values, and the mean, median and standard deviation for each individual DFN model realization.

Table 3-48 Conditioned DFN Model for TAGS Support Simulations (Extended Tract 17 Model)

Parameter	Model Assumption
Discrete Features	Large scale deterministic faults are not considered. Fractures representing features located during well logging are modeled by conditional simulation with correlation to curvature and shale content.
Orientation Distributions	The stochastic fracture orientation is correlated to curvature as described in Table 3-1 of Dershowitz et al, 1998
Size Distribution (Stochastic Fractures)	Power Law distribution D=1.81, minimum radius = 1ft, truncated between 1m and 100 m. (Dershowitz et al., 1998)
Intensity (Stochastic Fractures)	Intensity of stochastic fractures P_{32} is 0.105 to 0.21 m^2/m^3, depending on shale content and porosity. This corresponds to a vertical well fracture intensity of 1/30 to 1/60 m.
Transmissivity	Lognormal distribution, mean = 4.44 10^{-4} m^2/s, standard deviation =1.923 10^{-3} m^2/s
Aperture	Correlated to fracture transmissivity using the cubic law, such that a = $0.011T^{0.33}$
Model Dimensions and Boundary Conditions	Model is approximately 500 m by 500 m by 500 m, centered around each well.

Table 3-49: Variable name acronyms and calculation definitions for matrix block shape factors

Parameter	How Calculated
S_x	The dimension of the matrix block in the east-west direction, measured in meters
S_y	The dimension of the matrix block in the north-south direction, measured in meters
S_z	The vertical height of the matrix block, measured in meters
X/Y	The ratio of the two horizontal dimensions, calculated as S_x/S_y
Z/X	The ratio of the vertical dimension to the east-west dimension, calculated as S_z/S_x
Z/Y	The ratio of the vertical dimension to the north-south dimension, calculated as S_z/S_y
Z/A	The ratio of the vertical matrix block height to the horizontal cross-sectional area, measured in meters
Z/H	The ratio of the vertical matrix block height to the average horizontal dimension, measured in meters. The average horizontal dimension is computed as the average of S_x and S_y.
Sigma	The sigma factor, defined as $\sigma = 4\left(\frac{1}{S_x^2}+\frac{1}{S_y^2}+\frac{1}{S_z^2}\right)$

Since there were multiple realizations of the underlying DFN model, there were multiple values of median, mean, etc for each shape parameter for each well location. The statistics such as mean or median pertain to the properties of the many matrix blocks in the near-well region for a single DFN model realization.

3.5.1.3 Well Productivity Correlation

The most important aspect of this study is in establishing a correlation between the 18 matrix block shape measures (mean and median of the 9 factors) identified in Table 3-49 and well

productivity. Table 3-50 summarizes the correlations among the 18 matrix block shape factors for the five wells (1304, 1307, 1495, 2513, and 2722). Generally, mean and median sigma factors are negatively correlated with fracture spacing, as would be expected, since sigma factor is inversely proportional to the square of the fracture spacing. The median sigma factor is negatively correlated to all fracture spacings, whereas the mean sigma factor is far more strongly correlated to X (east-west) spacings than to spacings in the other directions. Mean sigma factor may be somewhat unique among all of the 18 shape parameters, in that it is the most sensitive to outliers. Thus, correlations to the mean sigma factor may not be as meaningful as the correlations to the median sigma factor.

The sigma factor is also positively correlated to the two ratios that describe matrix block height to matrix block width or cross-sectional area (z2h and z2a, respectively). This suggests that high values of sigma factor correspond to matrix blocks that are much taller than they are wide. The most significant correlation between median sigma factor and any matrix block shape parameter is with the height to the east-west dimension (z2x). Its coefficient (0.892) is significant at $\alpha = 0.05$. It is also positively correlated with other measures (for example, z2y) of block height to horizontal dimension.

The next analyses looks at whether the correlation structure seen among the 18 parameters in the five test well DFN models persists in the much larger area. Table 3-51 shows the correlation coefficients among the 18 matrix block shape measures for the surrounding wells. The shape measures z2a and z2h correlate well with both decreased north-south and east-west fracture spacing, and with blocks that are taller than they are wide, as did the test well set data. There are significant *positive* correlations with fracture spacing in the vertical direction for z2a and z2h for the total data set, and also to ratios such as z2x and z2y. This suggests that the factors that lead to tall blocks are in general related to decreased fracture spacings in the horizontal directions, and slightly increased fracture spacing in the vertical direction. The strong, statistically significant correlations between median z2x and z2y ratios with median z2h and z2a ratios suggest that it is a decrease in the vertical fracture intensity that produces tall blocks, rather than an increase in fracture spacing in the vertical direction. This is the same pattern that is shown for the five well test set correlation matrix (Table 3-50).

Thus, comparison of the correlation coefficients suggests that the relations between production characteristics and the matrix block shape parameters found in the five test wells is likely to be useful in other areas of the model.

Table 3-52 and Table 3-53 present the correlations and the correlation significance between well productivity and matrix block shape measures for the five wells 1304, 1307, 1495, 2513, and 2722. Correlations are sorted by the magnitude of correlation, from most positive to most negative. Although many matrix block shape parameters show what appear to be strong negative or positive correlations, the low number of samples (5) makes all but the correlation with mean sigma factor insignificant at the $\alpha = 0.05$ level. Two additional parameters, although not significant at the 0.05 level, may still be important and provide insight into what factors control the sigma factor; these are the mean block height to cross-sectional area (z2a mean) and the median ratio between the vertical set spacings (x2y median).

Productivity appears to correlate to a general decrease in fracture spacings, especially when the resulting matrix blocks are relatively taller than they are wide. Favorable areas for strategic completion may be where fracture spacings in one or both of the horizontal directions is relatively low, and high ratios of z2h or z2a occur (along with larger values of sigma factor). Attractive

areas may also be identified by the confluence of lower fracture spacings and values of z2a, z2h or sigma factor that reflect blocks that are taller than they are wide.

Table 3-50: Correlation coefficients for the fracture models surrounding the five wells: 1304, 1307,1495, 2513 and 2722

	X Spacing Mean	X Spacing Median	Y Spacing Mean	Y Spacing Median	Z Spacing Mean	Z Spacing Median	Z to H Mean	Z to H Median	Z to A Mean	Z to A Median	X to Y Mean	X to Y Median	Z to X Mean	Z to X Median	Z to Y Mean	Z to Y Median	Sigma Factor Mean	Sigma Factor Median
X Spacing Mean	***1.000***																	
X Spacing Median	***0.896***	***1.000***																
Y Spacing Mean	***0.991***	0.869	***1.000***															
Y Spacing Median	0.825	0.746	0.750	***1.000***														
Z Spacing Mean	***0.946***	0.736	***0.924***	***0.884***	***1.000***													
Z Spacing Median	0.376	-0.011	0.466	0.050	0.456	***1.000***												
Z to H Mean	***-0.924***	***-0.913***	***-0.935***	-0.680	-0.777	-0.329	***1.000***											
Z to H Median	***-0.896***	-0.852	***-0.893***	-0.765	-0.800	-0.328	***0.969***	***1.000***										
Z to A Mean	-0.735	***-0.931***	-0.734	-0.457	-0.491	0.096	0.820	0.687	***1.000***									
Z to A Median	***-0.906***	-0.809	***-0.930***	-0.657	-0.802	-0.503	***0.975***	***0.972***	0.682	***1.000***								
X to Y Mean	-0.583	-0.336	-0.539	-0.650	-0.759	-0.275	0.228	0.224	0.124	0.238	***1.000***							
X to Y Median	-0.310	0.085	-0.308	-0.455	-0.551	-0.662	0.164	0.336	-0.399	0.347	0.450	***1.000***						
Z to X Mean	***-0.883***	-0.770	***-0.920***	-0.585	-0.773	-0.569	***0.960***	***0.943***	0.665	***0.995***	0.213	0.340	***1.000***					
Z to X Median	***-0.897***	***-0.883***	***-0.896***	-0.737	-0.775	-0.292	***0.984***	***0.996***	0.746	***0.972***	0.194	0.253	***0.945***	***1.000***				
Z to Y Mean	***-0.946***	***-0.954***	***-0.911***	-0.829	-0.863	-0.087	0.848	0.790	0.833	0.763	0.603	0.065	0.723	0.808	***1.000***			
Z to Y Median	***-0.916***	***-0.918***	***-0.907***	-0.774	-0.795	-0.237	***0.983***	***0.990***	0.778	***0.956***	0.243	0.219	***0.924***	***0.996***	0.853	***1.000***		
Sigma Factor Mean	-0.224	-0.579	-0.218	0.008	0.053	0.493	0.337	0.150	0.809	0.138	-0.155	-0.857	0.130	0.235	0.448	0.280	***1.000***	
Sigma Factor Median	-0.773	-0.478	-0.831	-0.465	-0.780	-0.863	0.750	0.750	0.335	0.863	0.386	0.614	***0.892***	0.726	0.534	0.692	-0.220	***1.000***

H_0: The two parameters are not correlated.
Entries in RED indicate negative correlations that are significant at the 95% level
Entries in BLUE indicate positive correlations that are significant at the 95% level
All other entries are NOT significant at the 95% level

Table 3-51: Correlation coefficients for the fracture models surrounding all wells.

	X Spacing Mean	X Spacing Median	Y Spacing Mean	Y Spacing Median	Z Spacing Mean	Z Spacing Median	Z to H Mean	Z to H Median	Z to A Mean	Z to A Median	X to Y Mean	X to Y Median	Z to X Mean	Z to X Median	Z to Y Mean	Z to Y Median	Sigma Factor Mean	Sigma Factor Median
X Spacing Mean	***1.000***																	
X Spacing Median	***0.915***	***1.000***																
Y Spacing Mean	***0.894***	***0.816***	***1.000***															
Y Spacing Median	***0.844***	***0.794***	***0.936***	***1.000***														
Z Spacing Mean	0.066	0.056	0.070	***0.081***	***1.000***													
Z Spacing Median	***0.086***	***0.085***	***0.092***	***0.100***	***0.844***	***1.000***												
Z to H Mean	***-0.691***	***-0.649***	***-0.725***	***-0.675***	***0.122***	***0.092***	***1.000***											
Z to H Median	***-0.784***	***-0.708***	***-0.807***	***-0.716***	***0.252***	***0.233***	***0.855***	***1.000***										
Z to A Mean	-0.003	-0.007	-0.021	-0.035	0.014	0.004	***0.306***	0.026	***1.000***									
Z to A Median	***-0.757***	***-0.696***	***-0.792***	***-0.716***	0.041	0.032	***0.878***	***0.941***	0.034	***1.000***								
X to Y Mean	0.031	0.019	0.045	0.063	-0.049	-0.031	-0.039	-0.056	***0.164***	-0.049	***1.000***							
X to Y Median	***0.206***	***0.256***	***-0.173***	***-0.244***	-0.037	-0.026	0.046	-0.014	***0.097***	0.005	-0.041	***1.000***						
Z to X Mean	***-0.120***	***-0.118***	***-0.080***	-0.060	***0.096***	***0.127***	***0.148***	***0.142***	0.057	***0.123***	-0.010	***-0.127***	***1.000***					
Z to X Median	***-0.783***	***-0.742***	***-0.694***	***-0.611***	***0.214***	***0.191***	***0.797***	***0.913***	0.001	***0.892***	-0.050	***-0.286***	***0.150***	***1.000***				
Z to Y Mean	0.024	0.012	0.042	0.065	-0.044	-0.027	-0.034	-0.051	***0.242***	-0.046	***0.926***	-0.049	-0.018	-0.046	***1.000***			
Z to Y Median	***-0.669***	***-0.599***	***-0.802***	***-0.734***	***0.209***	***0.197***	***0.838***	***0.925***	0.061	***0.904***	-0.058	***0.262***	***0.107***	***0.745***	-0.055	***1.000***		
Sigma Factor Mean	-0.041	-0.045	-0.020	-0.028	0.073	***0.098***	0.039	0.015	0.017	0.001	-0.002	-0.028	***0.557***	0.018	0.001	0.020	***1.000***	
Sigma Factor Median	***-0.542***	***-0.521***	***-0.567***	***-0.541***	***-0.419***	***-0.377***	***0.651***	***0.547***	0.037	***0.735***	0.003	-0.003	***0.109***	***0.563***	0.009	***0.552***	-0.019	***1.000***

H_0: The two parameters are not correlated.
Entries in RED indicate negative correlations that are significant at the 95% level
Entries in BLUE indicate positive correlations that are significant at the 95% level
All other entries are NOT significant at the 95% level

Table 3-52 Correlation coefficients with barrels of fluid per day for the five wells 1304, 1307,1495, 2513 and 2722

Parameter	Correlation Coefficient with BFPD
Sigma Mean	***0.891***
z2a Mean	0.707
z2y Mean	0.558
Sz Median	0.531
x2y Mean	0.246
z2h Mean	0.219
z2y Median	0.189
z2x Median	0.115
z2h Median	0.046
z2a Median	0.015
z2x Mean	-0.011
Sz Mean	-0.116
Sy Median	-0.180
Sy Mean	-0.244
Sigma Median	-0.269
Sx Mean	-0.284
Sx Median	-0.561
x2y Median	-0.722

H_0: The two parameters are not correlated.
Entries in RED indicate negative correlations that are significant at the 95% level
Entries in BLUE indicate positive correlations that are significant at the 95% level
All other entries are NOT significant at the 95% level

Table 3-53: Probability (p-values) for the regression coefficients between independent matrix block shape parameters and BFPD for five wells: 1304, 1307,1495, 2513 and 2722

Independent Variable	p Intercept	p Slope
Sigma Mean	0.066	***0.042***
x2y Median	0.155	0.169
z2a Mean	0.655	0.181
Sx Median	0.200	0.325
z2y Mean	0.850	0.328
Sz Median	0.430	0.357
Sx Mean	0.490	0.640
Sigma Median	0.313	0.661
x2y Mean	0.881	0.690
Sy Mean	0.572	0.692
z2h Mean	0.922	0.723
z2y Median	0.950	0.761
Sy Median	0.550	0.772
Sz Mean	0.786	0.853
z2x Median	0.779	0.854
z2h Median	0.768	0.942
z2a Median	0.454	0.981
z2x Mean	0.476	0.986

H_0 for intercept: Intercept = 0.0
H_0 for slope: Slope = 0.0

Entries in BLUE indicate positive correlations that are significant at the 95% level
All other entries are NOT significant at the 95% level

3.5.1.4 Strategic Completion Recommendations

Contour maps were calculated from the well-based block shape statistics in order to provide a spatial distribution of block statistics for use in strategic completion design. For example, to produce a contour map showing the median sigma factor, the median sigma factor was first computed at each well location in each of the DFN realizations. The median values at each well location was then contoured.

The calculations were carried out at well locations, rather than on a regular grid, because results for these shape parameters were needed for specific wells, in order to evaluate them for possible workovers. Since the well density is quite high and even throughout the region, the interpolation required for contouring is mathematically robust, as can be seen by the dense well control on any of the maps.

Median values for the various shape parameters have been chosen for mapping since they are probably the most "stable" values. Many of the parameters, such as the sigma factor, can have extreme values if any of the spacing values are small and they are randomly selected to compute the parameter. As a result, the mean value is highly skewed by this one random draw of a small spacing. The median, on the other hand, is not nearly as sensitive to data outliers as is the mean. For this reason, the maps shown are based on median, rather than mean block values for each DFN realization.

Figure 3-120 through Figure 3-128 show contoured values of the selected matrix block shape parameters. Regions where the parameter is visually low or high are indicated, as well as the approximate boundaries of Tract 17 for reference.

Only the mean values for the matrix block shape factors are shown, with the exception of sigma factor, since (1) the correlations are stronger between the mean spacings and the z2a, z2h and sigma factor parameters, and (2) they are not as strongly impacted by outliers as are other parameters such as sigma factor.

Figure 3-120 and Figure 3-121 show that there is a region of higher east-west and north-south fracture spacings encompassing much of Tract 17 and extending to the south and east of Tract 17. The regions outlined for both these maps are largely coincident. A region of high vertical fracture spacing occurs in the central portion of the mapped area, and overlaps but does not entirely coincide with the other two spacing maps.

The maps showing the ratio of block height to either east-west or north-south spacing (Figure 3-123 and Figure 3-124, respectively) show that while the former parameter is homogeneously distributed throughout the area, the ratio of block height to north-south dimension is not. Areas where blocks are not tall relative to block height roughly coincide to the regions where fracture spacings were greater than the regional average, namely, in Tract 17 and to the southeast of Tract 17.

As might be expected, the maps showing block height to block cross-sectional area (z2a) Figure 3-126 and block height to average horizontal dimension (z2h). Figure 3-127 shows lower values coincident with the regions of higher than average horizontal spacings. Consideration of the variation of fracture spacing in the horizontal direction vs. the variation in the vertical direction, it is clear that this difference in block height to block width is primarily due to difference in the fracture spacings in the horizontal directions, rather than in the vertical direction. Figure 3-128,

which shows median sigma factor, further substantiates this. The regions with low sigma factor spatially coincide with regions of greater fracture spacings in the horizontal directions.

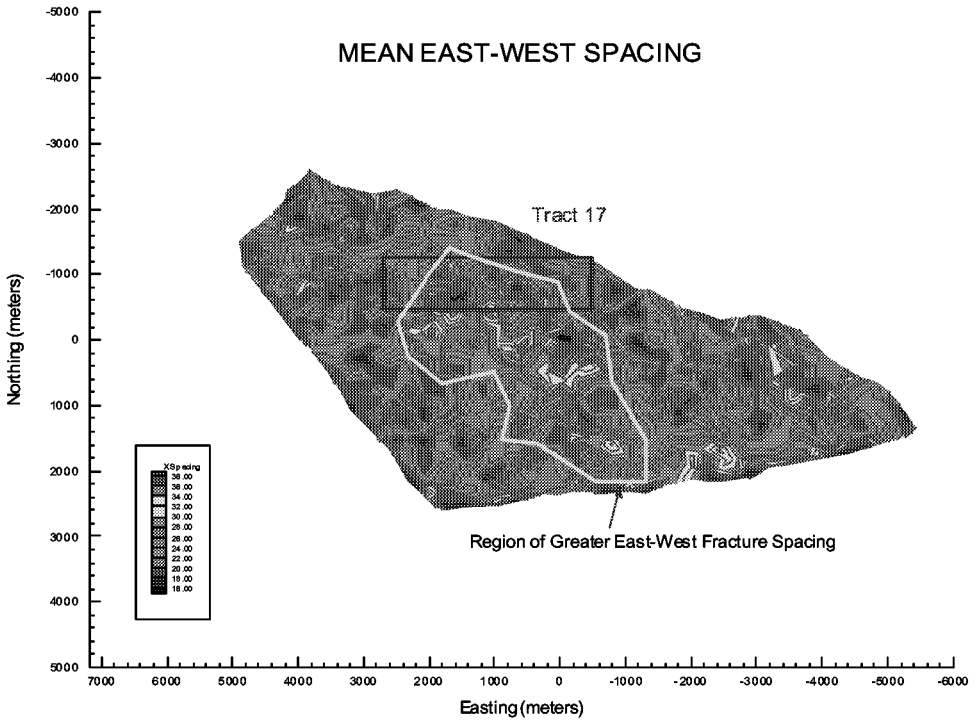

Figure 3-120: Mean East/West Fracture Spacing

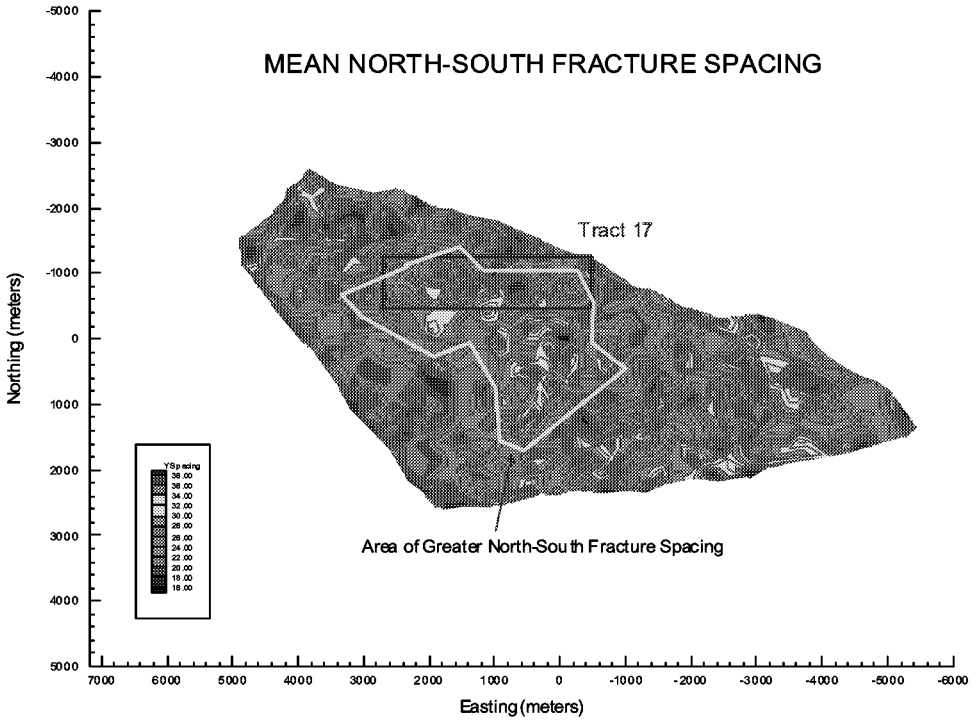

Figure 3-121: Mean North-South Fracture Spacing

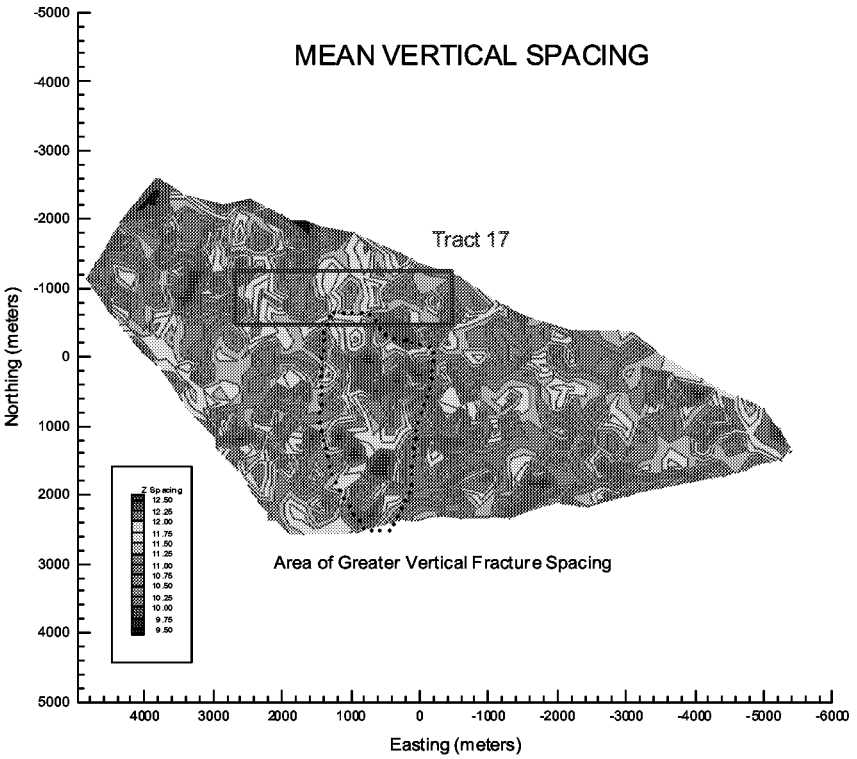

Figure 3-122: Mean Vertical Fracture Spacing

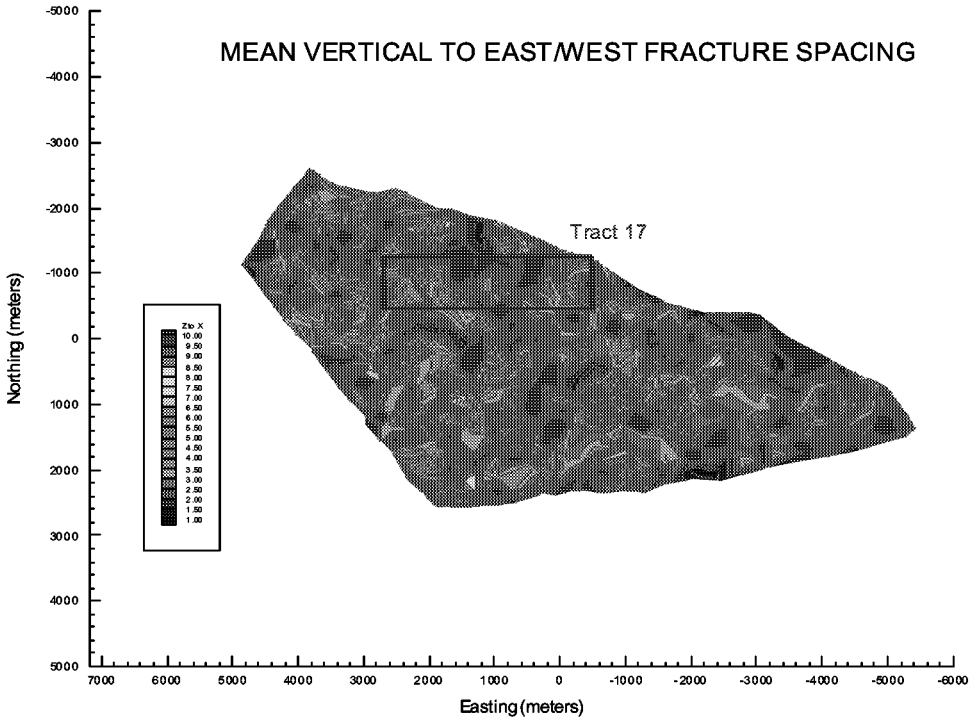

Figure 3-123: Mean Vertical to East/West Fracture Spacing

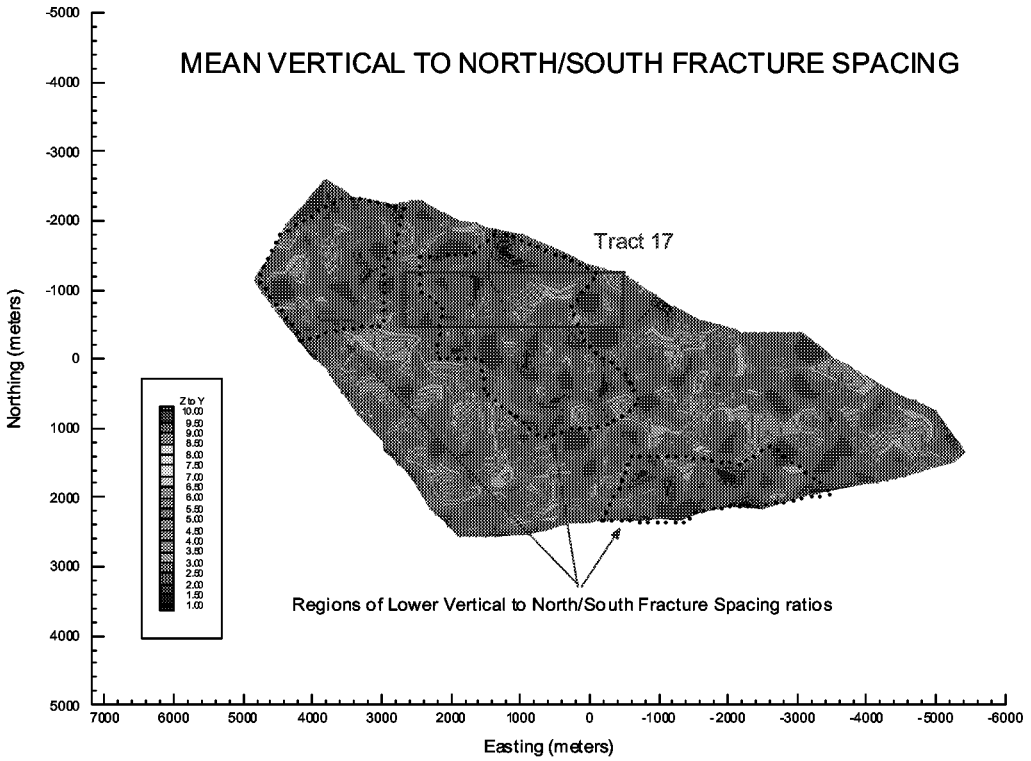

Figure 3-124: Mean Vertical to North/South Fracture Spacing

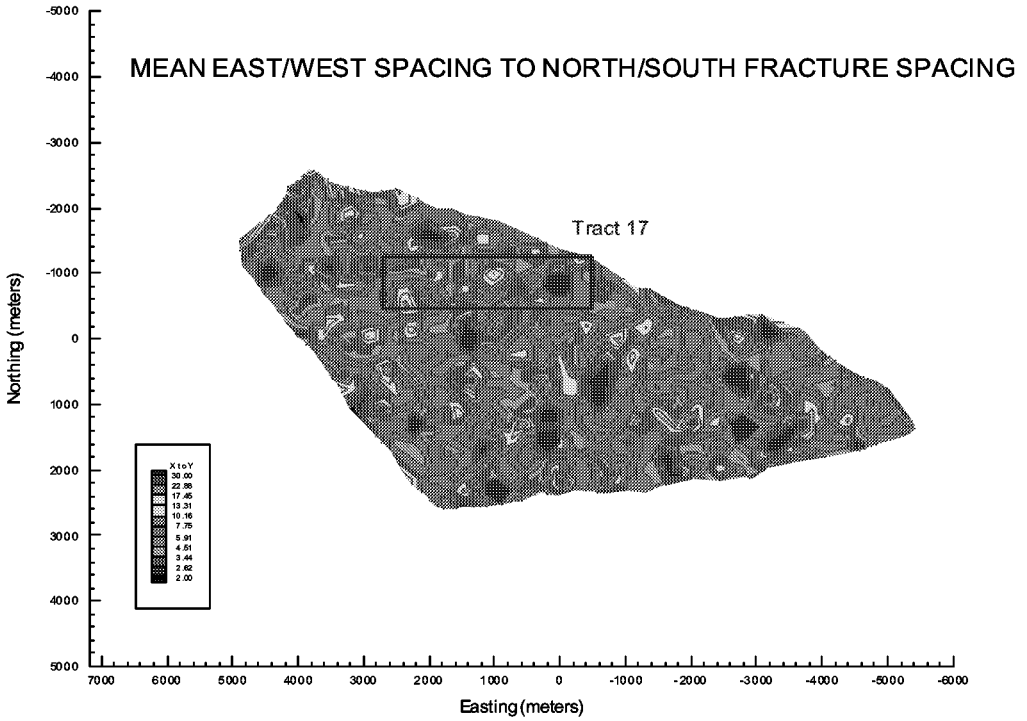

Figure 3-125: Mean East/West Spacing to North/South Fracture Spacing

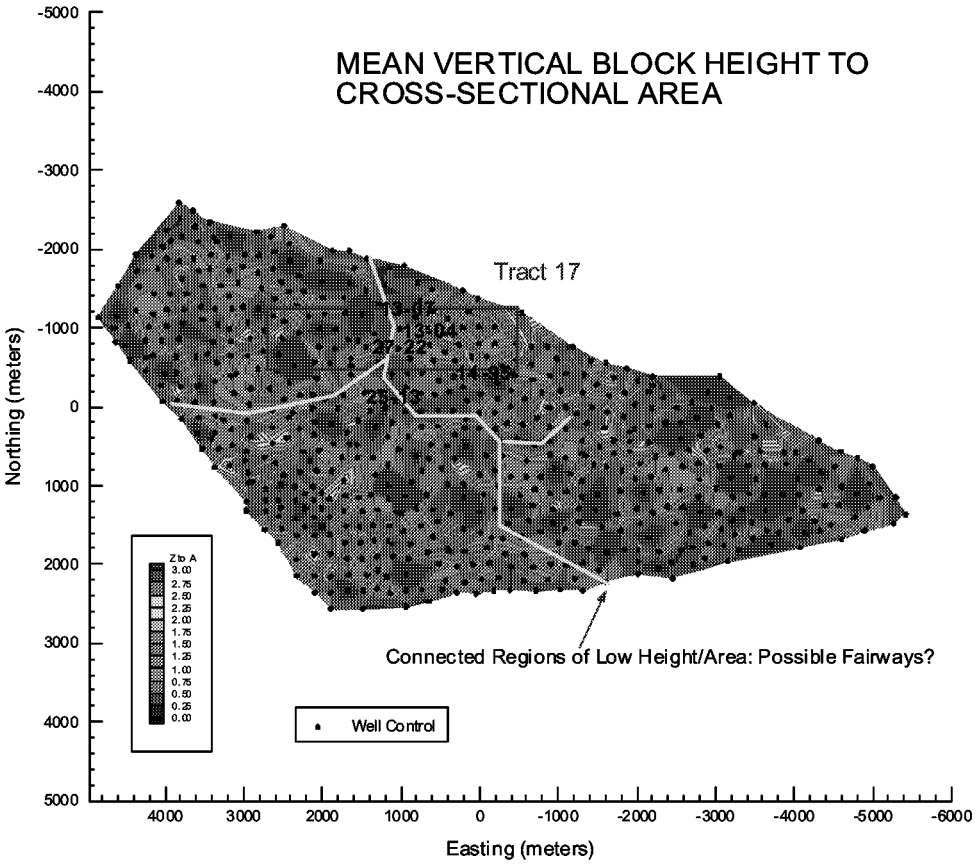

Figure 3-126: Mean Vertical Block Height to Cross-Sectional Area

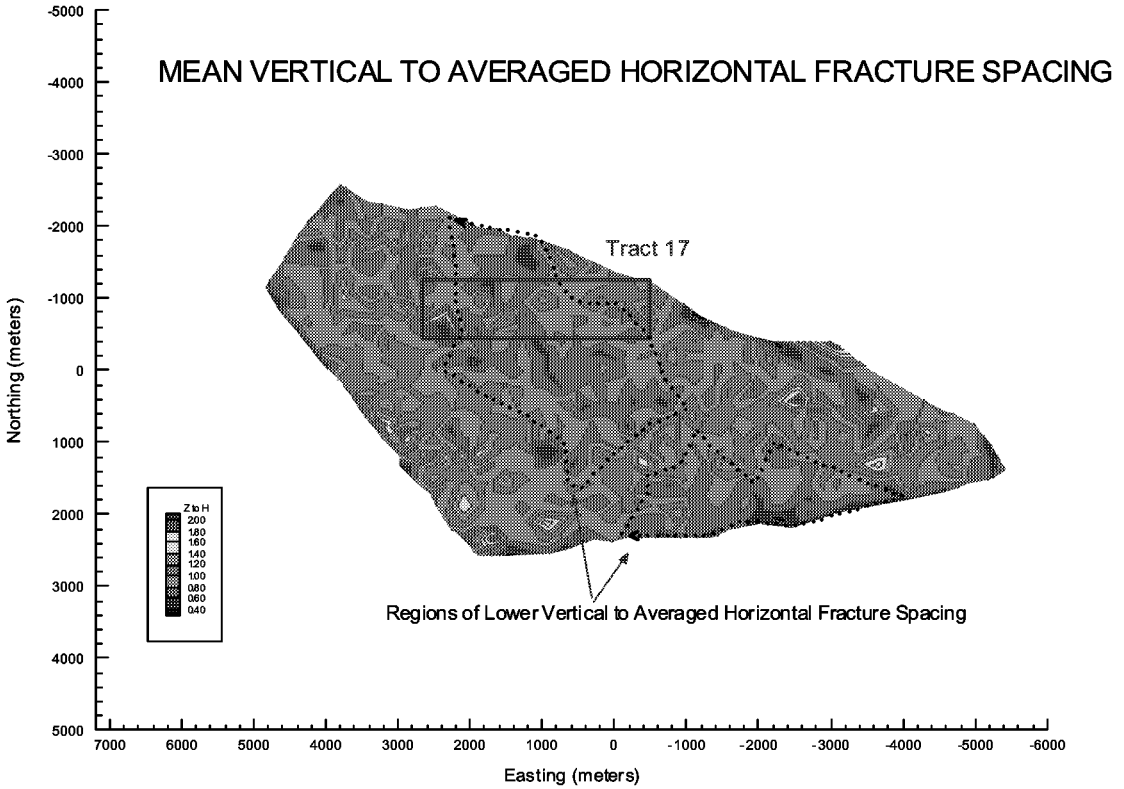

Figure 3-127: Mean Vertical to Averaged Horizontal Fracture Spacing

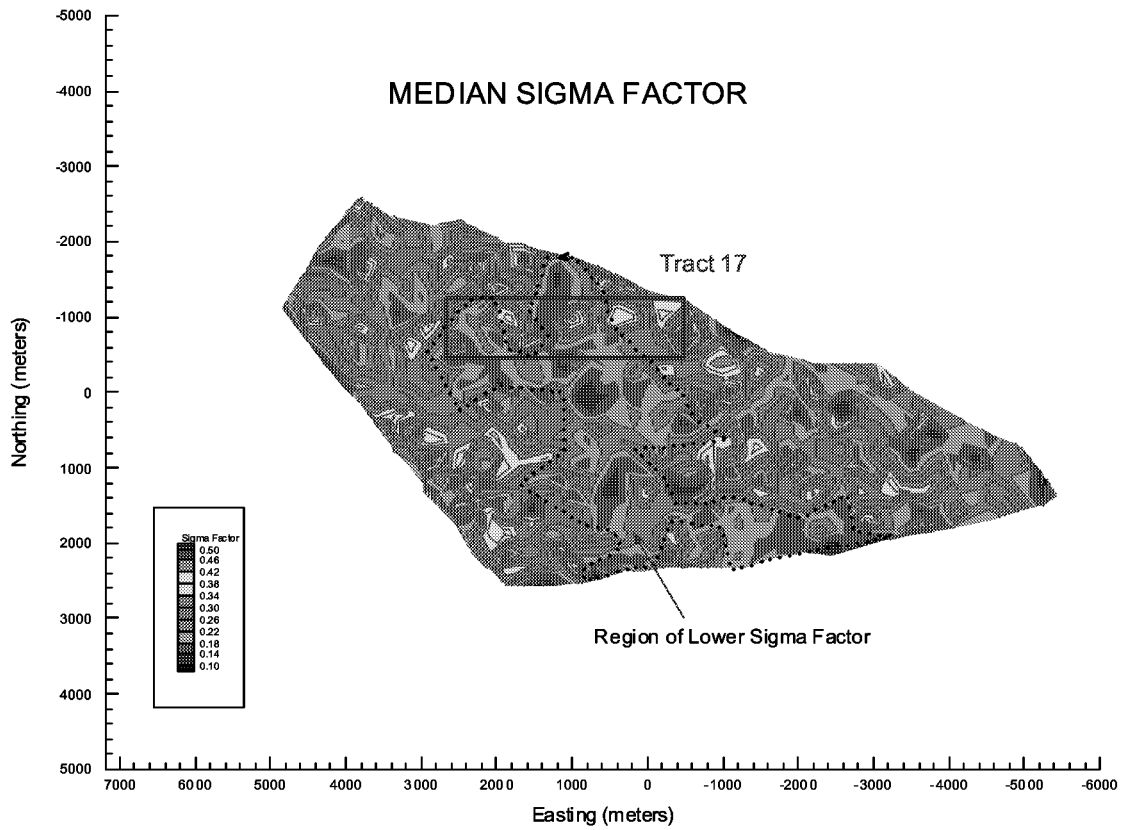

Figure 3-128: Median Sigma Factor

Taken together, these maps suggest that the areas with the least favorable production characteristics should be in the region including portions of Tract 17 and in the area to the southeast of Tract 17. This region appears to have less intense vertical fracturing, which gives rise to horizontally more extensive matrix blocks, and less fracture surface area for a given volume of reservoir. The recommendation for strategic completion based on these contour maps has been provided to Marathon Oil (MOC).

3.5.1.5 Evaluation

Marathon Oil's in kind contribution to this project was provided through recompletions to support evaluation of the DFN approach to IOR. A total of 16 wells were recompleted as part of this project, although only five were required for the in-kind contribution. Wells YU 1304, YU 1307, YU 1495, YU 2513, and YU 2722 provided the basis for the development of the IOR strategy. Based on the evaluation of these wells, the project team suggested that recompletion be carried out in area where the DFN model produced high sigma values (e.g., 3.0).

The eight strategic completion/deepening wells installed and evaluated for the DFN IOR analysis were YU 2112, YU 2325, YU 2335, YU 2722, YU 3532, YU 1771, YU 1776, and YU 2226. All

of these wells exhibited sigma values of over 3.0 based on the DFN model. Of the eight, the first five had been previously shut-in, due to unfavorable production behavior, and the remaining three were currently-producing wells, targeted for improved productivity.

The results of this evaluation were as follows. After the well work was completed, three of the first five demonstrated increased total fluid production, indicating improved reservoir connection. The post- to pre-recompletion ratios of daily total fluid production were 3.2, 9.2, and 2057. The remaining two wells exhibited small decreases in total fluid productivity, with ratios of 0.4 and 0.8. Of the three active wells, two showed increased fluid production ratios, with values of 1.5 and 3.0. The last well had a ratio of 0.7. The overall result, in terms of increased fluid production, then, was positive in five of eight wells, with an average total fluid ratio of 414.8.

As expected, the DFN approach did not provide 100% accuracy in its predictions. This is in part because the DFN approach only predicts fracture locations in a probabilistic sense – it is not currently possible to project fracture locations deterministically. Furthermore, in environments such as Yates Field, where the fractures are near vertical, sigma and fracture density values have more meaning in the lateral sense than the vertical. Therefore the DFN analysis predicted the likelihood of encountering fractures in a vertical well deepening for a given location, rather than the exact locations where these fractures will occur.

Each of these strategic completions was targeted for the base of the oil column. However, the no DFN IOR analysis was carried out to predict the effect of the strategic completions on water cut. Of the five wells where water and oil were produced both pre- and post-workover, the water-to-oil ratio increased in four cases. In fact, the net gain in daily oil production for the eight wells totaled only twenty seven barrels. As a result, the well recompletions may be considered moderately successful in a technical sense, but not economic. This clearly demonstrates the need for a more comprehensive integration of DFN analysis of water production, such as those developed for the North Oregon Basin with the strategic completion analysis developed for Yates.

In addition to well recompletions, a surfactant injection test continued to be monitored in the western portion of the study area. A large volume of surfactant-laden water was injected into the bottom aquifer, in well YU 2935, and a number of surrounding wells was then monitored for production response. Well YU 1106, which lies along a distinct trend of high sigma aligned with well YU 2935, exhibited the most marked response to the treatment (Figure 3-129). This indicates both lateral connectivity through the fracture system, as well as probable effective treatment of the matrix, due to small block size, i.e. high surface area of fracture/matrix interfaces.

The result of this surfactant test was an incremental recovery of about 30.6 thousand barrels of oil (Figure 3-130). This represents both a technical success and a promising economic outlook. Additional tests are planned for both the laboratory and the field, in which further quantification of various process parameters will be attempted.

The third area of testing for the DFN approach relates to positioning of lateral drain holes in the reservoir. Prior to mid-2001 the vertically-segregated fluid contacts have not been stable enough to confidently drill new laterals in the field. A five well package has been proposed, however, and should be completed in the fourth quarter of 2001. The goal is to connect the well bores with fractured zones, in order to more efficiently produce oil at a targeted elevation, with reduced co-production of gas or water. Two of the wells, YU 2220 and YU 2515, are located within the study area. The results of these wells will provide a further indication of the efficacy of the DFN approach for IOR.

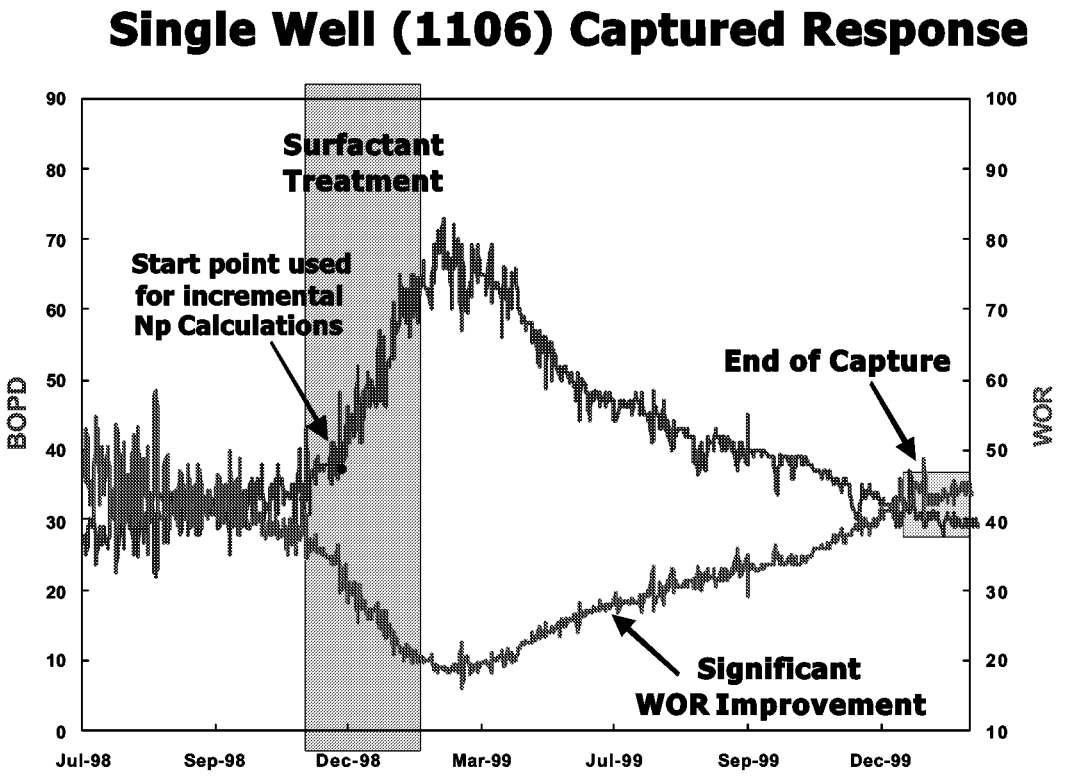

Figure 3-129 Efficacy of Surfactant Treatment on YU 1106

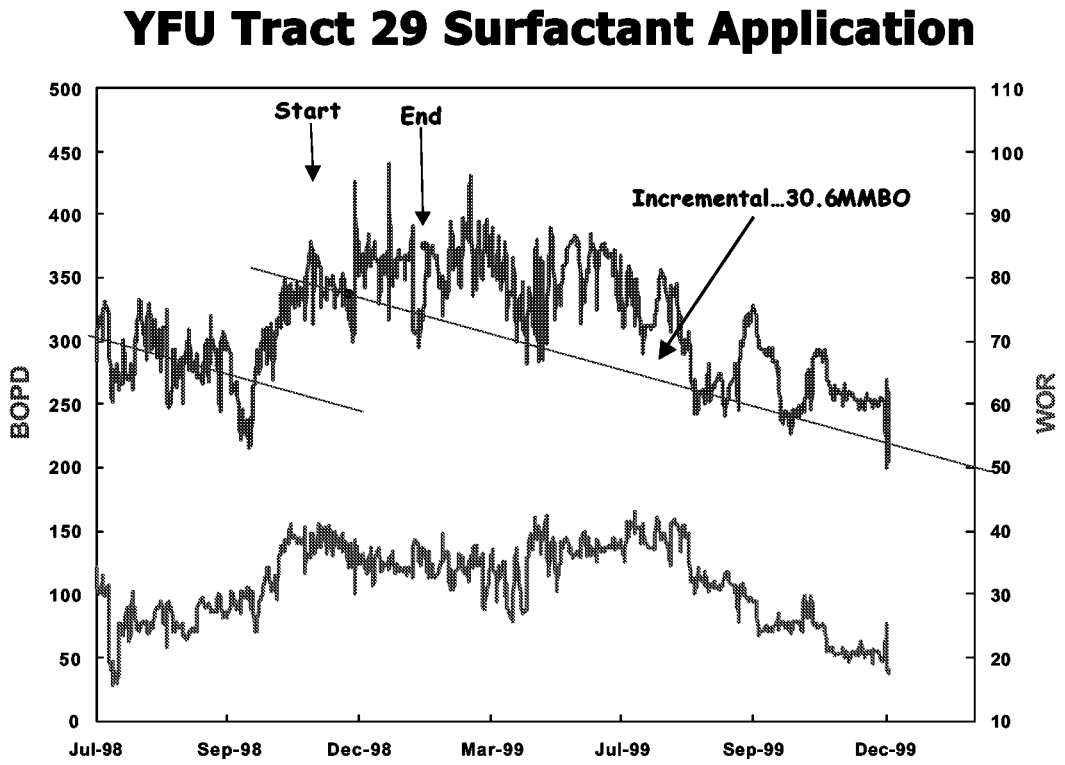

Figure 3-130 Efficacy of Surfactant Treatment on Project Study Site Yates (Tract 29)

3.5.2 Task 4.2 Reservoir IOR Demonstration, Stoney Point

The geologic and development background of the Stoney Point reservoir is reviewed in Dershowitz, 1999 and Dershowitz and Cladouhos, 1999. The Stoney Point Field produces from a linear trend of dolomitized carbonates in the Trenton and Black River Group of Southern Michigan. Although Stoney Point has over 20 million barrels of oil in place, the oil column is thin. The Stoney Point field suffers from severe water breakthrough problems, which may limit ultimate recovery. However, the geometry of the gas cap updip demonstrates that reservoir compartmentalization is effective at least for gas communication. The IOR analysis carried out here considers the possible effectiveness of gel treatment to improve reservoir compartmentalization and maintain oil production from individual hydraulic compartments, even when neighboring compartments have been invaded by water.

3.5.2.1 Discrete Fracture Network Model

The discrete fracture network model for Stoney Point for this analysis was implemented at a 2000 meter scale (Figure 3-131). Discrete Feature Network (DFN) models are derived through a combination of spatial and stochastic distributions for spatial structure, orientation, size, intensity, and mechanical/hydraulic properties of important structural features (Dershowitz and Cladouhos, 1999).

The compartments or sub-reservoirs at Stoney Point are controlled by a set of *en echelon* shear faults above a basement strike-slip fault. Hurley and Budros (1990) interpreted synclinal sags on seismic data to delineate the faults along which carbonate dissolution and dolomitization has taken place. This map was used to develop an initial conceptual DFN model of a fault pair. Reservoir compartments along each fault are hypothesized to be formed by fracturing along Riedel shears in ~200 m (~750') wide zones. Riedel shears form at an angle of ~15° to the shear plane (Twiss and Moores, 1992). The areas between faults tips are also hypothesized to be zone of intense fracturing. In the fault step-over region, fractures would be related to tension rather than shear and thus have an EW orientation.

Three fracture sets are hypothesized for the Stoney Point site based on the geological conjecture described in the previous section:

- Riedel Shears along the faults,
- Tension fractures in fault step-overs, and
- Background fractures.

The mean pole of the Riedel shears along the strike-slip faults is assumed to have a trend of 30° and a plunge of 0°. The dispersion coefficient (κ) was set to 20 to produce a range of orientations from 10 to 50°.

The mean pole of the tension fractures in the step-over region is assumed to have a trend of 0° and a plunge of 0°. The dispersion coefficient (κ) was set to 30 to produce a range of orientations from -15 to 15°.

Background fractures were assumed to be defined by a uniform orientation distribution (Fisher κ=0). Locations for background fractures are distributed with uniform intensity in space by a Poisson process.

The fracture size distribution assumed was based on the scale of model being considered. Since the model being considered is on the scale of 2000 meters, the fractures which control flow should be larger than approximately 10% of the model scale. The fracture size distribution was therefore defined assuming a truncated exponential fracture size with a mean radius of 66 feet (20 m). All fractures with radii less than the mean (66 feet) were excluded in the preliminary modeling. The same distributional assumption was used for all three sets.

Intensity in DFN modeling is expressed in terms of volumetric intensity P_{32}, the total feature area (m^2) per volume (m^3). The four fracture intensity cases varied from intensities of 0.001 m^2/m^3 to 0.3 m^2/m^3 per set. The highest fracture intensity model had a volumetric fracture intensity (P_{32}) of 0.01 m^2/m^3 in the Riedel shear set and an intensity of 0.3 m^2/m^3 in the tension fracture set. These values translate to 1228 and 1030 fractures in each set, respectively. The lowest fracture intensity model had a volumetric fracture intensity (P_{32}) of 0.001 m^2/m^3 in the Riedel shear set and an intensity of 0.03 m^2/m^3 in the tension fracture set. A 90% reduction in intensity results in a 90% reduction in fracture numbers; therefore, the lowest intensity set has 124 and 106 fractures in each set, respectively. All models have the same intensity of background fractures away from the faults: an intensity of 0.005 m^2/m^3 for a total of about 650 background fractures.

Four preliminary DFN models of the Trenton formation at the Stoney Point Field were constructed using the parameters shown in Table 3-54. Three-dimensional views of this conceptual model are shown in Figure 3-132 and Figure 3-133.
The gel treatment strategy studied was as follows:

1. Hydraulic connection between the overlying aquifer and the oil reservoir was assessed using pathway analysis. This result represents the current situation, and reflects the failure of compartmentalization to prevent water breakthrough.
2. Gel injection is simulated for wells near the compartment boundaries. For each gel injection, the quantity of gel injected is calculated based on the porosity of the fracture network connected directly and indirectly to the gel injection interval.
3. Following gel injection simulation, the effectiveness of compartmentalization is re-addressed to determine how well compartmentalization has been established to isolate the aquifer from the producing wells.

Figure 3-134 and Figure 3-135 illustrate the pressure distribution in the Stoney Point DFN Model before gel injection. The discrete fractures provide a route for the water from the overlying aquifer to breakthrough to the production wells. Following gel treatment particular water flow paths have been blocked, preventing increased water cut. This is illustrated in Figure 3-136 and Figure 3-137.

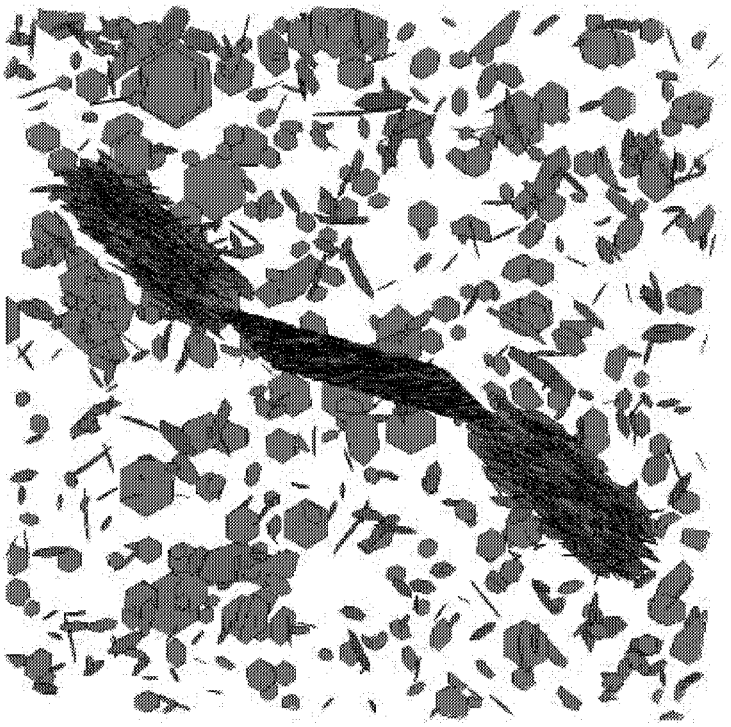

Figure 3-131: Stoney Point DFN Model, 2000 meter Extent, Fractures Only

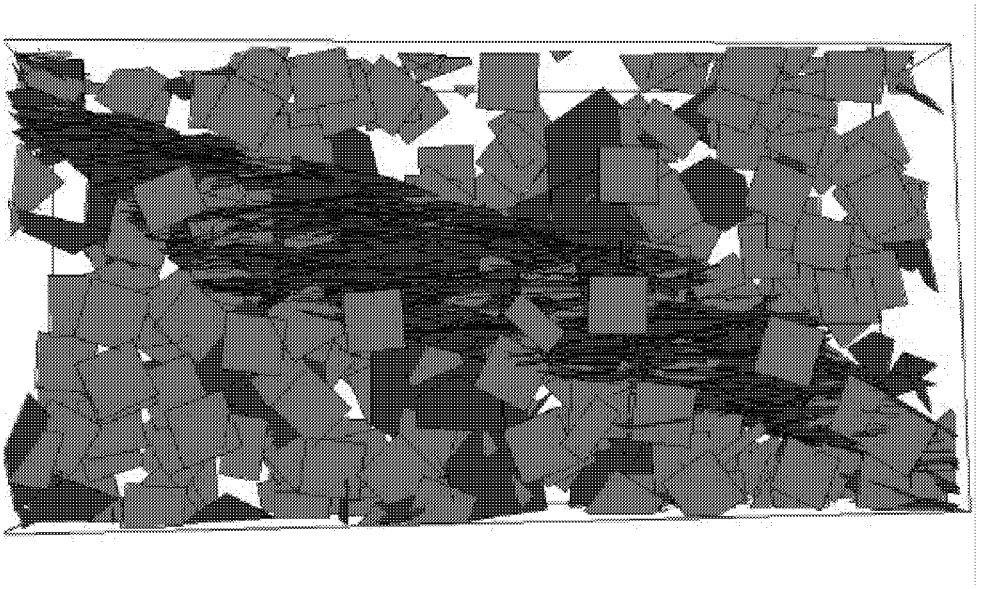

Figure 3-132: Simulation Volume (800x400x189m) Stoney Point DFN Model (Fractures and Matrix Features)

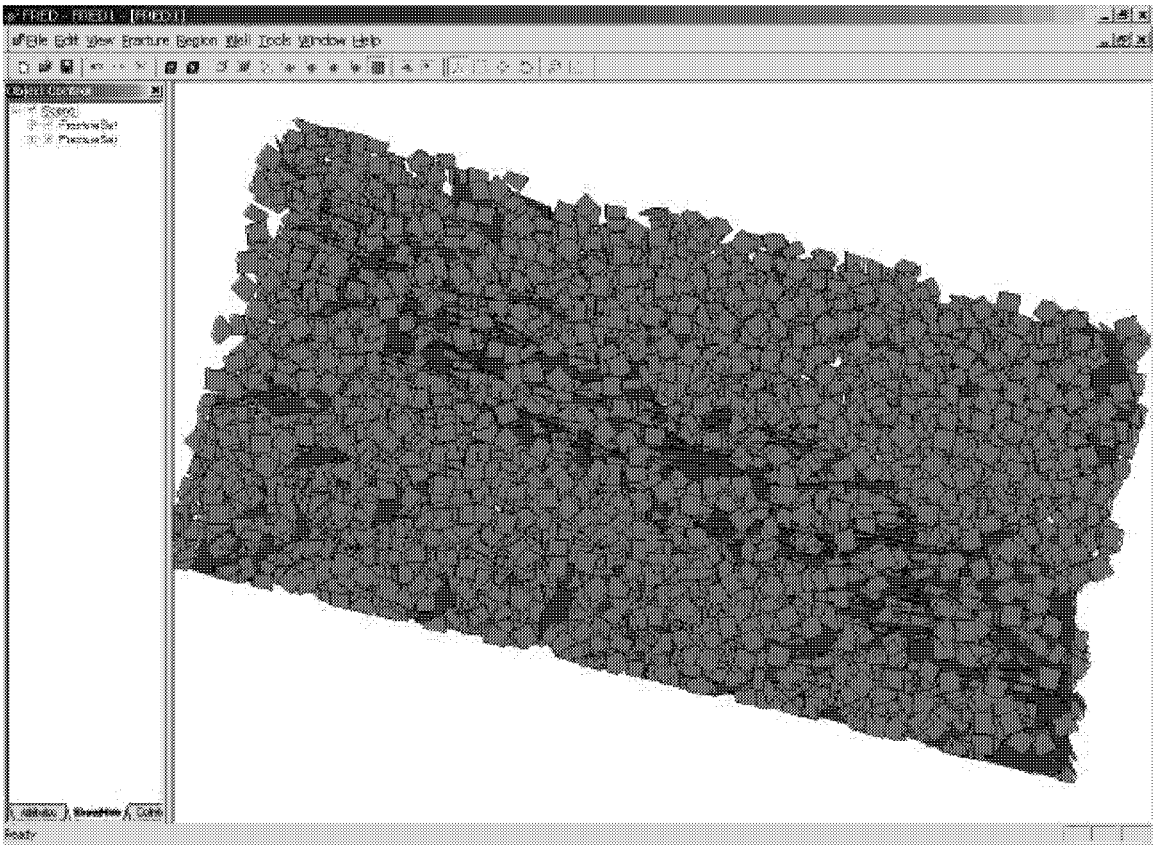

Figure 3-133: Full Fracture Set for Stoney Point, Fractures, and Matrix

Table 3-54: Stoney Point DFN Model Parameters, Trenton Formation

	Parameter	Basis
Fault Model DFN		
Generation Region	Adjacent to deterministic faults only	Figure 3-132
Conceptual Model	Nearest Neighbor, Exponent=10^7	Conceptual Model
Fracture Orientation	Fisher Distribution Mean Pole (Trend,Plunge)= (30,0) Dispersion $\kappa = 20$	Conceptual Model
Fracture Size	Exponential Mean = 20 m, Min. =20 m	Conceptual Model
Fracture Intensity	$P_{32} = 0.01\ m^{-1}$ (N=1228) $P_{32} = 0.005\ m^{-1}$ (N=615) $P_{32} = 0.0025\ m^{-1}$ (N=316) $P_{32} = 0.001\ m^{-1}$(N=125)	Sensitivity Assumption
Fracture Aperture	$1x10^{-6}$ m	Sensitivity Assumption
Fracture Transmissivity	$1x10^{-6}\ m^2/s$, LogNormal Distribution Standard Dev. = $5x10^{-7}\ m^2/s$	Sensitivity Assumption
Fault Tip Model DFN		
Generation Region	700 m x 250 m x 165 m 0.4 mile x 0.15 mile x 550 feet	Figure 3-132
Conceptual Model	Enhanced Baecher	Conceptual Model
Fracture Orientation	Fisher Distribution Mean Pole (Trend, Plunge)= (0,0) Dispersion $\kappa = 30$	Conceptual Model
Fracture Size	Exponential Distribution Mean = 20 m, Min. = 20 m	Conceptual Model
Fracture Intensity	$P_{32} = 0.3\ m^{-1}$ (N=1030) $P_{32} = 0.15\ m^{-1}$ (N=542) $P_{32} = 0.075\ m^{-1}$(N=246) $P_{32} = 0.03\ m^{-1}$(N=106)	Assumption
Fracture Aperture	$1x10^{-6}$ m	Assumption
Fracture Transmissivity	$1x10^{-6}\ m^2/s$ LogNormal Distribution Standard Dev. = $5x10^{-7}\ m^2/s$	Assumption
Background Fractures		
Generation Region	2000 m x 2000 m x 165 m ~1.2 mile x ~1.2 mile x 500 feet	Figure 3-131 and thickness of Trenton Formation
Conceptual Model	Enhanced Baecher	Conceptual Model
Fracture Orientation	Fisher Distribution Mean Pole (Trend, Plunge)= (0,0) Dispersion $\kappa = 0$ (Uniform)	Conceptual Model
Fracture Size	Exponential Distribution Mean = 20 m, Min. = 20 m	Conceptual Model
Fracture Intensity	$P_{32} = 0.005m^{-1}$ (N=~649)	Assumption
Fracture Aperture	$1x10^{-6}$ m	Assumption
Fracture Transmissivity	$1x10^{-6}\ m^2/s$ LogNormal Distribution Standard Dev. = $5x10^{-7}\ m^2/s$	Assumption

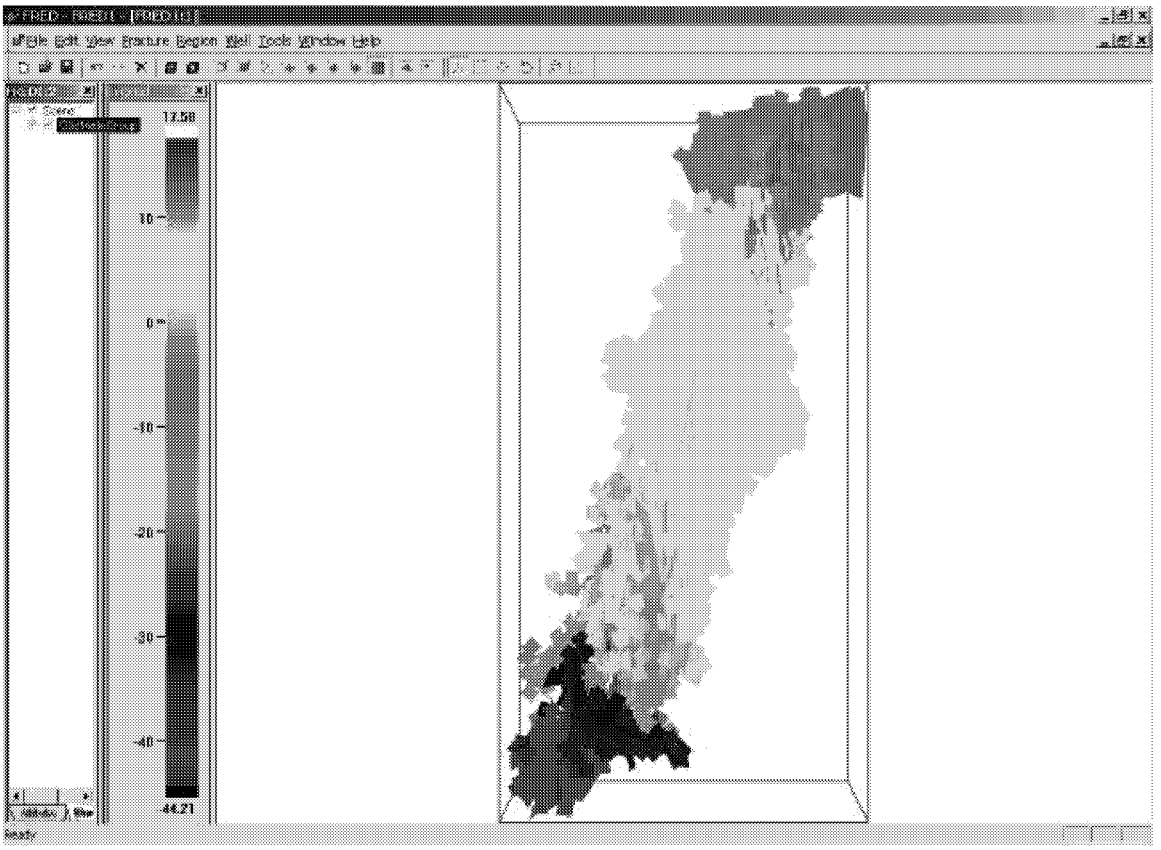

Figure 3-134: Flow solution after 0.1 hours, pre-gel treatment. Note pressure has connected directly from injector to producer

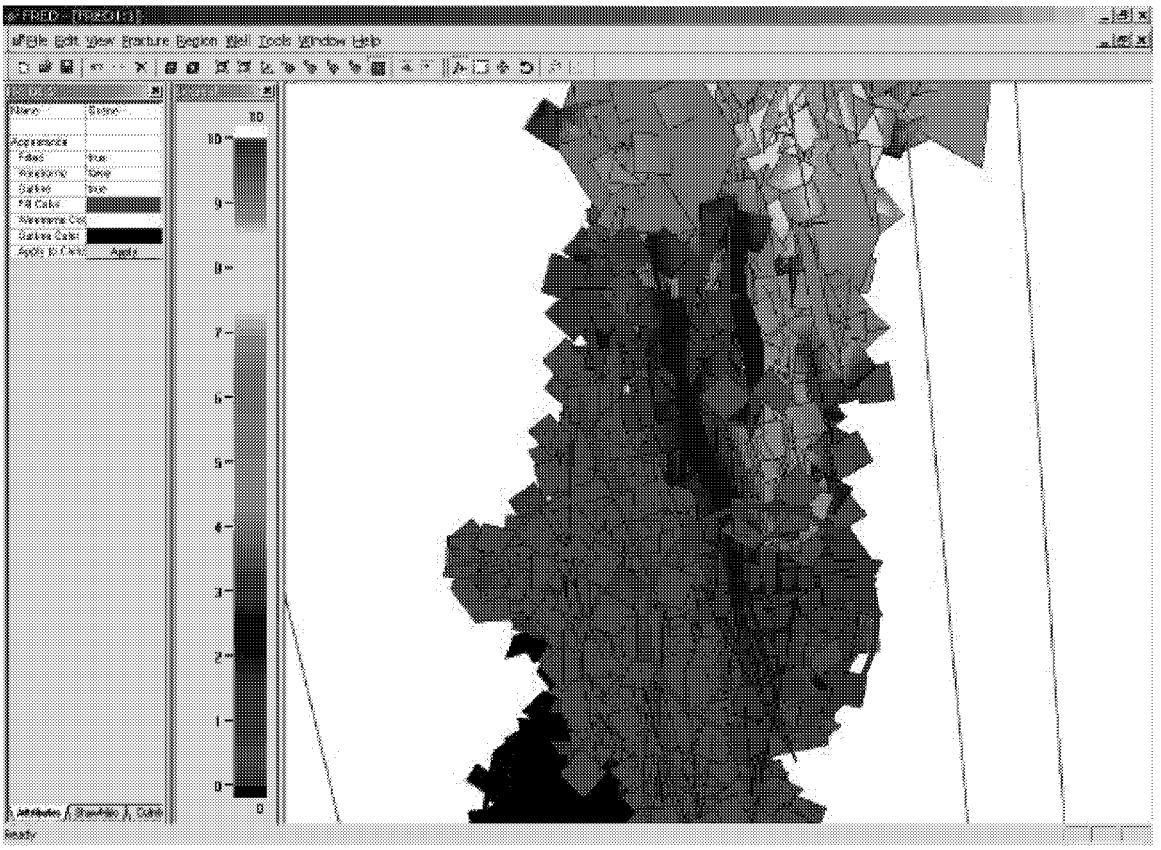

Figure 3-135: Stoney Point Flow Solution Pre-Gel treatment: Close up showing pressure bypassing matrix through fractures

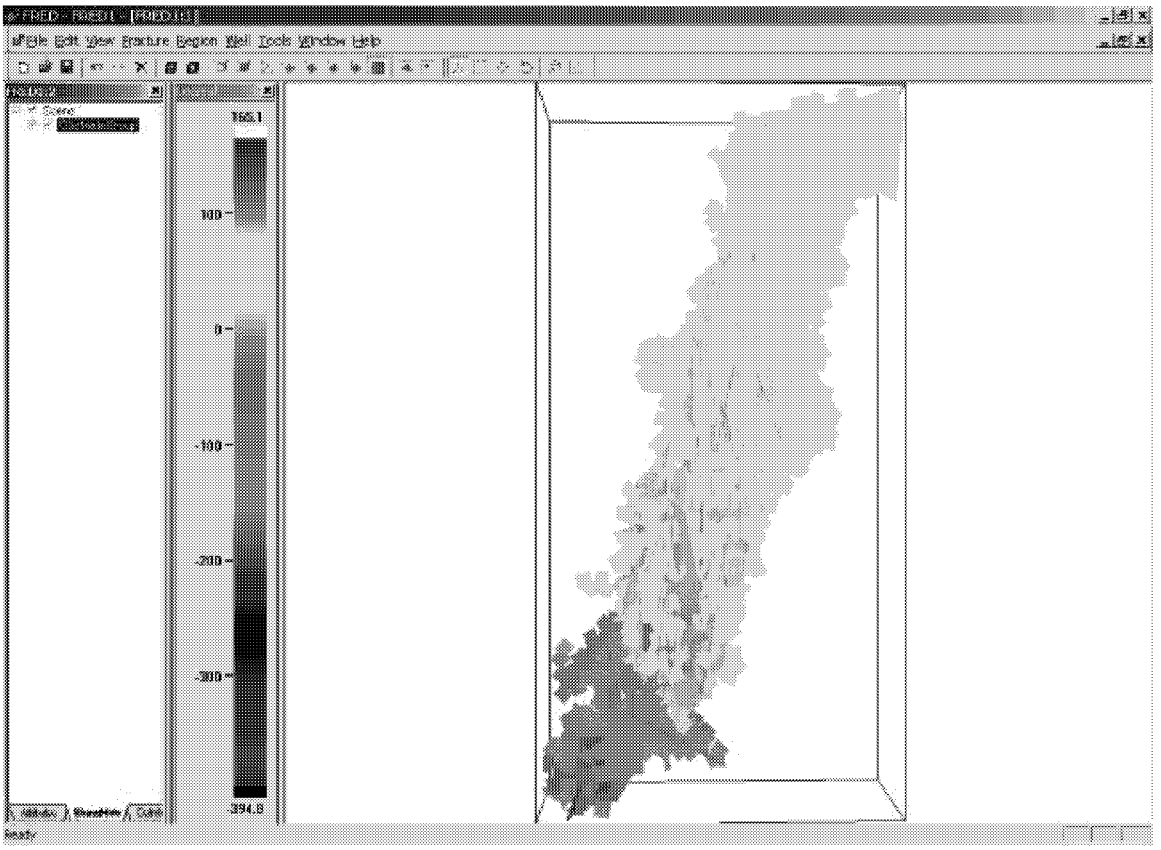

Figure 3-136 Stoney Point: Pressure after 0.1 with gel treatment reducing the fracture permeability by a factor of 10.

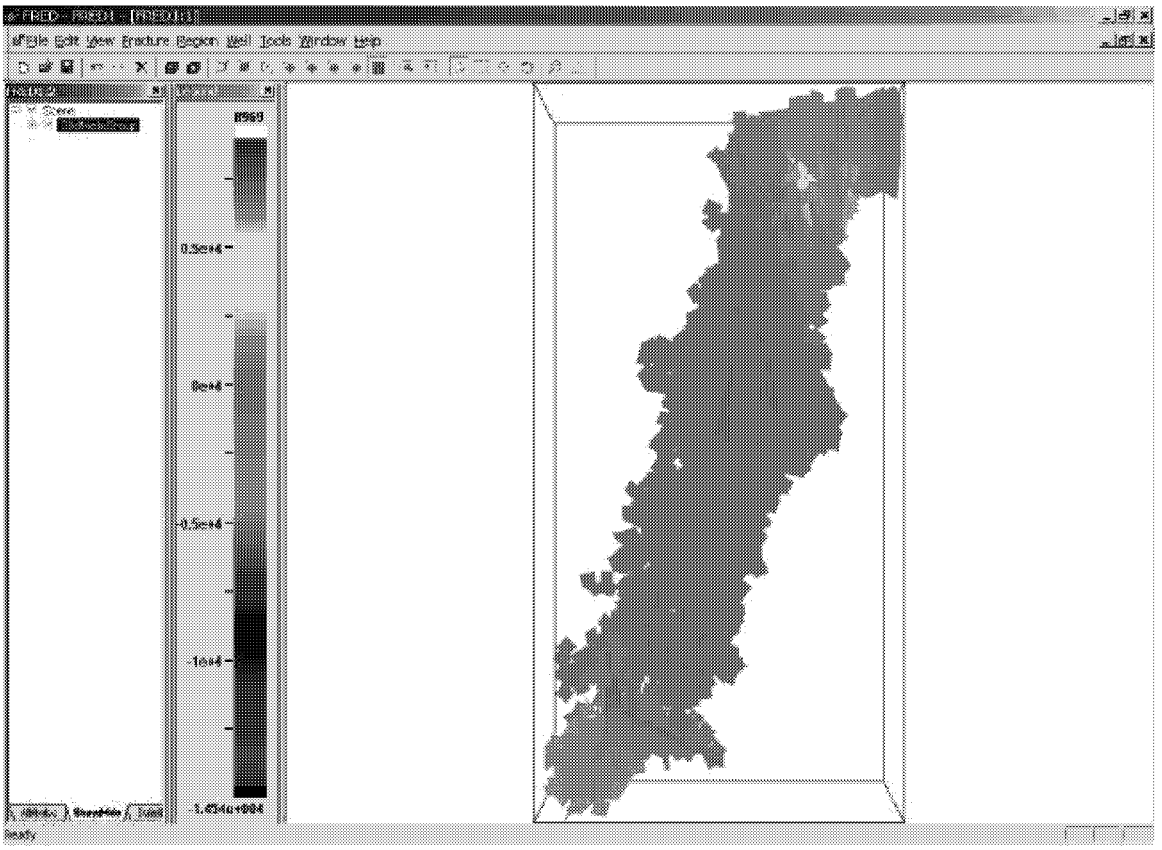

Figure 3-137 Stoney Point Pressure field at 0.1 hours after gel-treatment reduces permeability by a factor of 100

3.5.2.2 Evaluation

Due to the change of ownership of the Stoney Point field during the project, it was not possible to evaluate the value of the DFN analyses carried out in support of IOR. It is our understanding that unless water production problems are addressed using procedures such as those developed in this project, the oil in place at Stoney Point will not be produced, and only the gas reserves will be exploited in the future.

3.5.3 Task 4.3 Reservoir IOR Demonstration, South Oregon Basin

This section describes analysis of gel treatment for IOR at the South Oregon Basin study site. The effect of gel treatment on the reservoir hydraulics is analyzed using the single phase, dual porosity flow simulator MAFIC (Miller et al., 2000). This analysis involved updating of the DFN model for the study site, and evaluation of the effect of gel injection on sweep efficiency.

3.5.3.1 South Oregon Basin DFN Model

The DFN model for the South Oregon Basin study site was developed using the procedures by Dershowitz et al. (2000). Table 3-55 presents a summary of the lineament analysis carried out.

Figure 3-138 shows the orientation for sets as defined from the lineament analysis. This figure indicates four fracture sets, consistent with the lineament observations of Table 3-55. The four fracture sets identified from seismic data are: (1) and East to West trending set; (2) a North to South set; (3) a North-East to South West trending set; and (4) an East-South-East trending set. The four fracture sets identified from the seismic data are placed as small ellipses on Figure 3-138. It appears that the FMI is centered around the opposing axis of the NE-SW fracture set. Observations of the primary fracture sets at outcrops at the Amphitheater and Wind River Canyon sites are consistent with the NE-SW trend. The EW seismic set is consistent in orientation with secondary fracture set observed at the Amphitheater outcrop. The ESE set is consistent with the orientation observed as the secondary set at the Wind River Canyon. The NS set from the seismic data has no concurring observations in outcrop data.

The orientations given in Table 3-55 represent the mean poles for each set. The FMI wellbore data provides a mean pole for all data, without breaking the data into sets, which is not particularly useful. However, the FMI data does give relevant indications of fracture length and intensity based on the number of fractures intersecting per meter, and the number of fractures intersecting all four pads of the FMI tool. The four pad intensity analysis was presented in Dershowitz et al. (2000).

Figure 3-139 shows the seismic lineaments. Fracturing does not appear to be distributed uniformly through out the region with a strong North-South trending cluster of fractures on the west side of the seismic volume; and the highest fracture intensity of all sets occurring around the center of the seismic volume. Figure 3-140 through Figure 3-143 illustrate the seismic lineaments sorted by set. The ESE set shows two strong linear trends with a random distribution of fractures around them. The NE fracture set in Figure 3-142 has the highest intensity. All four fracture sets appear to have similar distributions of fracture size. The NS, EW and ESE fracture sets appearing to cluster along localized linear trends.

The lineaments shown in Figure 3-139 are at seismic detection scales of over 100 m. A fractal analysis was carried out to support extrapolation of these fracture sets for use with smaller scale discrete features. Figure 3-144 through Figure 3-148 illustrate fitting of distributions to the lineament trace-length. Fitted gamma distributions for trace length imply a possible fractal size distribution. When a fractal size is fitted, the distribution exponent can be maintained, and the minimum size censoring limit can be decreased to extend the distribution to smaller fractures. The fit of the power law (Pareto) distribution was successful only for the ESE set. The NS set was best fit to a lognormal distribution, which does not support fractal extrapolation. The NE and EW sets were best fits to a gamma distribution, which also does not support fractal scan-line.

Table 3-55: South Oregon Basin Lineament Analysis

ID	Fracture Set	Orientation Pole (Trend, Plunge)	Intensity (P32)	Length
1	East-West	2.8,0 (Seismic)	78 lineaments (22 int) Secondary 7	Gamma (3.1, 519)
2	North-South	260.9,0. (Seismic) or (170.9,0)	120 lineaments (3 int) Secondary 9	Log norm (6.987,0.77)
3	NE-SW	316.2,0 (Seismic)	292 lineament (28 int) Primary 6,8	Gamma (2.17,1108)
4	ESE	40,0 (Seismic)	94 lineament (10 int) Secondary 9	Power law (1100,2.2)
5	FMI	135,9.4 (FMI log)	(1.6) (guess?) (0.4) percolates	
6,7	Amphitheater; Primary field	Primary Azimuth 65 Secondary Azimuth 90 Localized south Related to NE tear Poles (135,0) (180,0)	Spacing 5m	
8,9	Wind River Can	Primary (70°) Secondary (160°) Poles (160,0), (70,0)	Cut Tensleep 10m spacing, Bedding confined, size and intensity controlled by thickness of mechanical layer	
10	300 foot cliffs in WR Canyon	Vertical cut	Vertical cut Tensleep 10m Bedding confined, down to 1m spacing, not as numerous or continuous as Phosphoria	
11	Samuel #58	SD(50,6.5 SE) (95,83.5)	27 fractures/70m (1.45 /m)	100% 4-pad
12	Baston A #29	SD(342,5 NE) (72.5, 85)	19 fractures/67 m (1.04 /m)	68% 4-pad 3 m
13	Pauline #9 (Hz)	SD(180,15 E) (90,75)	149 fractures/164 m (1.67 /m)	97% 4-pad 20 m
14	Govt 3b #16	SD(28,8 NW) (298,82)	14 fractures/ 150 m (1.15 /m)	50% 4-pad (1 m?)

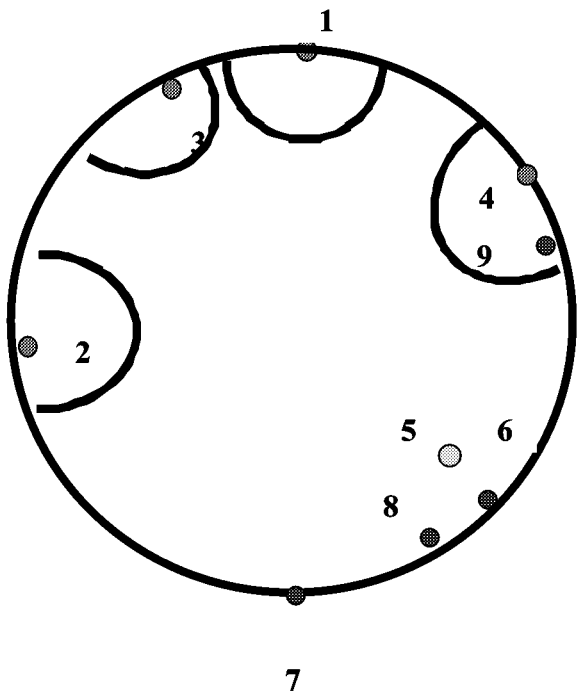

Figure 3-138: Fracture Set Orientations for South Oregon Basin

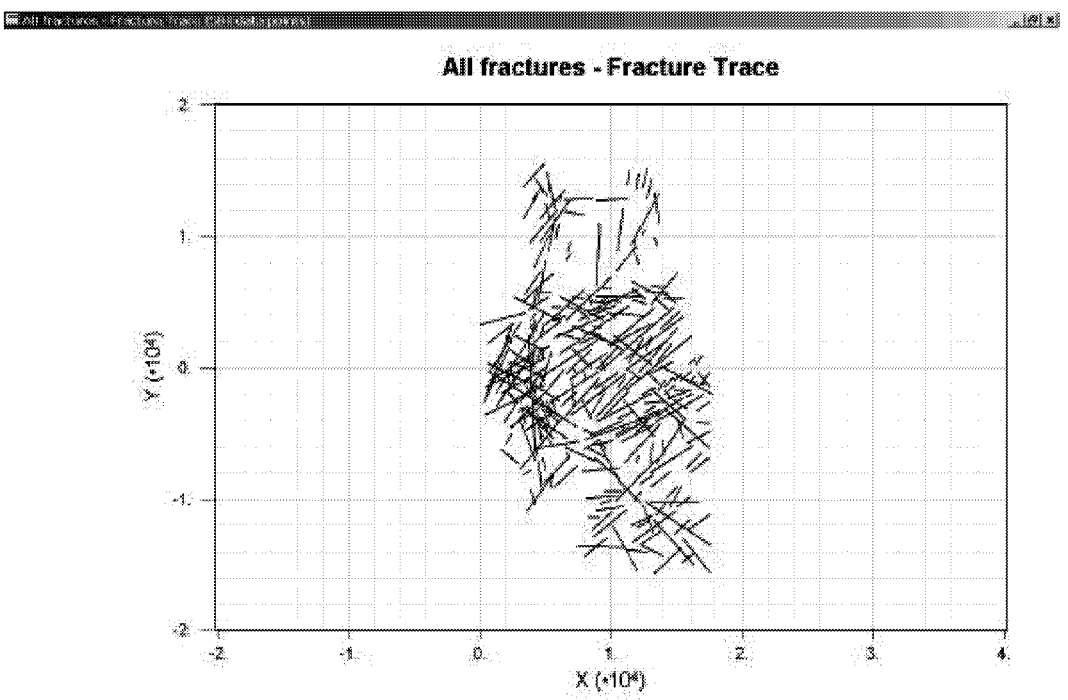

Figure 3-139: All Seismic Lineaments for South Oregon Basin

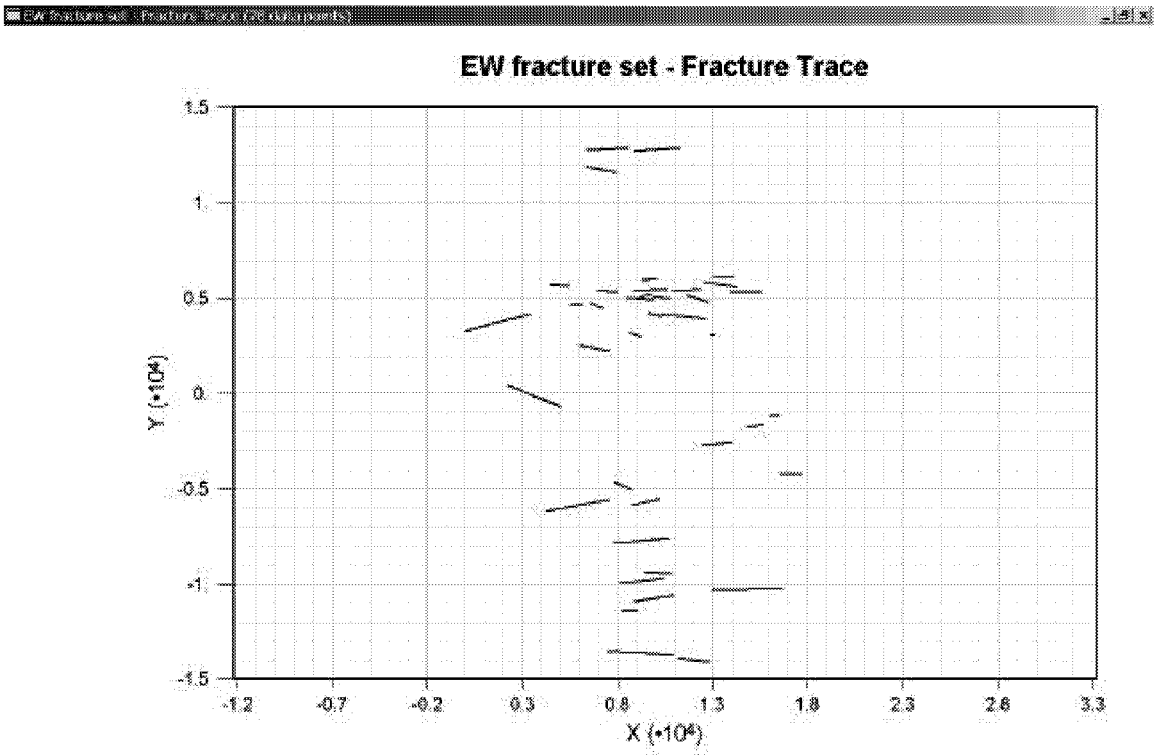

Figure 3-140 EW Seismic Lineament Set

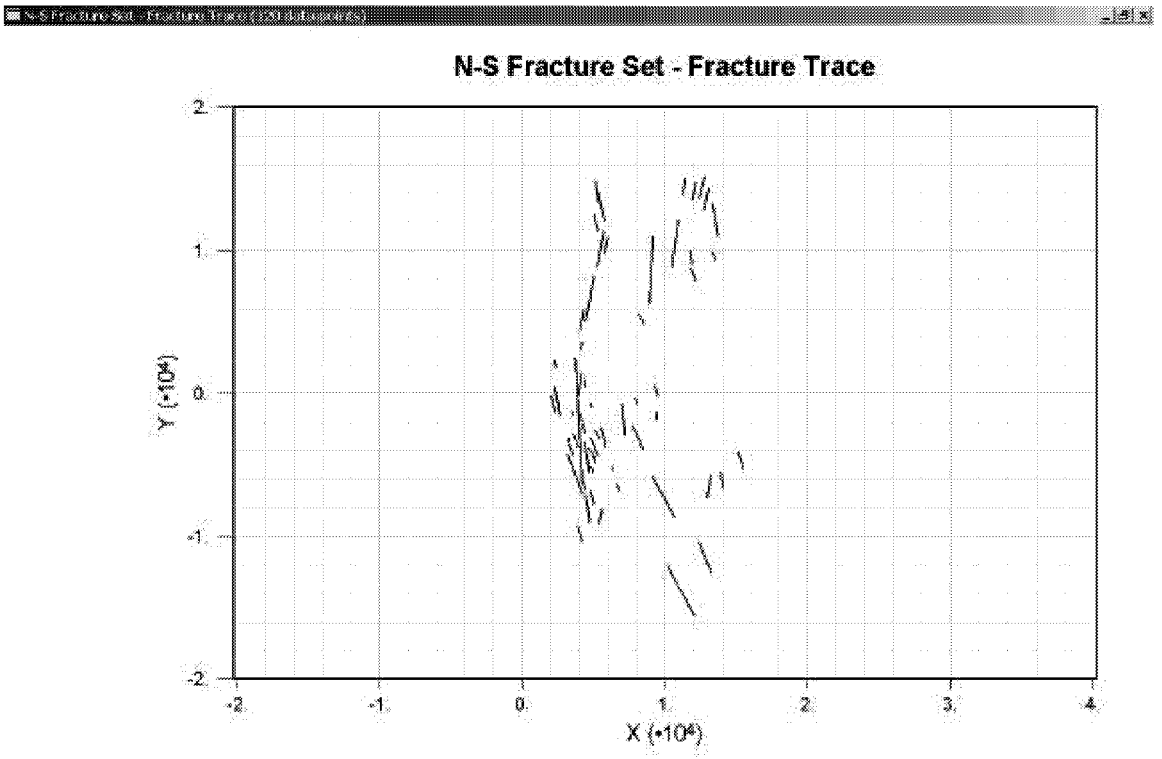

Figure 3-141: NS Lineament Set

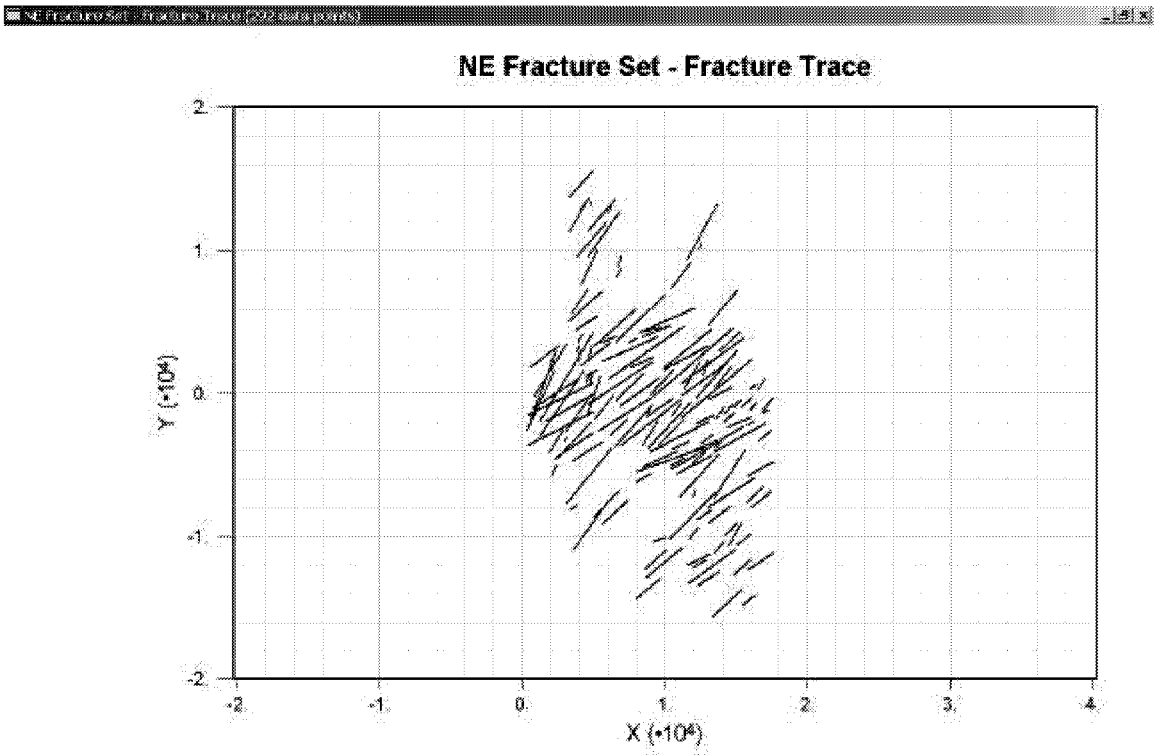

Figure 3-142: NE Lineament Set

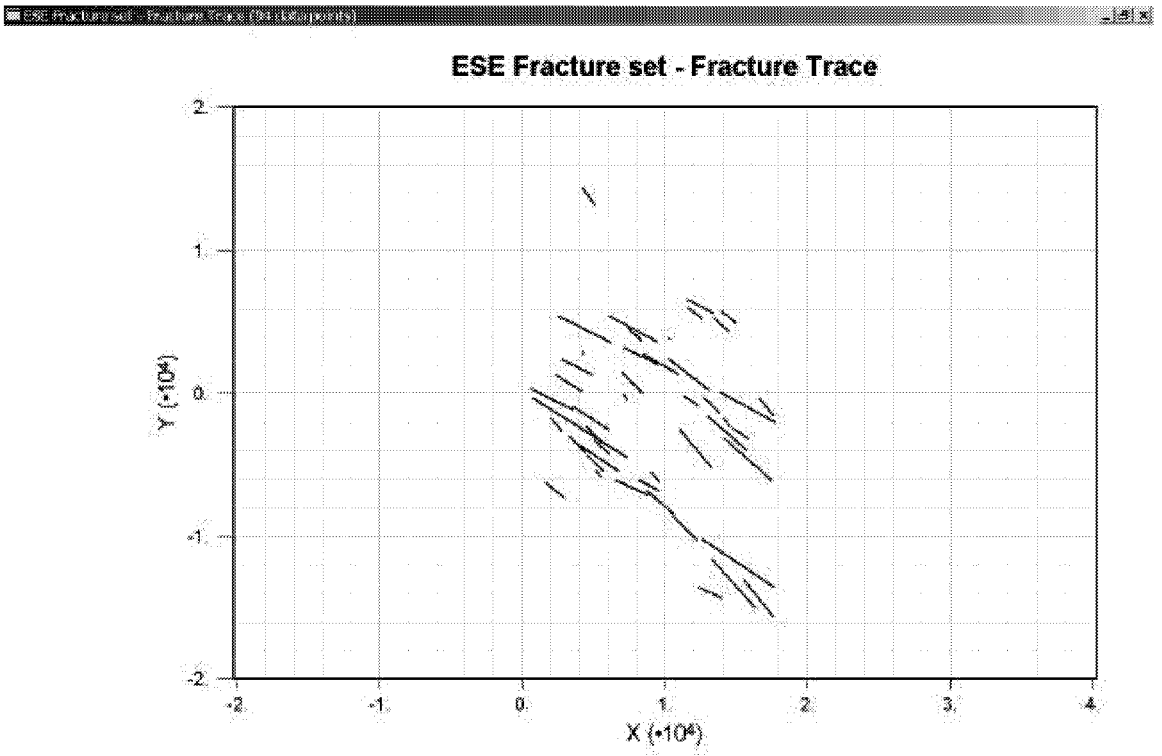

Figure 3-143 ESE Seismic Lineament Set

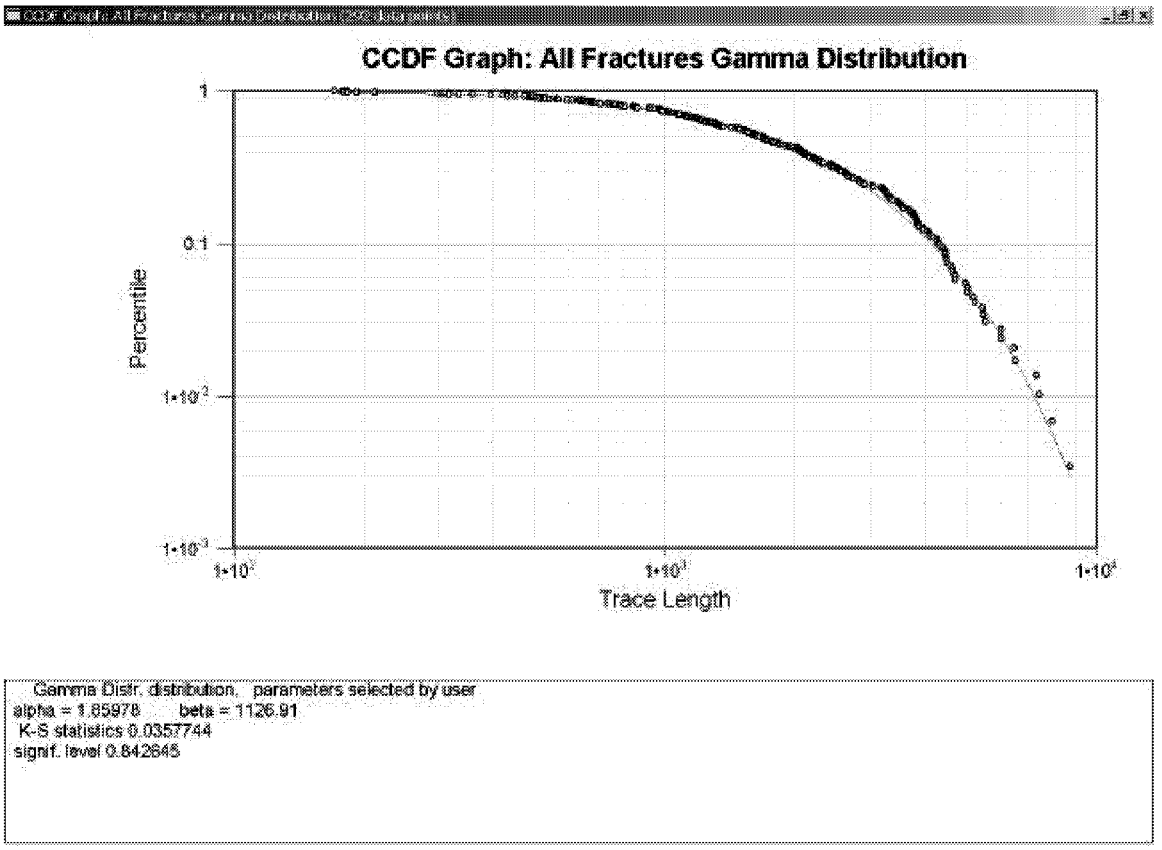

Figure 3-144: Trace Length Distribution, All Lineaments

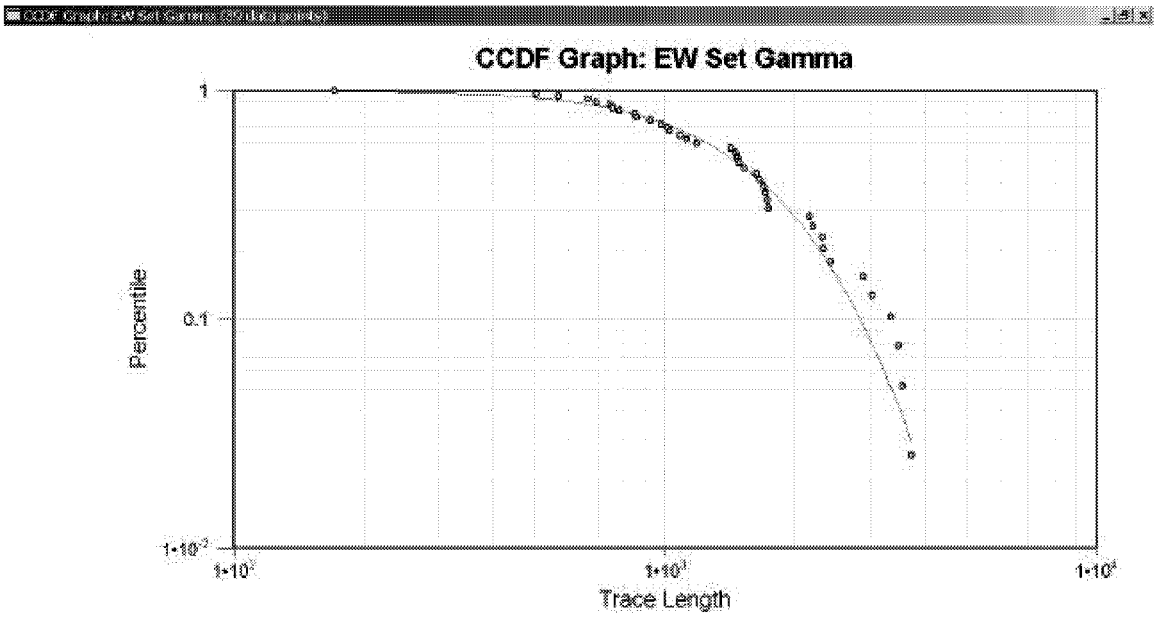

Gamma Distr. distribution, parameters selected by user
alpha = 3.11086 beta = 518.935
K-S statistics 0.0913781
signif. level 0.885693

Figure 3-145: Trace Length Distribution, EW Lineaments

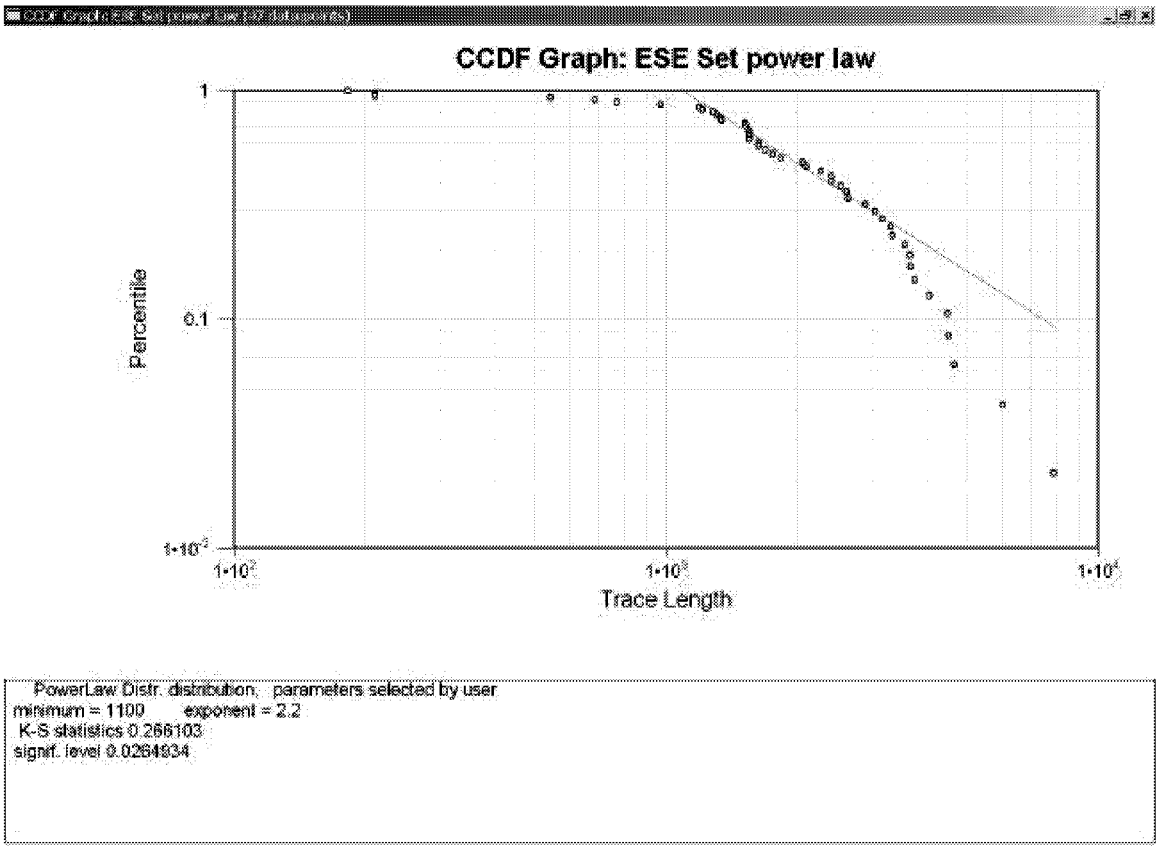

Figure 3-146: Trace Length Distribution, ESE Lineament

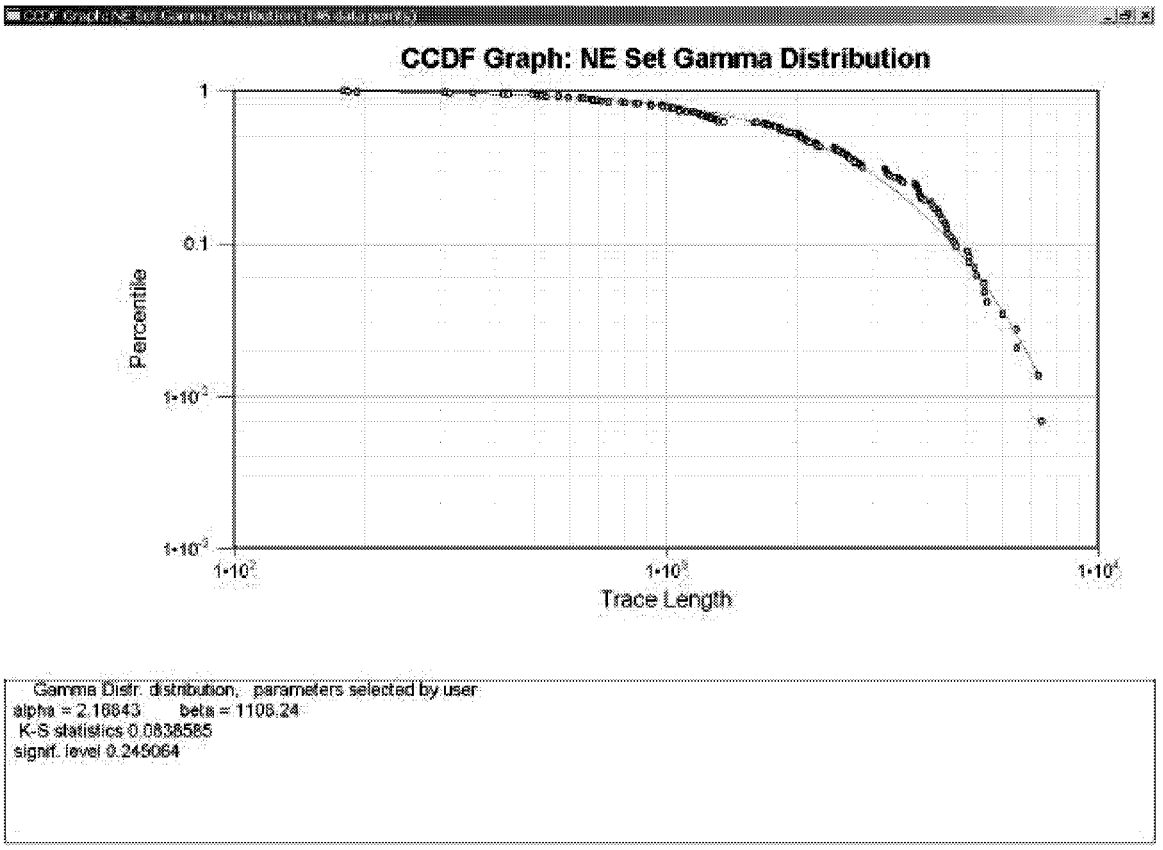

Figure 3-147: Trace Length Distribution, NE Lineaments

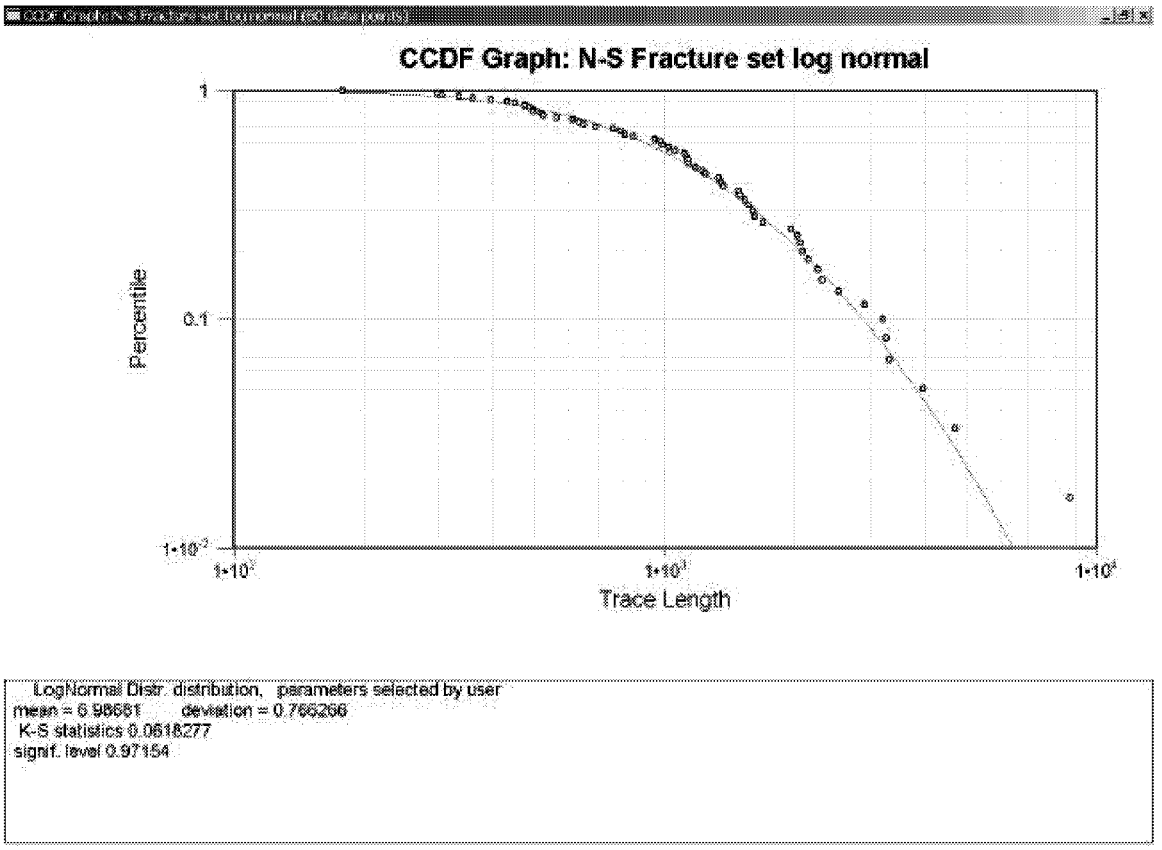

Figure 3-148 Trace Length Distribution, NS Lineaments

The fracture size distribution was calculated from the lineament distribution using the forward modeling approach of Dershowitz et al. (2000). Fractures were simulated in the 3D volume using assumed intensity and size distributions for the ESE set defined above. These fractures were then intersected by a simulated trace plane to obtain a simulated trace length distribution. The fracture radius distribution and intensity assumptions were then adjusted to obtain a match to the trace length distribution fitted to the measurements. The fitting of simulated trace length distributions is illustrated in Figure 3-149 through Figure 3-160.

Figure 3-149 through Figure 3-153 illustrate the change in the lineament trace length distribution as the fracture radius distribution r_{min} is increased from 10 feet to 2000 feet. Figure 3-154 through Figure 3-157 shows the effect of varying the power law distribution exponent from 1.5 to 3.5. Figure 3-158 through Figure 3-160 illustrates simulations in which the fracture radius distribution was not changed, while the intensity P_{32} was varied from 0.001 to 0.1 m^2/m^3.

Table 3-56 summarizes intensity and size analyses for the four sets. Based on trace mapping, the intensity of each set is expressed as P_{21}, the total length of tracer per unit area. The total intensity P_{32} for the four sets is consistent with that evaluated previously (Dershowitz, 2000) based on FMI data. This total intensity P_{32} was allocated to the four sets in proportion to the P_{21} for that set. This approach ignores the effect or orientation bias.

Table 3-56: Intensity from Lineament Data

Fracture SET	# in wells	# in Seismic	Mean lineament length (ft)	Relative P21 (m/m^2)	Estimated P32 (m^2/m^3)	Power law, min	Exponent
E-W	22	78	2022	0.19	0.04	570	1.7
N-S	3	120	1974	0.29	0.06	750	2.6
N-E	28	292	2798	1.00	0.22	700	1.7
E-SE	10	94	2771	0.32	0.07	1300	2.5

The gel treatment analysis depends upon explicit representation of both permeability and porosity for both the discrete features which will be effected by the gel, and the rock matrix from which oil is to be swept. The MAFIC discrete fracture –matrix interaction code is generally used for cases in which discrete features are the only flowing porosity, and the matrix serves only as a storage porosity. The South Oregon Basin model therefore includes both the discrete fracture network porosity derived above, plus a matrix flow and storage porosity. The matrix porosity is represented in the model using bedding plane elements.

The properties for bedding planes were derived in Dershowitz and Cladouhos (1999). These features represent a critical element of the model as the matrix provides the majority of the storage in reservoirs in the South Oregon Basin. Bedding features are implemented as rectangular elements dipping around an average orientation, and distributed randomly throughout the field.

Table 3-57 presents a summary of the DFN model implemented including fracture and bedding plane (matrix) elements. Figure 3-161, Figure 3-162, and Figure 3-163 show three dimensional representations of the fracture model. The model is implemented in a 400 m x 400 m x 10 m model domain. Length distributions within the model were approximated using lognormal assumptions. All fractures had a thickness of 0.025mm. The fracture system appears well connected with fractures from all of the four fracture sets.

Table 3-57: South Oregon Basin DFN Model

Set	Orientation Distribution Pole (Trend, Plunge) Fisher Dispersion κ	Length Lognormal Distribution (Mean, Std. Dev)	Intensity P_{32} (m^2/m^3)	Permeability (Darcy)
East-West	(2.8, 0) κ=30	3, 1.15	0.02	20 Darcy
East-South East	(40,0) κ=30	20, 10	0.035	20 Darcy
North-South	(260.9,0) κ=30	3, 1.5	0.03	20 Darcy
NE-SW	(316.2,0) κ=30	20, 10	0.11	20 Darcy
Bedding (Matrix)	(110,25) κ=10	20, 10	0.1	20 Darcy

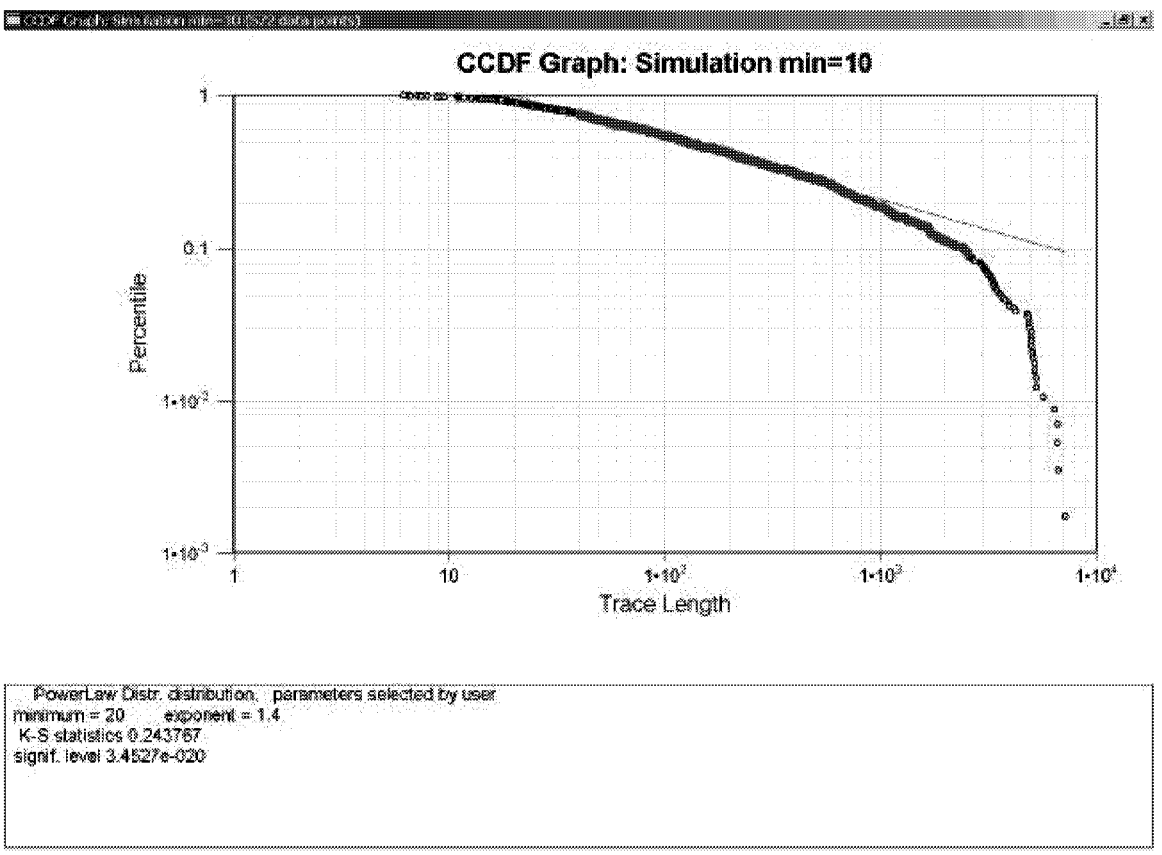

Figure 3-149: Simulation of ESE Lineaments 10 ft. Scale

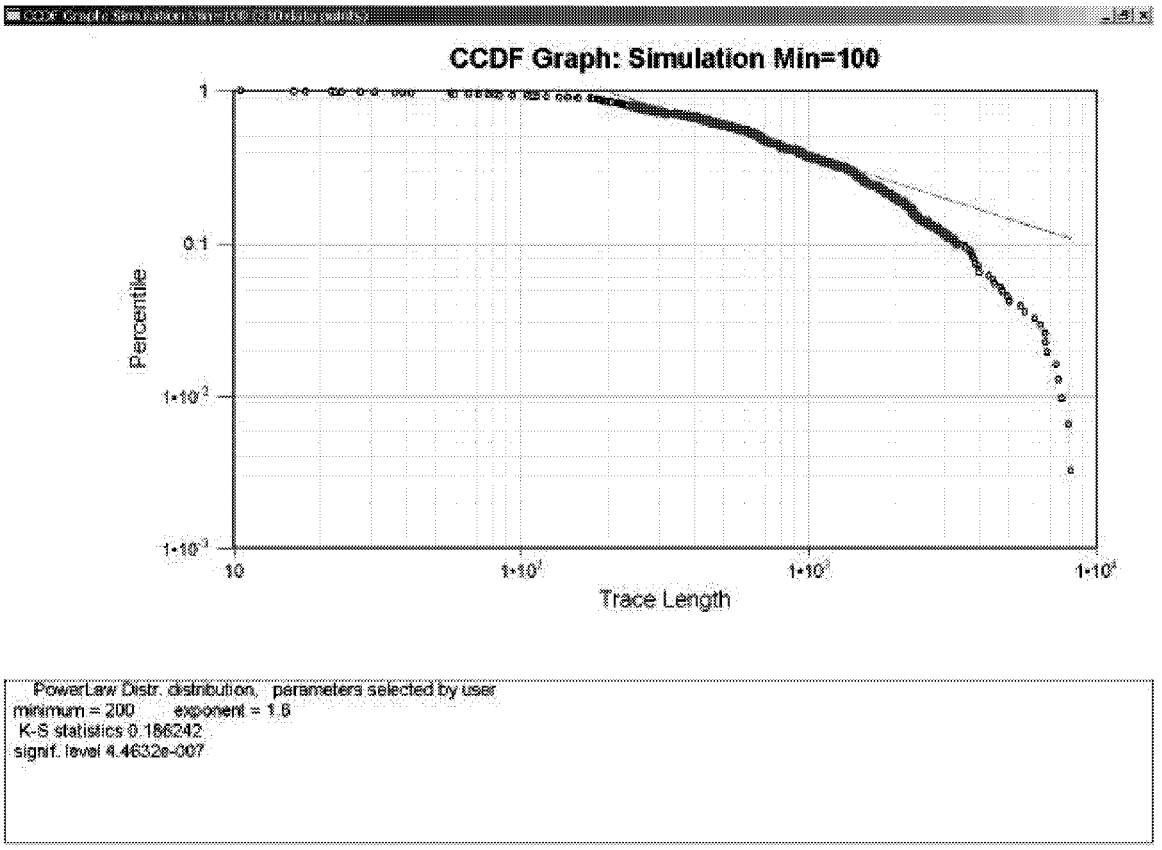

Figure 3-150: Simulation of ESE Lineaments, 100 ft. scale

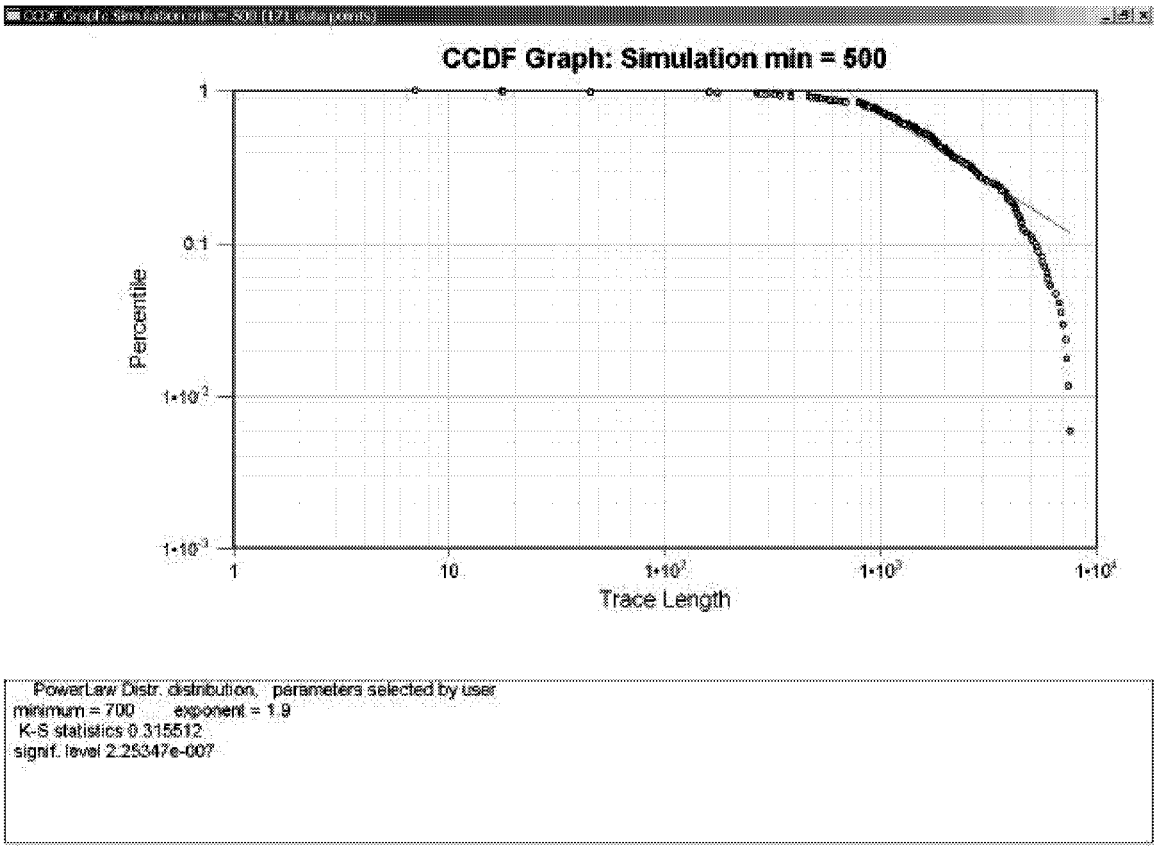

Figure 3-151: Simulation of ESE Lineament, 500 ft. Scale

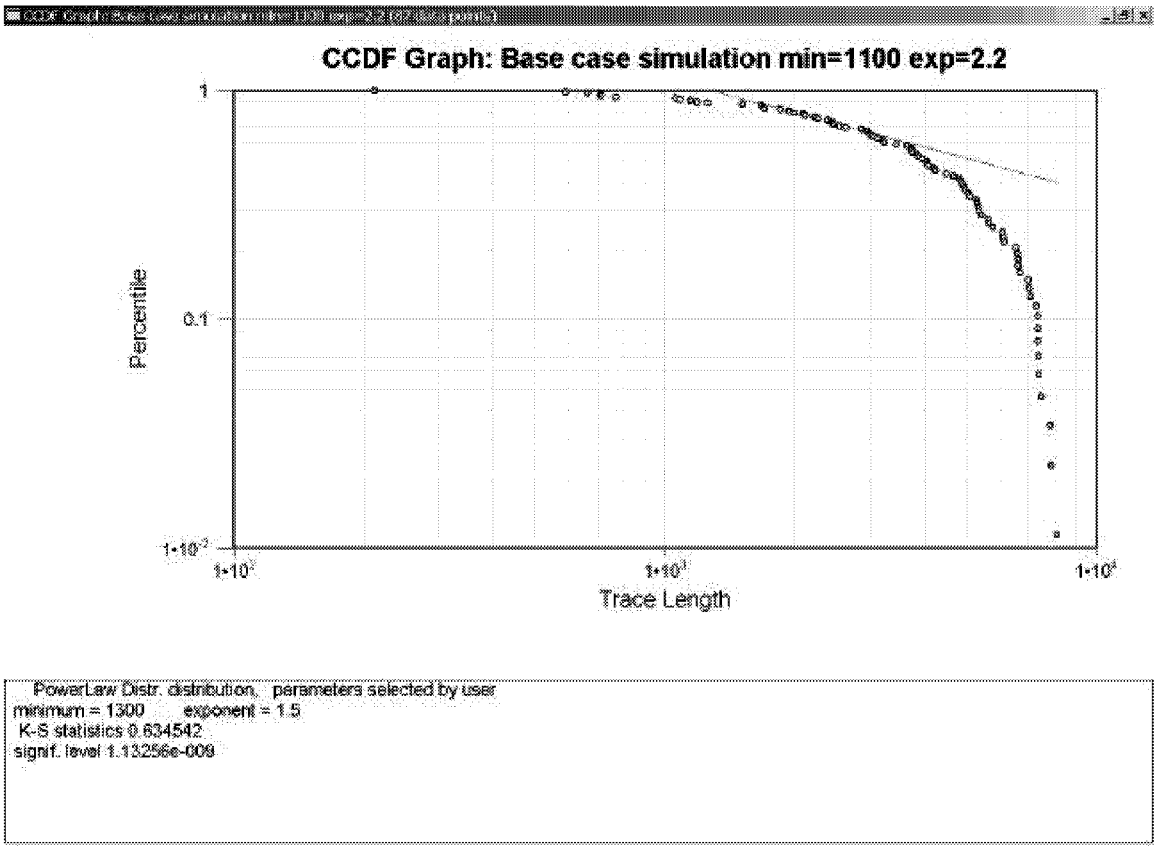

Figure 3-152 Simulation of ESE Lineaments, 1300 ft. Scale

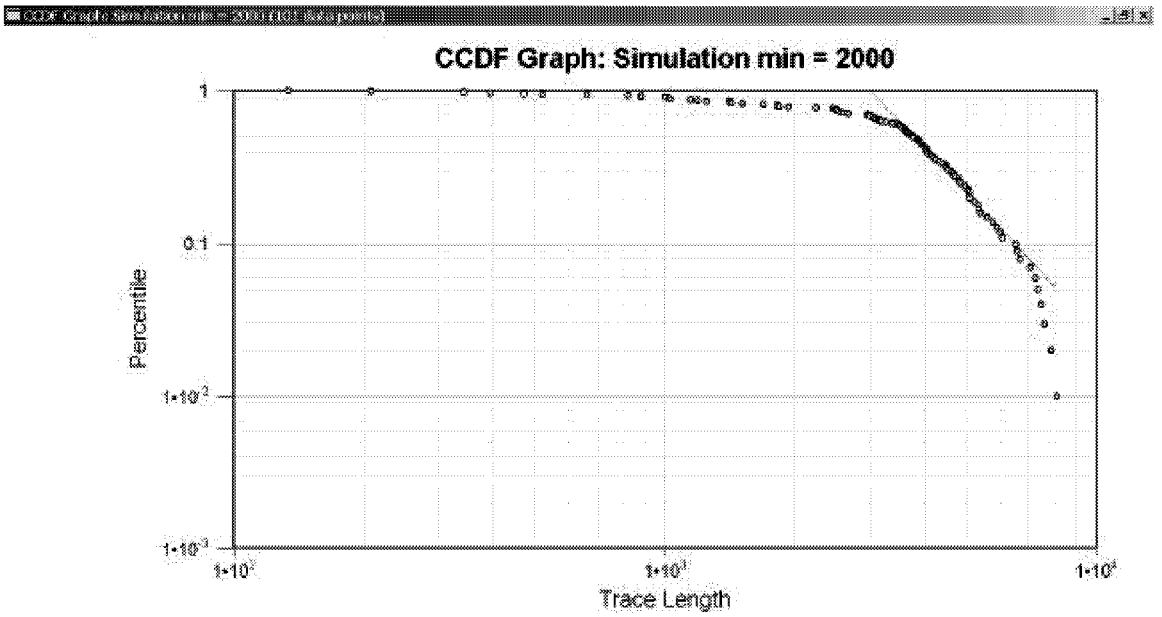

PowerLaw Distr. distribution, parameters selected by user
minimum = 3000 exponent = 4
K-S statistics 0.421562
signif. level 5.69199e-008

Figure 3-153: Simulation of ESE Lineaments, 2000 Ft. Scale

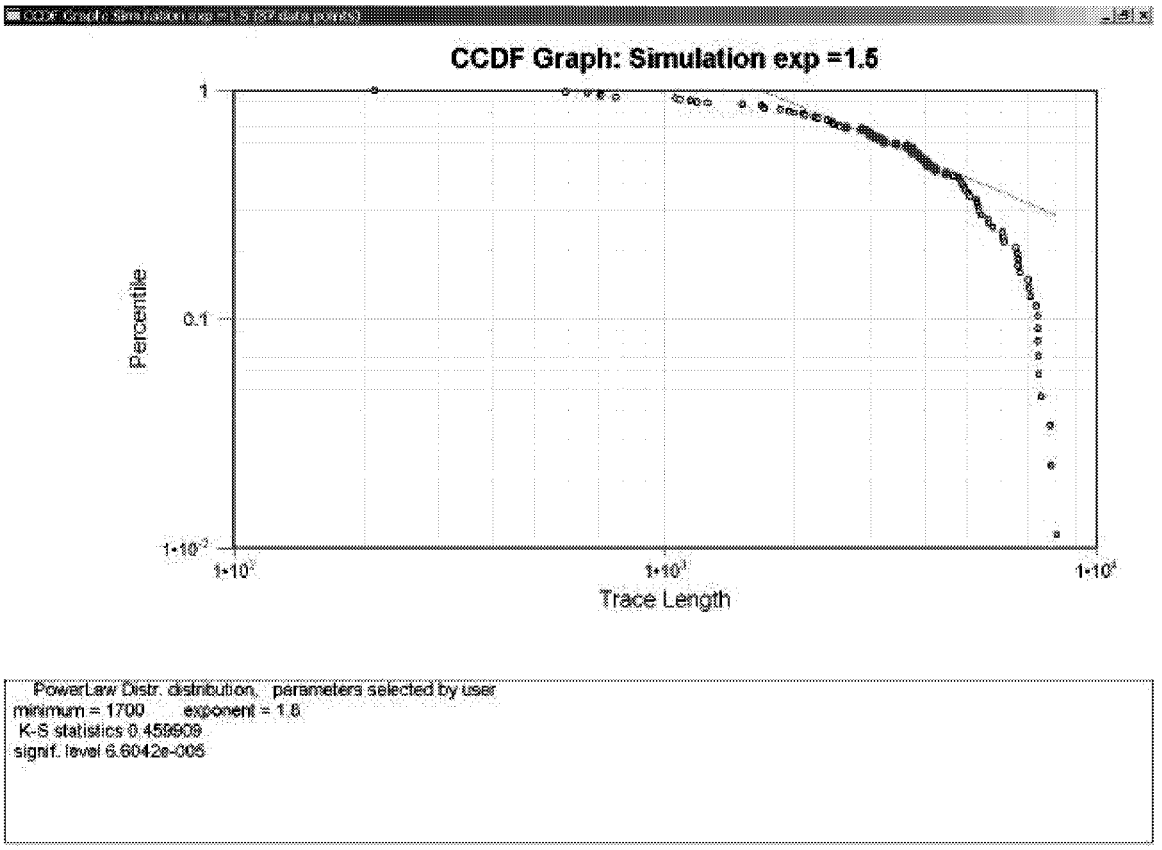

Figure 3-154 Simulation of ESE Lineaments, Exponent 1.5

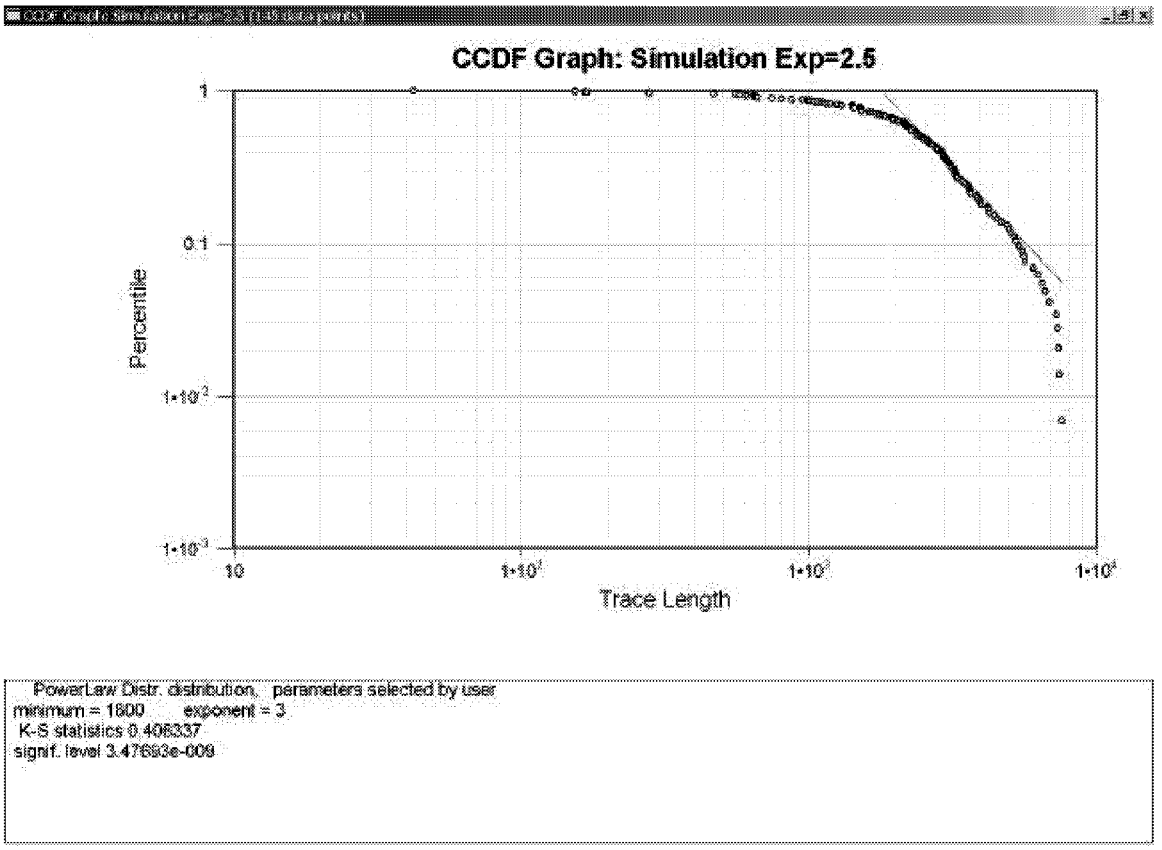

Figure 3-155 Simulation of ESE Lineaments, Exponent 2.5

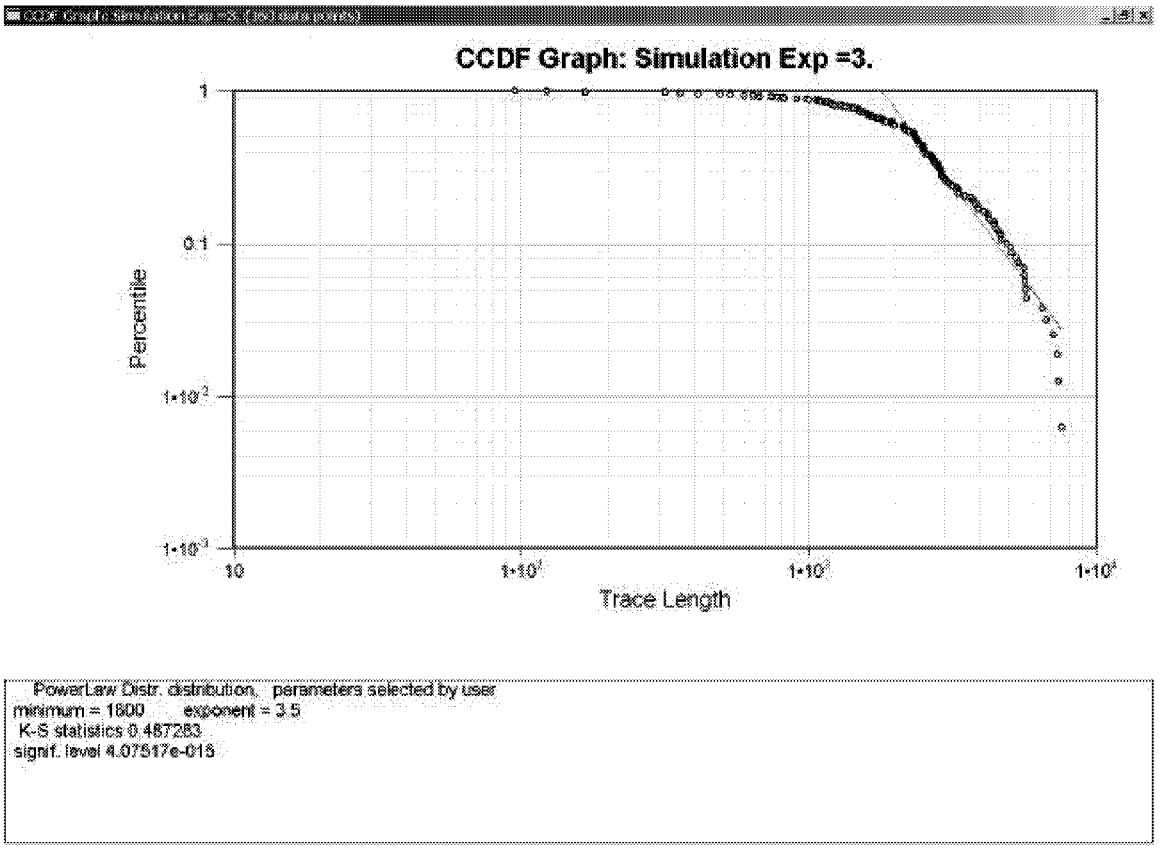

Figure 3-156: Simulation of ESE Lineaments, Exponent 3

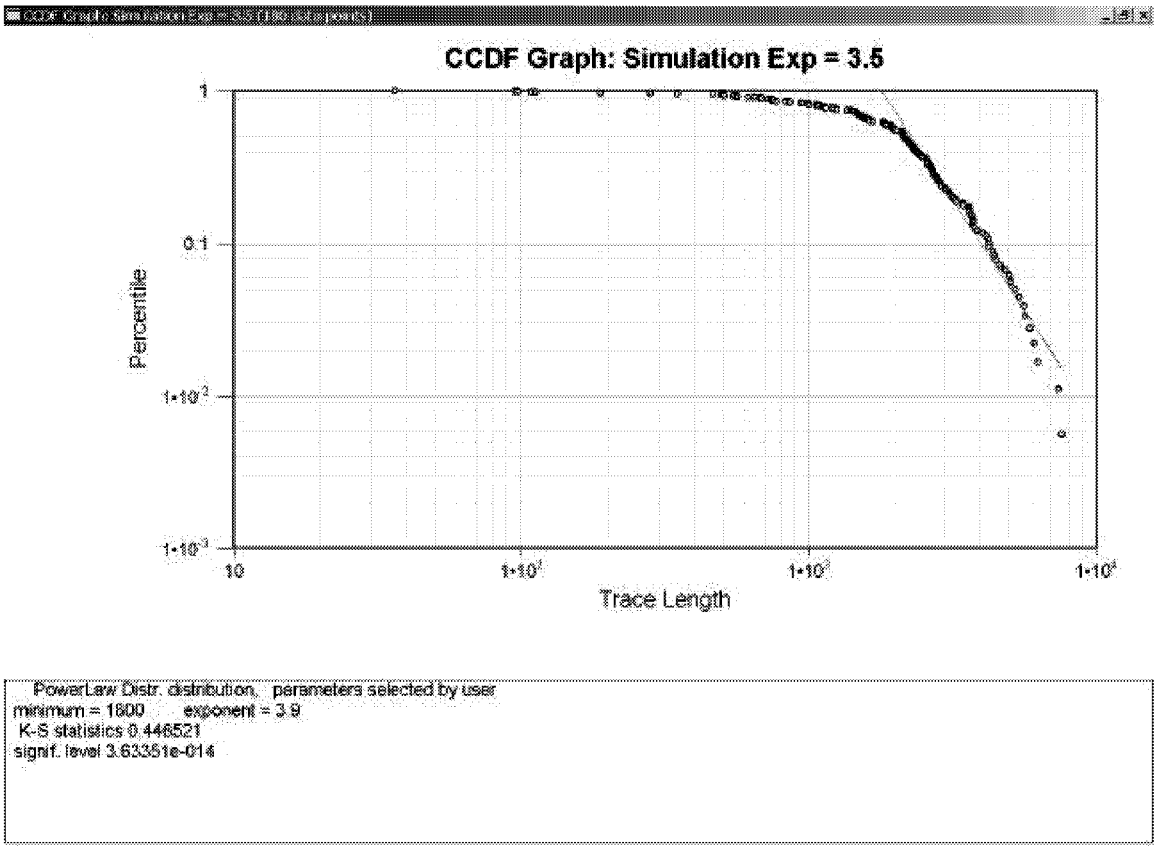

Figure 3-157: Simulation of ESE Lineaments, Exponent 3.5

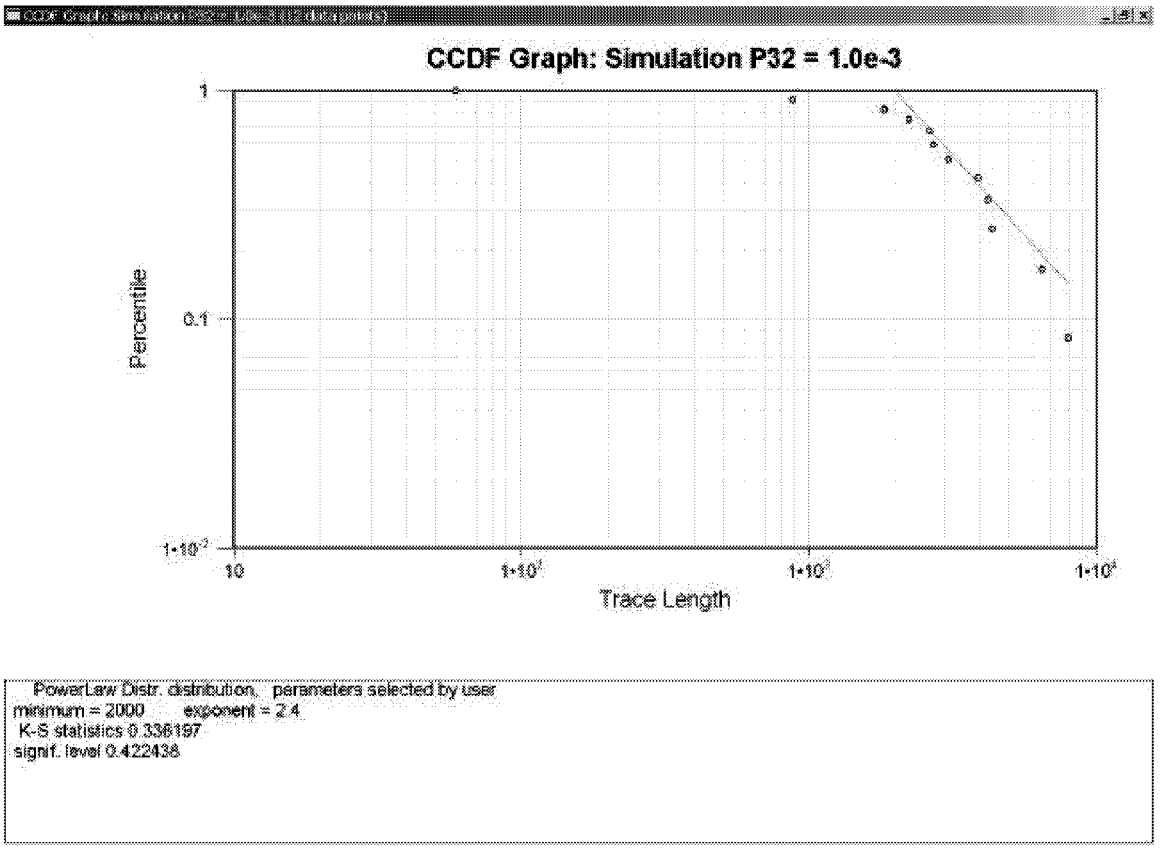

Figure 3-158: Simulation of ESE Lineaments, Intensity $P_{32} = 0.001\ m^2/m^3$

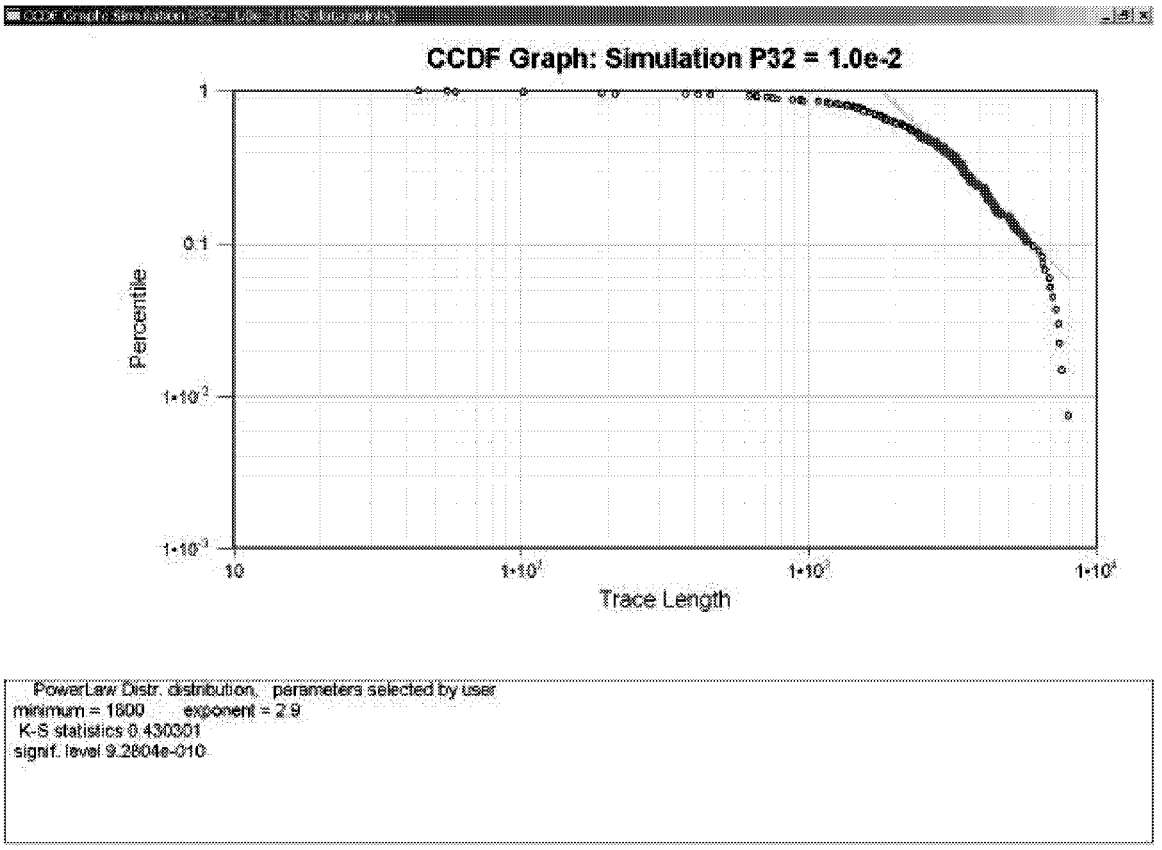

Figure 3-159: Simulation of ESE Lineaments, Intensity $P_{32} = 0.01\ m^2/m^3$

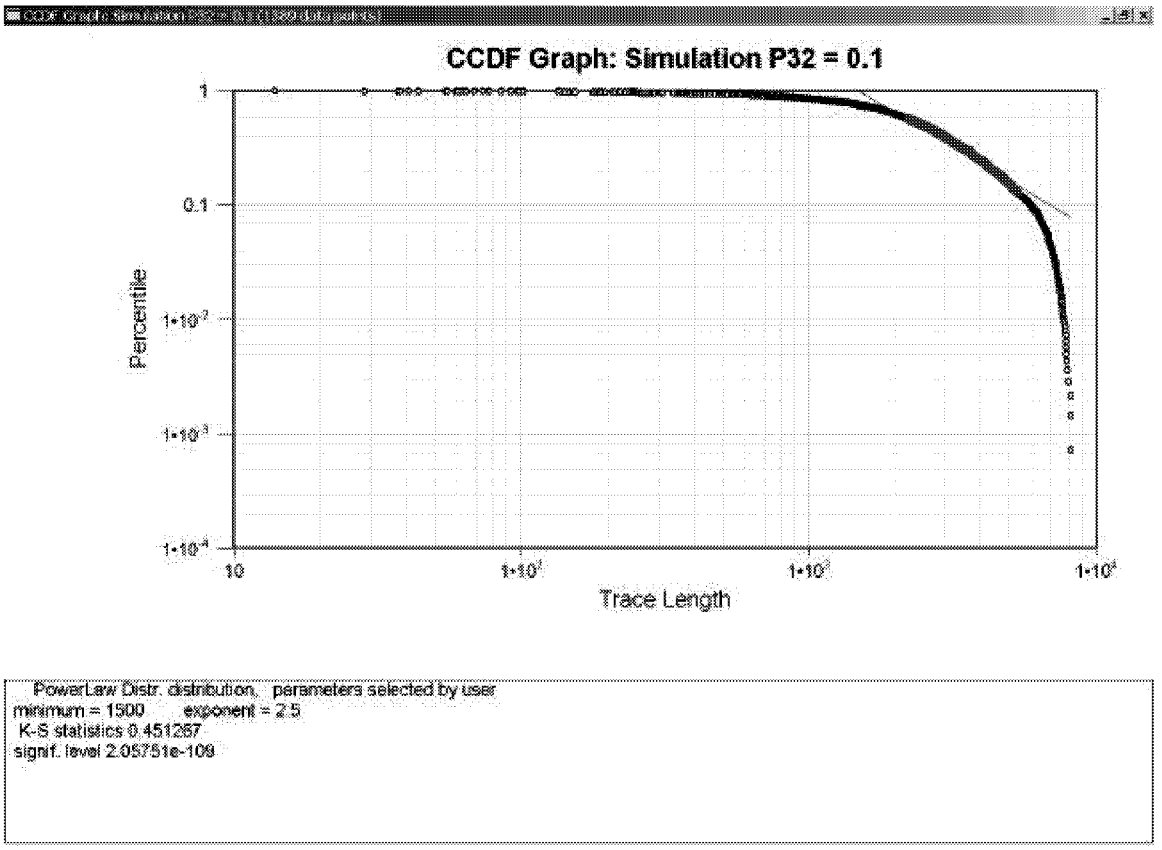

Figure 3-160: Simulation of ESE Lineaments, Intensity $P_{32} = 0.01\ m^2/m^3$

Figure 3-161: Fractures for South Oregon Basin Simulation

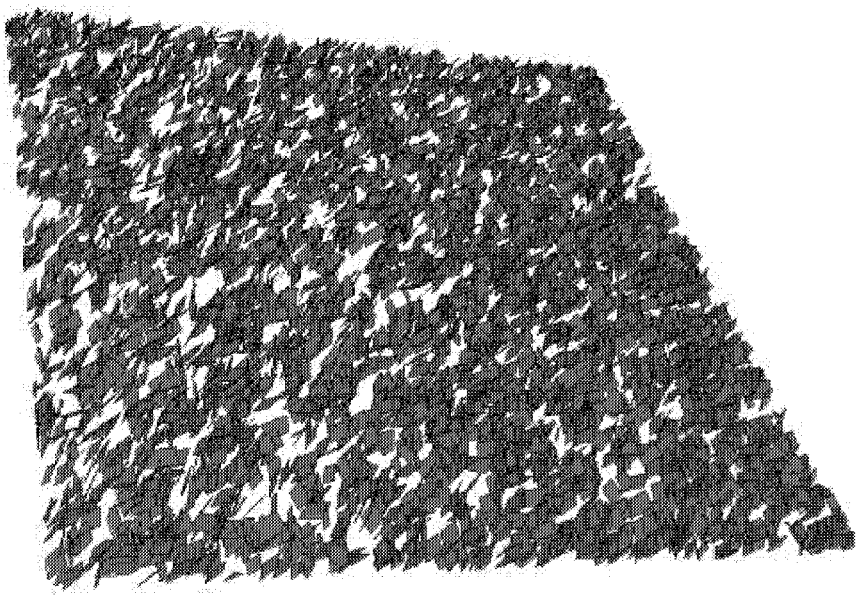

Figure 3-162: Matrix Discrete Features for South Oregon Basin Simulation

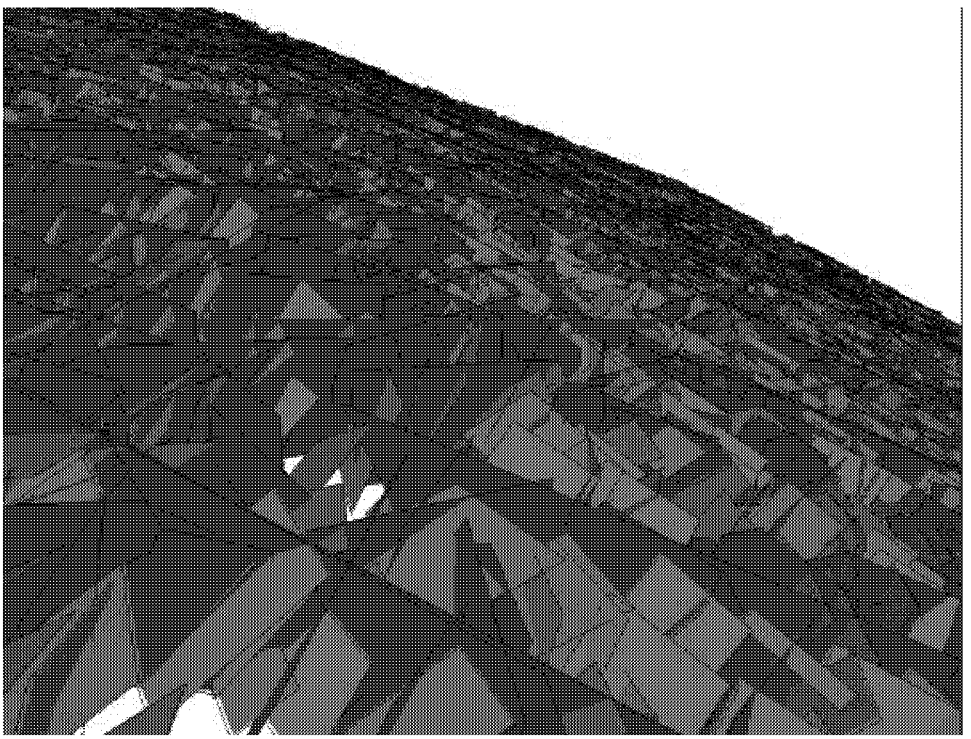

Figure 3-163: Fractures and Matrix Close up for South Oregon Basin Simulation

3.5.3.2 South Oregon Basin Gel Simulations

While fractures provide an efficient delivery system to deliver oil to the production well from the matrix storage, they can also provide a short circuit route between injectors and producers. This can limit the effectiveness of water injection, and at worse lead to increased water cut. Gel treatment aims to improve reservoir pressure maintenance and oil sweep efficiency by blocking the fractures in the vicinity of injectors.

The strategy for simulating this is to simulate the water injection/oil production pair using the single phase MAFIC flow simulator at 1250 BPD. First, we simulate the effect of balanced injection and production including the effects of the fracture network. Figure 3-164 through Figure 3-166 illustrate the pre-gel injection case. As the water injection increases, a pressure break-through occurs allowing water to travel directly from the injection well to the producer. The sweep efficiency is consequently low, and the pressure maintenance ineffective.

Figure 3-167 through Figure 3-169 present results for simulations in which the fractures connected to the injection well have been blocked by gel injection. Figure 3-167 presents the base case in which the fracture transmissivity is reduced one order of magnitude by gel to 2.0 Darcy. Figure 3-168 presents a reduction of transmissivity to 0.2 Darcy. Figure 3-169 presents the post effective gel treatment case, with the fracture transmissivity reduced to .02 Darcy. The fractures no longer provide short circuit pathways, such that the water injection is able to produce an increase the pressure in a consistent and evenly dispersed area. This provides an efficient sweep, driving oil out of the matrix and towards the producing well.

3.5.3.3 Evaluation

Marathon Oil Comparny (MOC) has carried out gel treatments targeting discrete fractures in the South Oregon Basin, consistent with the recommendations based on DFN modeling. These gel treatments have facilitated water injection which maintained formation pressures at 400 psig. Oil production at the wells effected by water injection totals approximately 10 BPD per well. Water extraction is currently about 1000 BWPD.

Reduction in water breakthrough due to gel injection is difficult to judge and nearly impossible to accurately measure. In 75-85% of the gel injections, Marathon does not report an immediate decrease in water production at the offset producers following an injection well gel treatment. It is assumed that gel is less than 100% effective in blocking off the fracture network, in part due the short circuiting effect seen in DFN simulations. Theoretically, we would expect a significant decrease in water production if fracture networks were well plugged with gel. However, Marathon does not report experiencing this in most cases. Rather, in the project study site gel injections have resulted in an increase in oil production or a shallowing of the oil decline rate. This indicates that these gel treatments have been at least partially successful. The observed increase in oil production may be due to improved sweep efficiency or to a change in the vertical profile of injection accessing a different area of the reservoir.

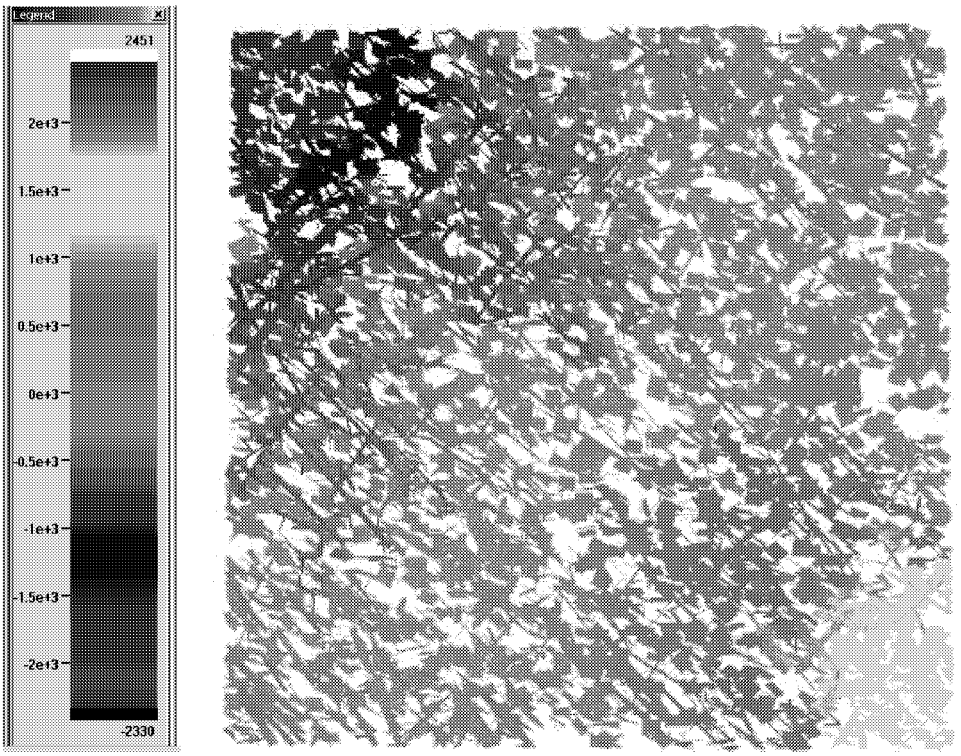

Figure 3-164 South Oregon Basin simulation pre gel. Time = 0.001 Hours

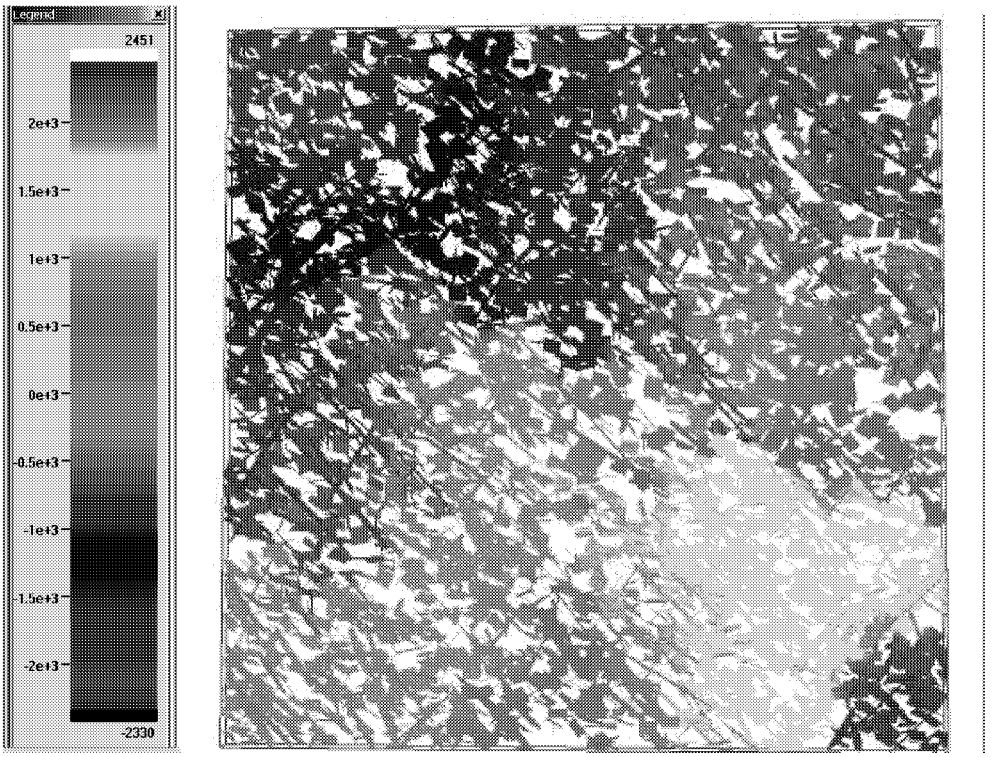

Figure 3-165: South Oregon Basin simulation pre gel. Time = 0.01 Hours

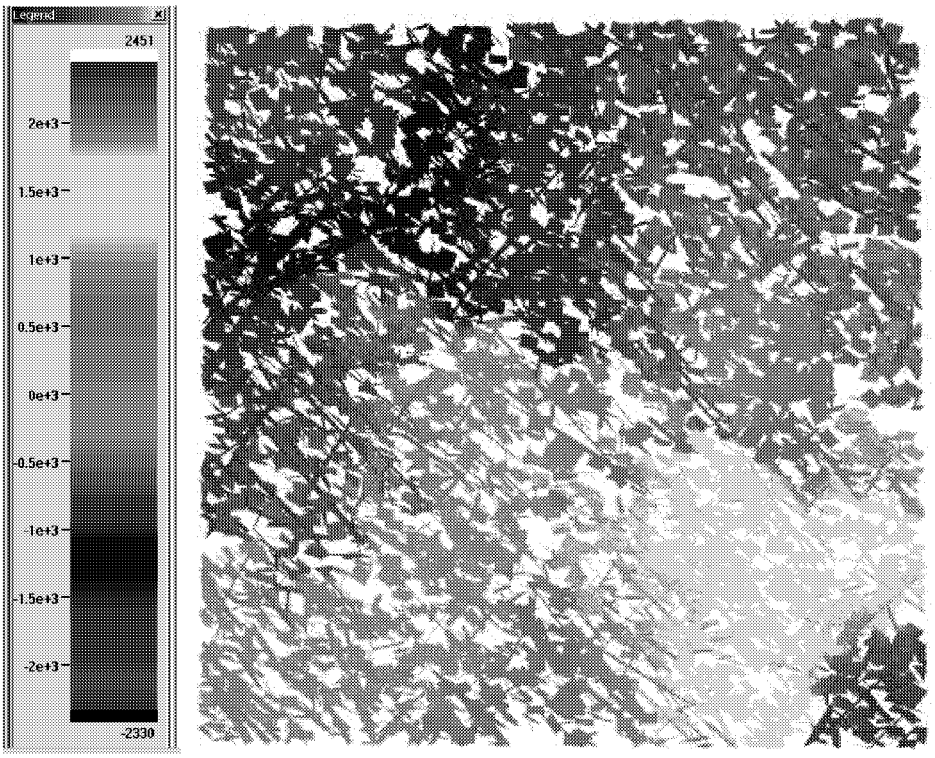

Figure 3-166: South Oregon Basin simulation pre gel. Time = 1 Hour

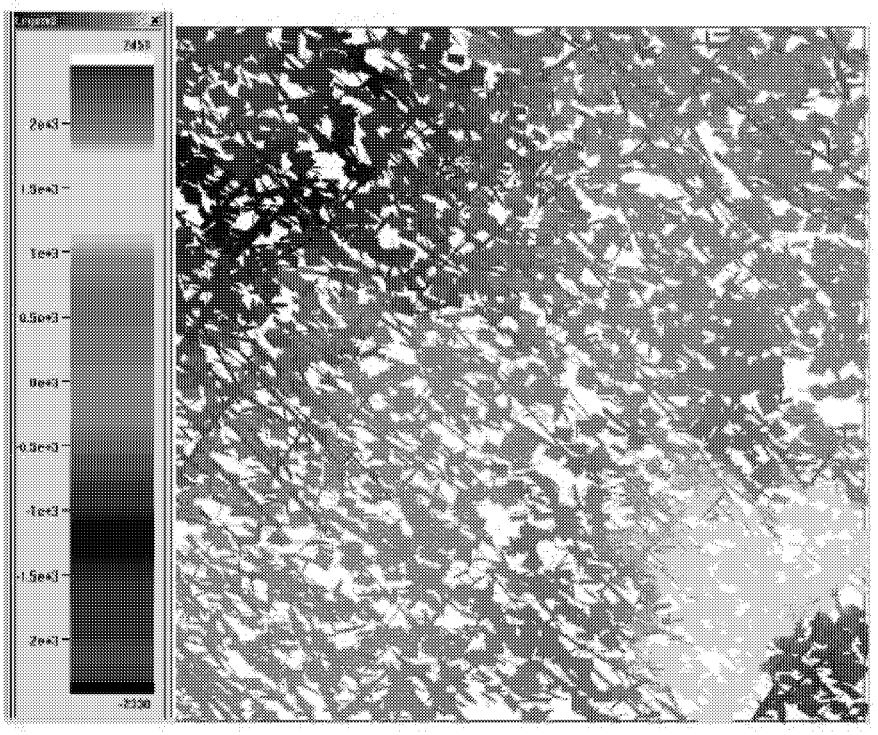

Figure 3-167: South Oregon Basin simulation after gel treatment reduces fracture permeability 1 order of magnitude

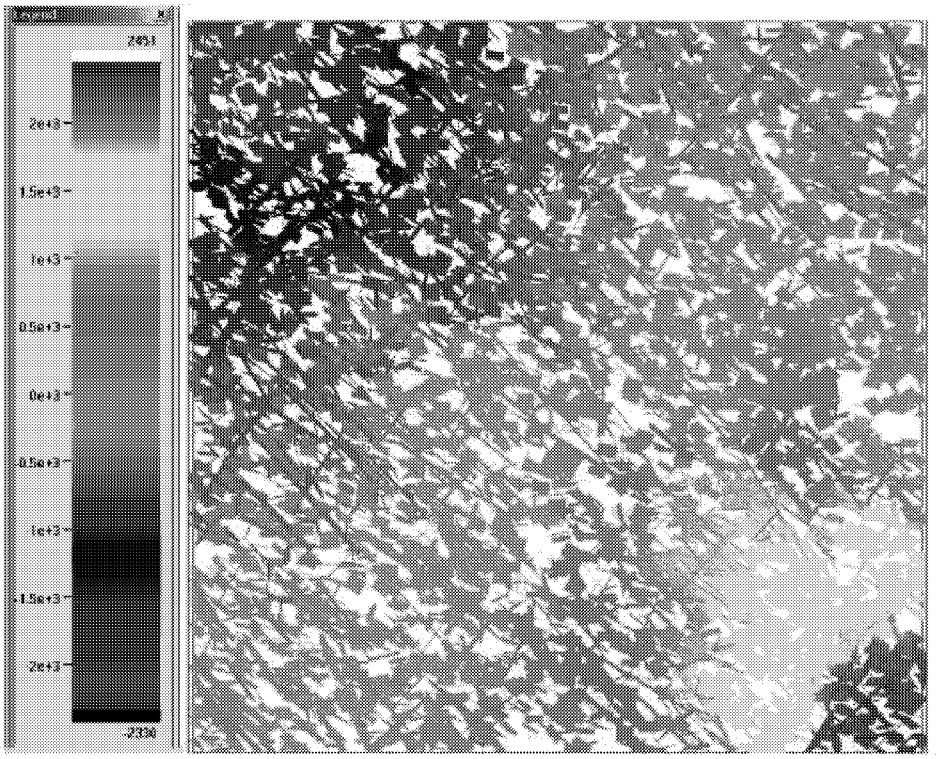

Figure 3-168: South Oregon Basin simulation after gel treatment reduces fracture permeability 2 orders of magnitude

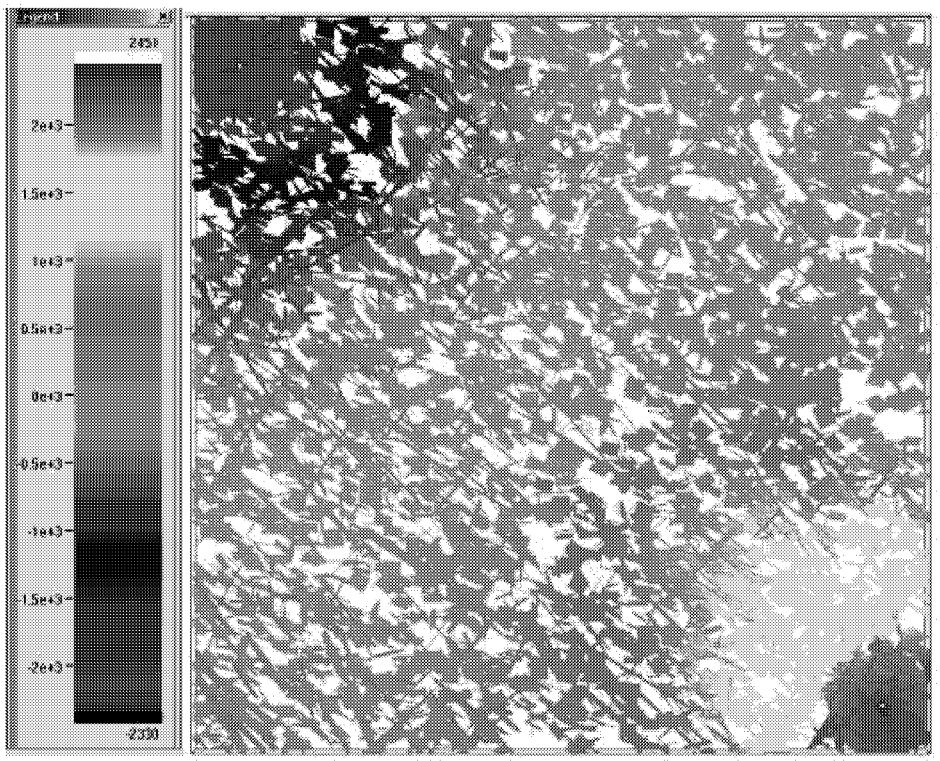

Figure 3-169: South Oregon Basin simulation after gel treatment reduces fracture permeability 3 orders of magnitude

3.5.4 Task 4.4 Reservoir IOR Demonstration, North Oregon Basin

Water injection is being used extensively in the North Oregon Basin, Wyoming Tensleep formation to improve oil recovery. Gel treatments have been used to reduce the water-cut by selectively restricting flow through the fractures without substantially reducing the matrix permeability. The discrete fracture network (DFN) model of the reservoir described in Dershowitz and Cladouhos (1999) was used to simulate the use of gel to improve the sweep efficiency of water injection. The analysis focus area is shown in Figure 3-170.

In the fractured, heterogeneous Tensleep formation, discrete fractures and eolian sandstones provide discrete pathways both for oil production and for water migration. The DFN approach addresses the geometry and occurrence of these pathways directly by explicitly modeling fractures, dolomite barriers, and conductive eolian bedding planes. In addition, the DFN approach is used to address the geometry of hydraulic compartments formed by networks of discrete features

Simulation of the problem of water-breakthroughs requires an understanding of:

- The geometry of the fractures that allows the water breakthroughs;
- The effect of the gel treatment on the relative permeability of the fractures and matrix;
- The transfer of fluids through both the fractures and matrix; and
- Any multi-phase effects of water passing through the oil.

The DFN analysis of gel control was carried out by implementing the DFN model to contain both the major conductive fractures, and the aeolian sandstones and dolomite layers which provide both significant conductivity and connectivity, and matrix storage. The DFN model is illustrated in Figure 3-171. Both the fractures and matrix are represented as discrete features. The matrix is modeled in this fashion because of the discrete nature of the sand beds, and also to facilitate modeling using the MAFIC code. The thickness of each bed in the model is provided in Table 3-58.

The simulation was carried out with both water injection and oil production at a rate of 1250 BPD. Figure 3-172 presents simulation results for the water injection without gel treatment. As a result of preferential flow through the fracture network, the injected water invades only a narrow band of the surrounding reservoir before finding a high permeability path to the production well. In this case the injection fails to introduce a significant pressure gradient across the matrix and will result only in an increase in the water cut at the producing well.

Gel treatment was simulated by reducing the permeability of the fractures connected to the injection well to 0.2 Darcy. The pressure distribution following gel treatment is illustrated in Figure 3-173. The water injection then provides for efficient pressure maintenance and oil sweep. Due to the gel treatment the pressure gradient is now more evenly applied across the reservoir and should more effectively move oil out of the matrix towards the producing well.

The North Oregon Tensleep model is now being adapted for use at particular injection producer pairs to study gel treatment design alternatives.

3.5.4.1 Evaluation – North Oregon Basin

In the North Oregon Basin, Marathon Oil Company (MOC) has not yet carried out gel treatments based on DFN analyses. As a result, it is not yet possible to quantify the value of these activities.

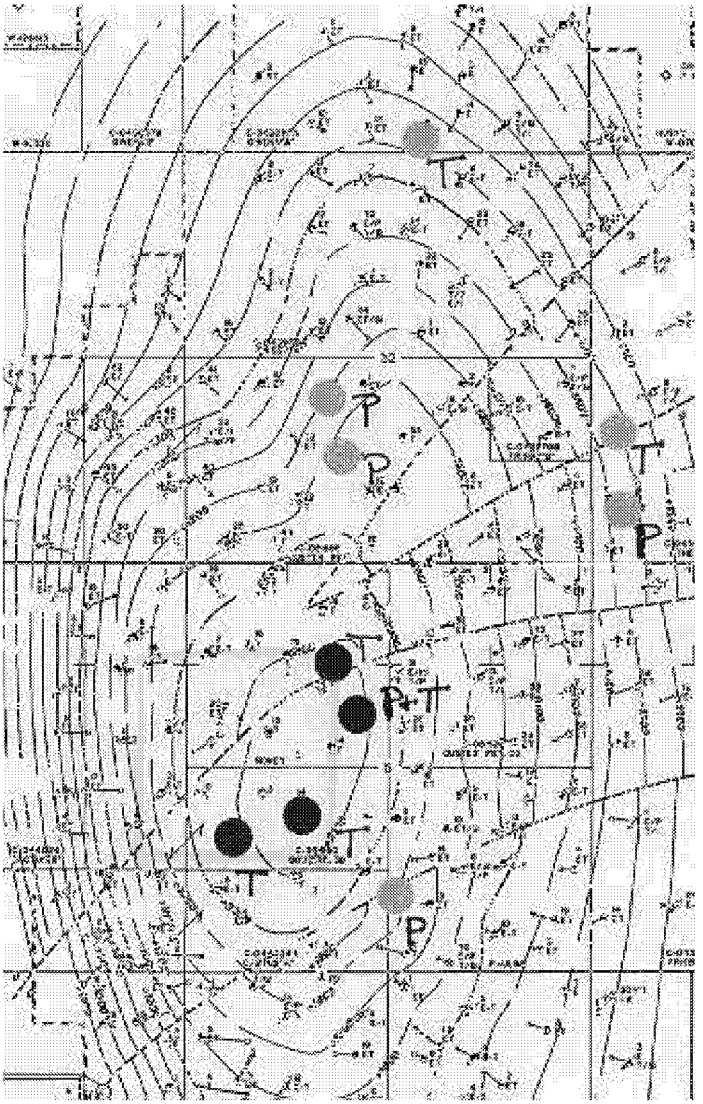

Figure 3-170: North Oregon Basin Structure and Well Control

Table 3-58: North Oregon Basin Bed Thickness

Rock Type	Thickness (m)	Layer Center (m)
Dolomite	2	15
Sandstone A	7	10.5
Dolomite	2	6
Sandstone B	3	3.5
Dolomite	3	0.5

Sandstone C	3	-2.5
Dolomite	2	-5
Sandstone DE	10	11

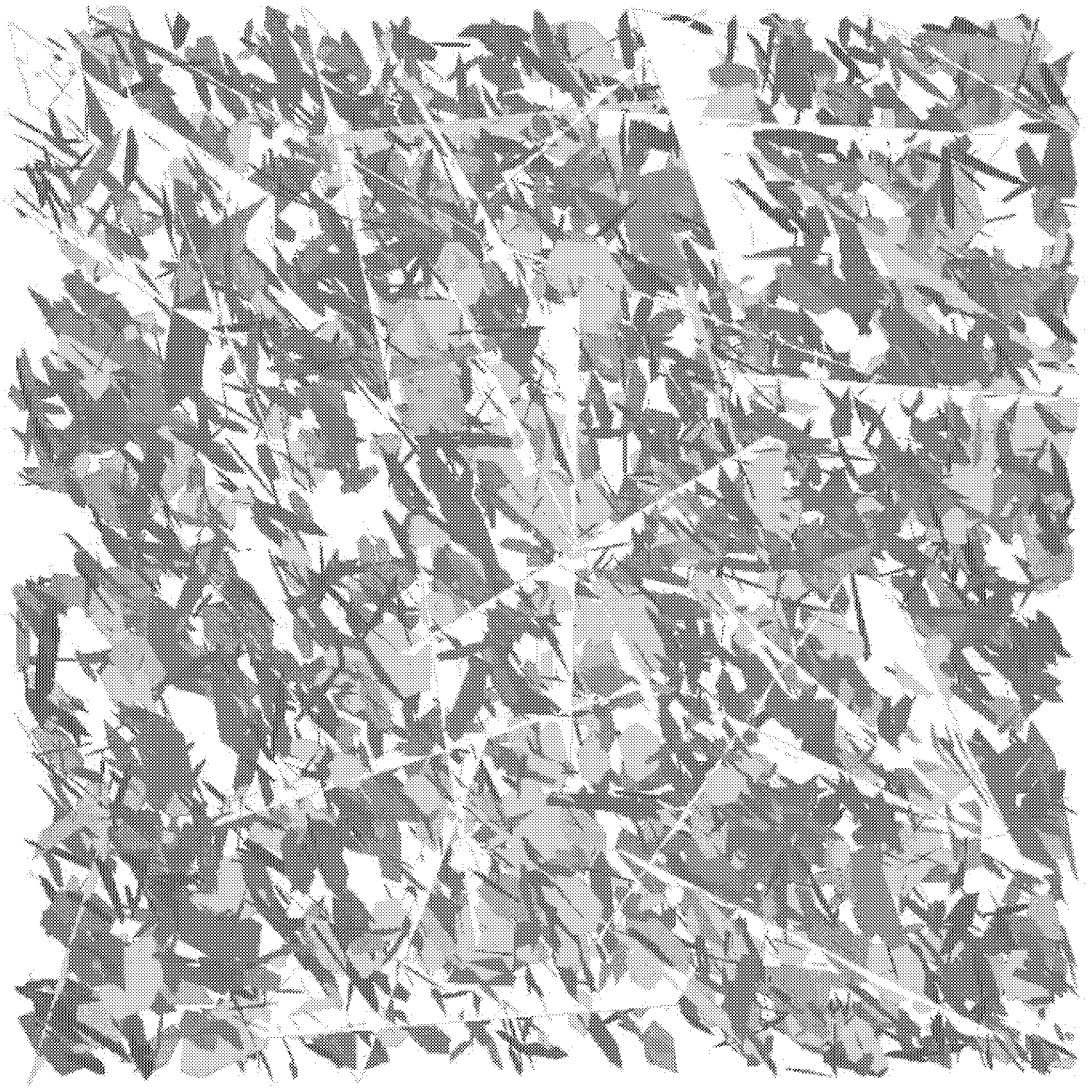

Figure 3-171: North Oregon Basin DFN model

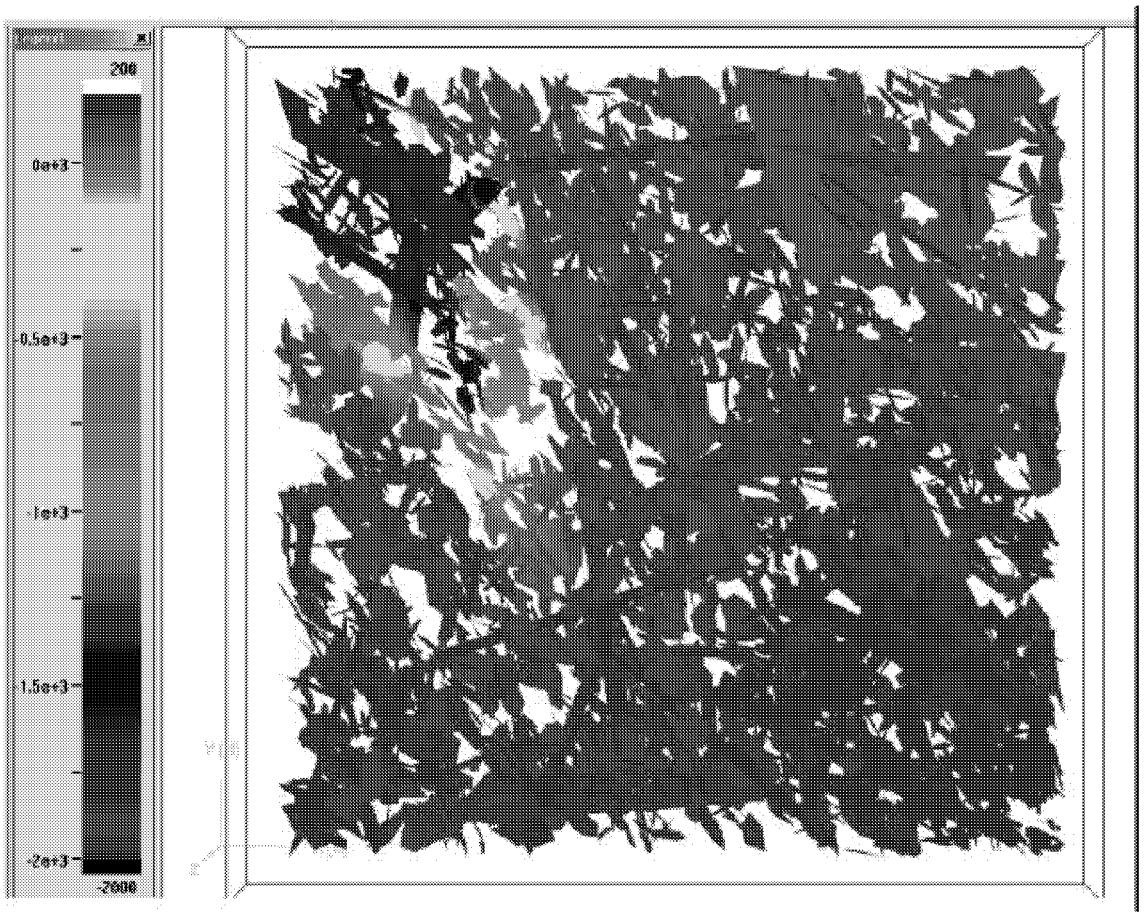

Figure 3-172: North Oregon Basin DFN model before gel treatment

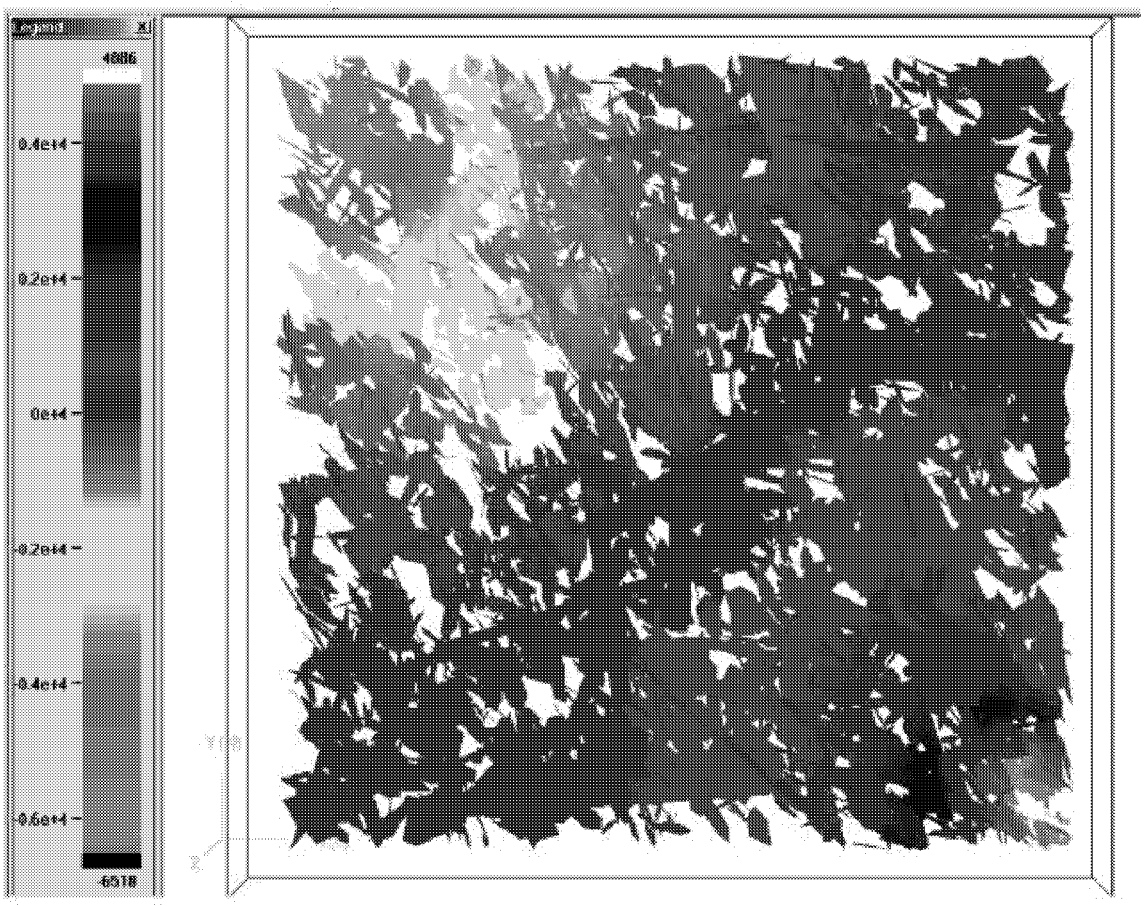

Figure 3-173: North Oregon Basin DFN model after gel treatment

3.6 Task 5: Technology Transfer

3.6.1 Task 5.1. Project Web Site

Throughout the project, project data, simulations, and publications were made available through the project web site, http://HeterOil.golder.com. These included posting of site data provided by Marathon Oil Company (MOC), project presentations, and progress reports.

3.6.2 Task 5.2.1 Reports

The reports produced during this project are listed above in Section 3.1.

3.6.3 Task 5.2.3 Presentations and Publications

The presentations made during the project are listed above in Section 3.1.

4. CONCLUSIONS

Fractured and heterogeneous reservoirs present unique challenges for "Discrete Feature Approach for Heterogeneous Reservoir Production Enhancement." The report presents summaries of technology development for discrete feature modeling in support of the improved oil recovery (IOR) for heterogeneous reservoirs. In addition, the report describes the demonstration of these technologies at project study sites.

In the discrete feature network (DFN) approach, conductive and flow barrier structures are modeled explicitly, facilitating a more realistic analysis of flow of fluids. The DFN approach models these features at all scales simultaneously, from the individual fractures intersecting a well to the major faults which define the reservoir. There discrete features are extrapolated from geological and geophysical measurements using a combination of geological and geostatistical methods.

During this project, Golder Associates' team improved the data analysis and geological modeling capabilities of the DFN approach, and developed practical applications of that approach for IRO in heterogeneous reservoirs.

Major accomplishments of this research project are summarized in Table 1. These include development of approaches for gel treatment, strategic completion, and water control in heterogeneous reservoirs. The discrete fracture network technologies developed within this project are directly applicable to a large percentage of the secondary and tertiary oil recovery projects currently underway in the United States, and can be of significant value to the design of future oil recovery projects.

This project achieved significant technological advances in the development of the discrete fracture network modeling approach for heterogeneous oil reservoirs. Advances include:

- the first large scale, fracture network multiphase DFN flow simulations (Oregon Basin)
- direct DFN simulation of gel injection to realistic fracture networks (Oregon Basin, Stoney Point)
- three dimensional, heterogeneous, geo-cellular based DFN modeling for strategic completion (Yates)
- development of an advanced neural network algorithm for fracture set identification
- fractal, analytical, and numerical solutions for calculation of fracture size distributions from geological and geophysical trace data,
- discrete fracture network approach for conditioning of fractured reservoir connectivity based on tracer tests.
- new approaches to evaluating fracture shapes and correlations between fracture properties
- extension of the DFN approach from fractured and single porosity reservoirs to multiple porosity reservoirs with complex, heterogeneous geologies

As a result of this project, the DFN approach can now be applied to improve recovery in a wide range of situations including water and steam floods, strategic completions, and gel treatments.

5. REFERENCES

ASCE (1998). Geophysical exploration for engineering and environmental investigations, Technical Engineering and Design Guides as Adapted from the US Army Corps of Engineers, No. 23, ASCE Press, Reston, VA.

Baecher, G. N., N. A. Lanney, and H. H. Einstein, 1977. Statistical Description of Rock Properties and Sampling. 18th U.S. Symp. on Rock Mechanics, 5C1-8.

Baecher, G. N., Lanney, N. A., 1978. Trace Length Biases in Joint Surveys." 19th U.S. Symp. on Rock Mechanics, 1, 56-65.

Barton, C. M., 1977. Geotechnical Analysis of Rock Structure and Fabric in CSA Mine NSW." Applied Geomechanics Technical Paper 24, Commonwealth Scientific and Industrial Research Organization, Australia.

Barton, C. M., 1978. Analysis of Joint Traces. 19th U.S. Symp. on Rock Mechanics, 1, 38-41.

Barton, C.C. and E. Larson (1985), "Fractal Geometry of Two-dimensional Fracture Networks at Yukka Mountain, Southwest Nevada", Fundamentals of Rock Joints, Proceedings of the International Symposium of Rock Joints, Bjorkliden, Lapland, Sweden, O. Stephannson, editor, Centrek Publishers, Lulea, Sweden, 74-84.

Barton, C.C. and P.A. Hsieh (1989), "Physical and Hydrogeologic-Flow Properties of Fractures", 28th International Geological Congress Field Trip Guidebook T385 (American Geophysical Union, Washington, DC, 1989).

Benito, P. H., et al. (1999). "Cross-well air-injection packer tests for the assessment of pneumatic connectivity in fractured, unsaturated basalt." Rock Mechanics for Industry, 843-850.

Bridges, M. C., 1975. Presentation of Fracture Data for Rock Mechanics. 2nd Australia-New Zealand Conf. on Geomechanics, Brisbane, 144-148.

Cacas, M. C., 1999. Fraca Fractured Reservoir Modeling Software. IFP, Rueil-Mamalson, France.

Call, R. D., J. P. Savely, and D. E. Nicholas, 1976. Estimation of Joint Set Characteristics from Surface Mapping Data." 17th U. S. Symp. on Rock Mechanics, 2B2, 1-9.

Call, R.D.; Nicholas, D.E., 1978., Prediction of Step Path Failure Geometry for Slope Stability Analysis, Proc. 19th U.S. Symp. on Rock Mechanics .

Carter, B.J., Wawrzynek, P.A., Ingraffea, A.R., 2000. "Automated 3D Crack Growth Simulation", Gallagher Special Issue of Int. J. Num. Meth. Engng, 47, 229-253.

Carter, R. D., G. C. Howard and G. R. Fast, 1957. Optimum Fluid Characteristics for Fracture Extension, Drilling, and Production Practice.

Chakrabarty, C. and T. Doe, 1999. Analysis of Well Tests in Two-Zone Composit Systems with Different Spatial Dimensions. Submitted to Water Resources Research.

Chan, L. P., 1986. Application of Block Theory and Simulation Techniques to Optimum Design of Rock Excavations. Ph.D. thesis, University of California, Berkeley.

Chan, M. H. Einstein, and V. Li., 1990. "A hybridized displacement discontinuity and indirect boundary element method to model fracture propagation", International. Journal of Fracture, Vol. 45, pp. 263-282.

Cruden, D. M., 1977. Describing the Size of Discontinuities." Int. J. Rock Mech. Min. Sci. & Geomech. Abstr., 14, 133-137.

Cummings, D. (1990). "Surface geophysical investigations for hazardous waste sites." Geophysical Applications for Geotechnical Investigations, Editors: Paillet, R. L. and Saunders, W. R., ASTM, Philadelphia, PA, STP1101, 9-16.

Deng, Z. (1996). The application of ground penetrating radar for geological characterization in three dimensions at Gypsy Outcrop Site, Northeastern Oklahoma, USA. MS thesis, University of Oklahoma, Norman, Oklahoma,

Dershowitz, W., J.E. Geier, and K. Lee, 1988. Field Validation of Conceptual Models for Fracture Geometry. American Geophysical Union, 1988 Fall Meeting, San Francisco, EOS, Transactions, American Geophysical Union, vol. 69, no. 44 p. 1177.

Dershowitz, W. S., 1992. Interpretation and Synthesis of Discrete Fracture Orientation, Size, Shape, Spatial Structure and Hydrologic Data by Forward Modeling." Proc., Fractured and Jointed Rock Masses, Tahoe, NV, 579-586.

Dershowitz, W. S, Lee, G., Geier, J., Foxford, T., LaPointe, P., and Thomas, A. (1993). FracMan, Interactive discrete feature data analysis, geometric modeling, and exploration simulation. User Documentation, Version 2.3, Golder Associates Inc., Seattle, Washington.

Dershowitz, W., Busse, R., J. Geier, and M. Uchida, 1996. A Stochastic Approach for Fracture Set Definition. Rock Mechanics Tools and Techniques. AA Balkema, Rotterdam. pp 1809-1813.

Dershowitz, W.S., Einstein, H.H., LaPointe, P.R., Eiben, Th., Wadleigh, E., and Ivanova, V., 1998, Fractured Reservoir Discrete Feature Network Technologies, National Petroleum Technology Office, U.S. Department of Energy, Tulsa, Oklahoma.

Dershowitz, W.S. and Cladouhos, T., 1999: Discrete Feature Approach for heterogeneous reservoir production enhancement. January 1, 1999 – June 30, 1999 Progress Report, Fundamental Geoscience for Reservoir Characterization.

Dershowitz, W.S., Wadleigh, E., LaPointe, P.R., and Einstein, H.H., 2000, Discrete Feature Approach for Heterogeneous Reservoir Production Enhancement, January 1, 2000 – June 30, 2000 Progress Report, Fundamental Geoscience for Reservoir Characterization.

Doe, T. and J. Geier, 1991. Interpretation of Fracture System Geometry Using Well Test Data. SKB Stripa Project Report TR-91-03. SKB, Stockholm

ECL, 1997.ECLIPSE User Documentation. Schlumberger Geoquest/ECL, Henley-on-Thames, UK.

Einstein H. H., G. B. Baecher, and D. Veneziano, 1979. Risk Analysis for Rock Slopes in Open Pit Mines, Parts I-V, USBM Technical Report J0275015, Department of Civil Engineering, MIT.

Einstein, H. H., and G. B. Baecher, 1983. Probabilistic and Statistical Methods in Engineering Geology (part I). Rock Mechanics and Rock Engineering, 16(1), 39-72.

Goff, J.A., 1990. Comments on "Fractal Mapping Of Digitized Images: Application To The Topography Of Arizona And Comparison With Synthetic Images" by J. Huang and D.L. Turcotte. J. Geophys. Res., 95(B4), 5159.

Grandjean, G., and Gourry, J. C. (1996). "GPR data processing for 3-D fracture mapping in a marble quarry." J. Applied Geophysics, 36, 19-30.

Grasmueck, M. (1996). "3-D ground-penetrating radar applied to fracture imaging in gneiss." Geophysics, 61, 1050-64.

Griffith, A., 1921. The Phenomenon of Rupture and Flo w in Solids. Phil. Trans. Royal Society, London. Vol. 221, pp 163-198.

Huang, J. and D.L. Turcotte, 1989. Fractal Mapping Of Digitized Images: Application To The Topography Of Arizona And Comparison With Synthetic Images. J. Geophys. Res., 94(b6), pp. 7491-7495.

Hurley, N.F., and Budros, R., 1990. Albion-Scipio and Stoney Point Fields – U.S.A., Michigan Basin, *in* Beaumont, E.A. and Foster, N.H., eds., Stratigraphic Traps I: AAPG Treatsie of Petroleum Geology, Atlas of Oil and Gas Fields, p. 1-37.

Ivanova, V., 1995. Three-Dimensional Stochastic Modeling of Rock Fracture Systems. MS thesis, Massachusetts Institute of Technology, Cambridge, MA.

Ivanova, V., 1998. Geologic and Stochastic Modeling of Fracture Systems in Rocks. Ph.D. thesis, Massachusetts Institute of Technology, Cambridge, MA.

Journel, A., 1974. Geostatistics for the Conditional Simulation of Ore Bodies. Economic Geology, Vol. 69, pp 673-6778.

Journel, A.G. and C.J. Huijbregts, 1978. Mining Geostatistics. Academic Press, London.

Kearey, P., and Brooks, M. (1991). An introduction to geophysical exploration, 2nd Ed., Blackwell Scientific Publications, London, UK.

Kohonen, T. (1988). Self-Organization and Associative Memory. Springer-Verlag, New York.

Kulatilake, P. H. S. W., and T. H. Wu, 1984. Estimation of Mean Trace Length of Discontinuities. Rock Mechanics and Rock Engineering, 17, 215-232.

Kulatilake, P. H. S. W., 1993. Application of Probability and Statistics in Joint Network Modeling in Three Dimensions. Proc. of the Conf. on Probabilistic Methods in Geotechnical Engineering, Lanberra, Australia, 63-87.

Kulatilake, P. H. S. W., D. N. Wathugala, and O. Stephansson, 1993. Stochastic Three Dimensional Joint Size, Intensity and System Modeling and a Validation to an Area in Stripa Mine, Sweden. Soils and Foundations, 33(1), 55-70.

Lake, L. W., 1989. Enhanced Oil Recovery. Prentice Hall, Englewood Cliffs, New Jersey.

LaPointe, P. R. and J. A. Hudson (1985). Characterization and Interpretation of Rock Mass Joint Patterns. Special Paper 199, Geological Society of America Book Series.

LaPointe, P., P. Wallmann, and W. Dershowitz, 1993. Flow Compartmentalization of Effective Permeability in 3D Fractal Fracture Networks. International Journal of Rock Mechanics and Mining Sciences. Vol. 34, no. ¾ p 390.

LaPointe, P. R., P. C. Wallmann, and W. S. Dershowitz, 1993. Stochastic Estimation of Fracture Size through Simulated Sampling. Int. J. Rock Mech. Min. Sci. & Geomech. Abstr., 30(7), 1611-1617.

LaPointe, P. R., J. Hermanson and T. Eiben (2000). 3-D reservoir and stochastic fracture network modeling for enhanced oil recovery, Circle Ridge Phosphoria/Tensleep reservoir, Wind River Reservation, Arapaho and Shoshone tribes, Wyoming. Semi-Annual Technical Report - May 1, 2000 through October 31, 2000. DOE Award Number: DE-FG26-00BC15190

Long, J., 1983. Investigation of Equivalent Porous Medium Permeability in Networks of Continuous Fratures. Ph.D. Thesis, University of California, Berkeley, CA.

Malinverno, A. and D.J. Rossi, 1993. Applications of Projection onto Convex Sets to Stochastic Inversion. SPE 25659, Middle East Oil Show, Bahrain, April.

Mandelbrot, B.B., 1985. Self-Affine Fractals and Fractal Dimension. Physica Scripta 32:257-260.

Mandelbrot, B. B., 1983. The Fractal Geometry of Nature, W.H. Freeman and Company, New York.

Marx, J. and R. Langenheim, 1959. Reservoir Heating by Hot Fluid Injection. Presented at the 1959 Regional Fall Meeting of the Los Angeles Basin, San Joaquin Valley and Coastal Sections of Society of Petroleum Engineers, Cot. 22-23, 1959, Pasadena California.

Mauldon, M., 1994. Intersection Probabilities of Impersistent Joints. Int. J. Rock Mech. Min. Sci. & Geomech. Abstr., 31(2), 107-115.

Mauldon, M., and J. G. Mauldon, 1997. Fracture Sampling on a Cylinder: From Scanline to Boreholes and Tunnels. Rock Mechanics and Rock Engineering, 30(3), 129-144.

Meyer, T., Ivanova, M.V. and Einstein, H.H. 1999, Geologic Stochastic Fracture Modelling of Fracture Systems Related to Crustal Faulting, Proc. Of the 9th Int'l. Congress of the ISRM, Paris.

Meyer, T., 1999. Geologic Stochastic Modeling of Rock Fracture Systems Related to Crustal Faults. MS thesis, Massachusetts Institute of Technology, Cambridge, MA.

Midland Valley, 2001. 3Dmove (website: www.mve.com).

Miller, I, G. Lee, W. Dershowitz, and G. Sharp, 2000. MAFIC Matrix/Fracture Interaction Code with Solute Transport. User Documentation, Version 1.6. Golder Associates Inc, Seattle.

Mitra, S., 1986, Duplex structures and imbricate thrust systems: geometry, structural positions and hydrocarbon potential: AAPG Bulletin v. 70, p. 1087-1112.

Mitra, S, Namson, J., 1989, Equal-area balancing: American Journal of Science, v. 289, p. 563-599.

Mitra, S., 1990, Fault-propagation folds: Geometry, kinematic evolution, and hydrocarbon traps: Bulletin of the American Association of Petroleum Geologists, vol. 74, no. 6, p. 921-945.

Mostyn, G. R., and Li, K. S., 1993. Probabilistic Slope Analysis – State-of-Play. Proc. of the Conf. on Probabilistic Methods in Geotechnical Engineering, Lanberra, Australia, 89-109.

Mühlhaus, H-B., H. Sakaguchi and Y. Wei, 1997. Particle Based Modelling of Dynamic Fracture in Jointed Rock. Proceedings of the Ninth International Conference of the International Association for Computer Methods and Advances in Geomechanics - IACMAG 97, Wuhan, China, 2-7 November 1997.

Nicol, A., J. Watterson, J. J. Walshand, and C. Childs, 1996. The Shapes, Major Axis Orientations and Displacement Patterns of Fault Surfaces. Journal of Structural Geology, 18(2/3), 235-248.

Novakowski, K. S., Flavelle, P. A., Raven, K. G., and Cooper, E. L. (1985). "Determination of groundwater flow pathways in fractured plutonic rock using a radioactive tracer." Int. J. Radiat. Isot., 36(5), 399-404.

Oda, M., 1984. Permeability Tensor for Discontinuous Rock Masses. Geotechnique, Vol. 35, pp 483-495.

Pahl, P. J., 1981. Estimating the Mean Length of Discontinuity Traces. Int. J. Rock Mech. Min. Sci. & Geopmech. Abstr., 18, 221-228.

Paillet, E. L. (1993). "Using borehole geophysics and cross-borehole flow testing to define hydraulic connections between fracture zones in bedrock aquifers." Journal of Applied Geophysics, 30, 261-279.

Paradigm Geophysical, 2001. GeoSec 3D (website).

Petit, J.-P., G. Massonnat, F. Pueo, and K. Rawnsley, 1994. Rapport de Forme des Fractures de Mode 1 Dans les Roches Stratifiees: Une Etude de cas Dans le Bassin Permian de Lodeve (France). Bulletin du Centre de Recherches Elf Exploration Production, 18(1), 211-229.

Potyondy, D. , P. Cundall and C. Lee, 1996. "Modeling Rock Using Bonded Assemblies of Circular Parti-cles," in Rock Mechanics Tools and Techniques (Proceedings of the Second North American Rock Mechanics Symposium, Montréal, June 1996), pp.1937 - 1944. M. Aubertin, et al., Eds. Rotterdam: A. A. Balkema, 1996.

Priest, S. D., and J. Hudson, 1976. Discontinuity Spacing in Rock. Int. J. Rock Mech. Min. Sci. & Geomech. Abstr., 13, 135-148.

Priest, S. D., and J. Hudson, 1981. Estimation of Discontinuity Spacing and Trace Length Using Scanline Surveys. Int. J. Rock Mech. Min. Sci. & Geomech. Abstr., 18, 13-197.

Priest, S. D., 1993. Discontinuity Analysis for Rock Engineering, Chapman & Hall.

Robertson, A., 1970. The Interpretation of Geologic Factors for Use in Slope Theory. Proc., Symp. on the Theoretical Background to the Planning of Open Pit Mines, Johannesburg, South Africa, 55-71.

Selley, R. C. (1998). Elements of Petroleum Geology. 2nd Ed., Academic Press, San Diego, California.

Sharma, P. V. (1997). Environmental and engineering geophysics, Cambridge University Press, Cambridge, UK.

Soonawala, N. M., Holloway, A. L., and Tomsons, D. K. (1990). "Geophysical methodology for the Canada Nuclear Fuel Waste Management Program." Geotechnical and Environmental Geophysics, 1, Soc. Explor. Geophys., Tulsa, 309-331.

Stevens, K. M., Holloway, A. L., and Soonawala, N. M. (1995). "The application of ground penetrating radar for mapping fractures in plutonic rocks within the Whiteshell Research Area, Pinawa, Manitoba, Canada." J. Applied Geophysics, 33, 125-141.

Suppe, J., 1983, Geometry and kinematics of fault-bend folding: American Journal of Science, v. 283, p. 684-721.

Suppe, J., 1985, Principles of structural geology: Englewood Cliffs, New Jersey, Prentice Hall, 537 p.

Suppe, J., 1989, Rates of fault slip and fold growth (abs): GSA abstracts with programs, v. 21, p. A28.

Suppe, J., Mount, V. S., Hook, S. C., 1990, A forward modeling strategy for balancing cross-sections, AAPG, v. 74 no. 5, p. 521-531.

Svensson, U. Representation of Fracture Networks as Grid Cell Conductivities. Report SKB TR-99-25 SKB, Stockholm.

Swaby, P. and K Rawnsley, 1996. An interactive 3D fracture modelling environment. Society of Petroleum Engineers, SPE 36004, Petroleum Computer Conference, Dallas, Texas.

Terzaghi, R. D., 1965. Sources of Error in Joint Surveys. Geotechnique, 15, 287-304.

Twiss, R.J. and Moores, E.M., 1992, Structural Geology, W.H. Freeman and Company, New York.

Villaescusa, E., and E. T. Brown, 1990. Maximum Likelihood Estimation of Joint Size from Trace Length Measurements. Rock Mechanics and Rock Engineering, 25, 67-87.

Warburton, P. M., 1980a. A Stereological Interpretation of Joint Trace Data. Int. J. Rock Mech. Min. Sci. & Geomech. Abstr., 17, 181-190.

Warburton, P. M., 1980b. Stereological Interpretation of Joint Trace Data: Influence of Joint Shape and Implications for Geological Surveys. Int. J. Rock Mech. Min. Sci. & Geomech. Abstr., 17, 305-316.

Wathugala, D. N., 1991. Stochastic Three Dimensional Joint Geometry Modeling and Verification. Ph.D. Dissertation, University of Arizona, Tucson.

Winberg, A. 1999. The Tracer Retention Understanding Experiments. Presented to IAEA Meeting, Nancy, France.

Zhang, L., and H. H. Einstein, 1998. Estimating the Mean Trace Length of Rock Discontinuities. Rock Mechanics and Rock Engineering, 31(4), 217-235.

Zhang, L., 1999. Analysis and design of drilled shafts in rock. Ph.D. thesis, Massachusetts Institute of Technology, Cambridge, MA.

Zhang, L., and Einstein, H. H. (2000a). "Estimating the intensity of rock discontinuities." *Int. J. Rock Mech. Min. Sci.*, 37(5), 819-837.

Zhang, L., and Einstein, H. H. (2000b). *The Planar Shape of Discontinuities.* Report to Golder Associates Inc. Dept. of Civil Engineering, MIT.